

Shape Memory Alloy Actuators For Design Applications

Liu, Q.

DOI

[10.4233/uuid:2a8963f5-bcaf-4717-8ff7-11de9dd1b8d6](https://doi.org/10.4233/uuid:2a8963f5-bcaf-4717-8ff7-11de9dd1b8d6)

Publication date

2024

Document Version

Final published version

Citation (APA)

Liu, Q. (2024). *Shape Memory Alloy Actuators For Design Applications*. [Dissertation (TU Delft), Delft University of Technology]. <https://doi.org/10.4233/uuid:2a8963f5-bcaf-4717-8ff7-11de9dd1b8d6>

Important note

To cite this publication, please use the final published version (if applicable).
Please check the document version above.

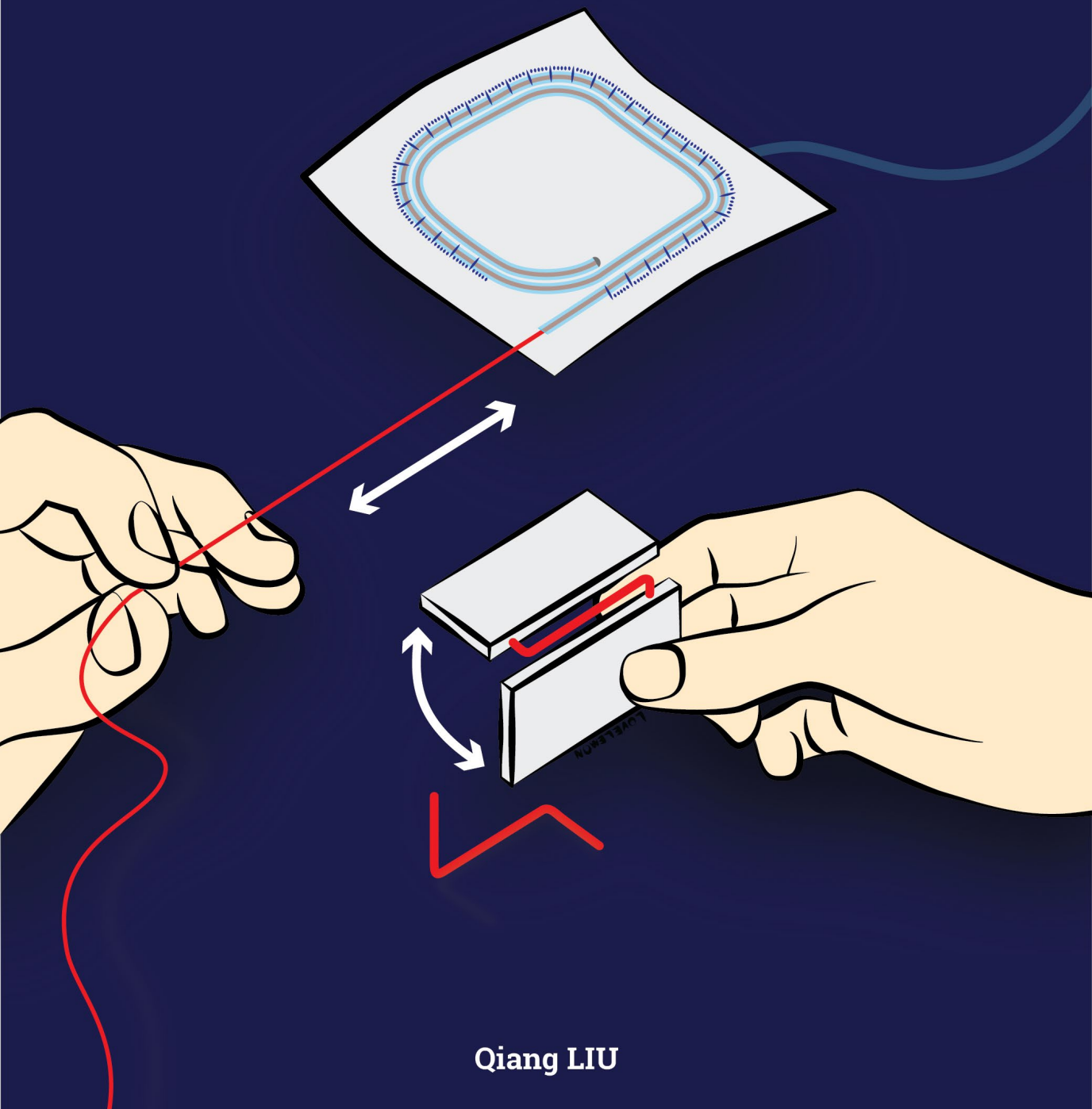
Copyright

Other than for strictly personal use, it is not permitted to download, forward or distribute the text or part of it, without the consent of the author(s) and/or copyright holder(s), unless the work is under an open content license such as Creative Commons.

Takedown policy

Please contact us and provide details if you believe this document breaches copyrights.
We will remove access to the work immediately and investigate your claim.

Shape Memory Alloy Actuators For Design Applications



Qiang LIU

Shape Memory Alloy Actuators For Design Applications

Dissertation

for the purpose of obtaining the degree of doctor
at Delft University of Technology
by the authority of the Rector Magnificus, prof. dr. ir. T. H. J. J. van der Hagen,
chair of the Board for Doctorates
to be defended publicly on
October 28th 2024 at 10 o'clock

by

Qiang LIU

Master of Fine Art in School of Design,
Hunan University, China
born in Guangdong Province, China

This dissertation has been approved by the promotors.

Composition of the doctoral committee:

Rector Magnificus	chairperson
prof. dr. ir. K. M. B. Jansen	Delft University of Technology, promotor
dr. S. Ghodrat	Delft University of Technology, copromotor

Independent members:

prof. dr. ir. Leo A. I. Kestens	Ghent University
prof. dr. ir. D. A. Abbink	Delft University of Technology
prof. dr. A. Roudaut	University of Bristol, The United Kingdom
prof. dr. L. Moreno	Universidad Carlos III of Madrid, Spain

Reserve member:

prof. dr. A. R. Balkenende	Delft University of Technology
----------------------------	--------------------------------



This research is funded by China Scholarship Council.

Cover design Qiang LIU
Layout Qiang LIU

Copyright © 2024 by Qiang LIU
ISBN/EAN: 978-94-6366-940-5

An electronic version of this dissertation is available at:

<http://respository.tudelft.nl>

To reference this document use:

<http://resolver.tudelft.nl/uuid:2a8963f5-bcaf-4717-8ff7-11de9dd1b8d6>

Table of Contents

Chapter 1 Introduction of the Thesis

1.1 Shape Memory Alloys (SMAs).....	- 2 -
1.1.1 What Is A Shape Memory Alloy.....	- 2 -
1.1.2 Stress-strain Response of Shape Memory Alloys.....	- 3 -
1.1.3 How to Obtain Desired SMA Shapes.....	- 4 -
1.1.4 How to Make An Actuator from SMAs.....	- 4 -
1.1.5 How to Enhance SMA Actuators' Performances.....	- 5 -
1.1.6 What Are the Features of SMA Actuators.....	- 8 -
1.2 Shape Memory Alloys in the Design Field.....	- 9 -
1.3 Challenges.....	- 11 -
1.4 A Proposed Strategy.....	- 12 -
1.5 Thesis Research.....	- 13 -
1.5.1 Research Gap.....	- 13 -
1.5.2 Research Question and Research Steps.....	- 14 -
1.5.3 Thesis Structure.....	- 15 -

Chapter 2 Shape Memory Alloy Actuators for Haptic Wearables: A Review

2.1 Introduction.....	- 18 -
2.2 Neurophysiology and Psychophysics of Touch in Relation to SMA Capabilities..	- 20 -
2.2.1 Haptic Perception Insights for SMA Actuators Design: Discrimination, Sensitivity and Affectivity.....	- 20 -
2.2.2 Haptic Types Provided by SMA Actuator Mechanisms.....	- 22 -
2.3 SMA-based Wearable Haptic Devices.....	- 24 -
2.3.1 Application Fields.....	- 24 -
2.3.2 Summary of Reported User Studies.....	- 28 -
2.4 Discussion and Outlook.....	- 29 -
2.4.1 Design Process for SMA-based Wearable Haptics.....	- 29 -
2.4.2 Future Applications.....	- 31 -
2.5 Summary.....	- 33 -

Chapter 3 Modelling And Design of A Flexible Tube-guided SMA Actuator

3.1 Introduction.....	- 36 -
3.2 Materials and Methods.....	- 37 -
3.2.1 Shape Memory Alloy Wire.....	- 37 -

3.2.2 Tube	- 38 -
3.2.3 Tube-guided SMA Actuator	- 39 -
3.3 Characterisation Results.....	- 40 -
3.3.1 Shape Memory Alloy Wire.....	- 40 -
3.3.2 Tube	- 43 -
3.4 Modelling.....	- 45 -
3.4.1 Mechanical Model.....	- 45 -
3.4.2 Correction for Thermal Expansion	- 46 -
3.4.3 Correction for Creep	- 46 -
3.4.4 Modelling of the tube-guided SMA actuator	- 47 -
3.5 Validation and Discussion	- 48 -
3.5.1 Parameters Fitting of the Model	- 48 -
3.5.2 Validation	- 48 -
3.5.3 Discussion.....	- 49 -
3.6 Applications	- 52 -
3.7 Conclusion and Outlook.....	- 53 -

Chapter 4* Modelling And Design of A Reversible SMA Hinge Actuator

4.1 Introduction.....	- 56 -
4.2 Materials and Configuration	- 58 -
4.2.1 Materials	- 58 -
4.2.2 Configuration of Torsion Tests	- 59 -
4.3 Testing methods of SMA and SE	- 59 -
4.3.1 Transformation Temperature Tests	- 59 -
4.3.2 Young's Modulus Tests	- 59 -
4.3.3 Shear Stress-strain Tests at Different Temperatures	- 60 -
4.3.4 Superelastic Effect Tests for SE	- 60 -
4.4 Characterisation results	- 61 -
4.4.1 DSC Thermogram for Transition Temperatures	- 61 -
4.4.2 Young's Modulus and Shear Modulus.....	- 62 -
4.4.3 Shear Stress-strain Curves at Different Temperatures	- 63 -
4.4.4 Superelastic Behaviour of SE.....	- 65 -
4.5 Modelling.....	- 66 -
4.5.1 Reversible Torsion Hinge Analysis	- 66 -
4.5.2 Modelling of SMA Shear Stress-strain Curve	- 67 -
4.5.3 Modelling of SE Shear Stress-strain Curve	- 69 -
4.6 Model Validation.....	- 72 -

4.6.1 Experiments with 5 Reversible Hinges	- 72 -
4.6.2 Model Predictions	- 74 -
4.6.3 Comparison of Experimental Data with the Hinge Model.....	- 76 -
4.7 Discussion and Application Examples	- 77 -
4.7.1 SMAs' Geometric Parameters Influence on System Angles.....	- 77 -
4.7.2 Applications	- 78 -
4.8 Conclusion.....	- 79 -

Chapter 5 * Mimosa: A Modular Hinges Kit for Creating Shape-changing Objects

5.1 Introduction.....	- 82 -
5.2 Related Work	- 83 -
5.2.1 Motor-based Shape-changing Toolkits	- 83 -
5.2.2 Pneumatic Shape-Changing Technologies	- 84 -
5.2.3 Pin-based Shape-Changing Displays.....	- 85 -
5.2.4 SMA-based Shape-Changing Toolkits	- 86 -
5.3 Mimosa Kit Components	- 86 -
5.3.1 Shape Memory Alloys (SMAs)	- 87 -
5.3.2 Hinge Leaves.....	- 87 -
5.3.3 Other Components	- 88 -
5.4 Shape-Changing Objects Construction Steps	- 88 -
5.5 Hinge Actuation Performance	- 90 -
5.5.1 Actuation force.....	- 90 -
5.5.2 Response Time	- 90 -
5.5.3 Durability	- 90 -
5.5.4 Energy Consumption	- 91 -
5.6 Hardware	- 91 -
5.7 Application Examples	- 92 -
5.8 Workshop Study.....	- 93 -
5.8.1 Set-up.....	- 93 -
5.8.2 Participants.....	- 93 -
5.8.3 Procedure	- 93 -
5.8.4 Findings	- 94 -
5.9 Discussion, Limitation, And Future Work.....	- 97 -
5.9.1 Mimosa Supports Creative Practices	- 97 -
5.9.2 Opportunities of Connecting Crafting Circuits Research.....	- 98 -
5.9.3 Limitations And Future Work	- 98 -

5.10 Conclusion - 99 -

Chapter 6 Discussion and Conclusion

6.1 Reflection on the Research Question - 102 -
6.2 Reflections on the Research of the Two Actuator Elements - 103 -
6.3 Mimosa Toolkit for Rapid Prototyping - 105 -
6.4 Promoting SMA-based Haptic Wearable Devices - 106 -
6.5 Limitation and Future Work - 106 -
 6.5.1 SMA Actuator Elements - 106 -
 6.5.2 Computer Design Tools for SMA Actuators - 107 -
 6.5.3 Testing and Improving the Models with User Studies - 108 -
 6.5.4 Upgrading the Toolkit for Complex Shape-changing Objects - 108 -
6.6 Conclusion of the Thesis - 108 -

Appendix 1* Supplement Information for the Tube-guided SMA Actuator

Appendix 2* Comparison of Different SMA Hinge Actuators

Appendix 3* Supplement Information for the Reversible SMA Hinge Actuator

References

Acknowledgements

About the Author

List of Publications

Chapter 1

Introduction of the Thesis

Shape memory alloys (SMAs) are metal alloys that, after being deformed, can revert to their original shapes when heated. SMAs are characterized by their lightweight nature and small form factors, making them suitable for developing compact actuators to facilitate shape-morphing elements. Despite their potential appeal to designers, SMAs are underutilized due to a lack of methods and guidelines.

This chapter offers a brief introduction to shape memory alloys and their applications in the design field. It introduces the research gap, articulates the main research question, outlines the research approach, and delineates the thesis structure.

1.1 Shape Memory Alloys (SMAs)

1.1.1 What Is A Shape Memory Alloy

The most well-known shape memory alloy (SMA) is nitinol, which consists of nickel and titanium. Other types of SMAs also exist, incorporating various metal components such as copper and iron (Mohd Jani et al., 2014; Rao et al., 2015). Although SMAs can be fabricated into various shapes, the commercially prevalent form is a wire.

Shape memory alloys can be deformed and then return to their original shapes after being activated (see Figure 1.1). For example, pre-stretched SMA wires can revert to their initial lengths upon heating, and pre-bent SMAs can also restore to their unbent shapes. SMAs can be activated either by exposing them to an environment with a high enough temperature or by applying an electrical current to the material, causing it to heat up (referred to as the Joule effect).

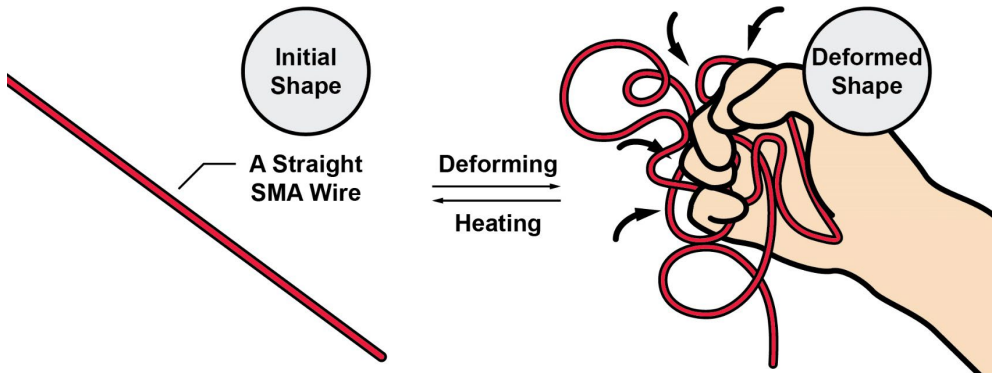


Figure 1.1 A pre-deformed SMA wire returns to its original shape after heating.

The temperature which activates the SMA is called the activation temperature (or transformation temperature). SMAs are commercially available with ranges of pre-determined activation temperatures, and the activation temperature thus should be considered as one of the design parameters. An SMA with an activation temperature between 20-30 °C will be activated when brought close to the human body, whereas an SMA with the activation temperature of 50 °C or a higher temperature should typically be activated by applying an electrical current.

SMAs have widespread applications across diverse fields, with aerospace being one of the most prominent domains (Murat et al., 2018). Examples include the TiNi *PinPuller* utilized for the *Mars Global Surveyor* and NASA's superelastic NiTi-based wheels earmarked for forthcoming moon and Mars missions (Viscuso et al., 2021). SMAs are often used in antenna deployment of spacecraft (Kalra et al., 2017) and the adaptive aircraft wings (Seelecke et al., 2004; Sofla et al., 2010). Moreover, SMAs' excellent compatibility with *magnetic resonance imaging (MRI)* as well as its biocompatibility have contributed to their widespread adoption in medical

applications (Rao et al., 2015), such as nitinol stents (Stoekel, 2000) and orthodontics (Fernandes et al., 2011).

1.1.2 Stress-strain Response of Shape Memory Alloys

The mechanical behaviour of SMA is very different from conventional metals. A typical stress-strain curve of a shape memory alloy is shown in Figure 1.2(a).

During loading from ① to ②, the SMA wire exhibits the classical elastic deformation observed in metal materials. If the SMA is unloaded between ① and ②, its length can restore to be the same as its initial. As the loading force continues to increase, the SMA then enters a strain plateau between 1%-4% (② to ③), followed by a steeper upturn (③ to ④). This phenomenon is attributed to a crystalline phase transition. Below the SMA's transformation temperature, it assumes the *twinned martensite* phase, characterized by softness and susceptibility to deformation under stress (Stöckel, 1995). Further deformation beyond 4% induces a transition to the *detwinned martensite* phase, in which SMA's stable microstructure makes it resistant to deformation. After unloading (still at low temperature), the SMA retains its deformed shape instead of returning to its original state (④ to ⑤). This behaviour resembles the classical plastic deformation process observed in metals (Rao et al., 2015). Nevertheless, shape memory alloys can regain their original shapes upon heating (⑤ to ①). The ability of SMA to recover to its predetermined shape upon heating above its transformation temperature is referred to as *shape memory effect (SME)*, which is depicted as curves ①-⑤ in Figure 1.2(a) (Rao et al., 2015).

When designing SMA actuators, it is essential to ensure that the counter force applied at low temperatures is high enough to induce deformation of the SMA into its detwinned martensite phase, achieving strains exceeding 4%. This can maximize the potential of the SMAs' shape-changing abilities. However, caution is necessary, as applying excessive forces, particularly those resulting in a high strain above 6%, can damage SMAs' microstructure, which can result in the SMA being unable to fully recover its original shape upon heating.

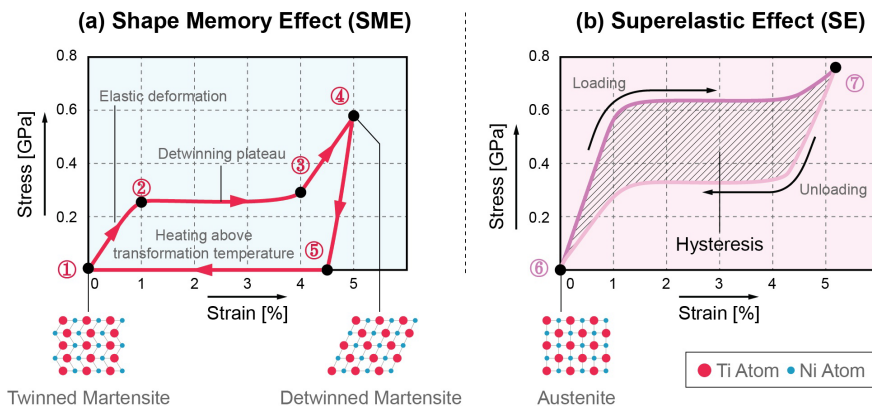


Figure 1.2 (a) Shape memory effect; (b) Superelastic effect (Rao et al., 2015).

At high temperature above SMAs' transformation temperature, SMAs transform to the *austenite* phase, in which atoms are arranged in cubic structure (see Figure 1.2 (b)). SMA austenite phase can withstand large deformations without permanent change. The *superelastic effect* refers to the fact that shape memory alloy can fully revert to its original shape upon unloading, even though the material undergoes large deformation (up to 8%) (Mohd Jani et al., 2014; Rao et al., 2015). Note that although the recovery is complete after unloading, the loading and unloading stress-strain curves follow different paths (curve ⑥-⑦ and ⑦-⑥), and they form a large *hysteresis* (see shaded region in Figure 1.2(b)). Such large hysteresis make SMAs very efficient energy dissipation systems (Janke et al., 2005). In fact, a superelastic SMA can be considered as a fully-actuated SMA.

1.1.3 How to Obtain Desired SMA Shapes

Desired SMA shapes can be achieved through the SMA training process. As depicted in Figure 1.3, the straight SMA wire from the material supplier must first be deformed and then secured tightly to a fixture using screws before being placed in an oven. Generally the temperature for heat treatment ranges from 400 °C to 500 °C, and the soaking time in ovens vary between 5 and 30 minutes (Rao et al., 2015). Specific heat treatment conditions can be obtained by inquiring material suppliers. Research shows that the training temperature and duration time have influence on the SMA material's mechanical response, transformation temperatures, plateau strain and energy dissipation capabilities (Morgan et al., 2004; Sadiq et al., 2010). After heat treatment, the fixture should be removed from the oven and quenched in cold water for cooling.

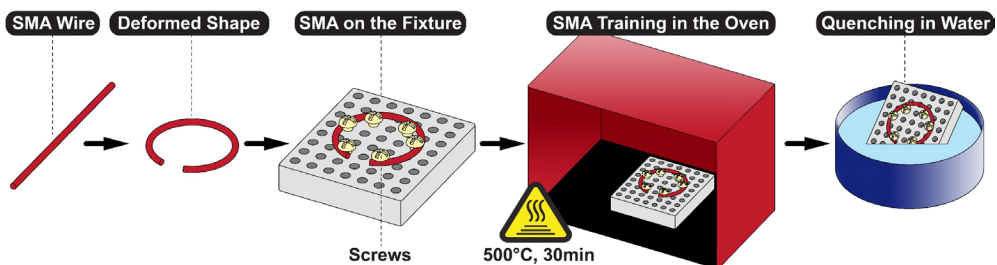


Figure 1.3 Shape memory alloy training process for desired shapes.

1.1.4 How to Make An Actuator from SMAs

SMAs can be reshaped following in an arbitrary shape, and recover to their original forms upon heating. The problem is that returning from the complex deformed shape to its initial shape is a one-way process (as shown in Figure 1.1). To restore the deformed shape, a series of well defined local forces is required. Such restoring forces can be generated by a counter spring, an elastic component of a structure, or through another opposing SMA acting as an antagonist. However, designing an actuator system that can reliably transition between two complex shapes is far from simple.

To explain this, two examples are provided here. As depicted in Figure 1.4(a), an SMA wire is stretched by a weight. When reaching its activation temperature, the SMA contracts and the weight is lifted. Conversely, upon cooling, the gravity acting on the weight stretches the SMA. Note that insufficient weight could fail to elongate the SMA wire at the cold state, while excessively heavy weight may impede the contraction of the heated SMA wire. Therefore, selecting an appropriate weight is essential for the actuator system to function effectively. Similarly, for a shape-changing interface which has a curved SMA wire embedded in a flat thin elastic substrate (see Figure 1.4(b)), in ideal conditions, the system rolls up upon activation, and returns to a flat form after cooling due to the elastic force of the substrate. Nevertheless, if the substrate is too stiff, the interface cannot roll up when heated; whereas a low elasticity substrate would not be able to provide enough force to flatten the system at low temperature.

For simple actuator systems, balancing between the actuation force and the counter force can be achieved through trial and error. However, more complex designs necessitate a systematic approach, such as using the stress-strain diagram depicted in Figure 1.2(a). To fully utilize SMAs' shape-changing capabilities, it is needed to select a counter stress in the range between points ③ and ④ of Figure 1.2(a) which can transform the SMAs to its detwinned martensite completely. Overall, designing advanced SMA actuator systems consequently demands expertise in both design principles and materials science.

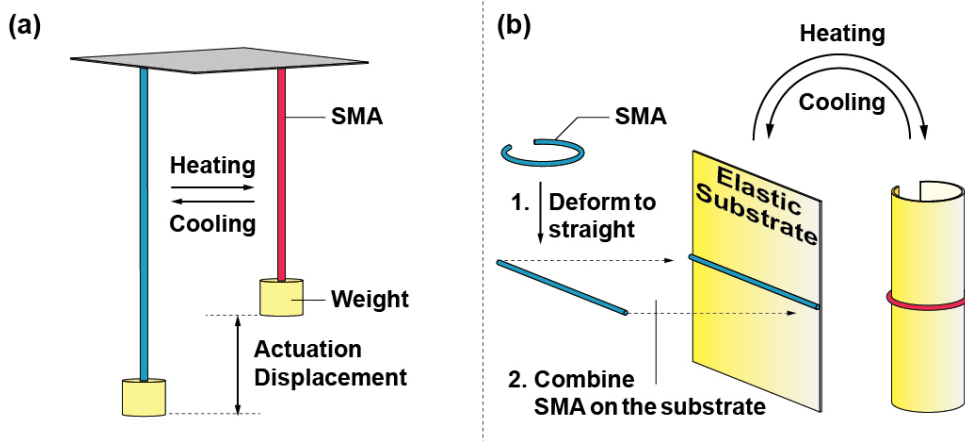


Figure 1.4 (a) An SMA wire suspending with a weight to form an elongation actuator. (b) An SMA wire and an elastic flat substrate combine as an SMA bending actuator.

1.1.5 How to Enhance SMA Actuators' Performances

To design an SMA actuator capable of delivering enough force or achieving desired displacement, some methods are frequently used to enhance its mechanical performances.

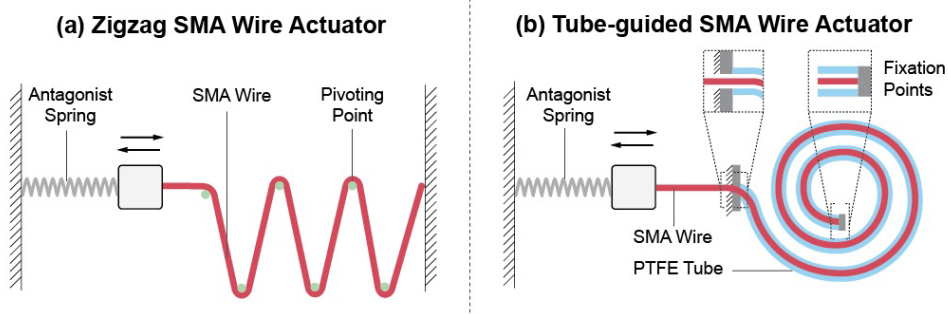
(1) Increased Actuation Force

Actuation stress of a pre-stretched nitinol wire is typically 150-200 MPa (DYNALLOY, 2021a; Hartl et al., 2007; Kim et al., 2008), indicating that a 0.1 mm diameter NiTi wire of 0.01 g weight can exert a force of about 1.2-1.6 N during actuation. To obtain higher actuation force, a large diameter SMA wire can be used. For example, a 0.5 mm diameter SMA can produce 30-40 N, which is much higher compared to that of the 0.1 mm diameter SMA. However, large diameter SMA wires are stiff and rigid, rendering them unsuitable for some application scenarios (e.g. wearable devices). An alternative approach is to use multiple thin wires in parallel, which can increase the actuation force while preserving flexibility.

(2) Increased Actuation Displacement

Nitinol-type SMA wires exhibit a maximum actuation strain of approximately 4% of their total length (e.g., 4 cm for a 1 m SMA wire), meaning that the actuation displacement of the bare SMA wire mechanism is limited. To achieve a large displacement, longer wires are required, posing a challenge in embedding such extended wires into compact devices.

There are several methods to address this issue. The first method is to arrange a long SMA wire into a zigzag shape with several pivoting points (see Figure 1.5(a)). The second option is the tube-guided SMA wire actuator. As can be seen in Figure 1.5(b), a long SMA wire is inserted into a plastic tube, which can be rolled up and only needs two fixation points (Helps et al., 2019; Liu, Ghodrat, et al., 2022). The third actuator structure is a SMA spring coil, which can also generate larger displacement in comparison with the SMA wires (Figure 1.5(c)). However, the increase of actuation displacement for spring coil actuators is accompanied by a reduction in actuation force. Knitted SMA wire actuators (see Figure 1.5(d)) are also an option which can provide large displacement and force, but they are difficult to manufacture in comparison with other methods. The actuation displacement of knitted SMA is complex and depends on details of the knitted structure (Eschen, Granberry, & Abel, 2020; Eschen, Granberry, Holschuh, et al., 2020; Yi et al., 2017).



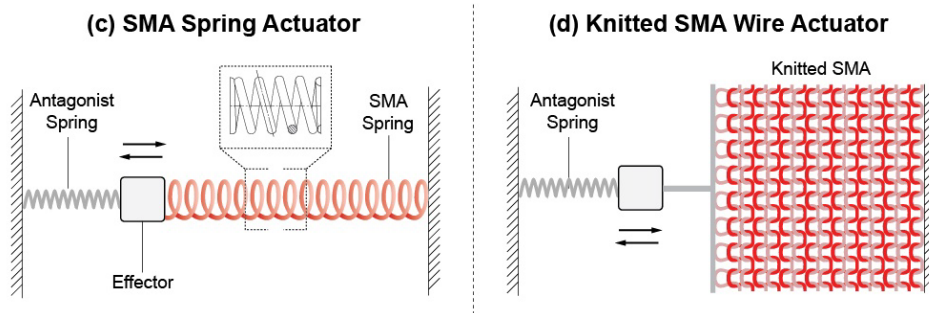


Figure 1.5 Constructions for increasing the actuation displacement. (a) A zigzag SMA wire actuator. (b) A tube-guided SMA wire actuator. Note that the tube can be wound in a same diameter circle or in spiral. (c) An SMA spring coil actuator (An et al., 2012). (d) A knitted SMA wire actuator (Eschen, Granberry, Holschuh, et al., 2020).

(3) Shortening the Actuation Time

Actuation time refers to the time taken for a single actuation cycle, including both the time needed for actuation (during heating) and returning to the initial state (during cooling). It mainly depends on the heat exchange speed with the environment. SMA actuators with effective insulation heat up rapidly but may experience prolonged cooling time.

Heating can be achieved by changing the environmental temperature or by Joule heating of the SMA wire. Since the electrical resistivity of SMA is rather high ($0.5\text{--}1.1 \times 10^{-6} \Omega\text{m}$), it is easy to heat the wire by applying an electric current (Rao et al., 2015). However, it is much more difficult to reduce the cooling time because the cooling rate is constrained by the heat transfer rate to the surrounding environment (Nizamani et al., 2017). It is estimated that for a 0.2 m long 0.5 mm diameter SMA wire and a required temperature change of $\Delta T = 65^\circ\text{C}$, about 6 s is needed for heating, while the cooling process lasts for 40 s (Rao et al., 2015).

A reduction in cooling time can be achieved by using thinner wires, enhancing airflow (Mao et al., 2020), or using wires with higher actuation temperatures which have a faster initial cooling rate. Studies indicate that when exposed to an airflow of 20 l/min, a 0.4 mm diameter SMA wire with a length of 0.2 m undergoes a cooling period of around 7 s. In contrast, the same wire requires approximately 20 s to cool down in the absence of airflow (Lara-Quintanilla et al., 2016). Circulating cold fluid with a high thermal conductivity around SMA is another effective way (Nizamani et al., 2017). Nevertheless, incorporating either airflow or cold fluid techniques adds weight and volume to the SMA devices, potentially compromising the comfort and shape factor of wearables. Moreover, the airflow approach might generate noise. The cold fluid technique necessitates proper sealing, and the requirement of a liquid tank could restrict user mobility.

(4) Enhancing the Energy Efficiency

Energy efficiency is often calculated as a ratio of the useful work output to the energy input, in which work output is equal to the actuator exerted force multiplied by the distance over which the force is applied, and the energy input is assessed by measuring the electrical energy consumed. Energy consumption of SMA actuators mainly depend on geometric dimensions (e.g. cross-sectional area, total length) and transformation temperatures. The maximum energy efficiency of SMA actuators are reported in a range of 10-15% in the literature (Cismasiu, 2010; Jackson et al., 1972; Manfredi et al., 2017). Note that the main reason for this low efficiency is the fact that it requires a continuous supply of energy to keep the actuator in its actuated state. Energy consumption can be reduced by introducing a latch mechanism, which can maintain the actuator at its actuated state with mechanical structure without continuous heating. Research also shows that high voltage pulses which lead to actuation time in the millisecond range can improve the energy efficiency (Motzki, 2020).

1.1.6 What Are the Features of SMA Actuators

Five features of SMA actuators are summarized in this subsection, which indicates SMA actuators' working conditions and advantages for future applications.

(1) Low Voltage Requirement

A 0.25 mm diameter SMA wire ($A_f = 75\text{ }^\circ\text{C}$) of 50 cm length requires approximately 5.4 V (0.7 A) for activation (Liu, Ghodrat, et al., 2022). For the SMA bending deformation, a 1.00 mm diameter SMA wire ($A_f = 45\text{ }^\circ\text{C}$) with a length of 5 cm only requires 1 V to activate. Commercial AA batteries are capable of meeting voltage requirements at this level.

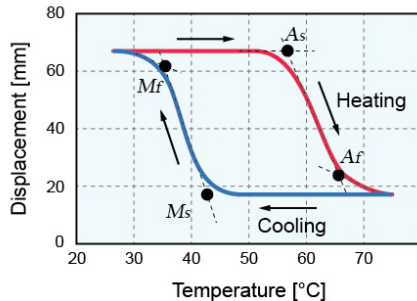
(2) Transformation Temperatures

The transformation temperatures refer to the onset and end temperatures of the phase transformations in SMAs: the *martensite start temperature* (M_s), *martensite finish temperature* (M_f), *austenite start temperature* (A_s) and *austenite finish temperature* (A_f). The displacement-temperature graph depicted in Figure 1.6(a) shows the transformation temperatures of the SMA actuator in Figure 1.2(a). During the heating, the SMA wire starts to contract at $57\text{ }^\circ\text{C}$ (A_s) and completely transforms to austenite at $66\text{ }^\circ\text{C}$ (A_f) (see the red curve in Figure 1.6(a)). Throughout the cooling process, the SMA transforms to martensite between $43\text{ }^\circ\text{C}$ (M_s) and $36\text{ }^\circ\text{C}$ (M_f), during which the SMA wire is stretched by the weight and the displacement increases.

Transformation temperatures of SMAs mainly depend on the material composition and, to a minor extent, affected by thermal annealing conditions (Surbled et al., 2001). Transformation temperatures of nitinol are quite sensitive to the percentage of Ni. Studies show that an increase of 0.1 Ni atomic percent from its equiatomic composition can lead to $10\text{ }^\circ\text{C}$ decrease of the transformation temperature (Buehler

et al., 1963; Lagoudas, 2008). Similarly, Frenzel et al.'s research reveals that 1% increase of the Ni content from 50.0% to 51.0% results in about 130 °C reduction in martensite start temperature (Figure 1.6(b)) (Frenzel et al., 2010).

(a) Displacement-temperature Graph with Transformation Temperatures



(b) The Effect of Ni content on Martensite Start Temperatures

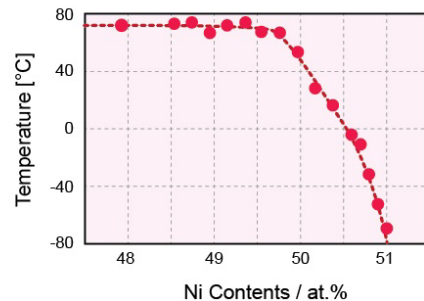


Figure 1.6 (a) Displacement-temperature graph of the SMA actuator in Fig 1.3(a). Transformation temperatures are indicated in the graph as A_s , A_f , M_s , M_f . (b) The effect of Ni content on NiTi's martensite start temperatures (Frenzel et al., 2010).

(3) High Flexibility and Small Form Factor

Compared with rigid mechanical structures, SMA wires are thin, bendable and lightweight. Such features make it them easy to be embedded into textiles or other thin material surfaces (e.g. TPU).

(4) Noiseless

In contrast to other conventional actuators like electric motors, SMA actuators operate with no friction or vibration, allowing extremely silent movements (Cismasiu, 2010). It makes SMA actuators especially suitable for silence circumstances such as conference rooms and healthcare facilities.

(5) Lifetime

Lifetime assessment is necessary for engineering devices which need to be subjected to cyclic mechanical motion. It is often recommended to maintain SMAs strain change below around 6% (for uniaxial stretching deformation), within which SMAs can have over 10^6 actuation cycles (Li et al., 2009). Operating above this limit induces the formation of microcracks, resulting in irreversible damage to SMAs and eventual failure

1.2 Shape Memory Alloys in the Design Field

In recent years, SMAs have been employed in some design applications, such as *SMA-based haptic wearables* (Hamdan et al., 2019; Kim, Huang, et al., 2021), *toolkits for shape-changing interfaces construction* (Nabil et al., 2019) and *SMA*

morphing interfaces for creative expression (Genc et al., 2021). This subsection will briefly introduce these three types of SMAs' applications.

(1) SMA-based Haptic Wearables

SMAs have the advantages of small form factor, lightweight and high flexibility, which make them easy to incorporate into wearables. During actuation, SMA-based actuators can generate different types of force feedback on the human's skin, simulating various types of haptic feedback like press, squeeze, pinch, etc. There have been many research about SMA-based haptic wearables, such as *ShareHaptics* (Nakao et al., 2019) and *PhantomTouch* (Muthukumarana et al., 2019) (Figure 1.7(a)) for mixed reality, *Affective Sleeve* for emotion regulation (Papadopoulou et al., 2019), and *Tactile Vest* as a notification interface (Jones et al., 2004).

(2) Toolkits for Shape-changing Interfaces Construction

Some HCI researchers use SMAs as actuation materials to develop toolkits or prototyping platforms for designers, with which they can customize tangible and engaging shape-changing interfaces in an efficient way. For example, with Qi's *Animating Paper*, users can make a shape-morphing origami cranes (Figure 1.7 (b)) or wall hanging decorative strips (Qi et al., 2012). Prototyping platform *ClothTiles* enables designers to fabricate customized actuators (with SMAs and 3D printing) for cloth applications such as a face-mask loosener and eye-mask massager (Muthukumarana, Messerschmidt, et al., 2021). *NURBSforms* can be used for prototyping curved interfaces (Tahouni et al., 2020).

(3) SMA Morphing Interfaces for Creative Expression

With the shape-changing ability, SMAs can also be incorporated in everyday objects or artworks to enrich their expressions. For example, Probst et al. presented sticky paper notes *Move-It*, which can deform and remind users an approaching event (e.g., 5 minutes before) by triggering SMA bending deformation (Probst et al., 2011). The *Luminescent Tentacles System* is a scalable kinetic surface system for kinetic art, ambient display, and animatronics (Figure 1.7(c)). The 256 SMA actuator wires react to hand movement, and they behave like the waving tentacles of sea anemones (Nakayasu, 2016). Similarly, *Himawari* is a sunflower prototype with shape-changing petals which can interact with users (Nakayasu, 2010). *Shadow Lamp* is a novel concept of textile-based shadow displays that incorporates SMAs on fabrics to cast dynamic shadows as an ambient information display. A user study shows that it feels like a decorative addition to the living spaces (Genc et al., 2021).

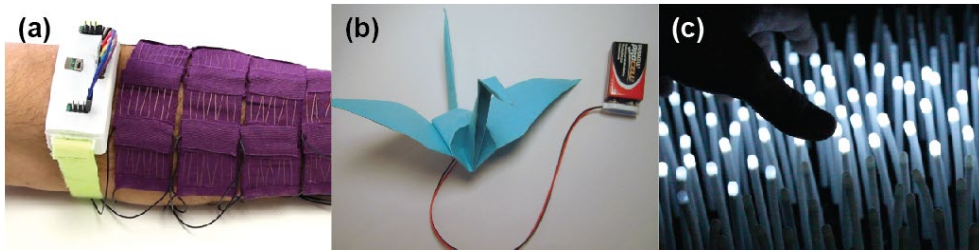


Figure 1.7 (a) *PhantomTouch* (Muthukumarana et al., 2019); (b) *Animating Paper*: a shape-morphing origami cranes (Qi et al., 2012); (c) *Luminescent Tentacles System* (Nakayasu, 2016).

A survey indicates that published articles about SMAs exceed 70,000 during the period from 2020 to 2029 (Sellitto et al., 2019). These articles involve a variety of fields like material science, engineering and biomedical technologies (Balasubramanian et al., 2021; Mohd Jani et al., 2014). Nevertheless, only a few interdisciplinary research labs, such as MIT Media Lab, Hybrid Body Lab, and Morphing Matter Lab, are exploring the potential of SMAs in design applications. It is surprising that SMAs are not currently used more often within the realm of design.

1.3 Challenges

The limited application of SMAs in the design domain stems from various challenges. Here four main challenges are introduced.

(1) High Cost

SMA wires are now priced at USD 1-8 per meter. It is considered expensive for common uses. The price is expected to continuously decline due to advancements in production technologies like manufacturing processes (Rajput et al., 2022; Rao et al., 2015). Historical data indicates that it decreased from USD 1100 per kilogram in 1999 to USD 111 per kg in 2004 (Chang et al., 2016). In addition, mass production is expected to lead to price reductions. For instance, some commercial products manufactured with SMAs, such as nitinol spectacle frames, dental braces and bras supports, have become relatively affordable due to the large-scale production.

(2) Constraints of Material Forms

Most commercially available SMA materials are sold in the wire form, with only a few material suppliers offering SMA coil springs, strips, and foils. The restricted material forms presents a challenge to the widespread application of SMAs. For example, the fabrication of an SMA knitted actuator necessitates the use of a knitting machine compatible with SMA wires, which is a procedure that demands specialized skills. When intricate forms are required, designers are compelled to negotiate with manufacturers to develop solutions. Generally, manufacturers tend to produce custom SMA shapes only when receiving substantial volume orders.

(3) Difficulty of Achieving Complex and Reversible Movements

Although the basic working principles of shape memory alloys may seem easy to understand, creating reliable SMA actuators capable of producing intricate movements remains far from simple. Challenges exist particularly in resetting the SMA actuators with the aid of counter forces at low temperature, which is essential for the preparation of the subsequent heating actuation, so as to make the SMA actuators *two-way*.

For instance, the deformed shape depicted in [Figure 1.1](#) locally involves various types of deformation, such as stretching, bending, and rotation. Upon heating, the SMA will revert to its initial straight form. However, during subsequent cooling the wire remains straight and to the deformed shape as shown on the right hand side of [Figure 1.1](#) could only be retained by applying a complex series of deformations. The construction of a system with distributed elastic counterforces that would reproduce a complex shape such a that in [Figure 1.1](#) would thus be nearly impossible or at least very impractical. So far, there is no structural solution for designing SMA actuators which can produce complex and reversible movements.

(4) Challenge of Designing SMA Actuators with Desired Performance

Trial and error methods are still often used during the design phase. For example, achieving a precise effector position for the SMA spring actuator depicted in [Figure 1.5\(c\)](#) often requires designers to test different combinations of antagonist springs and SMA springs, which is an inefficient approach. Though there have been many models which can be used for predicting SMAs' actuation behaviours, most of them are constitutive models based on thermodynamics, such as Tanaka et al.'s model ([Tanaka et al., 1982b](#)) and Brinson et al.'s model ([Brinson et al., 1996](#)). These models try to describe as accurate as possible the relation between the phase transition state temperature, stress and strain, involving thermodynamics of nucleation, growth or interface friction at a molecular level ([An et al., 2012](#)). Such models include many technical terminologies and are less practical for those outside the field of materials science.

1.4 A Proposed Strategy

To mimic more complex and reversible movements, **I propose a strategy** of first decomposing an arbitrary movement into a series of connected simple movements. For each fundamental movement type, a simple, controllable, and reliable actuator system will be designed. The desired movement is then reconstructed by combining these actuator systems.

The direction and magnitude of forces both have influences on the trajectories of objects' movements. The force types depicted in [Figure 1.8\(a1-c1\)](#) align with three fundamental motions: translation, bending, and rotation ([Figure 1.8\(a2-c2\)](#)). Essentially, all complex movements can be seen as combinations of these three basic types. An example is provided in [Figure 1.8\(d\)](#): a snake-like movement can be

decomposed into a series of units. Each unit is able to generate translational, bending and rotational motion. By integrating multiple units, complex movements can be achieved.

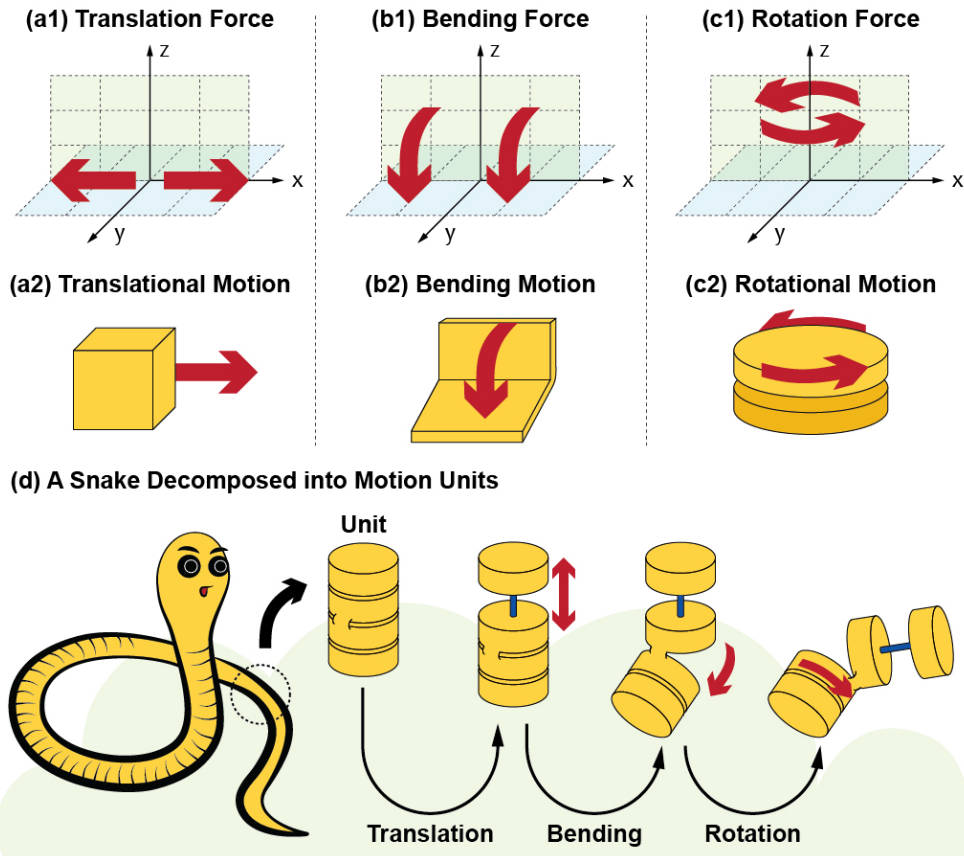


Figure 1.8 Three types of force (a1)-(c1) lead to different motions (a2)-(c2). (d) A snake-like movement decomposed with a series of movement units.

1.5 Thesis Research

1.5.1 Research Gap

SMA s have shown huge potential in a variety of applications. However, they are not commonly used in the design field due to numerous challenges as introduced in subsection 1.3. It can be seen that with the commencement of mass production and an increase in demand, some challenges such as *high cost* and *constraints of material forms* will be effectively resolved. Therefore, the priority of expanding the SMA s utilization is to remove impediments for designers in using SMA materials. It can facilitate the development of high-quality applications and consequently stimulating demand. To achieve this, this thesis will address the challenge (3) *Difficulty of*

Achieving Complex and Reversible Movements, as well as (4) Challenge of Designing SMA Actuators with Desired Performance.

1.5.2 Research Question and Research Steps

This research aims at providing designers and HCI scholars with tools and resources to improve the efficiency of designing and prototyping with shape memory alloys, thereby expanding SMAs' utilization in the design field. The main research question in this thesis is: ***How to open up the potential of shape memory alloys for designers?***

I propose to tackle this by dealing with the challenge (3) and (4) mentioned above and using the decomposition strategy outlined in [subsection 1.4](#). To accomplish this, the following steps will be employed.

(1) Identifying fundamental actuator elements

As mentioned in [subsection 1.4](#), I propose to decompose complex movements into three types of fundamental motions: translation, bending, and rotation ([Figure 1.8\(a2-c2\)](#)). Therefore, in the first step, I first will develop these basic actuator elements consisting of SMAs and passive materials that can provide the counter force for reverting the actuators at the cold state. Each actuator element is tailored for a specific type of motion, and they will serve as fundamental building blocks for reconstructing more complex movement patterns.

(2) Measuring constituent materials of the actuators

Characterizing the properties of the constituent materials in SMA actuators is fundamental to understanding their actuators' working principles. This entails conducting material characterization both on the SMA wire and the passive materials that generate the counter force. The variables considered include stresses, strains, and changes in temperature.

(3) Developing mechanical models for SMA actuator systems

In order to predict the behaviour of an actuator system, a mechanical model is needed for linking the geometry parameters like lengths and diameters to the material behaviour of the SMA and the other elements of the system. The output of this model will be the typical actuator's responses, such as the actuation displacement and angle. The data for the material models will be derived from step 2 above.

(4) Verifying the mechanical models

To determine the accuracy of the actuator predictions, a series of dedicated validation experiments will be conducted.

(5) Designing with SMA actuators

In order to showcase the potential of the actuator elements and inspire designers to use them, several shape-morphing demonstrators will be presented.

1.5.3 Thesis Structure

The structure of this thesis is arranged as follows (see Figure 1.9). Chapter 1 introduces shape memory alloys and their design applications. The research gap, primary research question, and research methodology are outlined. Chapter 2 reviews the state-of-the-art of shape memory alloy haptic wearable devices. It is provided as an entrance for understanding the capabilities of SMA actuators in the design field. In Chapter 3, the translational SMA actuator element, which is a tube-guided SMA actuator, is described, and a mechanical model is presented to predict the actuation displacement. As two example, a haptic navigator for visually impaired people and a brush-stroke haptic bracelet based on the tube-guided SMA actuator are developed. In Chapter 4, an SMA hinge actuator (i.e., the bending actuator element) and its model are proposed. Chapter 5 introduces a modular shape-changing toolkit based on the SMA hinge actuator. A workshop is organized to evaluate the user experience of the toolkit. Finally, Chapter 6 discusses the thesis in general and concludes the research outcome. Note that the design and validation of the third fundamental actuation type, the rotational actuator element, is still an open task.

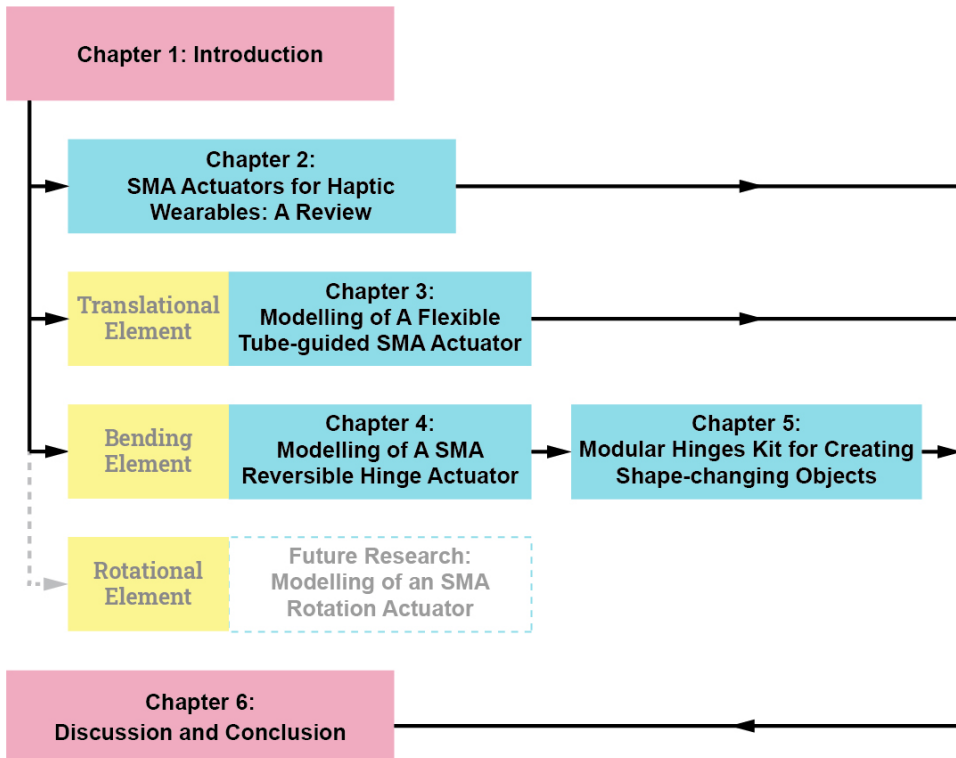


Figure 1.9 Thesis structure.

Chapter 2 ^{*}

Shape Memory Alloy Actuators for Haptic Wearables: A Review

Before developing the fundamental actuator elements, the applications of SMAs in the design field are first explored. Our investigation reveals that haptic wearable devices constitute a major area of application, yet a comprehensive review of this topic is still underrepresented in current research. Hence, this chapter provides the state-of-the-art of SMA haptic wearables, serving as an entry for understanding SMA applications in the design field. Specifically, it shows how the SMA capabilities are related to psychophysics of touch. Future applications of the SMA actuator systems in the haptic field are discussed.

* This chapter is based on:

Liu, Q., Ghodrat, S., Huisman, G., & Jansen, K. M. B (2023). Shape memory alloy actuators for haptic wearables: A review. *Materials & Design*, 112264.

DOI: [10.1016/j.matdes.2023.112264](https://doi.org/10.1016/j.matdes.2023.112264)

2.1 Introduction

The term “haptic” refers to the sense of touch (Alur et al., 2014). Studies on haptic perception originated in the field of physiology pioneered by Weber in the late 19th-century (Parisi, 2018). After that, researchers started to use haptic technologies for teleoperation (El Saddik et al., 2011), such as Goertz and Thomson’s teleoperation robot developed for nuclear environments (Goertz et al., 1954). These machines enabled operators to feel the contact force encountered by the end effectors when they manipulated the control devices (Goertz, 1952). Such devices are often referred to as “force displays”, which dominated the haptic field until the mid-1990s (El Saddik et al., 2011). Relevant products include *GROPE* (Brooks Jr et al., 1990), *PHANToM* (Massie et al., 1994), and *CyberGrasp* (Burdea, 1999). The progress in computer science facilitated the integration of haptic technology into numerous commercial fields such as computer-assisted design, medical applications, military, and videogames (Eid et al., 2016; El Saddik et al., 2011; Heikkinen et al., 2009; Parisi, 2018). Nowadays, haptic technologies evolved beyond merely force displays, leading to a growing diversity of applications and interactions. In addition to vibration, which has remained in commercial use to the present day (Fukumoto et al., 2001), other types of actuators (e.g. pneumatic, ultrasonic, smart materials) have been successively developed.

Researchers are foreseeing low-cost, lightweight, compact, energy-efficient, and highly mobile devices capable of delivering diverse haptic feedback modalities in the near future (El Saddik et al., 2011). However, there remain many challenges in haptic technology development nowadays. On the software side, substantial computational demands associated with complex haptic rendering algorithms and models necessitate the utilization of high-performance computer chips (Catkin et al., 2023; El Saddik et al., 2011; Lin et al., 2008). On the hardware side, there is a trade-off between the quality of actuators and bulkiness (El Saddik et al., 2011). The “quality” refers to the volume, weight, flexibility and richness of the haptic feedback types that the actuators can provide. For example, despite vibration actuators are small and lightweight, they cannot provide haptic feedback such as pressing or squeezing. In contrast, pneumatic actuators generate haptic sensations through alternating pressurization and depressurization of chambers (Agharese et al., 2018; Choi, Lee, et al., 2021; Zhang et al., 2021), yet their size and dependency on air pumps make them less compact.

To address these challenges, the incorporation of smart materials into the haptic field has emerged as a promising approach. Smart materials are materials which can be active and responsive to various stimuli, such as temperature, electricity, magnetism, humidity, and light (Murat et al., 2018). They have the potential to facilitate the development of innovative haptic interfaces through various means. On the one hand, some smart materials can be employed in designing flexible sensors or electronic components that conform to the skin’s compliance (Park et al., 2015; You et al., 2018; Zhu et al., 2020), which can improve mechanical transmission and promote

ergonomic comfort (Miriyeve et al., 2017). Several literature reviews address these aspects specifically. For example, Yang et al. provided an overview of current active materials-based sensors and actuators for haptic technologies in virtual (VR) and augmented reality (AR) (Yang et al., 2021), while Yin et al. also concentrated on VR and AR systems (Yin et al., 2021). Biswas and Visell highlighted the potential of emerging materials (e.g. organic electronic materials and carbon nanomaterials) to enable high mechanical flexibility in haptic devices (Biswas et al., 2019). Moreover, Ho et al. reviewed the advancement in material designs for electrically driven soft actuators (Ho et al., 2022). On the other hand, some shape-changing materials (e.g. electro active polymer (EAP) (Gratz-Kelly et al., 2023; Wang et al., 2022), shape memory alloy (SMA), magnetorheological fluid (MRF) (Liu, Gao, et al., 2022; Lutanto et al., 2023)) can function as actuators in haptic systems, and generate rich haptic feedback types.

SMA has been used in a range of wearable devices. Based on their functionalities, these wearables can be categorized into two main types: assistive devices and haptic devices. Assistive devices refer to the applications which are developed to aid people with disabilities in performing functions (Cook et al., 2014), or maintain users' physical functions in extreme environments. For example, Xie et al. developed an elbow exoskeleton with SMA springs (Xie, Meng, Yu, Xu, et al., 2023), while Ali and Kim designed a small-scale knee exoskeleton (Ali et al., 2023). For more research about SMA wearable exoskeletons refer to (Kim, Jeon, et al., 2022; Kumar et al., 2022; Srivastava, Singh, et al., 2022; Zhang, Cong, et al., 2022). Rehabilitation is another type of assistive devices, with relevant research found in (Lai et al., 2023; Xie, Meng, Yu, Wu, et al., 2023; Zuo et al., 2023). Nair and Nachimuthu reviewed SMA applications in the medical field, where they also documented some assistive devices such as wearable exoskeletons and SMA prostheses (Nair et al., 2022). Moreover, SMA can be used to develop smart garments to support astronauts' cardiovascular systems (Eschen, Granberry, Holschuh, et al., 2020; Holschuh et al., 2016). Compared with SMA assistive devices, there is less research about wearable haptic devices. Srivastava et al. analyzed the recent research work in the field of SMA-based smart wearables, followed by a discussion regarding the diverse applications of SMA in human-robot interaction and industry 5.0 (Srivastava, Alsamhi, et al., 2022). Their review article only provides limited coverage of SMA haptic wearables.

This chapter reviews the opportunities of SMA wire-based actuators for wearable haptic devices, which is currently absent in current research. In section 2.2, the correlations between haptic and SMA material fields are elucidated, within which different SMA mechanisms and their provided haptic feedback types are emphasized. Haptic wearables documented in existing literature are classified and reviewed, along with an analysis of their reported user studies in section 2.3. Finally, a discussion and outlook section is provided.

2.2 Neurophysiology and Psychophysics of Touch in Relation to SMA Capabilities

2.2.1 Haptic Perception Insights for SMA Actuators Design: Discrimination, Sensitivity and Affectivity

Haptic perception relies on two types of systems: the cutaneous and kinesthetic systems (Loomis et al., 1986). Although both systems are essentially underpinned by nerve cells, they play different roles in humans' somatosensory system. The kinesthetic system is to manage internal signals (e.g., body position, limb direction, and joint angle, etc.) sent from the muscles, tendons and joints about the position or movement of a limb (Lederman et al., 1987). Receptors of the kinesthetic system are generally embedded in muscle fibers and joints. The cutaneous system is responsible for handling sensations gained from skin sensitivity, including vibration, touch, pressure, temperature, and texture. Despite their distinct functionalities, most everyday haptic perception is a combination of cutaneous and kinesthetic sensations.

From a deeper perspective of neurophysiology, four principal types of mechanoreceptors distribute inside human skin, which are *Pacininan corpuscles*, *Ruffini corpuscles*, *Merkel corpuscles* and *Meissner corpuscles* (Figure 2.1) (Johnson, 2001). These corpuscles have different sensibilities for distinct haptic types. For instance, *Ruffini corpuscles* can sense stretch and pressure, while *Meissner corpuscles* have a higher sensitivity to vibration (Teyssier, 2020). Once receiving a touch single, massages are conveyed quickly through myelinated nerve fibers, and finally reached and processed by the somatosensory cortex (Figure 2.1).

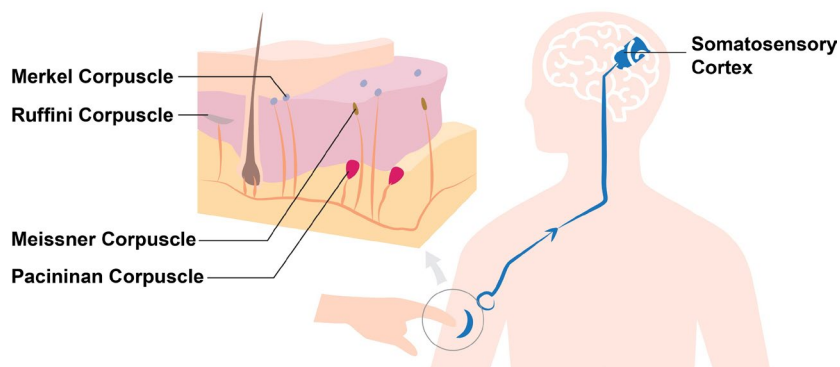


Figure 2.1 Haptic perception process basing on cutaneous system (Medical, 2014).

(1) Two-point Discrimination Threshold

Two-point discrimination threshold is often used to measure tactile spatial acuity. The two points are distinguishable from one only when they are sufficiently separated to evoke spatially distinct neural activity patterns (Mountcastle et al., 1968; Vallbo et al., 1978). The discernible minimum distance between the two points depends on the skin area, ranging from 1 mm on the tip of the tongue to 68 mm on the back and thigh (Eskildsen et al., 1969; Woodworth et al., 1954). This threshold is able to guide the

design of haptic devices by determining the appropriate resolution and actuator distribution. For skin areas with high tactile acuity, densely packed haptic actuators can provide more realistic and natural haptic feedback. In contrast, fewer actuators are needed for skin with lower thresholds, which can reduce material and manufacturing costs.

Given the SMA characteristics of small size, it is suitable to employ SMAs in high-resolution haptic devices within limited space. Taylor et al. showcased this by incorporating a sixty-four-element tactile array in a compact 4×2 cm area (Taylor et al., 1998). Similar studies are referenced in (Kontarinis, 1993; Singhal et al., 2013). Even though these dynamic braille displays are not wearable devices, SMAs have demonstrated their potential for creating wearables for skin areas with low two-point discrimination thresholds.

(2) Absolute-thresholds of Force Perception

Owing to the varying density and distribution of mechanoreceptors in different skin regions, skin at different locations exhibits distinct sensitivity to force, which is referred to *absolute-thresholds* of force perception (Hatzfeld et al., 2016). Fingertips and facial skin show a heightened responsiveness to tactile sensations (Weinstein, 1968). A fingertip has an absolute-threshold of 0.8 mN, while the value is 1.5 mN for the palm (Burdea, 1996). The values can be affected by other parameters like contact area, stimulation duration, skin temperature and user age (Jones et al., 2006). A sensitivity experiment based on the *Von Frey Monofilaments* method also shows that the forehead and palm can detect the minimum force of 0.07 g, followed by the arm at 0.4 g, and the thigh and shin with a higher threshold of 1.0 g (Ackerley et al., 2014). The actuation force level of SMAs is sufficient to satisfy the minimum threshold necessary for perceiving tactile stimuli on the skin. However, it also depends on SMA mechanism designs, as the actuation force generated by SMAs often differs from the force experienced by the skin in most scenarios.

(3) Tactile Direction Discrimination

Tactile direction discrimination measures humans' abilities to differentiate the direction of an object moving across the skin (Norrzell et al., 2001). The discrimination thresholds of the arm, palm, thigh and shin vary from 18 mm to 27 mm (Ackerley et al., 2014). To achieve the desired displacement using a bare SMA wire with an actuation strain of 4%, a length ranging from 45 to 67.5 cm is required.

(4) Temperature Discrimination

Temperature perception relies on two distinct types of thermoreceptors: cold receptors and warm receptors (Hensel et al., 1984). Cold receptors are up to 30 times more abundant than their warm counterparts, indicating a higher sensitivity to detecting changes in colder temperatures (Jones et al., 2002). Warm receptors respond

to increasing skin temperatures, with their discharge rate reaching a peak at around 45 °C (Stevens, 1991). When the temperature is maintained at 30-36 °C, individuals typically are not able to experience a noticeable thermal sensation (Jones et al., 2002).

Commercially available SMAs typically have an activation temperature range of 20-100 °C. Many existing SMA-based haptic wearables focus on isolating heat during SMA actuation rather than incorporating thermal feedback alongside force feedback. Everyday haptic interactions between individuals inherently involve thermal sensations. In this regard, SMA technology holds an advantage over alternative approaches like vibration or pneumatic systems, as it can potentially integrate both force and thermal feedback for a more comprehensive haptic experience.

(5) *CT Afferents for Affective Touch*

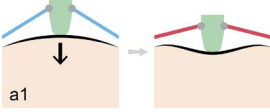
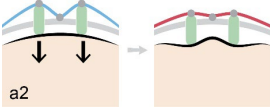
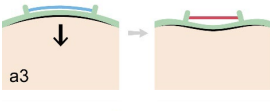
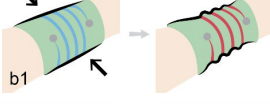
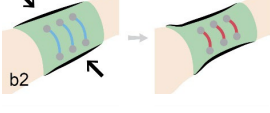
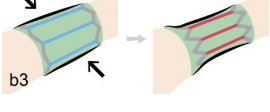
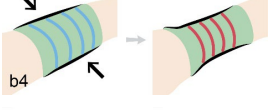
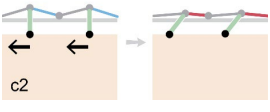
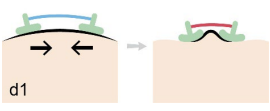
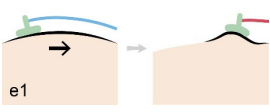
Distinct from the discriminative touch, which relies on the four types of receptors illustrated in Figure 2.1, *affective touch* is a unique type responding optimally to gentle stroking (Johansson et al., 1988). This form of touch is conveyed through *C-Tactile (CT)* afferents, predominantly found in hairy skin, and is processed in the insular cortex, an area associated with emotional processing (Gordon et al., 2013; Nagi et al., 2011). Affective touch is considered to have evolutionary significance due to its critical role in social bonding and attachment (Jablonski, 2021; Morrison et al., 2010).

Studies indicate that a stroke speed of 1-10 cm/s is generally perceived as comfortable (Löken et al., 2009; McGlone et al., 2014). In particular, users tend to prefer a stroking speed of 1-3 cm/s on the arm, shin, or palm for enhanced pleasantness (Ackerley et al., 2014). This information can serve as a guideline for determining the actuation speed of SMA haptic devices, which can be regulated by adjusting the applied voltage.

2.2.2 Haptic Types Provided by SMA Actuator Mechanisms

There are different classifications of haptic types in literature. Morrison et al. defined three categories of social touch, which are simple (e.g. tapping), protracted (e.g. pressing), and dynamic (e.g. stroking) (Huisman et al., 2013; Morrison et al., 2009). Stanley and Kuchenbecker presented several forms of human physical contact, including tapping, dragging, squeezing, and twisting (Stanley et al., 2011). In order to categorize SMA-based haptic wearables, we identified five distinct haptic feedback types, which are press, squeeze, stroke, pinch, and drag. Visual representations of each haptic feedback type, along with their associated SMA actuator mechanisms, are provided in Table 2.1.

Table 2.1 Haptic Types and Corresponding Mechanisms.

Haptic Feedback Type	Mechanisms	Descriptions	Reference
a. Press		Two SMA wires/springs are fixed with an actuator point. Upon activation, the SMAs contract and the actuator point moves down.	(Hwang et al., 2017; Jones et al., 2004)
		The actuator features a pair of actuation points capable of vertical movement, either upward or downward, as a result of temperature changes during the cooling or heating phases.	(Yoshikawa et al., 2006)
		Activation of SMAs induces a bending deformation of the elastic material (e.g. TPU) adhered to the skin. It is essential to avoid using soft textiles, as they may wrinkle and hardly exert pressure on the skin during deformation.	(Hamdan et al., 2019)
b. Squeeze		A long SMA wire that has two fixed ends wraps around a human's limbs or torso.	(Nakagaki et al., 2015)
		Several SMA springs are fixed on the device in parallel. It should be noticed that the green part material should be soft textile. During actuation, the textile slides on the surface of skin, and it is pulled taut to generate a squeeze sensation.	(Compton et al., 2021; Duvall et al., 2016)
		The actuator consists of two circular zigzag parts (grey color) and a row of parallel SMA springs. Actuation of the SMA causes deformation of the zigzag part and results in a squeezing movement.	(Simons et al., 2020)
		Multiple large-diameter SMA wires are pre-trained in an open circle which has a smaller circumference in comparison with the arm. When heated, SMAs tend to roll up, thereby generating a squeeze sensation.	(Kim, 2023)
c. Stroke		The actuator point is pulled from left to right during the heating process. When it is cooled down, the antagonist spring/elastic band can pull the actuator point back to its original position.	(Liu, Ghodrat, et al., 2022)
		A parallel array of actuator points which is perpendicular to the skin before actuation. Once it is actuated, the actuator points are pulled by the SMA, and the tilting movement leads to a stroke sensation.	(Knoop et al., 2015b)
d. Pinch		Two actuator points are fixated on two areas of skin. The part of the skin between the two actuator points is pinched during actuation.	(Haynes et al., 2019; Messerschmidt et al., 2022; Simons et al., 2020)
e. Drag		An actuator point is fixated on the skin or fingers. When the SMA is heated, the actuator point is dragged.	(Nakao et al., 2020)

2.3 SMA-based Wearable Haptic Devices

2.3.1 Application Fields

Upon reviewing the current literature on SMA-based wearable haptic devices, we categorized their applications into three fields: virtual reality/augmented reality, affective haptics and notification interfaces. Table 2.2 provides an overview of the existing devices, organized by their respective application fields. *Body location* and *haptic feedback type* offer brief insights into the devices.

(1) Virtual Reality/Augmented Reality

In VR/AR environments, haptic devices convey the physical attributes of virtual objects, such as the shape, mass, texture, elasticity and thermal properties, to express physical perception and interactions with virtual objects (Scilingo et al., 2010). Current SMA-based haptic wearables for VR/AR focus on simulating the shape and weight of virtual objects. Most of the current SMA haptic devices in this category are designed for the fingers or the hand (see Table 2.2).

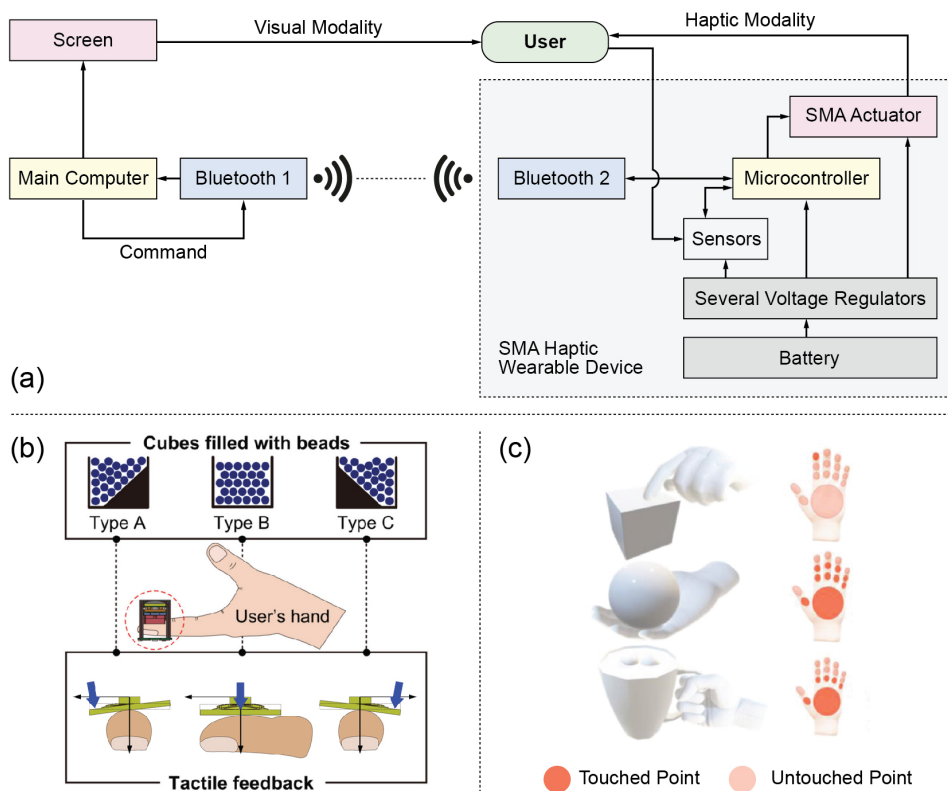


Figure 2.2 (a) A brief diagram of a type of SMA-based VR haptic device system (Hwang et al., 2017; Zhang, Kamezaki, et al., 2022). (b) *HaptiCube* has 5 degrees of freedom, and can simulate the weight of the falling beads (Lim et al., 2021). (c) A VR glove with several SMA actuators at the finger joints (orange dots). With different actuation points, users can feel shapes of different objects (Kim, Gu, et al., 2022).

Figure 2.2(a) is a diagram of a type of SMA-based VR haptic device system summarized from the literature (Hwang et al., 2017; Zhang, Kamezaki, et al., 2022). The position changes of the virtual objects on the screen should be synchronized with users' movements. Data collected by sensors in the wearable device is continuously sent to the main computer through Bluetooth. Once the preset conditions are fulfilled, i.e., a user's hand reaches a target position, the main computer will send an actuation command, and the microcontroller activates the SMA subsequently.

Lim et al. developed a finger-wearable tactile interface *HaptiCube* with several SMA wires (Lim et al., 2021). With different SMA wires actuated, the device displays five-degrees-of-freedom haptic feedback. *HaptiCube* is able to express pressure by the device increases in proportion to the falling beads (see Figure 2.2(b)). Kim et al. designed VR gloves by using several SMA textile actuators, which were placed at the finger joints. With different actuation points, users can feel virtual objects in diverse shapes (see Figure 2.2(c)) (Kim, Gu, et al., 2022). Similarly, "Skin+" made with SMA and auxetic structures was able to provide users with a simulated feeling of "catching something" (Cao et al., 2018). "Touch me gently" can provide feedback which was close to real touch (Muthukumarana et al., 2020).

To obtain realistic haptic feedback, the force generated by the SMA actuators during interaction with virtual objects should be consistent with the force that users feel in real life. The actuation force of SMA increases with higher temperature, which means that to avoid excessive force, a method to regulate SMA's temperature should be used. The first option is to figure out the relationship between SMA actuation force and temperature by performing material tests, and then link the temperature to the applied current (refer to Rao's work in chapter 7 (Rao et al., 2015)). This option might involve modelling processes. With the models, the main computer can predict the SMA actuation force with the applied current values, and can cut off the power or lower the current when the force is too high. Some existing SMA constitutive models (Brinson et al., 1996; Tanaka et al., 1982a) and practical models (Liu, Ghodrati, et al., 2022; Rao et al., 2015) are valuable references for this method. The second option is to embed extra temperature or force sensors, to detect SMA's working status and collect data for further evaluation (e.g. *HaptiCube* (Lim et al., 2021)). Compared with the first option, the second one is relatively simple, but it might increase wearable devices' weight and volume.

In addition to force feedback, response time is another factor that affects users' haptic experience when using VR/AR wearables. For example, in Hwang's study, they found that when a user moved out of the surface of the virtual objects, SMA actuators still generated force feedback on users' fingertips (Hwang et al., 2017). It is because the cooling speed of the SMA is relatively slow. In VR/AR environments, excessive latency can lead to a decrease in immersion, inconsistency in motion, and may even result in symptoms such as motion sickness (Brunnström et al., 2020; Kundu et al.,

2021). Therefore, it is necessary to reduce the cooling time with a current-modulation method or cooling mechanism.

(2) Affective Haptics

Affective haptics refers to the design of devices and systems that can detect, process, or display the emotional state of humans by means of the sense of touch (Eid et al., 2016). *Social touch technology* and *mediated social touch* are similar concepts, which emphasize the employment of haptic technology for social interactions, including human communication via technology and interactions with responsive artificial social agents (Haans et al., 2006; Huisman, 2017; Van Erp et al., 2015).

Most of the current SMA-based affective haptic devices focus on the squeeze-type haptic feedback (see Table 2.2). The sensation of squeezing in haptic devices is particularly suitable for simulating *deep touch pressure*, which is a type of tactile input received when firmly touching, holding, swaddling, or hugging (Grandin, 1992). Research shows that *deep touch pressure* can help reduce anxiety (Chen et al., 2013). A relevant example is “*Hugging Vest*” (see Figure 2.3(a)), enabling parents or occupational therapists to give remote warm “hugs” to children with mental illness (Duvall et al., 2016). Similarly, Kim also designed *SereniSleeve* for anxiety regulation (Figure 2.3(b)) (Kim, 2023).

Yarosh et al. developed the *SqueezeBands* system, which augments social gestures over videochat with haptic actuation (see Figure 2.3(c)) (Yarosh et al., 2017). They demonstrated that *SqueezeBands* was appropriate for easing mental and physical demands in high-emotion tasks. Wang and Quek designed an upper arm squeeze-type SMA-based haptic device, and their research showed that remote touch can reinforce the meaning of a symbolic channel reducing sadness significantly (Wang et al., 2010a).

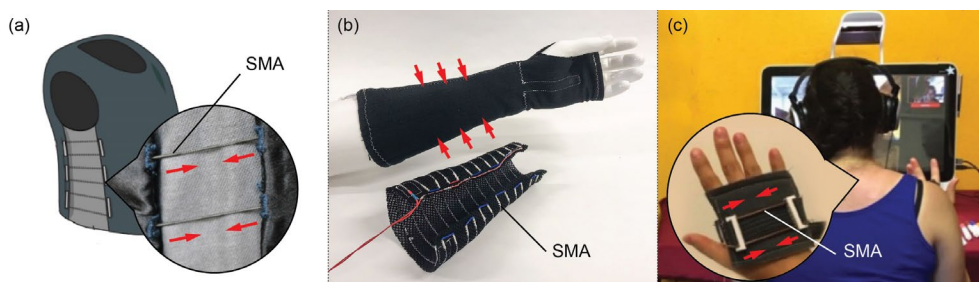


Figure 2.3 (a) *Hugging Vest* can generate a squeeze sensation on users’ trunk (Duvall et al., 2016). Red arrows indicate the actuation behaviours upon heating. (b) *SereniSleeve* for anxiety regulation (Kim, 2023). (c) *SqueezeBands* for videochat (Yarosh et al., 2017).

Table 2.2 SMA-based haptic wearables documented in literature.

Applications	Wearable Haptic Device	Body Location	Haptic Feedback Type
VR / AR	(Lim et al., 2021)	Fingertip	Press, Shear Force
VR / AR	(Zhang, Kamezaki, et al., 2022)	Fingertip	Press
VR / AR	(Esposito et al., 2018)	Fingertip	Press
VR / AR	(Lim et al., 2017)	Fingertip	Press, Stroke
VR / AR	(Nakao et al., 2020)	Finger	Press
VR / AR	(Hwang et al., 2017)	Finger	Press, Shear force
VR / AR	(Terrile et al., 2021)	Finger	Drag
VR / AR	(Cao et al., 2018)	Hand	Squeeze
VR / AR	(Kim, Gu, et al., 2022)	Hand	Press
VR / AR	(Muthukumarana et al., 2020)	Wrist	Stroke
VR / AR	(Priebe et al., 2020)	Torso, Arm, etc.	Squeeze
VR / AR	(Nakao et al., 2019)	Wrist, Ankle, etc.	Press
Affective Haptics	(Simons et al., 2020)	Wrist	Pinch, Squeeze, etc.
Affective Haptics	(Muthukumarana, Elvitigala, et al., 2021)	Arm	Stroke, Press, etc.
Affective Haptics	(Wang et al., 2010b)	Arm	Squeeze
Affective Haptics	(Papadopoulou et al., 2019)	Arm	Warm Press
Affective Haptics	(Kim, 2023)	Arm	Squeeze
Affective Haptics	(Duvall et al., 2016)	Torso	Squeeze
Affective Haptics	(Compton et al., 2021)	Torso	Squeeze
Affective Haptics	(Foo et al., 2019)	Torso, Arm, etc.	Squeeze
Affective Haptics	(Yarosh et al., 2017; Yarosh et al., 2022)	Hand, Arm, etc.	Press
Notification Interfaces	(Chernyshov et al., 2018)	Finger	Squeeze
Notification Interfaces	(Liu, Ghodrat, et al., 2022)	Arm	Stroke
Notification Interfaces	(Ghodrat et al., 2023; Sandhir, 2021)	Arm	Stroke, Press
Notification Interfaces	(Jones et al., 2004)	Torso	Press
Tele-operation	(Kobayashi et al., 2012)	Finger	Drag
Interpersonal Toolkit	(Suhonen et al., 2012)	Wrist	Squeeze
Prototyping Platform	(Muthukumarana, Messerschmidt, et al., 2021)	Various Positions	Stretch, etc.
Not Defined	(Solazzi et al., 2011)	Fingertip	Stroke
Not Defined	(Lücker et al.)	Hand	Stroke, Press
Not Defined	(Knoop et al., 2015b)	Wrist	Stroke
Not Defined	(Gupta et al., 2017)	Wrist	Squeeze
Not Defined	(Nakamura et al., 2003)	Torso	Press
Not Defined	(Hamdan et al., 2019)	Arm, Neck, etc.	Pinch, Press, etc.
Not Defined	(Sun et al., 2020)	Arm, Leg, etc.	Pinch
Not Defined	(Kim, Huang, et al., 2021)	Hand, Ankle, etc.	Pinch, Twist, etc.

(3) Notification Interfaces

Notification interfaces can be defined as applications that facilitate the delivery of reminders, updates or alerts to the users (Saket et al., 2013). The *SCWEES*, made by 3D printed semi-flexible structure and SMA wires, can generate displacement and force on the wrist's skin (Simons et al., 2020), which enables non-intrusive notifications. Some researchers have not explicitly defined the specific purposes of their devices; however, their prototypes also demonstrate the potential for use as

notification interfaces. Examples include “*Tickler*” (Knoop et al., 2015a) (refers to Table 2.1(c2)), *Fingertip Tactile Glove* (Mun et al., 2018a).

2.3.2 Summary of Reported User Studies

The focus of user studies largely depends on the application domains of haptic devices. Research on notification interfaces primarily emphasizes the evaluation of device performance. In contrast, studies in the realms of VR/AR and affective haptics tend to concentrate on users’ emotional experiences (e.g., happiness, sadness and anger) while interacting with SMA wearable haptic devices.

Usability evaluation involves many parameters, such as force, displacement, and the actuation speed of the SMA system. As explained in section 2.2.1, these parameters can affect the noticeability and discriminability of devices and have a significant impact on usability. Some research has included relevant performance studies, such as “*SCWEES*” (Haynes et al., 2019) and “*In contact*” (Simons et al., 2020), which investigated the strength of sensation perceived by participants. Effective devices should elicit positive emotional responses from users. Various methods are employed to assess users’ feelings during device usage. Researchers can ask participants to rate their experiences, such as “*pleasantness*”, “*displeasure*”, “*comfort*” and “*immersion*” with *Likert Scale* (Simons et al., 2020; Wang et al., 2010a), or request them to describe their experiences through questionnaires (Cao et al., 2018). Wang and Quek used *Pre- and Post-positive Affective Negative Affective Schedules* to measure the changes in users’ feelings and emotions before and after they used the haptic device (Wang et al., 2010b; Watson et al., 1994).

Note that in most cases, a user study is not the final step of the research. It usually accompanies the entire mid- and late-stage process of haptic device development, as the results of the user study can guide the design (Lazar et al., 2017). For example, in Kim’s research, which is an SMA-based squeeze device (see Figure 2.3(b)), several user studies were conducted (Kim, 2023). At the early stage, different SMA mechanisms (including b1, b2 and b4 in Table 2.1) were developed to evaluate which can generate desired squeeze sensations, and then mechanisms b4 based on different SMA wire diameters were fabricated for another test. SMA with larger diameters can generate higher force, but would reduce the comfort of wearables as the prototype becomes stiffer. In the final user study, they investigated whether the haptic device could reach its design goal. Moreover, with the results of the user study, Hamdan et al. summarized the noticeability, discriminability, comfort, and reaction time of *Springleet* on different body locations (e.g. wrist, arm, shoulder, neck, chest and back) (Hamdan et al., 2019), which is valuable information when deciding on where to attach SMA-based haptic devices to the body.

2.4 Discussion and Outlook

Working performance and features of SMA technologies are clarified in [section 1.1](#). Prior to selecting the SMA materials for wearable haptics design, it is recommended to conduct a thorough assessment and contrast with other emerging technologies (e.g. EAPs, MRFs). Generally, SMA actuators can produce different haptic feedback types as listed in [Table 2.1](#). They are especially suitable for squeeze and stroke feedback types owing to their characteristic of shrinkage upon heating. As for EAPs, they might be more applicable for haptic devices which can generate press feedback (e.g. fingertips devices ([Mun et al., 2018b](#))) due to their large deformation capacity. However, EAPs' actuation force is relatively low and they often require a much higher voltage to activate (from hundreds of volts to a few kilovolts). Most of the existing MRFs-based haptic wearable devices are gloves for VR ([Blake et al., 2009](#); [Winter et al., 2007](#)), which can generate force feedback on users' fingers. Actually, MRFs have more applications in surgical instruments as they can give passive feedback by slowing down human-initiated movements ([Tsujita et al., 2013](#)). For more details about these smart materials refer to the literature ([Biswas et al., 2019](#); [Yang et al., 2021](#)).

2.4.1 Design Process for SMA-based Wearable Haptics

In the traditional product design process utilizing conventional materials, designers often explore various textures and finishes during the later stages of product development. Their primary considerations and choices emphasize aesthetic appeal. Compared with conventional materials, smart materials including SMAs serve as functional actuators in systems, influencing aesthetics as well. Thus, it is imperative to thoroughly assess material properties, performance, and associated factors during early design stages. Material-centered approaches are an option for developing smart materials-based devices, which emphasizes the importance of understanding and leveraging the unique attributes of materials in order to create innovative and functional products. As a type of material-centered approach, *Material Driven Design (MDD)* ([Karana et al., 2015](#)) has been used in research involving emerging materials ([Barati et al., 2020](#)). The material-centered approach can also be applied to the development of SMA-based wearable haptic devices ([Ghodrat et al., 2023](#)). Nonetheless, this method primarily emphasizes materials and their properties, advocating for the exploration of potential applications. It may not be entirely appropriate for developing products with pre-identified specific requirements. For designers with definitive objectives for their haptic devices, the subsequent design process based on material-centered approach can serve as a reference.

(1) Selection of Haptic Feedback Type

Five haptic feedback types that SMA actuators can provide are listed in [Table 2.1](#). Designers can make selections according to application scenarios of their conceptual haptic devices.

(2) SMA Materials Tinkering

This hands-on, exploratory activity can assist designers in acquiring a preliminary understanding of SMAs' shape-memory ability. Two experiments are recommended in this step. The first involves conducting a tensile test using a slender SMA wire measuring 50-100 cm in length. A counterweight can be attached to one end of the wire, causing it to stretch due to gravitational force. Subsequently, an electric current can be applied to heat the SMA wire, enabling it to counteract gravity and raise the counterweight. This tensile experiment demonstrates the high actuation force and small actuation displacement of SMAs. The second test involves custom shape training of SMAs. Designers can create desired shapes by bending wires with a suggested diameter of over 0.5 mm. SMA training process can be seen in [Figure 1.3](#). After cooling in cold water, the wires can deform at low temperatures but return to custom shapes when heated. This experiment exhibits the shape memory effect in the bending mode. For more information, refer to Rao's research ([Rao et al., 2015](#)).

(3) Reversible SMA Mechanism Design

Some SMA mechanisms are shown in [Table 2.1](#), categorized by haptic feedback types. Designers may choose an appropriate mechanism or create new ones. A challenging step involves pairing SMAs with suitable bias force (e.g. coil spring, elastic band, another SMA wire), which must be sufficiently strong to deform SMAs in their cold state without impeding their return to original shapes at high temperatures. Sequential tests with various SMA wires and antagonists may be required to identify the optimal pairing.

(4) Comparing Mechanism Working Performance with Haptic Perception Parameters

Utilizing SMA mechanism actuators, fundamental performance metrics like actuation force and stroke can be assessed and compared to haptic perception parameters. For a haptic navigation device designed to generate stroke sensations on the skin, it is essential to ensure that the actuation displacement of SMA actuators exceeds the perception threshold required for tactile direction discrimination.

(5) Design and Construction of Wearable Haptic Devices

The concept of "wearability" in wearable technology encompasses factors influencing the wearer's comfort, including physical, psychological, and social aspects ([Dunne et al., 2014](#); [Gemperle et al., 1998](#)), all of which must be taken into account during the design process.

(6) User Study of the Devices

User studies aim to explore the user experience of haptic devices, enabling the collection of valuable feedback for subsequent iterative design improvements.

2.4.2 Future Applications

(1) Designing with Visually Impaired People

There are approximately 285 million people with visual impairments in the world (He et al., 2020), and the number is expected to increase in the future. Auditory cues are a primary method of feedback in navigation and movement assistance tools, owing to the considerable capacity of the auditory sense to convey information (Pawluk et al., 2015). Nonetheless, the sole reliance on the auditory modality for information conveyance may prove insufficient, and sound-based cues can inadvertently mask delicate auditory signals utilized by visually impaired individuals (Brabyn, 1982), especially in emergencies (Amemiya et al., 2008). Therefore, haptic communication offers an alternative means of transmitting sensory information.

Visually impaired individuals necessitate adaptable haptic devices to cater to their varied requirements. Within the realm of education and learning, SMA technology has been employed in refreshable tactile displays (Bhatnagar, Marquardt, et al., 2021; Bhatnagar, Upadhyay, et al., 2021; Matsunaga et al., 2013; Takeda et al., 2013; Velazquez et al., 2005). However, their full potential has yet to be realized in the development of other diverse assistive equipment. For instance, educational activities that involve diagrams can pose challenges for those lacking visual image cognition, and collaboration between visually impaired individuals and sighted peers may prove difficult. Although some studies have tackled these issues (Nam et al., 2012; Siu et al., 2021), they have primarily focused on alternative haptic technologies. It is anticipated that the field will witness increased applications of SMAs in this domain.

In the navigation field, most existing haptic devices rely on vibration (e.g. *Travel Path Sounder* (Russell, 1965), *Miniguide* (Brabyn, 1982)). Given that roadway entities, such as vehicles and pedestrians, frequently exhibit dynamic and unforeseeable behaviors, vibration technology has an advantage owing to their response speed. However, it maybe not intuitive because users are required to learn the meanings of different vibration patterns (Amemiya et al., 2008). SMA-based haptic devices can address this by swiping in various directions on the skin with the stroke haptic type, which is an instinctive method for indicating direction. They are suitable for circumstances that do not require frequent directional adjustments. Thin SMA wires or other alternative methods can be adopted to reduce the response time.

(2) Immersive Technologies

Immersive technologies refer to technologies that blur the boundary between the physical and virtual worlds and enable users to experience a sense of immersion (Lee et al., 2013; Suh et al., 2018). The market for immersive technologies, including augmented reality and virtual reality, has expanded to various industry domains, such as tele-manipulation, medical training, gaming and entertainment (Yang et al., 2021). To emulate the perception of tactile sensations in a realistic manner, multiple points

of interaction should be facilitated, but this would dramatically increase the complexity and bulkiness of the hardware (El Saddik et al., 2011). SMAs are lightweight and have high power-to-weight ratios. It makes them an appropriate option for developing wearable haptic devices in the field of virtual reality where limiting the size and weight may be crucial for supporting satisfying user experiences.

In contemporary VR electronics, the harmonization of various output modalities, including visual, auditory, and haptic, can effectively enhance users' immersive experiences. Nevertheless, the majority of present research on SMA haptic devices primarily investigates the impact of diverse haptic feedback types on users' perceptions, without integrating visual and auditory elements. It implies that the potential of SMA technologies has yet to be thoroughly explored and harnessed.

(3) Remote Interpersonal Haptic Communication

Tactile signals constitute a vital component of daily affective communication. Research shows that mediated touch can help reduce stress and build social connections between users (Haans et al., 2006; Huisman, 2017; Takahashi et al., 2011). Individuals engage in various forms of physical contact, such as handshaking during greetings, seeking hugs for emotional support when feeling low, and clapping to express excitement. These tactile interactions serve as essential components of interpersonal communication, helping to establish social connections, convey emotions, and strengthen bonds between individuals.

Replicating the feel of authentic human touch contact is a formidable challenge, and current technology lacks the sophistication to mimic all the qualities of real touch (Raisamo et al., 2022). Vibrotactile actuators are small, inexpensive and easy to control (Choi et al., 2012). Nevertheless, research indicates that force feedback actuators are perceived as more natural compared to vibrotactile touch, leading to increased emotional interdependence (Ahmed et al., 2016). Jewitt et al. presented that to bring the richness of “real” touch into the digital, there is a need to “move beyond vibration” (Jewitt et al., 2021). A survey conducted during the COVID-19 lockdown revealed that over 90% of participants expressed missing hugs, while approximately 20% missed receiving a stroke or a pat on the shoulder (Ipakchian Askari et al., 2022), which is challenging to replicate with existing commercial haptic technologies. As depicted in Table 2.1, SMAs are able to generate various haptic types with different mechanism designs. By integrating various haptic modalities, such as thermal feedback, SMA-based haptic devices have the potential to generate more natural and realistic feedback. Moreover, In a longitudinal study examining the use of squeeze bracelets for couples, researchers discovered that the sound produced by the bracelets was occasionally perceived as annoying (van Hattum et al., 2022). This observation could highlight another benefit of SMA technology, which is noiseless during actuation.

2.5 Summary

In recent decades, the haptics field has experienced significant advancements, and the demand for advanced haptic technologies continues to grow. Despite this, only a few technologies have reached commercial success. One challenge in developing innovative haptic devices lies in balancing their size and the variety of haptic experiences they offer. Generally, haptic devices capable of offering sophisticated and natural tactile feedback tend to contain numerous mechanical components, resulting in bulkiness and difficulty to wear. Shape memory alloys (SMAs) are lightweight, compact, and possess high power-to-weight ratios. Additionally, they can be integrated with textiles and other soft materials like TPU, offering considerable aesthetic appeal. These attributes make SMAs suitable for designing wearable haptic devices.

In this chapter, the relations between haptic and SMA material fields are introduced. Haptic perception information can be guidance for designing SMA actuators, while distinct SMA actuator mechanisms can offer a variety of haptic types. Application domains of existing devices are categorized, and user studies of the devices are summarized. A recommended design process for SMA-based wearable devices is proposed in the discussion. Given the characteristics of SMAs, we believe they hold potential for designing haptic devices for visually impaired individuals and demonstrate significant promise in the areas of immersive technologies and remote interpersonal haptic communication.

This chapter serves as an entrance to understanding SMA applications in the design field. Starting from the next chapter, the focus will shift to the fundamental actuator elements.

Chapter 3 *

Modelling And Design of A Flexible Tube-guided SMA Actuator

In Chapter 1, we proposed to develop an SMA actuator for each of the fundamental movement types. This chapter focuses on the translational element, which is a tube-guided SMA actuator. We measure and model both the SMA and tube material properties, including the tube creep effects. Based on these simple material models, a mechanical model is proposed that can be used to predict the actuation stroke of the SMA system. Validation experiments showed that the predicted stroke during the second heating and cooling experiments agreed well with the measurements and that the average deviation is 9.6%.

* This chapter is based on:

Liu, Q., Ghodrat, S., & Jansen, K. M. B (2022). Modelling and mechanical design of a flexible tube-guided SMA actuator. *Materials & Design*, 216, 110571.

DOI: [10.1016/j.matdes.2022.110571](https://doi.org/10.1016/j.matdes.2022.110571)

3.1 Introduction

Shape memory alloy (SMA) wires are excellent candidates for wearable actuators since they are thin, low weight and have a high actuation force. The main drawbacks are that the wire should be kept straight and needs to be relatively long to enable a large enough actuation stroke. Embedding the SMA wire in a flexible tube largely enhances its applicability since then the counter forces are transferred by the tube material and the tube can be rolled up or attached to flexible surfaces or clothing layers. The performance of such tube-guided SMA actuators is however more complicated since it not only depends on the SMA behaviour but also on the tube materials and the actuator construction.

In this article, a tube-guided SMA actuator is studied. As shown in Figure 3.1, a SMA wire threads through a tube, and one end of the wire is fixed with the tube end at *C*. The function of the tube is to transfer the actuator load from the wire end *C* to the tube end *B* while still allowing shape flexibility. The maximum stroke over the actuator is then not 4% of *AB*, but 4% over the full SMA wire length *AC*, even if the tube is not straight but e.g., rolled up. Ideally, the tube should be bendable but stiff in compression. Such configuration has been used in smart garments (Veldhoen, 2019), soft wearable robots (Villoslada et al., 2015) as well as rehabilitation devices (Galiana et al., 2012). The tube-guided SMA actuator is flexible in bending and can provide thermal insulation during actuation of the SMA. When the SMA wire is activated, it contracts within the tube and does not require bearings to support the SMA wire (Helps et al., 2019). These advantages also make it a good choice as an actuator for smart textiles.

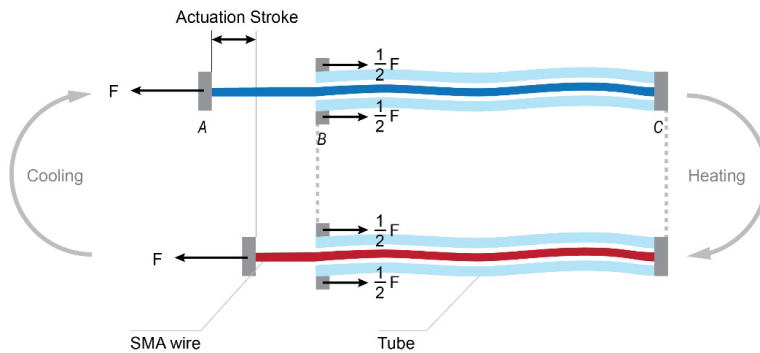


Figure 3.1 Configuration and activation process of the tube-guided SMA actuator. The actuation is between points *A* and *B*, whereas most of the actuator length is in the flexible tail *BC*.

Tube-guided SMA actuator systems have been studied in literature. For example, Helps et al. found that the stroke of a SMA-based system can be improved by up to 69.81% by using the tube-guided SMA wire actuator concept, which demonstrated the efficacy of the tube-guided SMA wire actuator concept (Helps et al., 2019). In addition, they showed that graphite powder and tungsten disulfide lubricant both

delivered better improvements in stroke (Helps et al., 2019). Copaci et al. proposed different kinds of configurations of SMA-based actuators, such as the multiple SMA wires actuator, double actuator configuration, etc. These configurations are designed to investigate influences of types of SMA wires, materials of the Bowden cable sheath, multiple SMA wires on the performances (e.g., work frequency, electrical consumption, total movement length) of SMA-based actuators (Copaci et al., 2019). Nizamani et al. conducted research on novel cooling techniques to decrease the cycle time of the SMA. In their study, oil and grease are used as two kinds of coolant, which are sealed inside PTFE tubes to help cool down the SMA temperature before testing. It was found that the grease cooling reduced the cooling time up to 30% and oil cooling by 20% (Nizamani et al., 2017). However, current research on tube-guided SMA actuators has not explained the relationships between parameters like the actuation force and stroke.

This chapter proposes a phenomenological model of the tube-guided SMA actuator to describe how the actuation stroke changes in relation to the applied stress and temperature. It can be used for predicting the end-state performance (between initial and end state displacement and force) of tube-guided SMA actuators. The structure of this chapter is arranged as follows. Section 3.2 describes materials and testing methods, whereas in section 3.3 the test results are analysed. Then, we propose a model of the tube-guided SMA actuator in section 3.4, taking thermal expansion and creep effects into account. To verify the model, results of a series of tube-guided SMA actuator force-control tests are used to compare with the model predictions in section 3.5. Application examples are provided in section 3.6.

3.2 Materials and Methods

In the first set of experiments, the shape memory alloy wire and tube were separately tested to obtain their basic material properties. Subsequently, a series of validation experiments was performed on the tube-guided SMA actuator. A Dynamic Mechanical Analyser (DMA) Q800[®] of TA instruments was used for all tests.

3.2.1 Shape Memory Alloy Wire

0.15mm diameter FLEXINOL[®] SMA wires purchased from Dynalloy, Inc. were used in experiments. The alloy consists of nickel and titanium atoms in a ratio of exactly 50%/50% and has a listed activation temperature of 90 °C (DYNALLOY, 2021b). To allow for repeated cycling without degradation, it is suggested that stress applied on the wire should be no more than 230 MPa at high temperature (DYNALLOY, 2021b). Four types of characterisation experiments were conducted.

(1) Transformation Stress Tests: The first experiment aims to figure out the martensite start transformation stress, martensite finish transformation stress, and their corresponding strain values. The force-control condition was selected in the DMA testing program. During the tests, the SMA wire was loaded to 2.0 N (113 MPa)

with a rate of 0.3 N/min, and then unloaded to 0.001 N with the same rate at room temperature (25 °C).

(2) SMA Young's Modulus Test: The second experiment is to find out how the Young's modulus of the SMA wire changes with temperature. The strain controlled dynamic measurement module was used for the experiment. The testing temperature was programmed to increase from 30 °C to 160 °C with a rate of 1 °C/min. In the program settings, we applied 15 µm displacement amplitude, 120% force track and 1 Hz frequency.

(3) Transformation Temperatures Test: In this test, the transformation temperatures are determined by heating and cooling specimens after uniaxial pre-straining in the martensite state (ASTM-E3098-17, 2018). The SMA wire was loaded with 2.0 N and heated to 120 °C with a rate of 10 °C/min, followed by a 5 minutes isothermal soaking, and then it was cooled down to room temperature.

(4) Force-control Tests: In this series of experiments, the SMA wire was loaded with constant force (0 to 2.0 N with 0.1 N intervals) at room temperature. Then, it was heated to 120 °C with a rate of 10 °C/min. After isothermal soaking for 5 minutes, the wire was cooled down to room temperature again. Strain values at 120 °C and 25 °C, as well as the SMA actuation strain generated by the heating and cooling process can be approximated in each force-control test. A similar way of testing has been reported by Eschen et al. (Eschen, Granberry, & Abel, 2020; Eschen, Granberry, Holschuh, et al., 2020).

3.2.2 Tube

A Polytetrafluoroethylene (PTFE/teflon) tube (outer diameter 0.9 mm, inner diameter 0.4 mm) was selected for the tube-guided SMA actuator because of its low friction. The deformation of the tube consists of a thermal expansion (reversible) and a creep (non-reversible) contribution, the latter of which is a function of temperature, applied stress and time. The following five types of experiments on the tube were planned to characterize and model these contributions.

(1) Thermal Expansion Tests: A tube specimen with clamping length of 11.0 mm was heated from 25 °C to 160 °C with a rate of 5 °C/min under a constant force of 0.01 N. In order to correct for the thermal expansion of the clamping configuration, a calibration test with a quartz specimen was performed.

(2) Tube Young's Modulus Test: The *displacement ramp method* was selected in the DMA program. The displacement of the tube specimen increased from 0 to 3.0 mm with a rate of 0.5 mm/min at room temperature.

(3) Preliminary Tests for Onset of Non-linear Creep: A series of 5 minutes creep tests were conducted with a range of forces (0 to 2.0 N at 0.2 N intervals, 3.0 N, 4.0 N) at a constant temperature of 120 °C. The testing time was chosen to be of the same

order as a typical actuation time in practical applications. Creep compliances of different forces at the fifth minute were recorded and compared. The sample lengths are again close to 11.0 mm. The tests are to identify the force range which would cause non-linear creep.

(4) Time-Temperature Superposition Tests: The fourth series of experiments aims to figure out the influences of time and temperature on creep compliance. It is known that for most polymeric materials, superposition is obtained when shifting creep curves at different temperatures along the time axis. The overlapping curves form a so-called “master curve” (Ferry, 1980). By plotting the shift factor versus temperature, a shift factor curve can be obtained. The shift factor curve and the master curve form a convenient way of modelling the creep compliance as a function of temperature and time. For this Time-Temperature Superposition (TTS) testing we performed 10 minutes creep tests with 1.0N force at temperatures between 30 °C and 120 °C. An isothermal soaking period of 5 minutes preceded the creep measurements. The temperatures were increased with 10 °C increments.

(5) Effect of Temperature Cycling on Creep: This experiment evaluates the effect of cyclic temperature change on the tube creep. A constant force of 1.0 N was applied to the tube after which the temperature was increased from 25 °C to 120 °C with a rate of 10 °C/min, kept isothermally for 15 minutes and then cooled down to 25 °C with the same rate. The heating-isothermal-cooling procedure was repeated three times.

3.2.3 Tube-guided SMA Actuator

To determine the thermal-mechanical behaviour of the full tube actuator system in a more typical configuration, a tube length of 114.5 mm was chosen. In order to be able to fit inside the oven of the Q800 instrument, the tube with SMA wire was fixated to a cork substrate in a circular shape (see Figure 3.2(a)). The nut fixed at one end of the tube was clamped directly in the lower fixture of the DMA. The free SMA wire end was tied as a knot and inserted in the upper clamp. The experimental setup can be seen in Figure 3.2(b) and (c). The entire tube-guided SMA actuator was fastened on the metal frame of the DMA machine with a rubber band.

To figure out how the displacement of the system changes under a constant force, the tube-guided SMA actuator was heated and cooled (from 25 °C to 120 °C) for three cycles with a rate of 5 °C/min under a constant force. Considering that the cork can delay the temperature change, a slower heating rate was selected for these system tests.

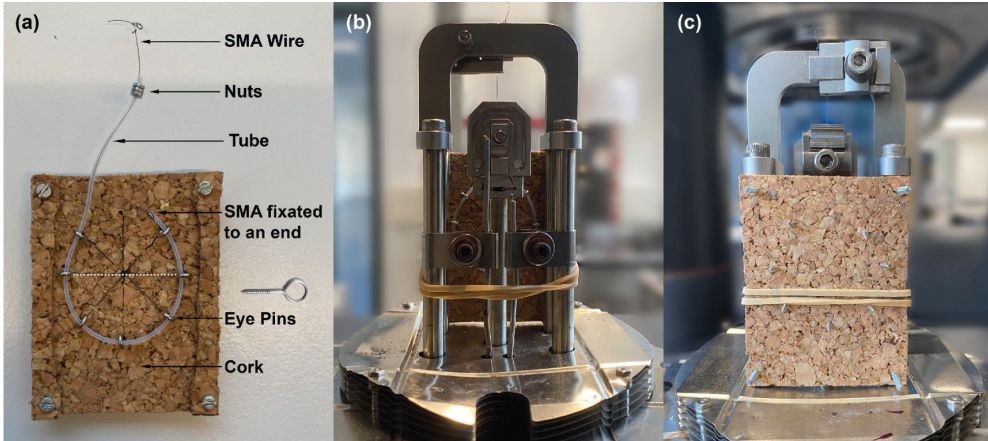


Figure 3.2 (a) Setting of the tube-guided SMA actuator. (b) Back view of the experimental set-up. (c) Front view of the experimental set-up showing how the system is placed into the DMA machine.

3.3 Characterisation Results

3.3.1 Shape Memory Alloy Wire

(1) Transformation Stress Test (at room temperature): As depicted in Figure 3.3, the stress-strain curve shows a first rapid elastic response followed by a second region with a much slower stress increase and a steeper upturn. The second region is attributed to the martensite to austenite transformation plateau. This room temperature stress-strain behaviour is modelled as three separate linear regions to get transformation stress and strain values, following the work of Rao (Rao et al., 2015).

The slope of $line_1$ can be interpreted as the Young's modulus of the twinned martensite SMA at room temperature. As for the $line_2$, it is suggested to be modelled as a horizontal line by using the stress level corresponding to 2.5% strain (Rao et al., 2015). However, there is an obvious upward trend of the detwinning plateau in our test, so we decided to model this as a line with non-zero slope. For this, we drew three tangent lines for corresponding regions and got the values of the intersection points. The fitting parameters related to the start and finishing of the martensite transition are denoted as σ_S^M , σ_F^M and ε_F^M , and the strain values at the 2.0 N end point as ε_{2N}^M . The values can be found in Table 3.1.

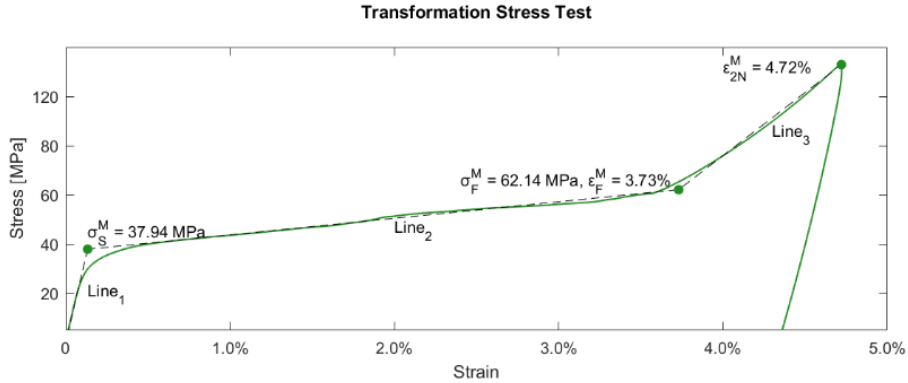


Figure 3.3 Transformation stress and corresponding strains of the SMA wire at room temperature. Three grey dashed lines are tangent lines obtained from the experimental data.

(2) SMA Young's Modulus Test: According to the testing results (Figure A1. 1 in the Appendix 1), the Young's Modulus of twinned martensite at room temperature is 24.4 GPa, which is very close to the slope of *line*₁ (25.7 GPa) in Figure 3.3. The modulus of austenite at 120 °C is 40.5 GPa. The two values are close to values reported in literature, e.g., 28 GPa (martensite) and 83 GPa (austenite) (Rao et al., 2015). More details can be found in Appendix 1.

(3) Transformation Temperatures Test: As depicted in Figure 3.4, in the heating process, the strain remains at an almost constant level of 4.8% until the austenite start temperature (A_s). During the martensite to austenite phase transformation, the wire shrinks until the temperature reaches point A_f (austenite finish temperature). In the subsequent cooling stage, we first observe a small strain increase due to thermal expansion, which is followed by a sudden larger expansion attributed to the martensite to austenite transformation (M_s to M_f). The transformation temperature points A_s , A_f , M_s , and M_f are obtained by plotting tangent lines to the experimental curves.

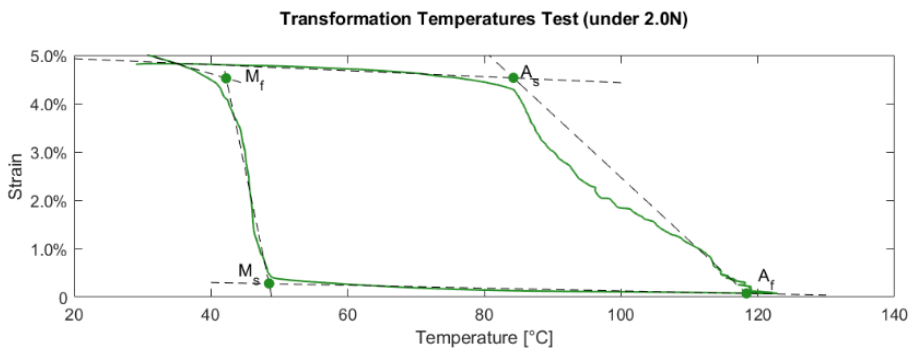


Figure 3.4 Transformation temperature diagram of the SMA wire (testing range: 20-120 °C).

(4) Force-control Tests: The strain values after room temperature loading corresponding to specified load values are referred to as the martensite strain (blue triangles in Figure 3.5). For stresses below 50 MPa, these strain values remain below 1%, but above the 50 MPa, much larger deformations are observed, which are attributed to the stress induced martensite to austenite transformation. Upon heating of these pre-stretched wires, they contract back to a strain value close to 0 (defined as the austenite strain, red open triangles in Figure 3.5). The difference between the pre-stretch and recovery strain is the SMA actuation strain that SMA wire can generate. It is shown separately in Figure 3.6.

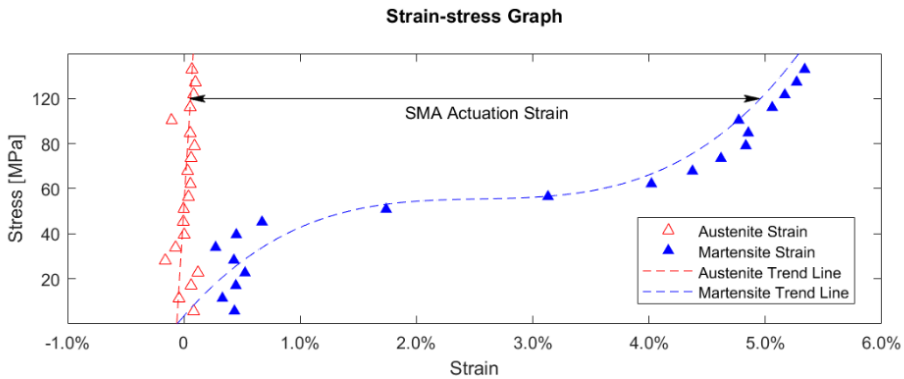


Figure 3.5 Strain values at 120 °C and 25 °C for different applied stress levels. Blue triangles: strain values after pre-stretching at 25 °C; Red open triangles: recovery strain values after heating to 120 °C. The blue dashed line is a 3rd degree polynomial trend line fitted to the martensite data, and the red dashed line is a linear line fitted to the austenite data.

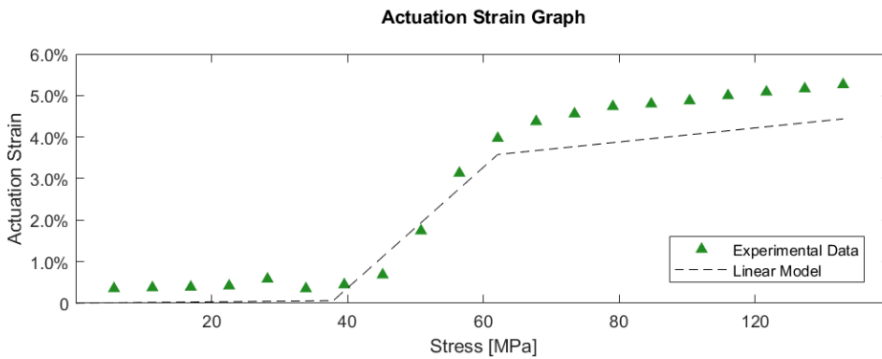


Figure 3.6 Actuation strain values under different constant stresses. The dashed line is based on Figure 3.3 and Figure 3.5, and fitted to Eq.(3.1)

The experimental results of the SMA wire are summarized in Table 3.1.

Table 3.1 Properties of the FLEXINOL® SMA as determined in the experiments.

Parameters of the FLEXINOL® Actuator Wire from DYNALLOY, Inc.		
Martensite start transformation stress	σ_S^M	37.9 MPa
Martensite finish transformation stress	σ_F^M	62.1 MPa
Strain value of the martensite SMA wire under σ_F^M	ε_F^M	3.73%
Strain value of the martensite SMA wire under σ_{2N}	ε_{2N}^M	4.72%
Young's Modulus of austenite at 120°C	E_A	40.5 GPa
Young's Modulus of twinned martensite at 30°C	E_M	24.2 GPa
Austenite start temperature	A_s	84 °C
Austenite finish temperature	A_f	118 °C
Martensite start temperature	M_s	49 °C
Martensite finish temperature	M_f	42 °C

3.3.2 Tube

(1) Thermal Expansion Test: The coefficient of thermal expansion of the tube is determined as $1.31 \times 10^{-4} \text{ }^\circ\text{C}^{-1}$. More details can be seen in [Figure A1. 1](#) of the [Appendix 1](#).

(2) Tube Young's Modulus Test: The Young's modulus of the tube at room temperature is determined as 533 MPa, which compares well with the value of 410 MPa established by Brown under slightly different test conditions ([Brown, 1999](#)). The graph of the Young's modulus also can be found in the [Appendix 1](#).

(3) Preliminary Tests for Onset of Non-linear Creep: To figure out the creep properties of the tube we first established the onset of the non-linearity. A series of 5 minutes creep tests with increasing force at a chosen temperature (120 °C) was performed. The non-linearity is assumed to start as soon as the ratio between measured creep and applied force (i.e., the creep compliance) starts to deviate from its initial value. Based on [Figure 3.7](#), we determined the linear creep range of the Teflon tube material to be between 0 and 2.0 N. Since the non-linear behaviour increases with rising temperature, the 0-2.0 N range is also expected to be valid for temperatures below 120 °C.

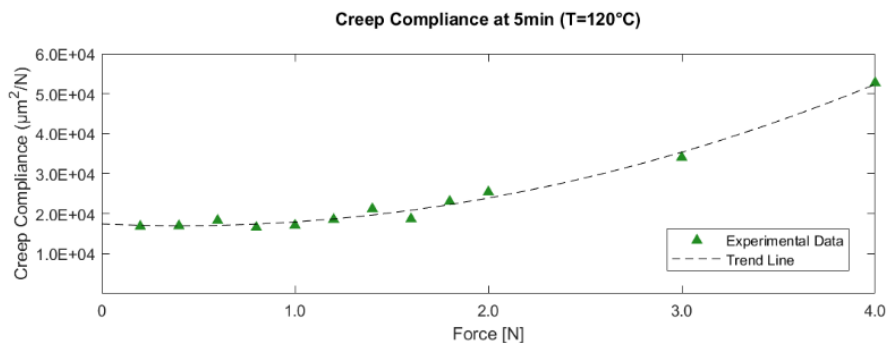


Figure 3.7 Creep compliance under different forces at the fifth minute ($T=120 \text{ }^\circ\text{C}$). The dashed line is a 2nd degree polynomial trend line fitted to the experimental data.

(4) Time-Temperature Superposition Test: Based on the above findings the creep tests were performed with a force of 1.0 N, and the resulting compliance curves between 0-10 minutes are shown in Figure 3.8 as the coloured lines. In polymer engineering it is customary to shift the creep curves obtained at different temperatures along the time axis to form a so-called *master curve* and determining the corresponding shift factor. This has the advantage that in this way only models for two experimental curves are needed to predict creep data within a large time and temperature range. For a more detailed explanation we refer to e.g. Ferry's research (Ferry, 1980). The grey line in Figure 3.8 is the above-mentioned master curve and the shift factor $a_T(T)$ is shown in the inset.

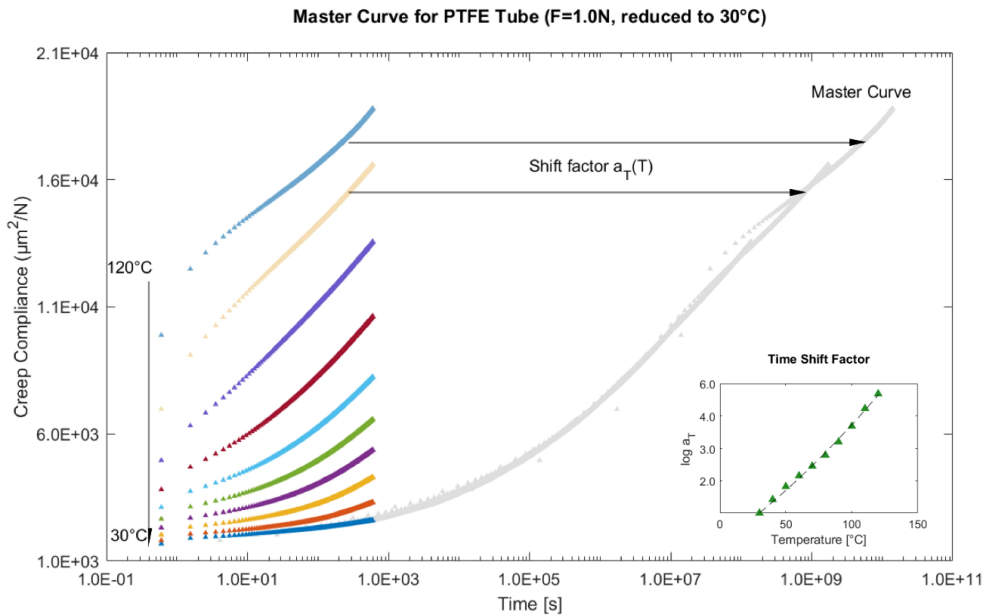


Figure 3.8 The master The master curve and shift factor for the tube ($F = 1.0\text{N}$, reduced temperature set at 30°C).

(5) Effect of Temperature Cycling on Creep: In this test, the influence of temperature cycles as used in the validation experiments on thermal expansion and creep is evaluated. Changes of temperature and strain during the experiment are plotted as red and blue accordingly in Figure 3.9. A single cycle consists of an 11 minutes heating period, a 15 minutes isothermal period and a cooling period of about 15 minutes. It can be seen that the strain shows a large increase (5.24%) during the first heating cycle and follows a more cyclic behaviour in subsequent cooling and heating cycles. The cyclic strains of the second and third cycles reflect the thermal contraction and expansion of the tube.

As seen in Figure 3.9 for the second cycle (40-80 minutes), the changes in strain during heating and cooling are 1.24% and 1.26% respectively, which are very close to the strain value 1.24% as calculated from the coefficient of thermal expansion in

combination with a temperature difference of 95°C. The total strain change over the 2nd cycle is about 0.27%, which is of the same magnitude as the creep strain (0.28%) during the 120°C holding time.

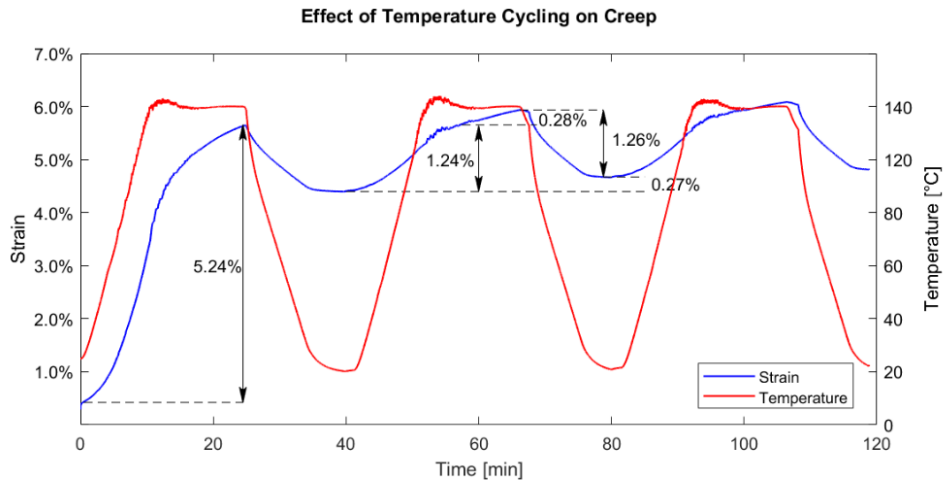


Figure 3.9 The effect of temperature cycling on tube creep (under a constant force of 1.0 N). Blue line is strain, red line is temperature.

3.4 Modelling

3.4.1 Mechanical Model

The actuation stroke of the system in Figure 3.1 depends on the actuation strain of the SMA wire and the compression strain of the tube. Both strain contributions are modelled as described in Eqs. (3.1) and (3.2) below. As shown in Figure 3.6, the SMA actuation strain versus stress curve can be modelled as 3 linear parts:

$$\Delta\varepsilon_M^{SMA} = a_i + b_i\sigma^{SMA} \quad (3.1)$$

where $\Delta\varepsilon_M^{SMA}$ is the actuation strain of the SMA wire, σ^{SMA} is the applied stress to the SMA wire, a_i and b_i are the constants corresponding to the 3 different parts ($i=1, 2, 3$). As an alternative, a more detailed model is presented in Appendix 1.

The compression of the tube is given as:

$$\Delta\varepsilon_M^{tube} = \frac{\sigma^{tube}}{E^{tube}} = \sigma^{tube} D^{tube} \quad (3.2)$$

where $\Delta\varepsilon_M^{tube}$ is the compression strain of the tube and E^{tube} is the Young's modulus of the tube, σ^{tube} is the applied stress to the tube, D^{tube} is the creep compliance.

With the Eqs. (3.1) and (3.2), the actuation stroke of the tube-guided SMA actuator, S_M , becomes:

$$S_M = S_M^{SMA} + S_M^{tube} = \Delta\varepsilon_M^{SMA} l^{SMA} + \Delta\varepsilon_M^{tube} l^{tube} \quad (3.3)$$

in which l^{SMA} and l^{tube} denote the lengths of the SMA wire and tube parts, respectively.

A series of pre-tests show that friction has little influence on the actuation stroke, so it is omitted in the model.

3.4.2 Correction for Thermal Expansion

In addition, the thermal expansion differences between tube and SMA wire has influence on the stroke of the tube-guided SMA actuator:

$$S_T = S_T^{SMA} - S_T^{tube} = (\alpha^{SMA}l^{SMA} - \alpha^{tube}l^{tube})\Delta T \quad (3.4)$$

where S_T is the thermal expansion displacement of the system, α^{SMA} is the coefficient of thermal expansion of the SMA wire, α^{tube} is the coefficient of thermal expansion of the tube, and ΔT is the change of temperature.

3.4.3 Correction for Creep

As for the creep, a Cross function is adopted to describe the measured creep compliance master curve:

$$D = D_g + \frac{D_r}{1 + (t_{red}/\tau)^{-m}} \quad (3.5)$$

where D_g is the glassy compliance, D_r is the rubbery compliance, τ and m are parameters and t_{red} is the so-called reduced time which is defined as (Ferry, 1980):

$$t_{red} = \int_0^t a_T dt \quad (3.6)$$

where t is the real time and a_T is the temperature shift factor.

Note that for a constant temperature, the reduced time reads as $t_{red} = a_T t$ which can be understood as that at a certain temperature, say 50 °C, the creep proceeds a factor a_T faster than at the reference temperature. In our case (see Figure 3.8) the shift factor at 50 °C is 10^2 so creep at that temperature is 100 times faster than at 30 °C. The integral in Eq. (3.6) is only needed for non-isothermal processes (Ferry, 1980).

Several models have been proposed for approximating the shift factor a_T , such as the *Williams-Landl-Ferry* and the *Arrhenius* equation (Laidler, 1984; Williams et al., 1955). Here a second order polynomial for $\log a_T$ was considered more convenient to describe the measured data:

$$\log a_T = c_1(T - T_r) + c_2(T - T_r)^2 \quad (3.7)$$

where c_1 and c_2 are constants, T_r is the chosen reference temperature and T is the temperature.

When taking creep into account the mechanical tube strain in Eq. (3.2), $\varepsilon^{tube} = \sigma^{tube} D^{tube}$, is replaced with the time and temperature dependent compliance: $\varepsilon^{tube} = \sigma^{tube} D^{tube}(T, t)$. The creep displacement part, S_C , then becomes:

$$S_C = \sigma^{tube} D(T, t) l^{tube} \quad (3.8)$$

3.4.4 Modelling of the tube-guided SMA actuator

The aim of the phenomenological model of the tube-guided SMA actuator is to predict how the actuation stroke of the system changes during heating and cooling under a constant force. Although the stress of the SMA wire and the tube are not the same owing to their different cross-sectional areas, the σ^{SMA} and σ^{tube} can be obtained easily with the formula $\sigma = F/A$. Hence, the stress σ^{SMA} and σ^{tube} are selected as input values and the system actuation stroke S is the output value of the model. The overall stroke can be considered as the sum of the actuation of the SMA wire, compression, thermal expansion and creep of the tube:

$$S(\sigma^{SMA}, \sigma^{tube}, T, t) = S_M(\sigma^{SMA}, \sigma^{tube}) + S_T(T) + S_C(\sigma^{tube}, T, t) \quad (3.9)$$

where S is the actuation stroke of the tube-guided SMA actuator in a loading/heating/cooling stage.

(1) Loading Stage: The strain change of the SMA wire during loading is shown as a blue curve in [Figure 3.5](#). To make the model more general for different stages, we still use the Eq. (3.1) to calculate the SMA actuation strain at this stage. As for the tube, if the loading is at room temperature, the tube displacement can either be obtained from Eq. (3.2) or, alternatively, from Eqs. (3.5) and (3.8) with $D = D_g$. The S_T and S_C are not considered at this stage.

(2) Heating Stage: During the heating process, both the S_M^{SMA} and S_T are negative, because actuation of the SMA wire and the thermal expansion of the tube would result in a shortening of the distance AB in [Figure 3.1](#). The coefficient of thermal expansion of the SMA which varies between 6.6 and $11 \times 10^{-6} \text{ }^\circ\text{C}^{-1}$ ([Rao et al., 2015](#)) is much smaller than that of the tube ($1.31 \times 10^{-4} \text{ }^\circ\text{C}^{-1}$, Thermal Expansion Test in [Figure A1. 2](#) of [Appendix 1](#)). We therefore omit the thermal expansion of the SMA wire in our model. The creep of the tube is the largest during the first heating stage and leads to extra tube compression, resulting in a positive S_C contribution and a larger stroke.

(3) Cooling Stage: Both the S_M^{SMA} and S_T are positive in this stage. As discussed in [section 3.3.2](#), there is little creep during the cooling process. Therefore, the S_C can be neglected during cooling.

3.5 Validation and Discussion

3.5.1 Parameters Fitting of the Model

With the material parameters listed in Table 3.1 and Eqs. (3.1)-(3.9), the a_i and b_i parameters for the SMA stroke model were calculated and presented in Table 3.2.

Table 3.2 Parameters for the SMA wire model.

a_1	b_1 [%/MPa]	a_2 [%]	b_2 [%/MPa]	a_3 [%]	b_3 [%/MPa]
0	0.0017	-5.4430	0.1451	2.5200	0.0170

For the creep model of the tube material, the master curve and shift factor parameters as well as their error bounds were determined by using a Matlab fitting procedure. The parameters of Eq. (3.5) and (3.7) are listed in Table 3.3.

Table 3.3 Parameters for the tube model.

D_r [MPa ⁻¹]	D_g [MPa ⁻¹]	τ [s]	m	T_r [°C]	c_1	c_2
2.05×10^4 (± 280)	1600 (± 50)	4.01×10^7 ($\pm 0.4 \times 10^7$)	0.259 ($\pm 4.4 \times 10^{-3}$)	30	6.69×10^{-2} ($\pm 0.8 \times 10^{-2}$)	1.6×10^{-4} ($\pm 1 \times 10^{-4}$)

3.5.2 Validation

Here we consider the performance of the complete actuator system during a series of three heating and cooling cycles similar to the Teflon tube experiments of Figure 3.9. As depicted in Figure 3.10, the actuation stroke shows regular changes with temperature except for the first heating period of the system. To facilitate the discussion, we define four different zones (I - IV, see Figure 3.10).

(1) Zone I: The tube-guided SMA actuator is loaded with a constant force in the first few minutes. During the loading process, the SMA wire is stretched and transforms to the detwinned martensite phase whereas at the same time the tube is compressed. These lead to the displacement increase ΔS_1 in the Zone I.

(2) Zone II: The tube-guided SMA actuator is heated to 120 °C at a rate of 5 °C/min and isothermally kept for 15 minutes. At the beginning, creep and thermal expansion of the tube almost counteract with each other, so there is little change of the displacement. With the temperature increase, the SMA reaches its austenite start temperature, and leads to contraction. It explains why the displacement of the system decreases after the initial plateau. However, the creep of the tube always results in an increase in the displacement of the system. When contraction of the SMA is less than the expansion caused by creep of the tube, displacement of the system increases again. In the isothermal environment of 120 °C, the displacement rises slightly owing to the creep of the tube. Overall, the displacement of the actuator system during the first heating (ΔS_2) is very different from that of the following temperature cycles.

(3) Zone III: The system is cooled down to 25 °C and kept at this temperature for 15 minutes, the SMA wire transforms from the austenite state to the detwinned martensite state, which leads to an expansion of the system under a constant force. Its increase in length results in a larger displacement of the actuator system. As for the tube, the creep contributes to the displacement increase. However, in comparison with the previous process, the creep has much less influence on the displacement. Cooling contraction of the tube also leads to an increase of the system's displacement ΔS_3 .

(4) Zone IV: The tube-guided SMA actuator is heated to 120 °C and kept isothermally for 15 minutes again. In this process, the shape memory effect of the SMA wire and thermal expansion of the tube lead to a decrease of the displacement ΔS_4 .

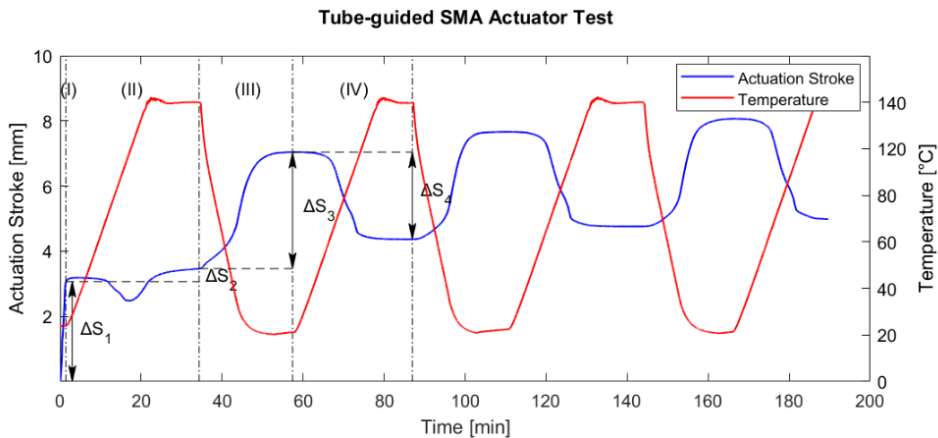


Figure 3.10 Analysis of the tube-guided SMA actuator test. Blue line is the actuation stroke; red line is the temperature. ΔS_1 : the displacement of the loading stage; ΔS_2 : the displacement of the first heating stage; ΔS_3 : the displacement of the cooling stage; ΔS_4 : the displacement of the second heating stage.

A more detailed analysis can be found in Model Simulation of the [Appendix 1](#), in which we can see how displacements of SMA actuation, thermal expansion and creep of the tube change in different stages.

In addition, it should be noted that all experiments were performed under controlled heating and cooling conditions which minimizes possible thermal gradients in the actuator. The actuator can also be activated by Joule heating outside the oven. In that case the actuation cycle is in the order of seconds/ minutes, which is much faster than it shows in [Figure 3.10](#).

3.5.3 Discussion

The displacements ΔS_1 , ΔS_2 , ΔS_3 and ΔS_4 as indicated in [Figure 3.10](#) are recorded for each force setting (0 to 1.6 N at 0.2 N intervals) and compared with the theoretical results of the model. The results are shown in [Figure 3.11](#).

Figure 3.11(a) shows the measured (dashed green line) and calculated (full green line) loading displacements during the loading stage ΔS_1 , as well as the corresponding results for the first heating stage, ΔS_2 (yellow lines). In both cases, the predicted values agree well with the measured stroke displacements (differences are about 1 mm or less) and the trend of an increasing stroke above 0.8 N for ΔS_1 is well captured.

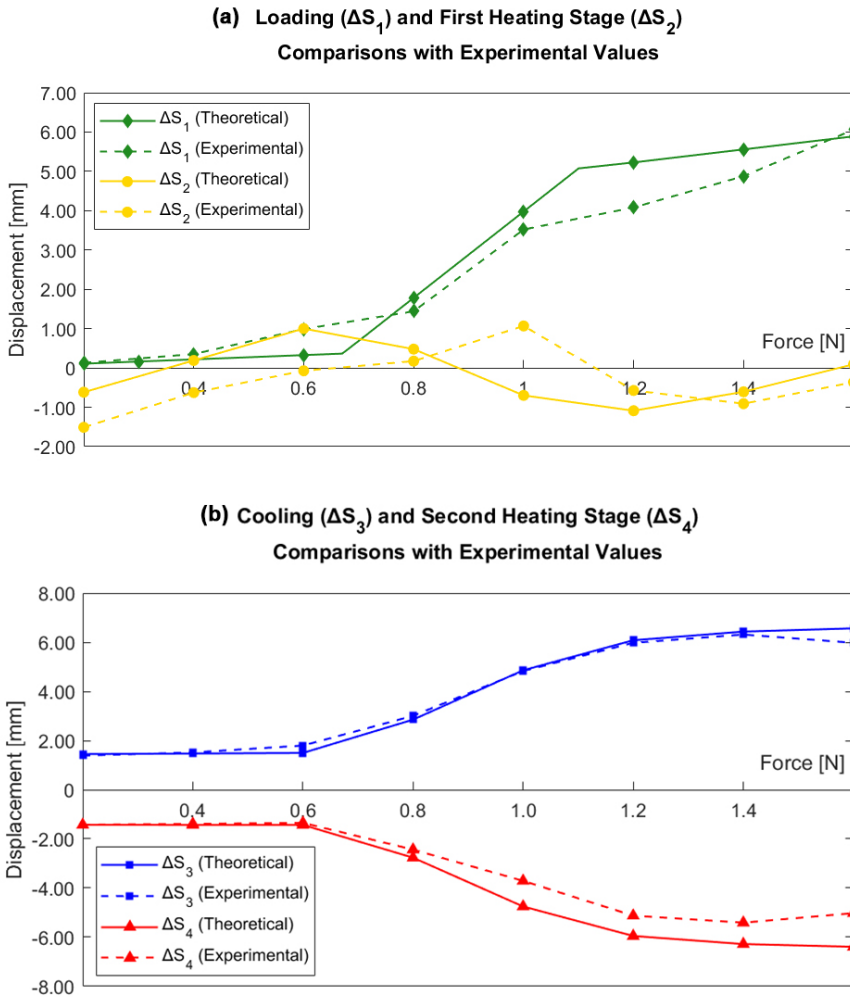


Figure 3.11 Comparisons between the theoretical (full lines) and experimental (dashed lines) results. The ΔS_i refers to Figure 3.10.

In addition, Figure 3.11(b) shows that also the stroke displacement during cooling, ΔS_3 , and during the second heating stage, ΔS_4 are well captured by the model.

In the following content, we discuss the measured and predicted actuator displacements during the four different stages in more detail.

(1) Loading Stage, ΔS_1

With Figure 3.11(a), the experimentally observed displacement ΔS_1 of the loading process agrees well with the theoretical results. Smaller deviations can be observed for forces above 0.8 N. There are two possible explanations for this. First, if the SMA wire is not fully stretched (especially the exposed part, AB in Figure 3.1), or there is an initial sliding between the tube-guide SMA actuator and the clamp, it can lead to larger displacement values. Second, even though the actuator is preconditioned by heating to 120 °C under a constant low force before each test, it is still difficult to ensure the SMA is initially at the fully twinned martensite phase, which may lead to lower displacement values.

(2) First Heating Stage, ΔS_2

During the loading step, the tube part is compressed but shows only a small compression displacement due to its relatively high modulus ($E^{tube} = 533$ MPa). When it is heated, two things occur in the tube. First, the tube starts to expand due to thermal expansion effects, leading to a decrease of the actuation stroke. Next to that, the material rapidly becomes softer at higher temperature and creep becomes noticeable. The creep effects are described by Eq. (3.8) and result in an increased actuation stroke. As for the SMA wire, the temperature driven conversion to the austenite phase leads to a contraction contribution. The combination of thermal expansion, creep and SMA actuation during the first heating period results in a stroke displacement decrease followed by a rapid increase, as observed in Zone II of Figure 3.10. Since all effects almost balance out, the net displacements during the first heating stages are close to zero. An effect which is well captured by our model predictions for ΔS_2 (see Figure 3.11(a)). A more detailed analysis can be seen in the Model Simulation of the Appendix 1.

(3) Cooling Stage, ΔS_3

As depicted in Figure 3.11(b), the experimental results for ΔS_3 (blue dashed line) fit well with the theoretical results (full blue line). During cooling additional creep effects are small and the stroke displacement is mainly determined by the SMA phase transformation strains plus the thermal expansion of the tube. The good agreement between observations and predictions here indicate that those two contributions are well modelled.

(4) Second Heating, ΔS_4

The second (and subsequent) heating stages under constant loading differ from the first heating period in their creep contributions. As explained before, during the first heating the creep which does not yet occur at room temperature sets in, resulting in a large first creep displacement effect. However, since the load is kept on the sample, all subsequent cooling and heating periods only result in a slowing down or acceleration of the *reduced* creep time but not to creep recovery. The first large creep effect is thus not repeated and the next temperature cycles are just subsequent parts

on the same creep curve. In order to illustrate this more clearly we replot the creep data at 120 °C and corresponding prediction on a linear time scale in Figure 3.12, and indicate the large differences in creep contributions during the first and the second heating cycles.

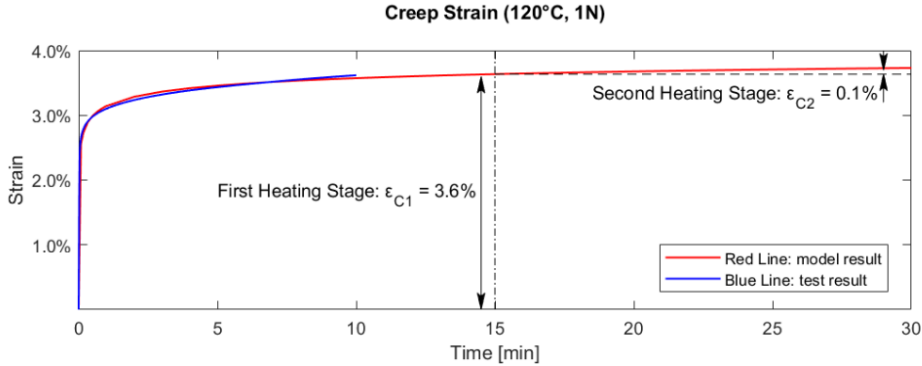


Figure 3.12 The creep strain of the tube at 120 °C. The red curve is modelled in Matlab with Eqs. (3.5)-(3.7). The blue curve is the result of the third test in section 3.3.2.

The deviation between the experimental and modelled results (ΔS_4) increases with higher force, which is larger than the difference in the cooling process. In section 3.3.2, even though we determine the linear creep range of the tube to be 0-2.0 N, there shows a slight upward trend above about 1.0 N, which means that the actual creep compliance above 1.0 N could be slightly larger than the calculated value in our model, which explains the deviation between the theoretical and experimental results after 0.8 N to some extent. In general, the predicted values also fit well with the experimental data.

3.6 Applications

Two wearable haptic prototypes are developed as application examples of the tube-guided SMA actuator. The first one serves as a navigator for visually impaired people. As shown in Figure 3.13(a), the effector is in direct contact with user's skin, and is mounted with 4 tube-guided SMA actuators. Activation of one of these actuators allows the effector to slide in the corresponding direction, thereby conveying navigation information to the user. The tubes of the actuators are fixated at the textile substrate around the centred part with the effector.

The second prototype is a brush-stroke bracelet, which also consists of 4 tube-guided SMA actuators (see Figure 3.13(b)). The effector is equipped with 9 rotatable brush units, which come into contact with the user's arm. When the right tube-guided SMA actuator is activated, the tips of the brush units are moved to the left side. By sequentially activating different actuators, the prototype can produce various haptic stroking patterns. An animation of this prototype can be viewed by scanning the QR code in Figure 3.13(b). The brush-stroke bracelet is designed for affective touch (e.g.,

for relaxation) or notification interfaces. User studies with these prototypes will be performed in the future.

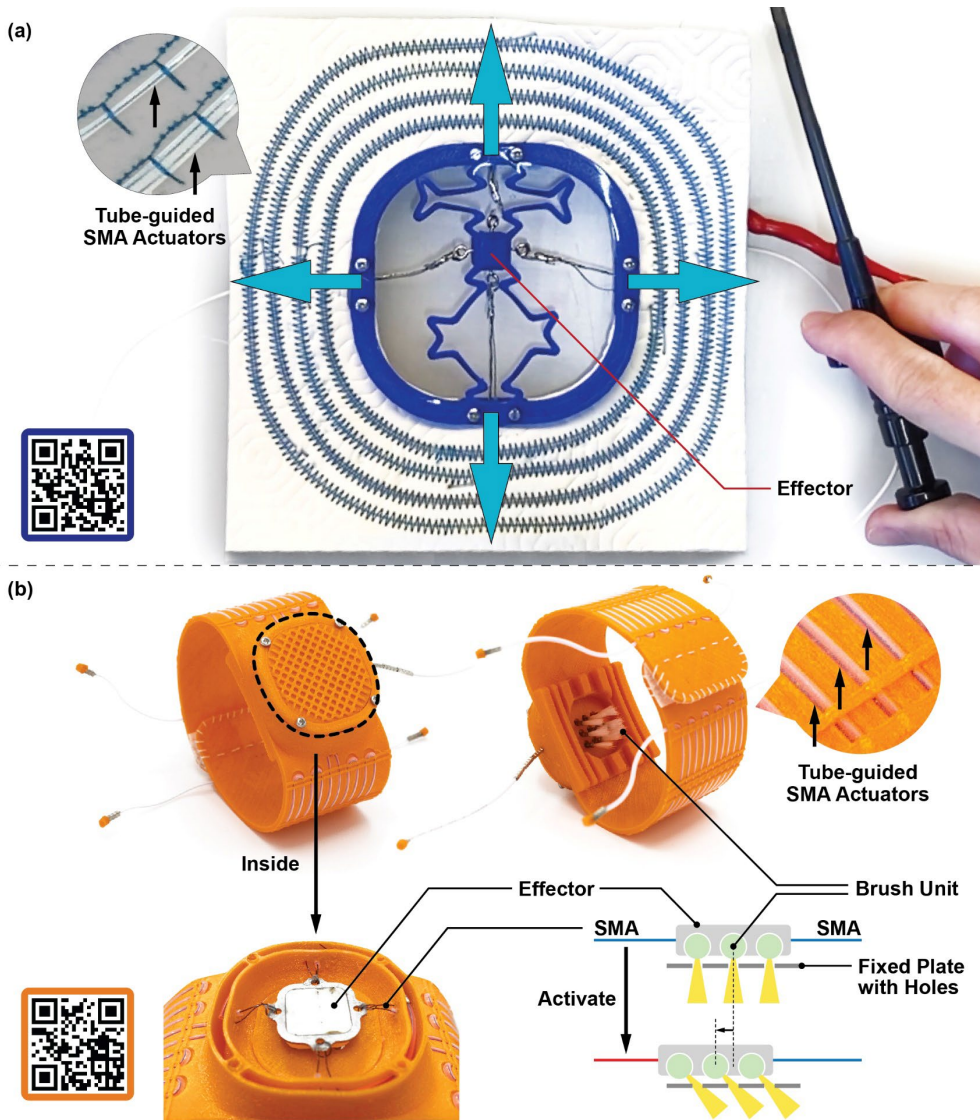


Figure 3.13 (a) A navigator for visually impaired people; (b) A brush-stroke bracelet.

3.7 Conclusion and Outlook

A phenomenological model of tube-guided SMA actuators is proposed in this chapter. For the cooling and second heating stage (blue and red curves in Figure 3.11), the average deviation over the full force range (0.2-1.6 N) between modelled and test results is 9.6%, although the deviation (27.3%) is much larger at the maximum force (1.6 N of ΔS_4). The model reveals the relationship between the actuation stroke and applied stresses, with time and temperature as independent variables. After

determining the basic parameters of the SMA wire (e.g., transition temperatures, diameters, Young's modulus of austenite and twinned martensite, transformation stress and corresponding strain), together with time-temperature dependence of the tube creep compliance, the actuation stroke of the entire system can be calculated for given input stress values. Creep of the Teflon tube is included in the model to show that, if needed, the model can fully capture the actuator behaviour. Our results also indicate that for the second and next heating cycles under constant loading, the creep contribution is negligible. In that case, the actuator model can be simplified by neglecting the creep term.

The model proposed in this research bridges the gap between the smart material science and practical design approach. It supports designers who are not specialized in the field of shape memory materials, to efficiently adopt the tube-guide SMA actuator system in their design without having to work with complicated constitutive material models.

Tube-guided SMA actuators are thin, flexible, light-weight, noiseless and still have a relatively large actuation stroke and force. They are particularly useful as the translational actuators in applications where motors or other actuator types are not suited like in clothing or directly on the human skin.

Chapter 4 *

Modelling And Design of A Reversible SMA Hinge Actuator

This chapter focuses on the second type of actuator elements, which is a reversible shape memory alloy hinge actuator. Each hinge unit consists of an SMA wire functioning as an actuation component and a superelastic wire serving as an antagonist, enabling the hinge to open reversibly 60° during heating and cooling. The actuator weighs only 2 g, and can generate relatively high actuation forces of up to 5 N. Material performance of the two types of SMA wire at different temperatures are measured. Based on the experiments, a mechanical model that can predict the opening and closing angles is proposed. Validation experiments showed deviations of 13.5±8.2%. Gripper and butterfly demonstrators constructed using the hinge actuators are provided as application examples.

* This chapter is based on:

Liu, Q., Ghodrat, S., & Jansen, K. M. B (2024). Design and modelling of a reversible shape memory alloy torsion hinge actuator. *Materials & Design*, 237, 112590.

DOI: [10.1016/j.matdes.2023.112590](https://doi.org/10.1016/j.matdes.2023.112590)

4.1 Introduction

Mechanical actuators serve to transform different types of input energy into mechanical motion (Hannaford et al., 1990). During the 1960s and 1970s, early iterations of these devices predominantly featured arm-like manipulators that used electric motors or pneumatic and hydraulic actuators (Greco et al., 2022). Despite offering benefits such as precise control and high actuation force, conventional actuators are often bulky, expensive and noisy, thus constraining their application scenarios. In addition, pneumatic and hydraulic actuators necessitate frequent maintenance due to their sensitivity to contamination (Greco et al., 2022). To develop portable, lightweight, and adaptive devices, some researchers are exploring the integration of smart materials into mechanical actuators (Mirvakili et al., 2013). Recent advancements include the applications of shape memory alloys (SMAs) and shape memory polymers (SMPs). These materials have numerous advantages, including lightweight, small form factor, simple structure, and wide selection of actuation force (Dong et al., 2022; Granberry et al., 2019; Greco et al., 2022; Wang, Rodrigue, Kim, et al., 2016).

Hinges as a form of bending mechanical actuators, find widespread application in various fields, such as foldable mechanisms for industrial manipulators and robotics. Smart materials have been used to exploit smart hinges in some research. For example, Yamamura et al. proposed a large-deformation hinge that combines shape memory polymer with a soft elastomer (Yamamura et al., 2021). More studies on shape memory polymers and their composites indicate promising applications in areas like packaging (Liu et al., 2012), solar arrays (Liu et al., 2020) and assembly structures (Felton et al., 2013). SMP-based hinges offer the advantages of being lightweight and capable of large deformation, but they produce low actuation force, and need additional heating circuits or other types of external stimulus (Wang, Rodrigue, Kim, et al., 2016).

SMAs present an option for creating lightweight hinges with small form factors and high actuation forces. Pre-stretched SMA wires can generate 4-8% of shrinkage as well as a relatively high actuation force when heated. Some researchers take the advantage of this property to develop tension-driven hinges (Kim et al., 2016; Wang, Rodrigue, & Ahn, 2016; Wang, Rodrigue, Kim, et al., 2016). Typically, such hinges are composed of SMA wires, rigid parts and strip-shape rubbery elements (see Table A2. 1 and Figure A2. 1(d) in Appendix 2). The length of the SMA wires significantly affects the bending angles of the tension-driven hinges. Owing to the limited contraction strain of the SMAs, these hinges are often designed to be thin and strip-like (e.g., 20 cm long) to accommodate enough wire length. Additionally, some researchers developed bending-driven hinges based on the bending deformation of SMA (Hawkes et al., 2010; Lee et al., 2020; Seigner et al., 2021). Bending-driven hinges that use large-diameter SMAs can be engineered with a compact form factor while delivering substantial actuation force. However, to prevent fracture at the

bending position, the SMA wires or plates must be bent with a larger radius, which consequently results in increased hinge thickness. Torsion-driven hinges represent another category of hinges that exploit the torsional deformation properties of SMAs. These hinges are compact and capable of generating high actuation forces. Related research can be found in (Koh et al., 2014). More details of the three categories of SMA-based hinges are provided in the [Appendix 2](#).

A reversible torsion SMA hinge actuator is investigated in this chapter. As depicted in [Figure 4.1](#), the hinge comprises two nitinol wires. The first wire (SMA, coloured blue) acts as the actuator wire and has an initial training angle of 180° . The second wire is a superelastic wire (SE, coloured red, pre-trained angle 0°) which supplies the antagonist force. Superelastic materials are SMAs which are already actuated at room temperature. When an SMA wire and an SE wire are combined at room temperature, the hinge finds an equilibrium position with an angle somewhere close to the SE's original angle (denoted as θ_{min} in [Figure 4.1](#)). When the actuator hinge is heated above the SMA's transition temperature, SMA is actuated, driving the hinge toward its pre-trained angle (180°), and balance with the SE wire at θ_{max} . Therefore, throughout the heating and cooling cycles, the actuator hinge can repeatedly alternate between two pre-set actuation angles. The actuation span $\Delta\theta$ is defined as the difference between the θ_{max} and θ_{min} .

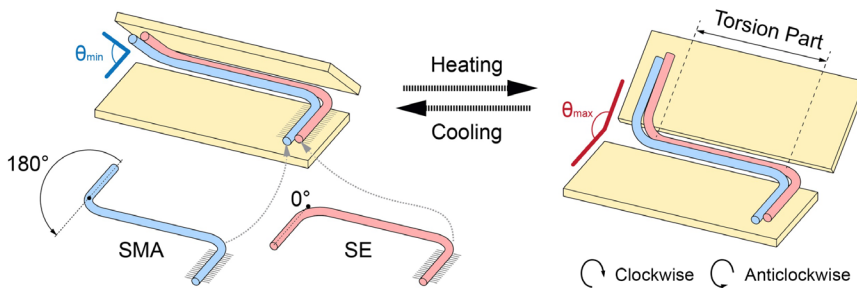


Figure 4.1 Configuration of the reversible torsion SMA hinge actuator. The blue wire represents the SMA wire, while the red wire corresponds to the superelastic wire. The hinge leaves are coloured yellow. 180° and 0° represent the pre-trained angle of SMA and SE respectively. θ_{min} and θ_{max} is the hinge angle at cold and heated states correspondingly.

Although the proposed hinge actuator in this chapter generate bending motion, it is a torsion-driven hinge, where the actual deformation occurs in the torsion part as illustrated in [Figure 4.1](#). Koh et al. presented a similar configuration, comprising two pre-trained SMA wires (Koh et al., 2014). By alternately activating the two SMA wires, the desired hinge deformation can be achieved. They also proposed a constitutive model based on the model of Liang et al. (Liang et al., 1997) to predict the angle-torque relationship. This model involves complex molecular-level parameters such as the thermodynamics of nucleation, critical strains and transformation tensors (An et al., 2012), which makes it less practical to apply. Compared to using two SMA wires, the reversible torsion hinge actuator presented in

this article consumes less energy, because it does not require additional heat sources for shape recovery. In addition, the two wires overlap and are situated in the pivoting line, resulting in a hinge structure with an extremely small form factor.

In this chapter, we develop a lightweight reversible hinge actuator which requires a single heating source, and propose a phenomenological model to predict their actuation angles based on given material properties and geometric parameters. The influences of the SMA pre-trained angle and torsion length on the hinge actuation angle are investigated. The structure of this chapter is organized as follows: Sections 4.2 and 4.3 detail the materials and testing methods, while section 4.4 presents an analysis of the experimental results. A model of the SMA-based torsion hinge actuators is proposed in section 4.5, followed by a validation study in section 4.6. Finally, the influences of SMA pre-trained geometric conditions on the hinge actuator angles are discussed and application examples are demonstrated in the discussion section 4.7.

4.2 Materials and Configuration

4.2.1 Materials

1.00 mm diameter nitinol wires (55.59Ni-44.41Ti wt%) purchased from Nanografi Nanotechnology are used in the experiments. The alloy's documented austenite finish temperature spans from 45 °C to 50 °C. Additionally, 0.75 mm diameter superelastic wires produced by Kellogg's Research Labs are employed, with an equal weight percentage of 50.00 for both nickel and titanium. The reported austenite finish temperature for these superelastic wires is 20 °C.

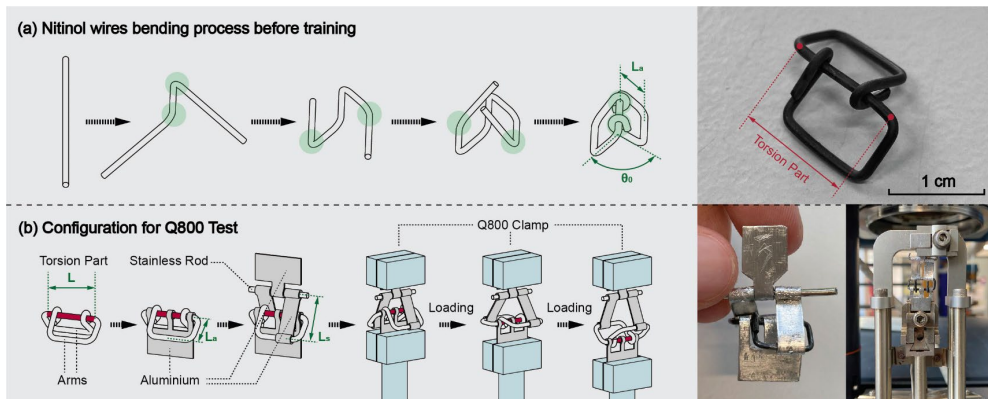


Figure 4.2 Construction of the tool for torsion tests on nitinol wires. (a) Bending process before SMA training. The green areas are the bending positions. (b) Configuration process for Q800 tests. The red areas are the SMA torsion deformation parts. The blue structures are the Q800 clamps. L is the length of the SMA torsion part. L_a is the length of the SMA arm. θ_0 is the initial angle between the two arms. L_s is the length of the aluminium structure.

4.2.2 Configuration of Torsion Tests

A TA instrument Dynamic Mechanical Analyser (DMA) Q800[®] is used for the torsion tests. The SMA wire deforming process of a nitinol wire is depicted in Figure 4.2(a). After annealing for 30 minutes in an oven at 550 °C, a hinge-shape specimen is acquired. To transform the uniaxial motion of the Q800 device into torque deformation, a special tool is constructed consisting of the SMA wire, aluminium tabs and a rod (Figure 4.2(b)). During extensional loading of the tabs, the *torsion part* of the SMA is loaded in torsion deformation. The configuration needs to be lubricated to reduce friction between the nitinol wire and aluminium structures before each test, and the setup is used in tests of section 4.3.3 and 4.3.4.

4.3 Testing methods of SMA and SE

4.3.1 Transformation Temperature Tests

Differential Scanning Calorimetry (DSC) is used to determine the transformation temperatures of the SMA and SE materials. To obtain a larger contact surface between the nitinol wire and aluminium pan, the wire is flattened using a hammer. Subsequently, the nitinol wire undergoes annealing in a 550 °C oven for 30 minutes and are then quenched in cold water (Sadiq et al., 2010).

A TA instrument Differential Scanning Calorimetry Q2000[®] is used for transformation temperatures assessments. Prior to testing, a 16.33 mg SMA specimen is placed into a Tzero[®] aluminium pan with a lid, weighing 50.72 mg. An empty aluminium pan (50.87 mg) serves as the reference. The testing procedure is programmed as follows: initially, the temperature is equilibrated at -60 °C and held isothermal for 2 minutes. It then increases to 100 °C at a rate of 10 °C/min, followed by a 2-minute isothermal soaking, and finally cools down to -60 °C. The preparation and testing procedures of the SE wire are identical to those of the SMA, with the only difference being the weight of the SE sample (7.59 mg) and its corresponding pan (50.39 mg).

4.3.2 Young's Modulus Tests

These tests are to investigate the relationship between Young's modulus and temperature, enabling the determination of the shear modulus for the SMA and SE materials. The *strain-controlled dynamic mode* of the DMA Q800 is chosen for these experiments. The temperature is programmed to decrease from 150 °C to -40 °C at a rate of 1 °C/min, followed by a 5-minute isothermal soak, and then reheated to 150 °C at the same rate. Pre-set parameters in the program include a 5 µm displacement amplitude, 125% force track and 1 Hz frequency. A 23.63 mm long bare SMA wire is used for the test, while the SE wire measures 25.22 mm in length.

4.3.3 Shear Stress-strain Tests at Different Temperatures

For understanding the hinge mechanism, we need the mechanical behaviours of the SMA and SE during heating and cooling. Therefore, it is necessary to conduct shear stress-strain experiments to access their torsion performance over a series of temperatures. In this work, for the characterization of the SMA, *the heated state* refers to the temperature when the SMA is fully transformed to the austenite state (here taken as 150 °C). To obtain SMA's mechanical behaviour during cooling, the temperature range starting from 20 °C downwards is selected for the shear stress-strain tests.

Specimen *SMA 1* is used for tests from 20 °C downwards. Prior to the experiments, the specimen is heated to 70 °C to guarantee complete recovery of its original shape before each test. Subsequently, it is cooled to the predetermined constant temperatures. During the testing process, the *torsion part* of *SMA 1* is pulled downwards (refer to Figure 4.2(b)) at a rate of 300 $\mu\text{m}/\text{min}$ until a displacement of 9 mm is achieved. *Displacement-control mode* is employed for the experimental setup to maintain a steadier rotational velocity of the torsion part. The shear stress-strain evaluations for the SMA are executed at temperature intervals spanning from -40 °C to 20 °C in 10 °C increments.

SMA 2 is selected for *the heated state* tests. The *force-control mode* is used to have better control close to the machine's force limit. *SMA 2* is heated to 150 °C first and kept at the constant temperature for 3 minutes. Then, the specimen is subjected to the predetermined force (6-18 N at 3 N interval) at a rate of 1 N/min. Once the pre-set force is reached, the sample is unloaded to 0.01 N at the same rate.

For the SE materials, we do not distinguish between *the heated state* and cooling, as they are expected to show superelastic behaviour, supplying the antagonist force during the whole actuation process of the hinge. The experimental methodology of *SMA 1* is implemented for *SE 1* and *SE 2*, albeit with distinct temperature ranges. *SE 1* undergoes testing from -20 °C to 20 °C, while *SE 2* is subjected to a higher range of 30-50 °C.

4.3.4 Superelastic Effect Tests for SE

To assess the superelastic behaviour, sample *SE 3* is used for a series of displacement-control tests covering a temperature scope from -40 °C to 40 °C in 10 °C intervals. For each constant temperature setting, 4-5 *loading-unloading cycles* are performed on *SE 3* using the *displacement-control method* with several pre-defined target displacements (2.0 mm to 8.0 mm in 2.0 mm increments, and 9.0 mm) at a rate of 300 $\mu\text{m}/\text{min}$. For the temperature below 0 °C, where the material starts to lose its superelasticity, a heating step to 70 °C is incorporated after each loading-unloading cycle to ensure full recovery. Similar tests can be found in chapter 4 of Rao's work (Rao et al., 2015).

Specific dimensions of nitinol samples used in experiments can be seen in [Table 4.1](#).

Table 4.1 Dimensions of the configuration SMA and SE samples used in tests.

Sample	Wire Radius r [mm]	Torsion Length L [mm]	SMA Arm Length La [mm]	SMA Initial Angle θ_0	Aluminium Structure Length Ls [mm]
<i>SMA 1</i>	0.50	12.30	6.60	100°	9.37
<i>SMA 2</i>	0.50	13.24	7.53	148°	6.00
<i>SE 1</i>	0.375	12.77	5.77	111°	8.40
<i>SE 2</i>	0.375	13.35	6.60	140°	8.21
<i>SE 3</i>	0.375	15.91	5.35	113°	9.30

4.4 Characterisation results

4.4.1 DSC Thermogram for Transition Temperatures

[Figure 4.3\(a\)](#) presents the DSC curves for both SMA and SE, with the black arrows on the thermograms denoting the heating and cooling processes. For the SMA specimen, the heating process from -60 °C to 100 °C results in an endothermic peak as the SMA transitions from martensite to austenite by absorbing heat energy. Four tangents (indicated by dash-dotted lines in [Figure 4.3\(a\)](#)) yield two inflection points: austenite start ($A_s^{SMA} = 30.2$ °C) and finish temperature ($A_f^{SMA} = 37.8$ °C). During the cooling process, two exothermic peaks can be observed. The first peak at a higher temperature corresponds to the transition from austenite to R-phase, whereas another exothermic peak corresponds to the reaction from R-phase to martensite ([Kus et al., 2010](#)). Thus, the SMA specimen on cooling exhibits a well-defined two-stage transformation sequence of *austenite-R phase-martensite*. Martensite start (M_s^{SMA}) and finish temperature (M_f^{SMA}) are determined by the exothermic peaks at 16.6 °C and -2.5 °C correspondingly. As for the SE specimen, represented by the blue curve in [Figure 4.3\(a\)](#), it displays one endothermic and two exothermic peaks. The cooling process of SE is plotted on small scales (see [Figure 4.3\(b\)](#)) to define the M_s^{SE} and M_f^{SE} . All transformation temperatures of SMA and SE are listed in [Table 4.2](#).

Table 4.2 Transition temperatures of Nitinol wires as determined in the experiments.

Transition Temperatures of Nitinol Wires		SMA	SE
Martensite Start Temperature	M_s	16.6 °C	0.5 °C
Martensite Finish Temperature	M_f	-2.5 °C	-44.8 °C
Austenite Start Temperature	A_s	30.2 °C	-18.5 °C
Austenite Finish Temperature	A_f	37.8 °C	12.5 °C

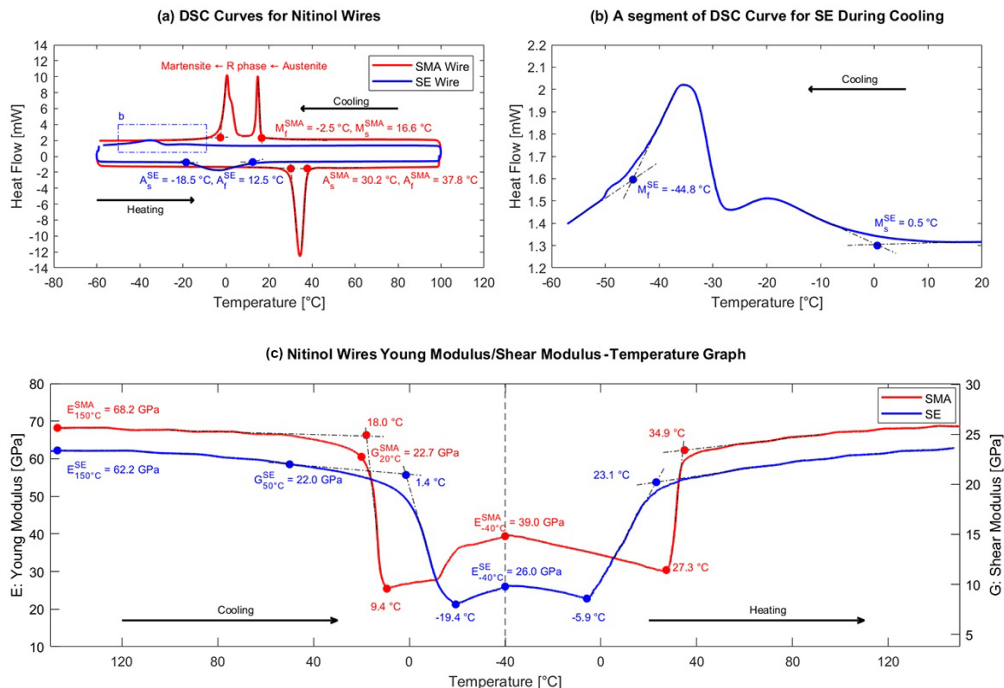


Figure 4.3 (a) and (b): DSC thermogram of SMA (red curve) and SE (blue curve). (c): The 1 Hz Young’s modulus of the SMA and SE wires as a function of temperature. E represents the Young’s modulus with scale on the left Y-axis. G stands for nitinol’s shear modulus on the right Y-axis, which is calculated with the Young’s modulus experimental data and the equation $G=E/[2(1+\nu)]$. Note that the X-axis follows the time line of the experiment: cooling from 150°C to -40°C , followed by heating to 150°C .

4.4.2 Young’s Modulus and Shear Modulus

Figure 4.3(c) shows the variation of Young’s modulus for the SMA and SE during the cooling and heating processes, as determined through dynamic tests at 1 Hz. When the temperature decreases from 150°C to 18°C , the Young’s modulus of the SMA (red line in Figure 4.3(c)) demonstrates a mild reduction (around 68.2 GPa), followed by a sharp decline to 25.4 GPa at 9.4°C , which corresponds to the transformation from the austenite to R phase (refer to Figure 4.3(a)). The modulus then increases to 39.0 GPa at -40°C . During heating, it produces a gradual decrease to 30.4 GPa at 27.3°C and subsequently experiences a significant increase to 62.3 GPa at 34.9°C due to the *martensite-to-austenite* phase transformation. A reduction in Young’s modulus prior to reaching the austenite start temperature during heating (-40°C to 27.3°C in our work) has also been documented in the literature (Cross et al., 1969; Duerig et al., 2013).

The SE wire has a lower austenite Young’s modulus (62.2 GPa at 150°C) compared to the SMA (68.2 GPa). This could potentially be attributed to the lower atomic percentage of Ni in the SE alloy (Huang et al., 2011). The cooling process reveals a marked decrease of the modulus, starting at 1.4°C , which is close to the martensite

start temperatures for SE observed in [Figure 4.3\(b\)](#) (0.5 °C). During the heating process, between -5.9 °C to 23.1 °C, there is a significant increase in modulus. These temperatures are roughly 10 °C higher than the austenite start and finish temperature (-18.5 °C and 12.5 °C) listed in [Table 4.2](#), which also can be explained by the *stress-induced phase transformation* ([Cross et al., 1969](#); [Duerig et al., 2013](#)).

With the equation $G=E/[2(1+\nu)]$, the shear modulus G can be calculated. The Poisson's ratio ν , is typically assigned a value of 0.33 in the literature ([Cross et al., 1969](#); [Salehi et al., 2013](#)). The right Y-axis in [Figure 4.3\(c\)](#) is designated as the shear modulus scale. The measured martensite shear modulus of SMA and SE at -40 °C are 14.7 GPa and 9.8 GPa respectively, which is within the range of 7.5-15.4 GPa reported in the literature ([Mabe et al., 2004](#); [Mohd Jani et al., 2014](#)). The observed austenite shear modulus values for the SMA and SE at 150 °C are 25.4 GPa and 23.4 GPa, which are also close to the 24.8-31.2 GPa documented in ([Cross et al., 1969](#); [Mohd Jani et al., 2014](#)).

4.4.3 Shear Stress-strain Curves at Different Temperatures

4.4.3.1 SMA Loading During Cooling

SMA shear stress-strain curves at different temperatures in the cooling range (from 20 °C downwards) are plotted in [Figure 4.4\(a\)](#). For the SMA shear stress-strain curve at 20 °C (yellow colour), an initial elastic deformation is observed. A black dash-dotted line, representing the SMA martensite shear modulus at 20 °C (22.7 GPa derived from [Figure 4.3\(c\)](#)), is plotted to compare with the slope of the elastic region (yellow dash-dotted line). The agreement confirms the reliability of the configuration presented in [section 4.2.2](#) ([Figure 4.2](#)). In the second region, the deformation transition from twinned to detwinned martensite results in a plateau, during which a minor increase in shear stress induces a substantial increment in shear strain. Following this, as the shear stress increases, the SMA fully transforms into detwinned martensite, and the shear stress-strain curve exhibits a steeper slope. Overall, applying a 150 MPa shear stress on martensite SMA yields an approximate shear strain of 8%, which is consistent with the findings of Melton et al. ([Duerig et al., 2013](#)).

When comparing the series of shear stress-strain curves at different temperatures, it is evident that the elastic modulus and martensite stress plateau values decrease with lower temperatures (20 °C to -20 °C), while they increase from -30 °C and -40 °C. This is also consistent with the SMA cooling process depicted in [Figure 4.3\(c\)](#), which shows an increase in modulus during cooling from -20 °C to -40 °C.

4.4.3.2 SMA Loading and Unloading at the Heated State

SMA shear stress-strain curves at 150 °C are depicted in [Figure 4.4\(b\)](#). At this temperature, the SMA material is much stiffer as compared to the lower temperature curves of [Figure 4.4\(a\)](#) (e.g. 1.2% shear strain at 150 °C versus 12% at 20 °C with 250 MPa) and does not show the characteristic detwinning stress plateaus.

4.4.3.3 SE Loading

SE shear stress-strain curves during loading can be observed in Figure 4.4(c). As the test temperature decreases, the detwinning martensite stress plateau consistently reduces, while the shear modulus (slope during the first 1% strain) displays a notable decrease at -20 °C, which aligns with the low SE shear modulus value at -19.4 °C observed in Figure 4.3(c). The SE shear modulus at 50 °C, acquired from the dynamic test, is added for comparison (black dash-dotted line in Figure 4.4(c)). Good correspondence can be observed between the quasi-static tests of Figure 4.4(c) and the dynamic test of Figure 4.3(c) for the measurements at 50 °C.

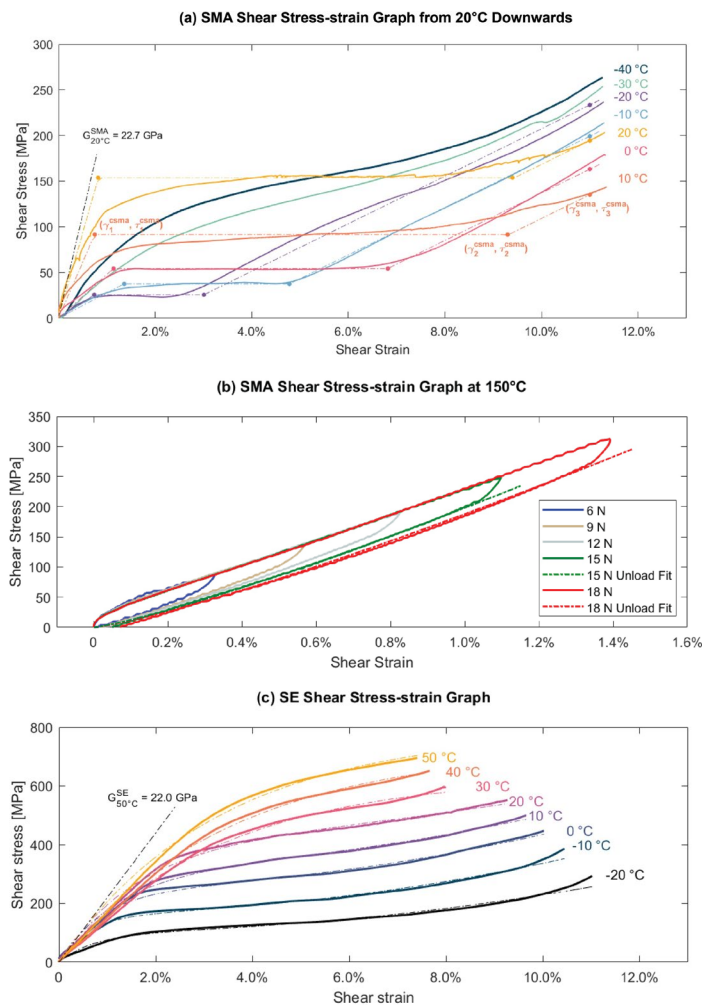
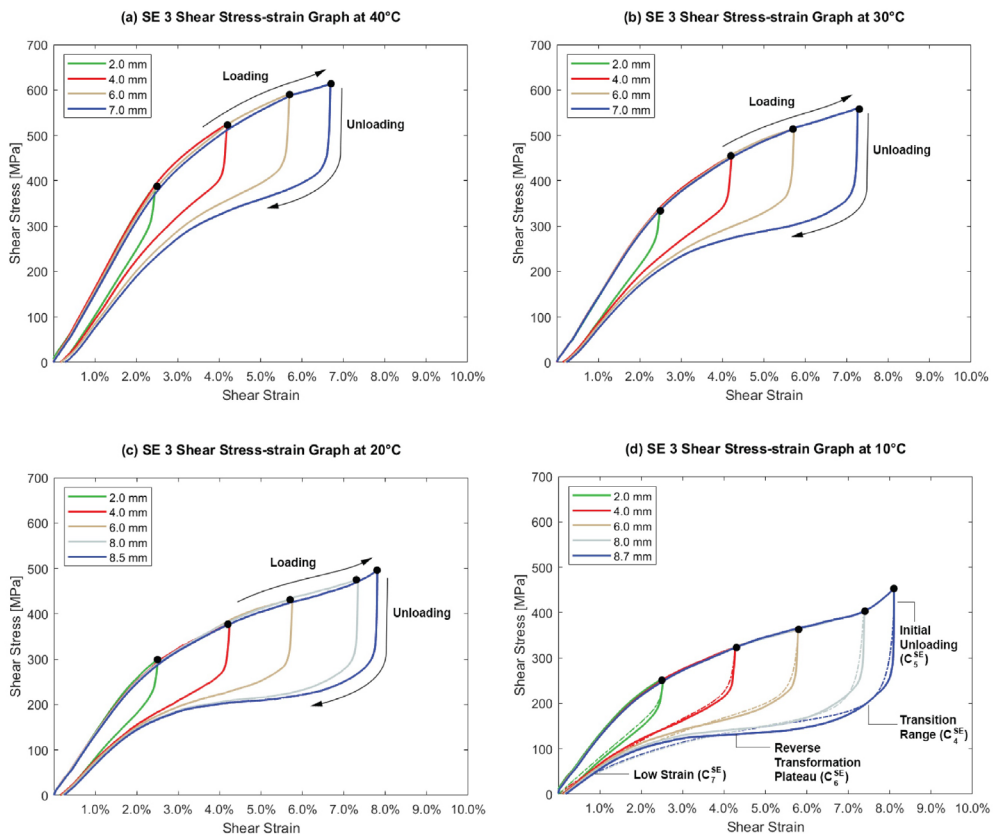


Figure 4.4 (a) SMA shear stress-strain curves from 20 °C downwards. The coloured dash-dotted lines and connection points $(\gamma_i^{cSMA}, \tau_i^{cSMA})$ are used for modelling in section 4.5.2.1. (b) SMA shear stress-strain curves at the heated state (150 °C). The coloured dash-dotted curves are also used for modelling in section 4.5.2.2. (c) SE shear stress-strain loading curves at different temperatures. The coloured dash-dotted curves are used for modelling in section 4.5.3.1. The dash-dotted black line corresponds to the shear modulus obtained from the dynamic measurements of Figure 4.3(c).

4.4.4 Superelastic Behaviour of SE

The outcomes of the loading-unloading experiments for the superelastic material are presented in Figure 4.5, where subfigures 5(a)-(d) reveal the performance of SE 3 for temperatures above 10 °C. It can be observed that SE 3 can fully recover to its original shape even after applying a strain up to 8%. For lower temperatures, significant residual strains start to build up and the material begins to exhibit diminished superelastic properties. Larger applied shear stress results in increased residual strains. For instance, a 9 mm displacement alteration of SE 3 at -10 °C induces 5.5% residual strain, whereas a 4 mm displacement alteration yields a 1.5% residual strain (Figure 4.5(f)). The test results from -20 °C to -40 °C can be seen in section A3.4 of the Appendix 3.



4

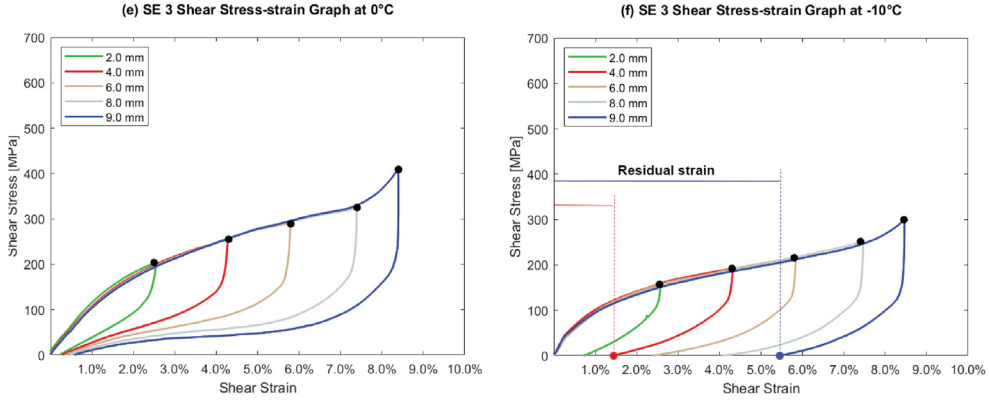


Figure 4.5 Superelastic tests in different temperatures. For each experiment, 4-5 loading-unloading cycles are conducted with the displacement-control method. Subgraphs (a)-(c) indicate the SE loading and unloading process with arrows. In subgraph (d), the coloured dash-dotted curves are the fits (for the unloading curves) established in section 4.5.3.2. Every unloading curve is divided into four segments: *initial unloading part*, *transition range*, *reverse transformation plateau* and *low strain*. Each segment of the unloading curve has a coefficient (corresponding to Eq. (4.9)) which affects its shape.

4.5 Modelling

With the experimental data obtained in section 4.4, we now have enough information to set up a model to describe the *minimum and maximum actuation angles* (θ_{min} and θ_{max}) of a hinge structure (Figure 4.1). In this section we will develop a phenomenological model which can directly relate the chosen geometrical parameters (wire diameters and torsion lengths, initial pre-trained angles) and material properties (modulus and its relationship with temperature) to predictions of the θ_{min} and θ_{max} of the hinge actuator.

Our aim is to develop a practical model which can be used by designers and engineers to understand and optimize the mechanical behaviour of objects with the hinge structures proposed in this paper. Because of that, we choose to simplify the constitutive behaviour (i.e. the loading and unloading curves) as much as possible without losing too much in the accuracy of the deformation predictions. Note that in general, the *shape of the deformation curves* of other nitinol SMA and SE materials will be very similar to the materials used in this study and mainly differ in the transition temperatures, which means that the model below remain valid and only the parameter values need to be adapted.

4.5.1 Reversible Torsion Hinge Analysis

The actuation span of our proposed hinge system in Figure 4.1 simply follows from a balance between the torque exerted by the SMA wire (which tries to open the hinge) and that of the SE (which closes the hinge):

$$T^{SMA}(\theta_0^{SMA}, L^{SMA}, r^{SMA}) = T^{SE}(\theta_0^{SE}, L^{SE}, r^{SE}) \quad (4.1)$$

where T is the torque of SMA or SE, and it is related to the initial pre-trained angle θ_0 , torsion length L and the nitinol wire radius r :

What makes the analysis more complex is that both materials have an intrinsic mechanical hysteresis (difference between the loading and unloading curves, see Figure 4.5). When the hinge structure is assembled, the SMA wire, which is initially at 180° , is loaded *anticlockwise* whereas the SE wire is deformed *clockwise* (see Figure 4.1). The initial angle of the hinge structure is thus found from the equilibrium of the *two loading curves*. When heated in the first actuation cycle, the SMA tends to move back towards its pre-trained initial angle (180°), while the SE wire further deforms to a larger opening angle. That is, during the first (and subsequent) heating cycles, *the SMA is unloading and the SE is loading*. When cooling down, the SMA modulus drops and the SE starts to close the hinge, i.e., *during cooling the SMA is in loading and the SE is in unloading mode*.

In the subsequent sections, we will set up approximate phenomenological models describing the loading and unloading behaviour of both the SMA and SE materials.

4.5.2 Modelling of SMA Shear Stress-strain Curve

4.5.2.1 SMA Loading During Cooling

The loading is characterised by a large shear stress plateau in which further stretching induces a phase transformation (from twinned to detwinned martensite (Rao et al., 2015)). Such transformation only requires a minimum of deformation energy (see Figure 4.4(a)). In order to capture the essentials of the deformation curves, we choose to approximate the data in Figure 4.4(a) with a curve consisting of three connected linear segments. The first segment represents the elastic deformation of the SMA in its twinned martensite state, the second part describes the material response during detwinning, which is assumed to be horizontal in our work. The third segment is the further loading in the fully detwinned state.

For every temperature, three *connection points* denoted as $(\gamma_i^{cSMA}, \tau_i^{cSMA})$ ($i = 1, 2, 3$) between the different segments are used to formulate the model:

$$\tau^{cSMA}(\gamma) = \begin{cases} \left(\frac{\tau_1^{cSMA}}{\gamma_1^{cSMA}} \right) \gamma & 0 \leq \gamma < \gamma_1^{cSMA} \\ \tau_2^{cSMA} & \gamma_1^{cSMA} \leq \gamma < \gamma_2^{cSMA} \\ \left(\frac{\tau_3^{cSMA} - \tau_2^{cSMA}}{\gamma_3^{cSMA} - \gamma_2^{cSMA}} \right) (\gamma - \gamma_3^{cSMA}) + \tau_3^{cSMA} & \gamma_2^{cSMA} \leq \gamma < \gamma_3^{cSMA} \end{cases} \quad (4.2)$$

We use MATLAB software to first determine the *connection points* $(\gamma_i^{cSMA}, \tau_i^{cSMA})$ for loading curves from -20°C to 20°C separately (dash-dotted lines in Figure 4.4(a)). γ_3^{cSMA} is assigned a same value of 11.5% for all temperatures. To determine the temperature dependency of shear strain, we plot (T, γ_i^{cSMA}) ($i = 1, 2$) as blue triangles and round dots in Figure 4.6(a). Similarly, (T, τ_i^{cSMA}) are plotted in red

colour. As the detwinning plateau is assumed to be horizontal, τ_1^{cSMA} and τ_2^{cSMA} have a same value for each temperature and both of them are presented as red round dots. MATLAB is used to experiment with various models for fitting data points shown in Figure 4.6(a). The *coefficient of determination* (R^2) is referred to for evaluating and deciding which model to use. Finally, the temperature dependency of the shear strain is modelled as a second-order polynomial, while for the shear stress, a combination of a linear and exponential term is used (Eqs. (4.3) and (4.4)). The fit parameters and its error bounds are determined by MATLAB and listed in Table 4.3.

$$\gamma_i^{cSMA}(T) = p_{1i}^{cSMA}T^2 + p_{2i}^{cSMA}T + p_{3i}^{cSMA} \quad (i = 1, 2, 3) \quad (4.3)$$

$$\tau_i^{cSMA}(T) = p_{4i}^{cSMA}e^{p_{5i}^{cSMA}T} + p_{6i}^{cSMA}T \quad (i = 1, 2, 3) \quad (4.4)$$

where $(\gamma_i^{cSMA}, \tau_i^{cSMA})$ are the the *connection points* of SMA shear-strain curves, T is the temperature.

With the Eqs. (4.2)-(4.4) and parameters in Table 4.3, we can model the SMA loading curves at any temperature from 20 °C downwards.

4.5.2.2 SMA Unloading at the Heated State

As explained in section 4.5.1, during the heating cycles of the hinge system, *the SMA is unloading and the SE is loading*. Therefore, for SMA, we only model the unloading curve at high temperature. The shear stress-strain curves at 150 °C in Figure 4.4(b) are used for modelling. Although the curves are nearly linear, for accurate prediction of the *maximum actuation angle*, it turns out to be necessary to use a power function (Eq. (4.5)) to fit the unloading curves (see dash-dotted lines in Figure 4.4(b)).

$$\tau^{hSMA}(\gamma) = p_1^{hSMA}\gamma p_2^{hSMA} \quad (4.5)$$

It can be seen that the SMA unloading curves at 150 °C are different owing to the distinct *initial unload shear strain*, which means the coefficients p_1^{hSMA} and p_2^{hSMA} are different among these curves. To evaluate how the *initial unload shear strain* affects p_1^{hSMA} and p_2^{hSMA} , we plot $(\gamma_{unload}^{hSMA}, p_1^{hSMA})$ and $(\gamma_{unload}^{hSMA}, p_2^{hSMA})$ with blue and red triangles accordingly (see Figure 4.6(b)). It can be seen that p_1^{hSMA} and p_2^{hSMA} vary linearly with the *initial unload shear strain* γ_{unload}^{hSMA} :

$$p_i^{hSMA}(\gamma_{unload}^{hSMA}) = q_{i1}^{hSMA}\gamma_{unload}^{hSMA} + q_{i2}^{hSMA} \quad (i = 1, 2) \quad (4.6)$$

in which q_{i1}^{hSMA} and q_{i2}^{hSMA} ($i = 1, 2$) are two parameters to define p_i^{hSMA} . Their values are provided in Table 4.3.

4.5.3 Modelling of SE Shear Stress-strain Curve

4.5.3.1 SE loading

The SE shear stress-strain curves during loading are showed in Figure 4.4(c) and can be approximated as:

$$\tau^{SE}(\gamma) = c_1^{SE} [1 - \exp(-c_2^{SE} \gamma)] + c_3^{SE} \gamma^2 \quad (4.7)$$

in which the coefficient c_1^{SE} is a measure of the shear stress level of the detwinning plateau, c_2^{SE} determines the slope of the initial elastic part (shear modulus), c_3^{SE} affects the increase rate of shear stress after the detwinning deformation.

To figure out the effect of temperature on c_1^{SE} , c_2^{SE} and c_3^{SE} , we plot (T, c_i^{SE}) ($i = 1, 2, 3$) with green triangles, blue squares and red round dots respectively in Figure 4.6 (c). It can be seen that they can be approximated with a linear model:

$$c_i^{SE}(T) = p_{1_i}^{SE} T + p_{2_i}^{SE} \quad (i = 1, 2, 3) \quad (4.8)$$

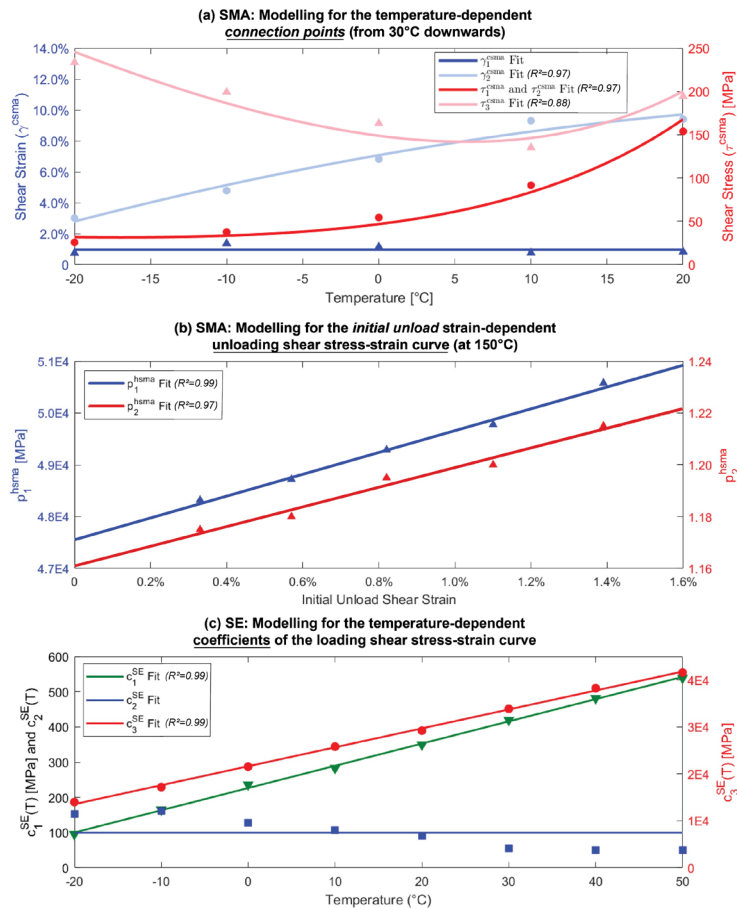


Figure 4.6 (a) Modelling for the temperature-dependent connection points (from 30 °C downwards). The data points correspond to $(\gamma_i^{cSMA}, \tau_i^{cSMA})$ of the fitting functions in Figure 4.4(a)

of the manuscript. The full lines are the fitting models (Eqs. (4.3) and (4.4)). (b) Modelling for the *initial unload strain*-dependent of the unloading shear stress-strain curve (at 150 °C). The data points are the fitting parameters (Eq. (4.5)) of the SMA unloading model (dash-dotted lines in Figure 4.4(b)). The full lines are the models which characterize the relationship between p_1^{hSMA} , p_2^{hSMA} and the *initial unload shear strain* (Eq. (4.6)). (c) Modelling for the temperature-dependent coefficients of the SE loading shear stress-strain curve. To simplify, c_2^{SE} is modelled as a constant. The data points correspond to the fitting parameters of the coloured dash-dotted lines in Figure 4.4(c). The full lines are the fitting functions of the data points.

Table 4.3 Parameters for the SMA model.

Parameters					
p_1^{cSMA} [%/°C ²]	0	p_1^{cSMA} [%/°C ²]	0	$p_{4_3}^{cSMA}$ [MPa]	143 (± 32)
p_2^{cSMA} [%/°C]	0	p_2^{cSMA} [%/°C]	0	$p_{5_3}^{cSMA}$	0.05 (± 0.010)
p_3^{cSMA} [%]	0.96 (± 0.343)	p_3^{cSMA} [%]	11.5	$p_{6_3}^{cSMA}$ [MPa]	-10 (± 2.9)
$p_{1_2}^{cSMA}$ [%/°C ²]	-2×10^{-3} (± 7.4×10^{-3})	$p_{4_1}^{cSMA}$ [MPa]	47 (± 16)	$q_{1_1}^{hSMA}$ [MPa]	2×10^5 (± 0.3×10^5)
p_2^{cSMA} [%/°C]	0.17 (± 0.088)	$p_{5_1}^{cSMA}$	0.07 (± 0.013)	$q_{1_2}^{hSMA}$ [MPa]	5×10^4 (± 310)
p_3^{cSMA} [%]	7.1 (± 1.93)	$p_{6_1}^{cSMA}$ [MPa]	-1.0 (± 1.47)	$q_{2_1}^{hSMA}$	3.7 (± 1.13)
				$q_{2_2}^{hSMA}$	1.2 (± 0.01)

4.5.3.2 SE Unloading

The unloading curves of the SE material are needed to describe the closing process of the hinge deformation. Figure 4.5 shows that the SE unloading curves depend on the temperature and the *initial unload shear strain*. All subgraphs show a large similarity in shapes. To illustrate this, we combined the unloading curves of 10-30 °C in a single plot. As can be observed from Figure 4.7(a) and (b), a vertical shift with factor α relative to the 10 °C curve indeed results in a good overlap. Therefore, we now only need to model the shape of 10 °C reference curve, to be able to predict the unloading behaviour at higher temperatures using the factors α . For a good prediction of the hinge angles, it turns out that we require a detailed description of the initial part of the SE unloading curve (i.e. the steep declining of the *initial unloading part* as well as the *transition range*, see Figure 4.5(d)). For this, we propose to use a tan function (first part of Eq. (4.9)). The second part of Eq. (4.9) describes the shear stress-strain behaviour near the origin. The fitting results are shown as coloured dash-dotted curves in Figure 4.5(d).

$$\tau_{unload}^{SE}(\gamma_{unload}^{SE}) = c_4^{SE} \tan\left(\frac{\pi \gamma_{unload}^{SE}}{c_5^{SE}}\right) + c_6^{SE} [1 - \exp(-c_7^{SE} \gamma_{unload}^{SE})] \quad (4.9)$$

where γ_{unload}^{SE} is SE shear strain of the unloading phase, τ_{unload}^{SE} is the SE shear stress as a function of shear strain at 10 °C, c_4^{SE} , c_5^{SE} , c_6^{SE} and c_7^{SE} are coefficients of the model. c_4^{SE} determines the *transition range* (see Figure 4.5(d)). c_5^{SE} relates to the *initial unloading part*. c_6^{SE} affects the shear stress level of the *reverse transformation plateau*, while c_7^{SE} has influence on the slope of *low strain part* before recover to 0.

A Similar shifting can be done for the temperatures below 10 °C, as shown in Figure 4.7(c) and (d). Note that with vertical shifting the *low strain part* is not captured well,

however, as mentioned before, we only need a detailed description of the initial unloading behaviour.

For a given temperature (10 °C), the unloading curves differ from each other owing to the distinct *initial unload shear strain*. To model this, we plot the coefficients c_4^{SE} , c_5^{SE} and c_7^{SE} as a function of the initial shear strain γ_{unload}^{SE} (see Figure 4.7(e)), and model these as linear functions:

$$c_j^{SE}(\gamma_{unload}^{SE}) = p_{1j}^{SE} \gamma_{unload}^{SE} + p_{2j}^{SE} \quad (j = 4, 5, 7) \quad (4.10)$$

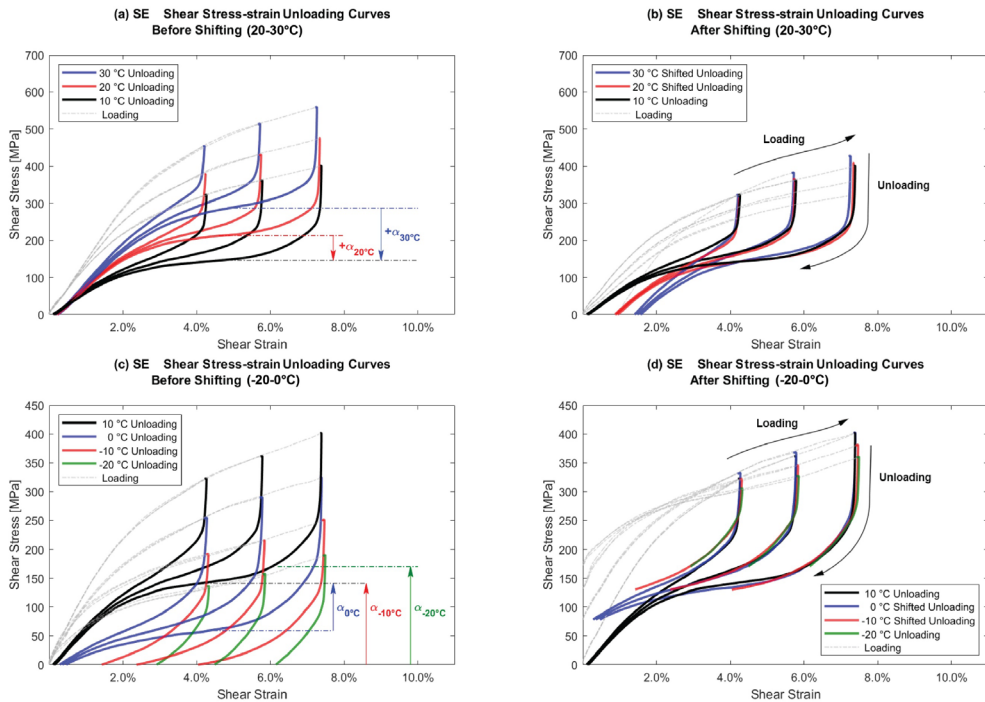
The coefficient c_6^{SE} is modelled as:

$$c_6^{SE}(\gamma_{unload}^{SE}) = p_{1_6}^{SE} (\gamma_{unload}^{SE})^{-p_{2_6}^{SE}} \quad (3.11)$$

In addition, the vertical shifts α are plotted as a function of temperature and also fitted to a linear model (full line in Figure 4.7(f)):

$$\alpha(T) = q_1^{cSE} T + q_2^{cSE} \quad (3.12)$$

With the Eqs. (4.7)-(4.12) as well as the Table 4.4, we can obtain the SE loading and unloading curve with given *initial unload shear strain* and temperature.



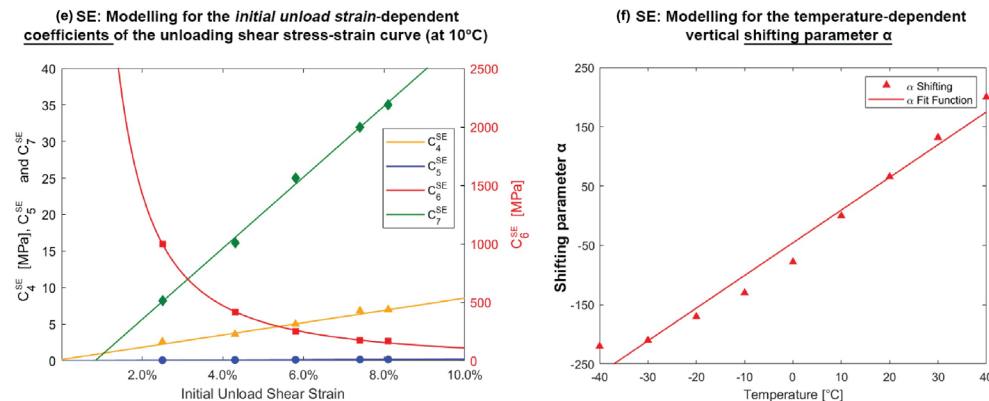


Figure 4.7 (a)-(d): SE unloading curves at other temperatures overlap with the curves at 10 °C after vertical shifting. (e): Modelling for the *initial unload shear strain*-dependent coefficients (at 10 °C). The data points are the fitting parameters of the coloured dash-dotted curves in Figure 4.5(d), which corresponds to Eq. (4.9). Full lines characterize their relationships with the *initial unload shear strain*. (f): Modelling for the temperature-dependent vertical shifting parameter α .

Table 4.4 Parameters for SE loading and unloading model.

Parameters					
$p_{1_1}^{SE}$ [MPa/°C]	6.3 (± 0.45)	$p_{1_2}^{SE}$	0	$p_{1_3}^{SE}$ [MPa/°C]	403 (± 30)
$p_{2_1}^{SE}$ [MPa]	226 (± 1)	$p_{2_7}^{SE}$	99 (± 3)	$p_{2_8}^{SE}$ [MPa]	2×10^4 (± 29)
$p_{3_4}^{SE}$ [MPa]	84 (± 12)	$p_{3_5}^{SE}$	2.0 (± 0.02)	$p_{3_6}^{SE}$ [MPa]	2.7 (± 0.90)
$p_{2_4}^{SE}$ [MPa]	0.15 (± 0.719)	$p_{2_5}^{SE}$	7×10^{-4} (± 14.0×10^{-4})	$p_{2_6}^{SE}$	-1.6 (± 0.09)
$p_{1_7}^{SE}$	486 (± 46)	q_1^{SE} [MPa/°C]	5.5 (± 0.82)		
$p_{2_7}^{SE}$	4.1 (± 10.91)	q_2^{SE} [MPa]	-45 (± 21.3)		

4.6 Model Validation

In order to validate our hinge angle prediction model (Eqs. (4.1)-(4.12)), we construct five different hinge structures, which differ in the lengths of the torsion element as well as in the initial deformation angles. These hinges are subjected to heating and cooling cycles and the corresponding angle changes are monitored. Using the models proposed in section 4.5, we then predict how the angle changes vary with temperature and compare this with our measurements.

4.6.1 Experiments with 5 Reversible Hinges

The validation tests of an opening and closing hinge structure could in principle be done by placing the hinge in an oven and using a camera system to infer the hinge angle changes during heating and cooling. In order to have a more accurate control of temperature and hinge deformation however, we prefer to do these tests in the DMA Q800 with a tool as shown in Figure 4.8. The hinge system is integrated with a SMA and SE using three galvanized steel spring pins. During the testing, only a small force (0.01 N) is applied and the testing machine essentially follows the movements of the hinge system. Eqs. (A3.1)-(A3.4) and (A3.8) in Appendix 3 are used to calculate the opening angle from the detected displacement.

Five tests are conducted with different hinge systems (labelled as *Sys 1-5* in Table 4.5) to examine the effect of SMA pre-trained initial angle and torsion length variation on the system angle change. The SEs of *Sys 1-5* are identically configured and trained in terms of initial angle (0°) and torsion length (10.45 ± 0.25 mm). SMA with varying initial pre-trained angles but an equal torsion length (11.0 ± 0.4 mm) is used for *Sys 1-3*. Conversely, *Sys 3-5* consist of SMAs with different torsion lengths but an equal initial angle (270°).

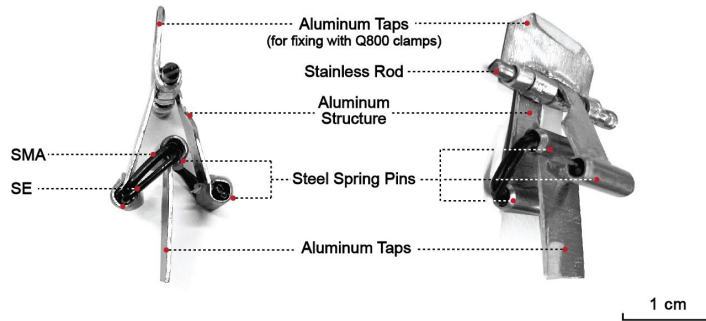


Figure 4.8 Configuration of the reversible torsion hinge system for validation tests in the Q800.

Table 4.5 Geometric parameters of hinge systems. Definitions of parameters refer to Figure 4.2.

Hinge System	Initial Angle θ_0	Torsion Length L [mm]	Arm Length L_a [mm]	Aluminium Structure Length L_s [mm]
<i>Sys 1</i>	SMA $104^\circ + SE 0^\circ$	SMA $10.6 \text{ mm} + SE 10.2 \text{ mm}$	7.3 mm	13.9 mm
<i>Sys 2</i>	SMA $175^\circ + SE 0^\circ$	SMA $11.1 \text{ mm} + SE 10.7 \text{ mm}$	7.2 mm	13.8 mm
<i>Sys 3</i>	SMA $270^\circ + SE 0^\circ$	SMA $11.3 \text{ mm} + SE 10.3 \text{ mm}$	7.3 mm	13.1 mm
<i>Sys 4</i>	SMA $270^\circ + SE 0^\circ$	SMA $13.4 \text{ mm} + SE 10.2 \text{ mm}$	7.3 mm	13.1 mm
<i>Sys 5</i>	SMA $270^\circ + SE 0^\circ$	SMA $17.6 \text{ mm} + SE 10.2 \text{ mm}$	7.5 mm	13.4 mm

Prior to the test, the temperature is decreased to -40°C and maintained constant for 5 minutes. Subsequently, the temperature is increased to 150°C at a rate of $5^\circ\text{C}/\text{min}$, followed by another 5-minute isothermal soaking. Then, the system is cooled down to -40°C at the same rate. The heating-cooling cycle is performed twice. The second recorded displacement variation of five systems is converted to the actuation angle of the hinge system, which is plotted versus temperature in Figure 4.9 (*Sys 1-3* in (a), *Sys 4* and *Sys 5* in (b) and (c) respectively).

As shown in Figure 4.9(b), during the heating process, the hinge angle of *Sys 4* (green curves) remains constant for a large part at 90° (*minimum actuation angle*), and only changes in a narrow temperature range from 46°C to 92°C during the SMA's phase transition. When the torque produced by SMA balances with SE's, the system angle becomes stabilize after 92°C . For the cooling process, the system angle starts to reduce at around 20°C . It completely recovers to 90° at -16°C . Similar results can also be observed with other specimens (see Figure 4.9(a) and (c)). For definitions of the *minimum and maximum actuation angle*, as well as the *angle span* refer to Figure 4.1.

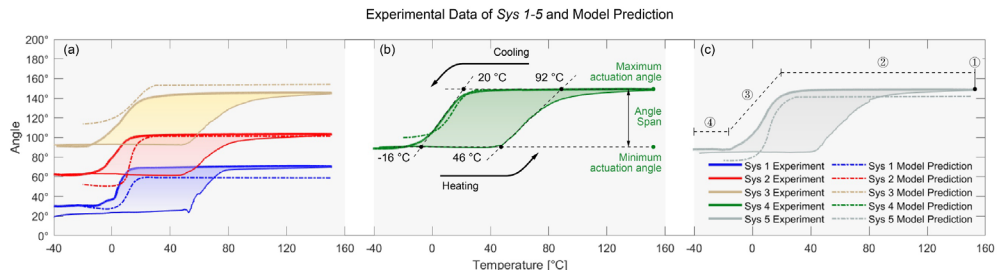


Figure 4.9 Experimental results of 5 reversible torsion hinges: *Sys 1-3* are plotted in (a), while *Sys 4* and *Sys 5* are in (b) and (c) respectively. The full lines are the experimental data, whereas the coloured dash-dotted lines are the prediction model of the cooling process. The shaded areas reflect the hysteresis. *Minimum and maximum actuation angle*, as well as the *angle span* correspond to Figure 4.1. The cooling curve in (c) is divided into 4 parts (①, ②, ③ and ④), of which more details are discussed in section 4.6.2.

4.6.2 Model Predictions

To better understand how the torques of the SMA and SE wires interact during the different parts of the cooling curves, we identify three states: *the heated state*, *locked state*, and *actuation state*. *The heated state*, denoted by the symbol ① in Figure 4.9(c), describes the condition where the system is held at its highest temperature (150 °C). During the first and the last parts of the cooling (② and ④ as shown in Figure 4.9(c)), the hinge system angle remains constant, which will be referred to as *the locked state*. *The actuation state*, represented by the part ③, refers to the temperature range in which the hinge angle changes. Our objective is to investigate how the SMA and SE behaviour determine the hinge angle of the system in each of these states.

4.6.2.1 The Heated State

As stated in section 4.5.1, the heating actuation process corresponds to the *loading phase of the SE and unloading phase of SMA*. In order to visualize the torque equilibrium between SMA and SE wires (Eq. (4.1)), we plot the unloading curves of SMA in Figure 4.10(a) and (b), together with the loading curves of the corresponding SE wires. The intersections indicate that the torques of the SE and SMA wire (from the same system) balance out, resulting in 5 predictions for the *maximum actuation angles* (all at 150 °C) (Koh et al., 2014). The relationship between shear strain and shear stress is given by Eqs. (4.1)-(4.12). Additionally, to achieve the angle-torque graphs, another three equations are required.

$$T = \frac{\tau J}{r} \quad (4.13)$$

$$\theta = \frac{\gamma L}{r} \quad (4.14)$$

$$J = \frac{\pi r^4}{2} \quad (4.15)$$

where T is the torque, J is the polar moment of inertia of SMA or SE, r is the radius of SMA or SE, L is the length of *torsion part* (see Figure 4.2).

Figure 4.10(a) and (b) illustrates the heated state of Sys 1-5. As listed in Table 4.5, Sys 1-5 share the same initial angle of 0° and have similar torsion lengths for the SE. Consequently, their angle-torque curves almost overlap in the graph (black curves in Figure 4.10(a) and (b)). Sys 1-3 have different SMA initial pre-trained angles (see black arrows in Figure 4.10(a)), resulting in different starting angles. The deformation curves however have identical shapes. The equilibrium angles for Sys 1-3 follow from the intersection points are determined as 58°, 101° and 154°, respectively. The effect of the torsion length for systems with constant SMA initial angles of 270° is shown in Figure 4.10(b). In this case, the intersection points turn out to be 142°, 149° and 154°, which are seen to vary much less.

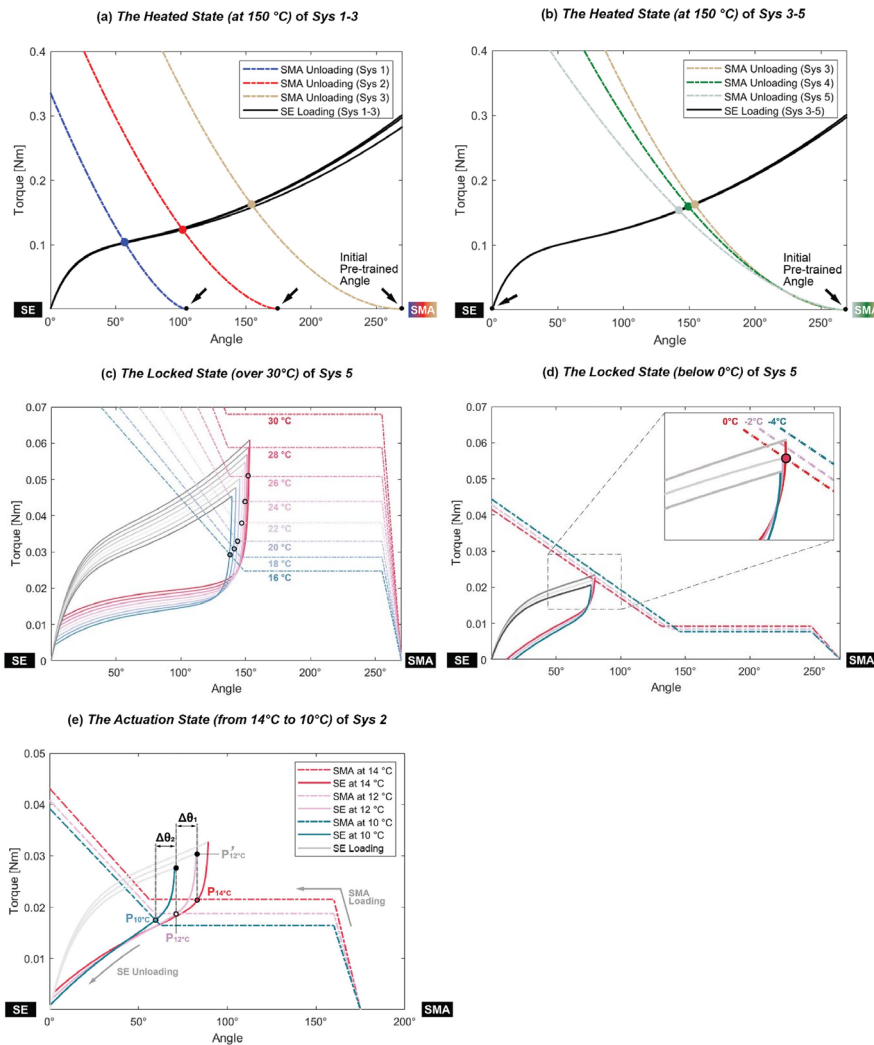


Figure 4.10 (a) and (b): The heated state of Sys 1-3 and Sys 3-5 at 150 °C. The initial pre-trained angles of the nitinol wires are shown as black arrows. The coloured dots represent the intersections between the SMA unloading and the SE loading torques. (c) and (d): Explanation of the locked

state for Sys 5. The coloured full lines represent the SE unloading at different temperatures, while grey lines are the SE loading curves. Coloured dash-dotted lines represent the SMA loading curves. There is no intersection between the torque-angle curves when the temperature is above 30 °C or below 0 °C. (e): *The actuation state* of Sys 2 from 14 °C to 10 °C. $\Delta\theta_1$ and $\Delta\theta_2$ are the angle change of two cooling steps (from 14 °C to 12 °C, and 12 °C to 10 °C).

4.6.2.2 Locked State

During the first part of cooling, the hinge angle remains locked at *the heated state* angle (⊙ in Figure 4.9(c)). The reason for this can be explained by the details of SMA and SE mechanical behaviour. As illustrated in Figure 4.10(c), when cooling toward 30 °C, the SMA wire is in its torque plateau region, which is above the torque generated by the SE material. This indicates that the SE, within the system, is incapable of producing and transferring sufficient torque to move the SMA. During further cooling of the system, the SMA torque plateau decreases (to about 0.06 Nm at 28 °C) until the unloading torque of the SE surpasses that of the SMA and *the actuation state* starts.

After the actuation, a second *locked state* can be observed (⊕ in Figure 4.9(c)). As can be seen in Figure 4.10(d), this happens below 0 °C, where the SE torque drops below the torque generated by the SMA.

4.6.2.3 Actuation State

During the cooling, the equilibrium hinge angles at *the actuation state* can be analyzed in a similar way. In Figure 4.10(e), we use Sys 2 as an example. At 14 °C, the SMA balances with SE at 84° ($P_{14^\circ\text{C}}$ in Figure 4.10(e)). When the temperature is decreased to 12 °C and 10 °C, the intersection points shift to 71° (point $P_{12^\circ\text{C}}$) and 59° (point $P_{10^\circ\text{C}}$) respectively. Note that the angle change is relatively large for only a small temperature variation.

4.6.3 Comparison of Experimental Data with the Hinge Model

With the analysis method mentioned in section 4.6.2, the angle-temperature curve of the system's cooling process can be modelled. Figure 4.9 presents the experimental data of the cooling process (coloured full lines) as well as the corresponding model predictions (coloured dash-dotted lines). The *angle span* of all five specimens closely matches the model's predictions, yielding an average deviation of 17.7% (mainly due to vertical shifts). The deviations between the predicted and experimental *maximum and minimum actuation angle* are 10.6% and 16.0% correspondingly. The overall deviation is $13.5 \pm 8.2\%$.

Going from Sys 1-3, Figure 4.9(a) shows that the predictions for the *maximum actuation angle* deviate from the observation by -12°, -2° and +9°, respectively. The *minimum actuation angles* are overpredicted by -3°, -11° and +23° correspondingly. Their *actuation states* (angles decrease) start earlier by about 10 °C. For Sys 4, the *maximum actuation angle*, as well as *the actuation state* (from 20 °C to -16 °C) is

predicted well (Figure 4.9(b)) and only the *minimum actuation angle* is somewhat overpredicted (+8°). The predicted *angle span* of Sys 5 aligns well with the experimental data, which only has 4° deviation, while both the *maximum and minimum actuation angle* are overpredicted by around 8°.

4.7 Discussion and Application Examples

The experiments with the five constructed hinges show that during most of the heating and cooling process the hinge angle does not change and that the actuation of the structure is limited to a relatively narrow temperature window. Interesting to see is that these temperature windows differ from the transition ranges of the SMA material as determined with DSC (see Figure 4.3(a) and Table 4.2). As is discussed in section 4.6, this is explained with the fact that the hinge actuation depends on details of the mechanical behaviour of both the SE and SMA material. More details about the actuation temperature of the hinge system can be seen in the Appendix 3. Our model which takes these details into account was seen to predict the actuation transitions of the hinge mechanism quite accurately.

4.7.1 SMAs' Geometric Parameters Influence on System Angles

The two main parameters for the design of the hinge actuator are the SMA pre-trained initial angle and the torsion length. In Figure 4.11(a), we plot the *maximum and minimum actuation angle* (θ_{max} and θ_{min}), as well as the *angle span* ($\Delta\theta$) for different SMA pre-trained angles. As can be seen, the *maximum actuation angle* (dash-dotted line) increases linearly with the SMA pre-trained angle, but this is not the case for the *minimum actuation angle* (dotted line), which starts to increase only for the pre-trained angle above 170°. Because of this, increasing the SMA pre-trained angle does not automatically lead to larger an actuation span, which actually shows a maximum of about 40° for a pre-trained angle of 170° (see the full line). The coloured symbols in Figure 4.11 refer to the results of the validation experiments (obtained from Figure 4.9) and are shown to closely follow the predictions.

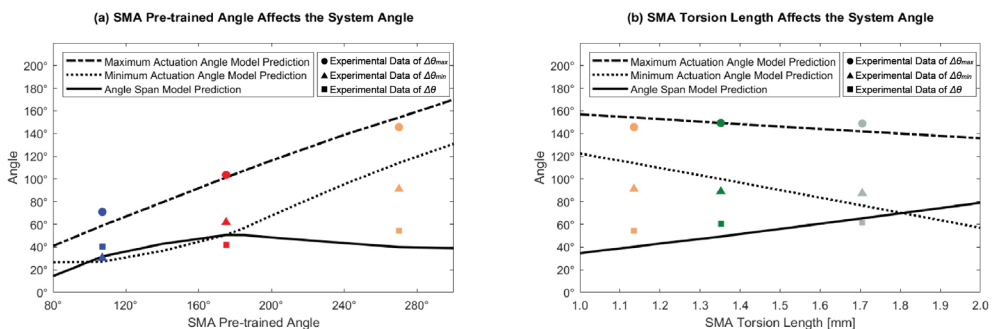


Figure 4.11 (a) Influence of the SMA pre-trained angle on the system angles. (b) Effects of the SMA torsion length on the system angles. Lines indicate model predictions, and symbols are the independent experimental data.

Figure 4.11(b) shows the effect of SMA torsion length on the system angles. Upon increasing the SMA torsion length, the *maximum actuation angle* shows a gentle decrease, while the *minimum actuation angle* declines faster, thereby leading to a growth in the actuation span. The *angle span* increases with the torsion length from 40° at 1 cm to 80° at 2 cm torsion length. The largest experimentally observed *angle span* is about 60°.

Overall, a greater SMA preset angle results in a larger *maximum and minimum actuation angle*, while a longer torsion length induce a larger *angle span*.

4.7.2 Applications

Reversible torsion hinge actuators are lightweight, and have a small form factor while delivering high actuation force. *Sys 5* only weighs 2 g, but can generate up to 5 N actuation force when heated at high temperature (see Appendix A2). These attributes render them a competitive alternative to motors or other forms of actuators in certain application scenarios.

To demonstrate its application potentials, prototypes of a gripper and a butterfly are developed. These prototypes require a hinge actuator which can close during actuation and open during cooling down. The geometric parameters of the SMA and SE wires used in the hinge actuator are listed in Table 4.6.

Table 4.6 Geometric parameters of SMA and SE samples used in the gripper and butterfly.

	Wire Radius r [mm]	Torsion Length L [mm]	SMA Initial Angle θ_0
SMA	0.50	15.8	0°
SE	0.375	17.0	180°

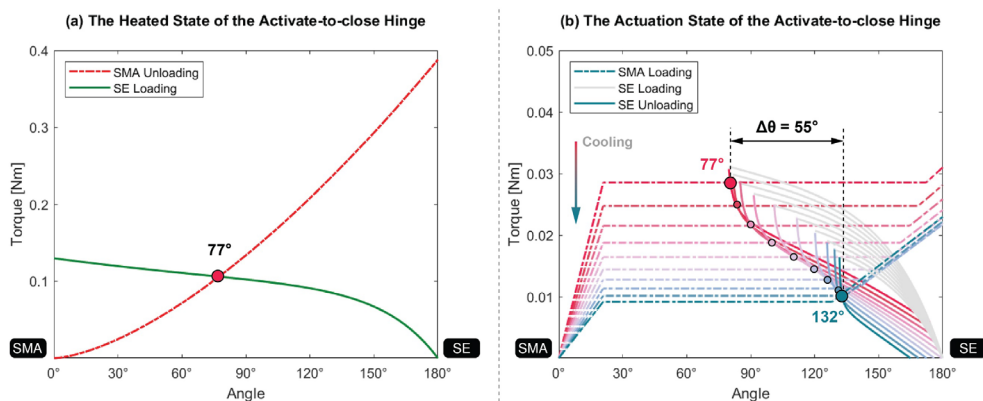


Figure 4.12 (a) *The heated state of the activate-to-close hinge for applications*; (b) *The actuation state of the activate-to-close hinge for applications*.

With the parameter values in Table 4.6 and the model described in section 4.5, the predicted *actuation angle span* is 55°, and the *maximum and minimum actuation angles* are 77° and 132° respectively (see Figure 4.12). By comparing these

theoretical values with the measured angles ($\Delta\theta = 48^\circ$, $\theta_{min} = 68^\circ$, $\theta_{max} = 116^\circ$) the average deviation is estimated to be 13.8%, which agrees with our previous findings.

The gripper constructed by these hinge actuators can securely grasp objects of various shapes and sizes (Figure 4.13(a) and (b)) without causing damage, whereas a motor-based gripper may require the integration of force-feedback sensors to prevent harm caused by excessive force. A butterfly demonstrator is represented as another example in Figure 4.13(c). Furthermore, these millimetre-scale hinge actuators have promising prospects applications with spatial constraints, such as aerospace and medical surgical instruments. The reversible torsion hinge actuator can be activated by electrical current within a few seconds. However, cooling down naturally in room temperature air requires much more time (30-40 seconds). It means that the actuator is not very suitable for applications which need high response speed, such as a robot hand with fast moving fingers, and real-time responsive VR devices. To reduce the cooling time, airflow speed can be increased, and thinner SMA wires can be used to developed the hinge actuators. The hinge actuator can also be activated in water, requiring about 3 to 5 seconds for both heating and cooling.

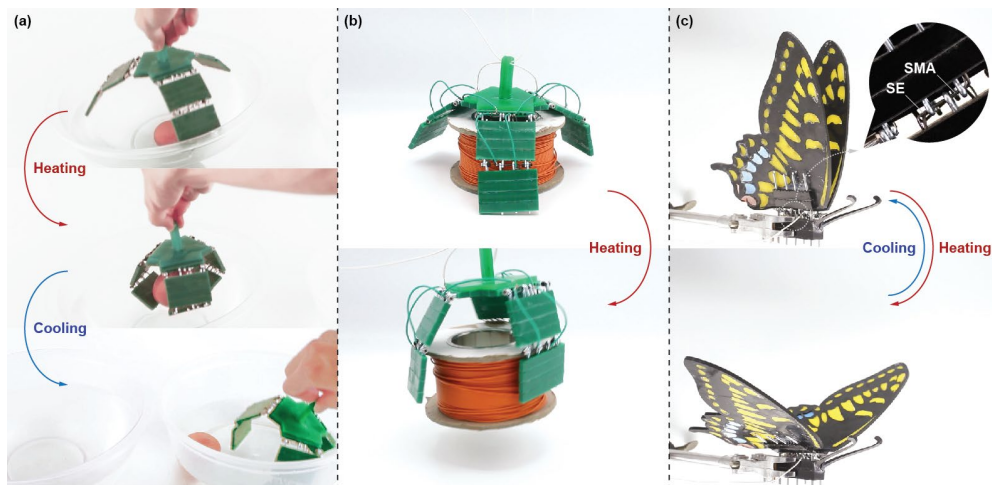


Figure 4.13 Application examples. (a) and (b) A gripper constructed by 6 reversible torsion hinge actuators. It is able to grab up an egg when actuated in hot water, and release in cold water. It can also lift up a 0.6 kg wire bundle easily. (c) A butterfly demonstrator is constructed by two reversible hinge actuators.

4.8 Conclusion

This chapter discusses a novel reversible hinge actuator composed of a nitinol shape memory alloy wire and a superelastic wire which are actuated in torsion. We measured and modelled the mechanical properties of these materials in detail, for which we constructed a special loading frame to convert tension to torsion deformation. The actuation behaviour of the hinge opening follows from the

equilibrium between the loaded SMA and SE wires, resulting in an overall model for the hinge behaviour. We constructed 5 reversible hinge systems with different SMA pre-trained angles and torsion lengths, and used these to validate our model. The angle *span* seems to increase with SMA torsion length up to a value of 60° at 1.7 cm torsion length. In general, the deviation between the model predictions and experiments was seen to be $13.5 \pm 8.2\%$. The model is practical because it directly relates geometrical design parameters to the opening and closing angles of the hinge system. It is therefore considered valuable for scientists, engineers as well as designers.

We showed that with a hinge structure which only weighs 2 g, the actuator can generate up to 5 N when actuated. A gripper and a butterfly demonstrator were constructed to show possible application scenarios. In the following chapter, to fully discover its application possibilities, we develop a toolkit based on the hinge actuator. The toolkit is designed for use by designers and enables the creation of various types of shape-changing objects.

Chapter 5 *

Mimosa: A Modular Hinges Kit for Creating Shape-changing Objects

In this chapter, a shape-changing constructive toolkit, Mimosa, is introduced. Key components of the toolkit are modular hinges, which is based on the SMA torsion deformation as described in Chapter 4. For the hinge leaves, a variety of common materials can be used, including cardboard, acrylic and textile, enhancing the versatility of the toolkit. Mimosa aims to inspire designers and HCI researchers to construct interactive shape-morphing objects with SMAs and everyday materials. A workshop study involving 6 participants demonstrated that the toolkit effectively motivated and inspired the participants, leading to generation of new ideas.

* This chapter is based on:

Liu, Q., Ghodrat, S., & Jansen, K. M. B (2024, February).

Mimosa: Modular Self-folding Hinges Kit for Creating Shape-changing Objects.

In *Proceedings of the Eighteenth International Conference on Tangible, Embedded, and Embodied Interaction* (pp. 1-13). DOI: [10.1145/3623509.3633381](https://doi.org/10.1145/3623509.3633381)

5.1 Introduction

“*High-tech*” usually refers to computation, and the rest of the material world is often regarded as “*low-tech*” (or craft) (Eisenberg et al., 1998). In 1999, Eisenberg defined “*middle tech*” as a “terrain in which programs and materials, complexity and concreteness, blend into new media” (Eisenberg et al., 1998). In the *middle tech* terrain, computation and crafting are deeply woven together without firm lines. On the craft side, computation enhances the expressive capabilities of existing materials. On the computation side, new software and programs are developed to support crafting activities (Blauvelt et al., 1999). The boundary between computation and craft gradually disappears. This can for example be observed in the smart textile domain, where many electronic toolkits and software are developed to blend with traditional textile manufacturing techniques (Friske et al., 2019; Katterfeldt et al., 2009; Vahid et al., 2021; Wu et al., 2020). Vallgård and Redström proposed that computational technology could be seen as a material like any other materials used to design things (Vallgård et al., 2007). In Seymour Papert’s project, students could use any materials to build devices for time measurement. The computation can be “*messed around with*”, just like pendulums, paints, clay (Follmer et al., 2013). Blending computation with traditional craft can be seen as a promising approach to develop new devices, increase technological literacy and broaden technology culture (Posch et al., 2019). Buechley also demonstrated such benefits of combination of craft and computation by integrating carving, sewing and painting into constructing electronics (Buechley et al., 2012). In recent year, pandemic lockdowns prompt reflections on crafting tangible interfaces in home (Jones et al., 2023).

Shape-changing interfaces are emerging as a new generation of devices which can change their shapes (Kim, Everitt, et al., 2021). A common form of shape-changing interfaces is represented by construction kits, which consist of interactive units that can be assembled and connected (Dancu et al., 2015; Ullmer et al., 2000). Construction toolkits can encourage users to explore creative concepts in an easy and efficient way (Youn et al., 2022). Many researchers have recently explored application potentials of shape-changing toolkits. Most of the existing toolkits are developed for particular applications, such as kinematic system education (Raffle et al., 2004), adaptive furniture (Sproewitz et al., 2009), and children entertainment (Kopic et al., 2016; Yang et al., 2019), and some toolkits have already incorporated the traditional crafting (Koizumi et al., 2010; Qi et al., 2012). However, the potential of shape-changing toolkit in the *middle tech* terrain has not been fully realized. Combining traditional craftsmanship with tangible user interfaces design is beneficial for the development of new devices, as crafting provides users with greater creative freedom, enabling them to customize the devices in a personalized manner (Jayathirtha et al., 2020; Perner-Wilson et al., 2010). It is worthy to encourage users to immerse themselves in the *middle tech*

exploration, by integrating crafting activities with “*high-tech*”. This chapter presents Mimosa*, a shape-changing constructive kit based on shape memory alloy (SMA) technology. By incorporating everyday materials (e.g. cardboard and textile), Mimosa encourages designers to participate in craftsman and aims to inspire them to create shape-changing objects for a variety of application scenarios. SMA can generate a relatively high actuation force, which may enhance the toolkit’s versatility. Additionally, SMA is lightweight with a small form factor, and thus has little effect on the overall aesthetics of the shape-changing objects.

Several ways of characterizing how physical tools support creative practices has been introduced in previous HCI research (McCullough, 1998; Terry et al., 2002; Torres et al., 2016; Zoran et al., 2014). Here 4 metrics are derived to evaluate Mimosa, which are *usability*, *transparency*, *quality* and *agency*. *Usability* refers to whether the toolkit is usable or not. *Transparency* addresses the awareness of the toolkit during creative practice (McCullough, 1998). *Quality* describes users’ satisfaction on the final objects constructed by the toolkit, and users’ affective feelings after using the toolkit. *Agency* refers to whether users are capable to make customized designs. We aim to ensure that Mimosa closely adheres to these metrics, thereby maximizing the toolkit’s support for users’ creativity.

With Mimosa, we make the following contributions:

- (1) We provide a toolkit for constructing shape-changing objects, by incorporating the crafting (e.g. sewing, papercraft) process. The toolkit’s compatibility with everyday materials allows for craftsmanship and boundless creative potential.
- (2) By making Mimosa simple and accessible, we offer an efficient way of using SMAs for constructing shape-changing objects. Users without any prior experience of similar toolkits can construct their shape-changing objects in one hour.
- (3) With a workshop study, we demonstrate the toolkit can inspire users to design, and provide a good user experience. Lessons we learn can inform future toolkit improvement.

5.2 Related Work

5.2.1 Motor-based Shape-changing Toolkits

Motors can be controlled easily and precisely (e.g. rotation angle, speed). They can provide lots of possibilities to achieve complex shape-changing behaviors. For examples, serpentine robotics *LineFORM* is a curve interface for display, interaction and constraint. It is comprised of a series chain of 1DOF servo motors with integrated sensors for direct manipulation (Nakagaki et al., 2015). Users can set their shapes in software. *Topobo* is a constructive assembly system actuated by motors and electronics (Figure 5.1(a)). It can be quickly assembled to produce dynamic

* Mimosa is a genus of plants that can change their shapes in response to external stimuli.

biomorphic forms like animals' skeletons (Raffle et al., 2004). *Topobo* is targeted at children, to help them understand certain physical principles affecting kinematic systems. Leigh et al. presented *Morphology Extension Kit*, which allows users to build and customize wearable robotics (Leigh et al., 2018). In addition, *Roombots* (Sproewitz et al., 2009) for adaptive furniture and self-assembling cubic robot *M-Blocks* (Romanishin et al., 2013) are also modular shape-changing objects actuated by motors.

Existing motor-based toolkits have limited versatility, as some of them are developed for specific purposes (e.g. *Topobo*, *Morphology*, *Roombots*), and some (e.g. curve interface *LineFORM*, cubic interface *M-Blocks*) cannot be used for constructing complicated shapes which can limit their application scenarios.

Using motors for developing shape-changing toolkits can produce some unavoidable problems. First, to achieve complex shape-changing behaviours, a certain number of motors is necessary which makes shape-changing objects bulky and heavy. Second, joint spaces need to be foreseen for placing the motors, that might affect the aesthetics of constructive shape-changing objects. Third, noise is generated when the motor is running.

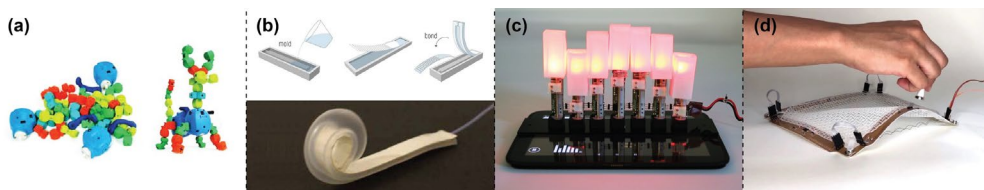


Figure 5.1 (a) *Topobo*, which can be assembled to produce dynamic biomorphic forms like animals' skeletons (Raffle et al., 2004). (b) Construction with *PneuUI* (Yao et al., 2013). (c) *ShapeClip*, which can transform any computer screen into a z-actuating shape-changing display (Hardy et al., 2015). (d) *Surfex*, a programmable tangible interface (Coelho et al., 2008).

5.2.2 Pneumatic Shape-Changing Technologies

A pneumatically actuated approach (e.g. with air-pumps) can be used to control movements or shape changes of devices. Some technologies and methods have been put forward to create shapemorphing objects. Such technologies encourage users to design air bubbles themselves, which can be seen as a crafting activity. It enables users to create customized shape-changing objects, but the duration time is long. For instance, *PneuUI* developed by Yao et al. is used to build shape-changing interfaces through pneumatically actuated soft composite materials (Yao et al., 2013) (see Figure 5.1(b)). For each *PneuUI* application, users need to design and construct different composite interfaces which include diverse air bubbles or channels and structural material layers (e.g. paper, fabric, wood). It involves the silicone casting process with 3D printed molds, which could be time-consuming.

MorpheusPlug, which covers seven shape-change features (such as length and

curvature change) with six types of widgets, can be used for designing different items (e.g. an anti-rain phone case and posture-correcting cushion) (Kim, Everitt, et al., 2021). *TEX(alive)* is another toolkit using 3D printing technology, which serves to help familiarize designers with the complexity and expressivity of temporal forms in shape-changing textile interfaces (Martinez Castro et al., 2022). *Therms-Up!* is a DIY method of creating inflatable soft actuators with wasted thermoplastic bags and a 3D printer (Choi & Ishii, 2021).

It is easier for users to construct shape-changing objects by providing ready-to-use modular components. *InflatiBits* is a modular construction kit consisted of soft inflatable air-chambers, airconnectors, and etc. By combining with standard LEGO parts, the constructed customized soft robotics can achieve fantastic appearances (Kopic et al., 2016). Similarly, *Legoons* is developed for constructing characters and artifacts (Yang et al., 2019). It consists of several types of inflatable widgets and decoration bricks for children to make inflatable animals, a long chain, and etc. Lee et al. developed a system of Lego-compatible pneumatic bricks for customizing soft robotics (e.g. children toy, gripper) (Lee et al., 2018).

In most cases, an air pump is necessary for the activation of pneumatic shape-changing objects, which could make the devices bulky. Even though there have been some pump-free designs available (Acome et al., 2018; Suzumori et al., 2013), there are still various restrictions when it comes to applications. For example, Lu et al. presented *Auto-Inflatables*, which can be activated by the chemical reaction in chambers, but it is a one-time activation mode (Lu et al., 2019). Lu et al. developed fluid-driven *milliMorph* (Lu et al., 2019). When filling with low boiling point liquid, it can be triggered by the environment temperature without any pump and rigid components. However, its actuation force is relatively low, which can limit its application scenarios. Similarly, many pneumatic toolkits, like *InflatiBits*, *Legoons* and *Soft LEGO*, only address at the field of entertainment for children owing to their low actuation force (Lee et al., 2018).

5.2.3 Pin-based Shape-Changing Displays

Pin-based shape-changing interfaces refer to interfaces that use an array of vertically moving pins to render different shapes and forms (Schoessler et al., 2015). Many relevant devices have been proposed in the HCI community (Follmer et al., 2013; Iwata et al., 2001; Leithinger et al., 2011). For examples, Hardy et al. developed modular *ShapeClip*, which can help users transform any computer screen into a z-actuating shape-changing display without requirement of electronics and programming knowledge (Hardy et al., 2015) (Figure 5.1(c)). Such pin-based displays have limitations on the types of shapes that can be achieved, as the pins can only move up and down without capacity to render any overhang or overpass structures. Philipp et al. addressed it with magnetic building blocks on the pins (Schoessler et al., 2015). Pin-based shape-changing displays generally are used for

enriching output modalities of existing displays instead of creating shape-changing objects, as the pins have to be installed in a “platform” to help them move vertically.

5.2.4 SMA-based Shape-Changing Toolkits

SMA have been applied in some shape-changing toolkits. For examples, Tahouni et al. presented *NURBSforms*, which is a modular shape-changing tool for prototyping curved surfaces (Tahouni et al., 2020). Each module represents an edge of variable curvature, and it enables designers to construct and adjust surface’s curvature when joined together with other modules. Similarly, *Surflex* is a programmable tangible interface which contains embedded SMA coils (Coelho et al., 2008) (Figure 5.1(d)). *Patch-O* is a deformable interface fabricated with versatile yarn materials and SMAs (Ku et al., 2022). It can enhance functionality of garments and aesthetically suited in the form of a woven patch. Application cases include a volumizing hair lifter, a shrinking patch for lifting sleeves and etc. (Ku et al., 2022). SMA shape-changing displays can also function as notification interfaces, such as *MorePhone* (Friske et al., 2019). In addition, there have been some shape-changing interfaces integrating crafting with SMA, such as the animated paper (Koizumi et al., 2010; Qi et al., 2012), and *Seamless Seams* which embeds SMA wires on fabrics (Nabil et al., 2019), but each of them only address at one application field (i.e., education, toy and interactive artefact).

5.3 Mimosa Kit Components

In this section, toolkit Mimosa will be introduced. Mimosa consists of 5 main components as depicted in Figure 5.2. Each element has been described further:

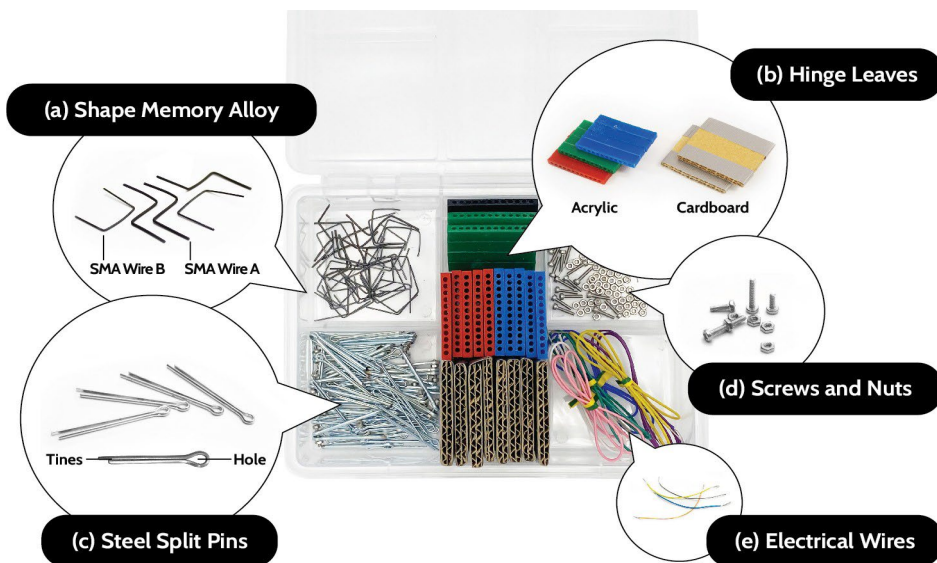


Figure 5.2 Mimosa Components. (a) Shape memory alloy; (b) Hinge leaves; (c) Steel split pins; (d) Screws and nuts; (e) Electrical wires.

5.3.1 Shape Memory Alloys (SMAs)

Working principles of the reversible hinge actuator are illustrated in [Figure 4.1](#) in [chapter 4](#). In the toolkit, we set out two types of actuator hinges (“*activate-to-open*” and “*activate-to-close*”) by combining SMA wires with varying initial SMA training angles. We used the 1.00 mm diameter SMA wire ($A_f = 47\text{ }^\circ\text{C}$) from Nanografi Nano Technology as the actuation wire, and 0.75 mm superelastic wire ($A_f = -4\text{ }^\circ\text{C}$) from Kellogg’s Research Lab. For the *activate-to-open* hinge, the predetermined angle of the actuation wire is 180° , while the superelastic wire is 0° . The *activate-to-close* hinge consists of an actuation wire with the preset angle of 0° , and a superelastic wire with the preset angle of 180° .

5.3.2 Hinge Leaves

Hinge leaves are developed in different materials, including acrylic, cardboard and textile. Comparing with commonly used 3D printed materials (e.g. PLA, ABS), acrylic has a higher glass transition temperature of $110\text{ }^\circ\text{C}$, which prevents them from melting or thermal deformation during actuation. Acrylic leaves are manufactured by laser cutting using 8 mm thickness acrylic plates (see [Figure 5.3\(a\)](#)). The size of the processed acrylic blocks measures $45 \times 8 \times 4\text{ mm}$ ([Figure 5.3\(a1\)](#)). By combining 4 pieces of acrylic blocks hole-to-hole together, a $45 \times 32 \times 4\text{ mm}$ acrylic hinge leaf can be obtained. Every acrylic hinge weighs 5.4 g. Users can customize their own shapes with software such as Auto CAD and Solidworks.

Another material for making hinge leaves is cardboard. The cardboard hinge weighs 2.1 g, which is the lightest among the three different materials versions. Double wall cardboard is recommended, which has two layers of corrugated fluting and three liners ([Figure 5.3\(b1\)](#)). Users can cut it with scissors or knives from package boxes, and tape can be used to enhance its edges to make it stronger and durable.

The third option is textile. Being similar to a sandwich, the textile hinge leaf consists of two layers of thick canvas fabrics with a middle layer of 0.2 mm thickness polypropylene (PP) film (see [Figure 5.3\(c3\)](#)). These three layers are sewed together by several columns of thread. Space is left between every two thread columns, for inserting the split pins and SMA wires. Fabric with different colors or pattern can be selected, which can enrich the aesthetics of textile hinge leaves.

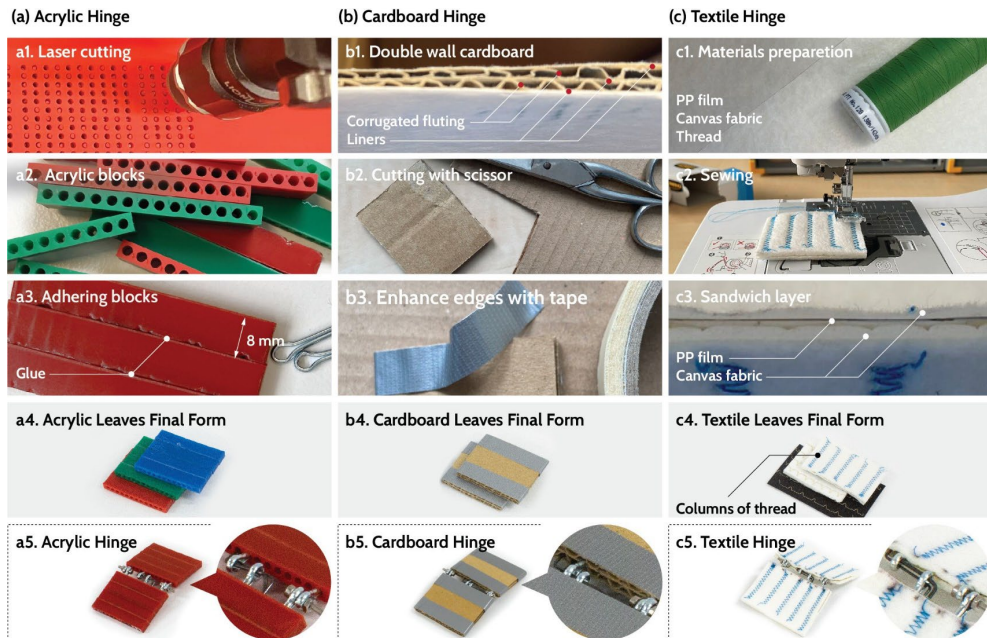


Figure 5.3 Hinge leaves based on three types of materials: configuration process and their structures. (a) Acrylic hinge leaves: acrylic blocks are manufactured by laser cutting, and then each four blocks are glued and combined together as a hinge leaf. (b) Cardboard hinge leaves: they are made from cardboard package box. (c) Textile hinge leaves: the sandwich structure leaves include two layers of fabric and one layer of PP film in the middle. Note that there is no limit of the type of fabric, but 2-3 mm thickness fabric is recommended. (a5), (b5) and (c5) show three types of hinges and their connection details. More details are explained in the *Hinge Construction* part of section 5.4.

5.3.3 Other Components

A split pin is also known as a cotter pin or cotter key which has two tines and one hole (see Figure 5.2(c)). With the help of split pins, the actuation hinges can be assembled easily. Each hinge requires six split pins to fix two leaves and the SMA wires. More details about the installation of the split pins use can be seen in the section 5.4. Screws and nuts act as “rotation shaft” of the actuation hinges. The shape-changing objects can be actuated by hot water or applying an electrical current through the SMA wires (Joule heating). Electrical wires should be used to connect the SMA with power when the Joule effect approach is selected.

5.4 Shape-Changing Objects Construction Steps

The shape-changing objects construction process is divided into three steps, which are *SMA pre-deformation*, *hinge construction* and *object body and hinge combination*.

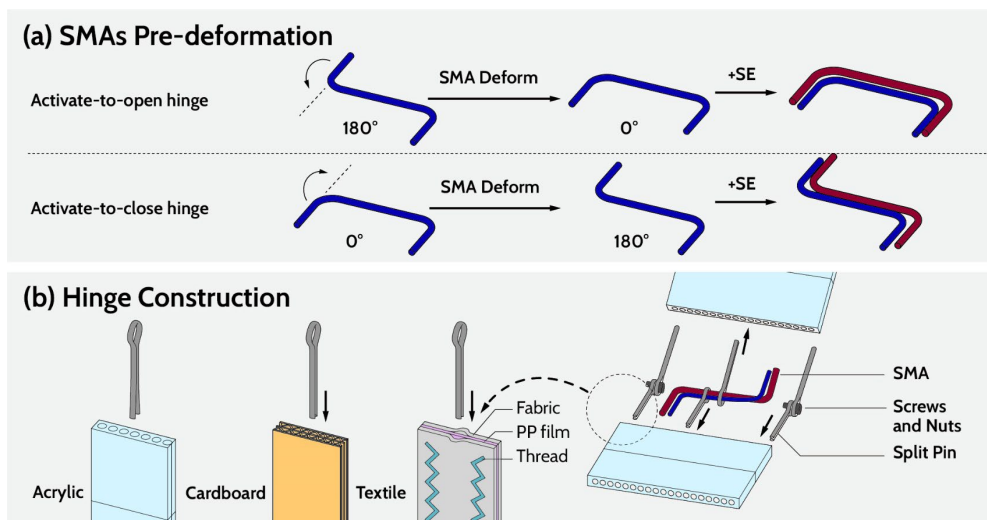
(1) SMA pre-deformation. For the construction of *activate-to-open* hinge, the actuation SMA wire should be selected and then deformed to 0° , so that it can combine with the superelastic wire easier (see Figure 5.4(a)). Regarding the *activate-to-close*

hinge, an actuation SMA wire with preset angle of 0° is used. It needs to be deformed to 180° before uniting with 180° superelastic wire.

(2) Hinge construction. Each actuation hinge needs six split pins and two pairs of screws and nuts. For the acrylic hinge leaves, the two tines of each pin can be split slightly before inserting into the acrylic bricks to prevent them from slipping out. As for the cardboard hinge leaf, the split pins can be clipped in the middle liner (Figure 5.3(b1)). Similarly, the split pins can be combined with the textile hinge leaves by clipping them on the PP film layer (Figure 5.3(c3) and Figure 5.4(b)). Of the six split pins, two of them are used to help fix the SMAs and two rigid plates. As shown in Figure 5.4(b), SMAs can thread through the pin holes before inserting into the plates, which can make the SMAs fix with the plates tightly. The constructed hinges based on three different types of materials and their details can be seen in Figure 5.3(a5), (b5) and (c5).

(3) Object body and hinge combination. The object body refers to the non-morphing parts of shape-changing objects (see Figure 5.4(c)). Users can customize the object bodies with different types of materials (e.g. acrylic, cardboard, textile) according to their design concepts. The object body and the hinge actuators can be connected with adhesive (e.g. superglue, UHU 150 glue) or other approaches depending on the selected materials.

If the shape-changing object is expected to activate by electrical current, the torsion deformation part of the SMAs need to be connected with wires. Electrical wire and SMA are connected by wrapping the exposed copper around the SMA (Figure 5.6(b) and (c)). If the actuation is done by placing in hot water, the electrical wire connection process can be skipped. It should be noticed that the hot water activation approach is inapplicable for cardboard and textile hinge leaves.



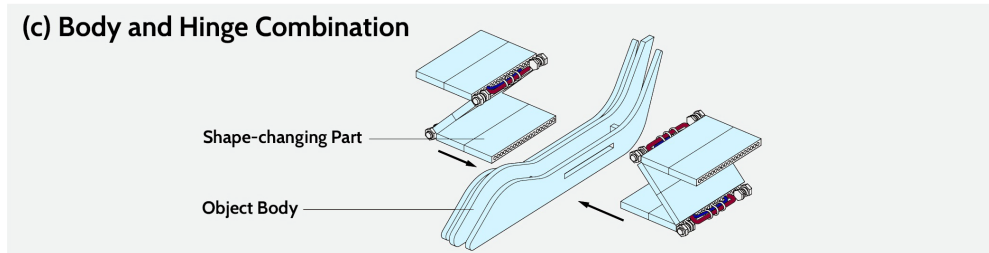


Figure 5.4 Construction steps of shape-changing objects. (a) The SMAs pre-deformation process is different depending on the selection of hinge type. (b) Hinge construction: the tines of the split pins can be inserted into the edge of the two hinge leaves, so as to form a complete hinge. (c) Acrylic hinges can combine with the object body by using superglue.

5.5 Hinge Actuation Performance

5.5.1 Actuation force

A push-pull gage (Success MODEL ANF-200) is used to measure the actuation force. Prior to the measurements, a leaf of an *activate-to-open* acrylic hinge is securely attached using a fixture at its close state, and the push probe of the gage is placed and secured in contact with another leaf (Figure 5.5(a)). When the hinge is actuated with 1.2 Amp, it tries to open but is blocked by the push probe, which can record the maximum actuation force during Joule heating. Experiments show a force range from 4.5-5.7 N. Considering the hinge actuator's lightweight (2.1-5.4 g), it is a considerable actuation force level.

5.5.2 Response Time

An *activate-to-open* acrylic hinge is used to measure the response time. The experimental findings indicate that when a current of 1.6 Amps is applied, the hinge takes approximately 4 seconds to reach its actuation angle. By increasing the current, the heating time can be reduced. For instance, if the current is increased to 3.2 Amps, the heating time is reduced to 3.5 seconds. However, in comparison to heating, the cooling process requires significantly more time, taking around 45 seconds at room temperature. To minimize the cooling time, it is advisable to increase the airflow speed (Lewis et al., 2013) and maintain a lower ambient temperature. With the water-activation approach, the response time is shorter. It can be actuated in 76 °C water within 3.4 s and cooled down in 21 °C water in 4.5 s.

5.5.3 Durability

SMAs within the deformation limitation can be used for 10^4 - 10^7 times without showing any fatigue (Eggeler et al., 2004). For the hinge, the most common failure is when the pins slip out of the holes. Several experiments on 180° hinges in different materials are conducted to investigate how much force could lead to the failure. The push-pull gage is used again to measure the force. As shown in Figure 5.5(b), the pull

hook of the gage is bound to one leaf of the hinge by two ropes. The gage records the maximum force during one leaf is completely pull out from the pins. The finding indicates that it needs 5-7 N to separate two leaves of a hinge.

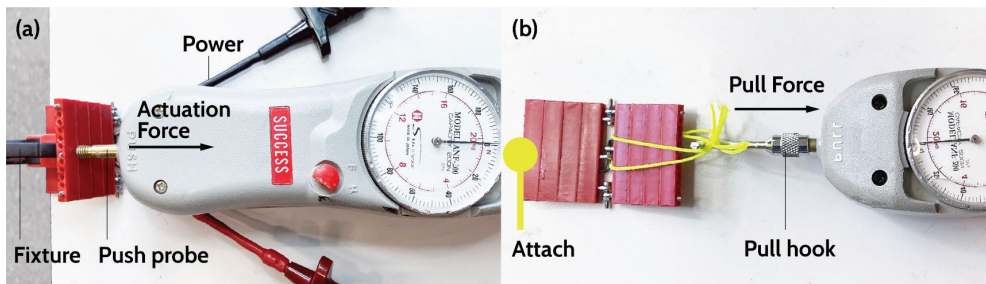


Figure 5.5 Hinge performance evaluation with a push-pull gage. (a) Actuation force measurement. (b) Tests of the durability of the hinges.

5.5.4 Energy Consumption

As shown in Figure 5.6(d), a gripper constructed with 6 SMA hinges can be activated by 4 AA alkaline batteries in series (6 Voltages). Total energy (E) stored in these batteries is about 15 watt-hours. With a digital multimeter, the current is tested as 0.65 Amps, and the power (P) consumed by the actuator (during activation) can be calculated as 3.9 watts. The power for maintaining the activation phase is about 1.4 watts (tested by a DC power analyzer), which is only 36% of that of the activation phase. Therefore, if the microcontroller can reduce the passing current once the hinges are actuated, the time that 4 AA batteries can maintain 6 SMA hinges at its activation phase is about 10 hours. If less SMA hinges are used in shape-changing objects, energy consumption will be lower.

5.6 Hardware

A Bluetooth control module is developed, which enables users to control their shape-changing objects remotely. As shown in Figure 5.6(a) and (c), hardware includes a Seeed Studio XIAO nRF52840, a Finder Relays 36.11.9.006.4001, a DC/DC converter and a 20V rechargeable power. All the SMA wires of the gripper need to be connected first (see Figure 5.6(b)). The microcontroller XIAO integrates Bluetooth 5.0 connectivity. After pairing with another Bluetooth device (e.g., a mobile phone or laptop), it can receive signals from users. The electrical current can be toggled by the Finder Relays, which in turn is controlled by XIAO (see Figure 5.6(a)). The DC/DC converter can handle the voltage of 8-30 V, and provide 1-12 V up to 8 Amps. The small copper screws on the top side of the converter are used to set the (maximum) values. In our cases, we set the maximum current to 2 Amps to prevent damage to sensitive control components. A simple website based on Python is developed, on which users can pair the Bluetooth of XIAO, activate the shape-changing object or cut off the current remotely.

Mimosa can also be combined with sensors to support more diverse electronic device designs. To demonstrate this, a distance-sensing triggered gripper is designed. Circuit connection can be seen in Figure 5.6(d), in which 4 AA batteries are used as power supply. When the proximity sensor detects an item within 20 cm, microcontroller of the Seeeduino board can activate the gripper through MOSFET. The activation process can be seen in Figure 5.6(e).

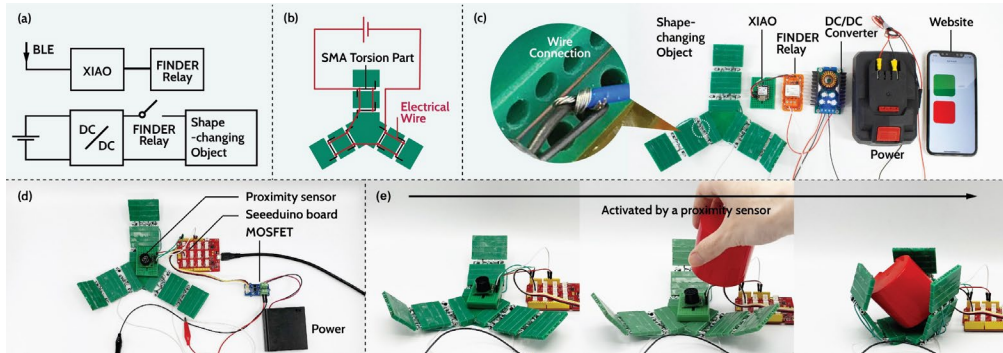


Figure 5.6 (a) Circuit diagram of the Bluetooth control module. (b) SMA wire connection of the gripper. The current needs to flow through all the SMA torsion parts. (c) Hardware for the Bluetooth control module. (d) Circuit connection of the distance-sensing triggered gripper. (e) Activation process of the distance-sensing triggered gripper.

5.7 Application Examples

Robotics. An adaptable gripper is made by acrylic plates and six *activate-to-close* hinges (see Figure 4.12(a) in chapter 4). In addition, a rolling robot is constructed with an acrylic object body and cardboard hinge leaves (Figure 5.7(a)). It is a cylindrical structure which includes four *activate-to-open* hinges. Each hinge has one leaf fixed to the object body (red cylinder in Figure 5.7(a)), and a second leaf is bonded with two acrylic semi-circular pieces. When the hinge is actuated, the second leaf opens and pushes the robot to rotate forward. Four hinges are actuated sequentially. The rolling robot can move about 25 cm in approximate 10 seconds (with two hinges actuated sequentially).

Toys. In addition to the butterfly shown in Figure 4.12(b), an airplane is also constructed with acrylic plates which can be activated with hot water or electricity (Figure 5.7(b)). It can be seen that the SMA hinge actuator is small and has little influence on the aesthetics of shape-changing objects.

Self-closing pocket. The self-closing pocket is made of textiles (see Figure 5.7(c)). The flap is embedded with an *activate-to-open* hinge. The design idea is that it can prevent things from dropping out or being stolen at close state. Once it is activated, it can open automatically. The self-closing pocket only needs a battery of 1 V to be activated.

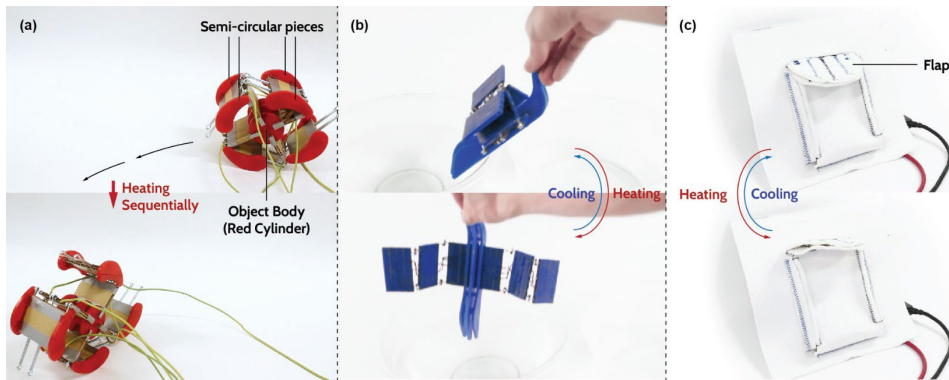


Figure 5.7 Application examples using the Mimosa toolkit. (a) A rolling robot; (b) An airplane; (c) A self-closing pocket. These three application examples show that the toolkit is able to combine with different types of materials like cardboard, acrylic and textile.

5.8 Workshop Study

A workshop with 6 design students was conducted to evaluate the usability and versatility of the toolkit. By examining user constructed shape-changing objects and participants' reflections on toolkit's application scenarios, we can access whether Mimosa can support creative practices. In addition, affective feelings after using the toolkit were investigated, and drawbacks of the toolkit were also identified for further improvement in our future work.

5.8.1 Set-up

The toolkit was placed on a large table in a room. *activate-to-open* and *activate-to-close* SMA hinges were provided. Hinge leaves were available in two types of materials: cardboard and acrylic. Participants can make their selections based on their design concepts and actuation methods (electricity or water). Other types of components such as split pins, screws and nuts, electrical wires, A4 size cardboard, 1mm thickness wood board, adhesive, etc. were provided in sufficient quantities. A camera was set up on a tripod to record participants' prototyping process with the toolkit.

5.8.2 Participants

6 design students including 4 master students and 2 PhD students were recruited for the workshop. They were divided into 3 groups. All of them do not have prior experience in using similar toolkits.

5.8.3 Procedure

The workshop began with an introduction session, in which participants got familiar with the components of the toolkit, prototype construction steps and methods of activation. Afterwards, they were given 15 minutes to think and discuss their prototypes. Once participants had concrete ideas, they can start constructing their

prototypes in approximately 30 minutes. After finishing, they activated their prototypes to see whether the shape-changing processes could match their expectations. The workshop was completed with a questionnaire and post-study semi-structured interview on their experience of using the toolkit.

Four types of data were collected during the workshop study, including video recordings of the construction process, questionnaires, photos of final prototypes and notes from the interview part.

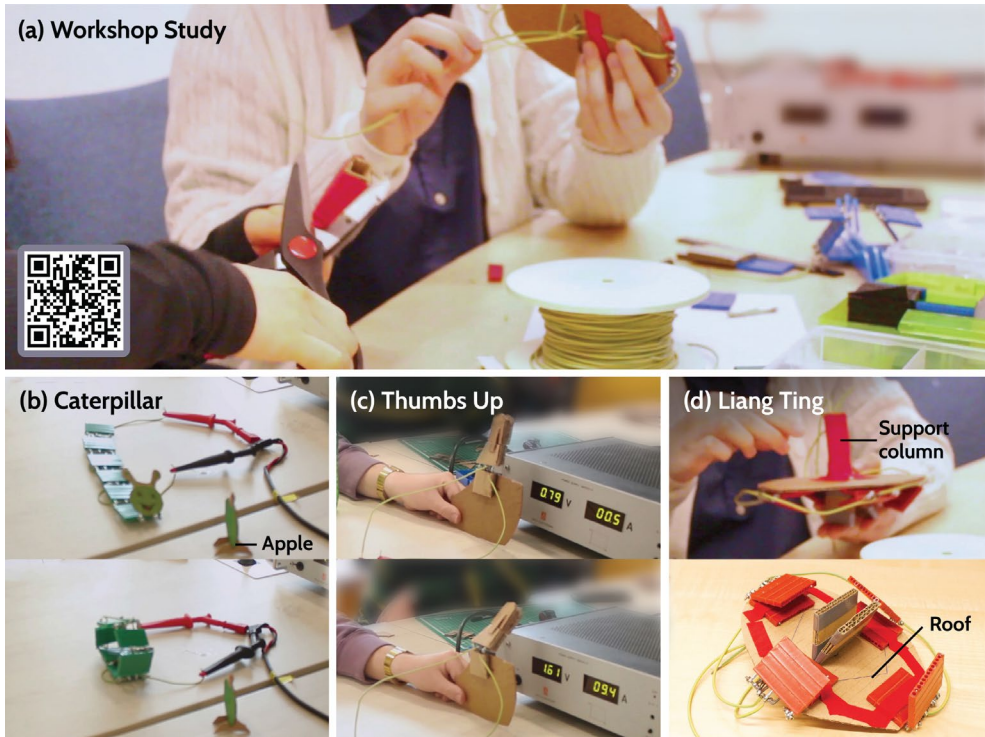


Figure 5.8 (a) Workshop photo. Introduction of the toolkit Mimosa can be viewed by scanning the QR code. (b) *Caterpillar* constructed by Group A; (c) *Thumbs Up* from Group B; (d) *Liang Ting* made by Group C.

5.8.4 Findings

Findings of the workshop study are divided into three parts, which are *user-constructed shape-changing objects*, *analysis results of the questionnaires*, and *observation and interview reflections* which summarized from the workshop constructing session and the post-study interview.

5.8.4.1 User-constructed shape-changing objects.

Group A (P1 and P2) designed a playful interaction toy, *caterpillar*, with 6 acrylic hinges and two customized cardboard shapes, on which they drew a cute face and an green apple (see Figure 5.8(b)). They expected that when it was actuated with

electricity, the *caterpillar* can contract its body (into a zigzag shape) toward the apple. However, they did not take the hinge flipping motion (clockwise or counterclockwise) into consideration when placing the nitinol wires into the hinge leaves. The *caterpillar* changed to an “O” shape when it was applied electric current, as all hinges flipped counterclockwise (Figure 5.8(b)).

Group B (P3 and P4) constructed an interaction device *Thumbs Up*, which composed of a cardboard palm and a thumb, connected by an *activate-to-close* actuator (Figure 5.8(c)). The concept of *Thumbs Up* was that it can be linked to social medias, and activated when friends give “likes” on posts or messages. It was the group that used cardboard only without acrylic material, and the hinge leaves were all made into customized shapes instead of using the provided rectangular hinge leaves.

In contrast with the previous two groups, Group C (P5 and P6) developed “*Liang Ting*”, which is an architecture design concept for children. *Liang Ting* is a traditional Chinese pavilion that serves as a sheltered outdoor resting place, providing a cool and pleasant area for relaxation and social gatherings. It was made with a cardboard support column, a roof, a cardboard hinge actuator, and four red *activate-to-open* acrylic hinges (Figure 5.8(d)). *Liang Ting* was expected to be actuated by environment temperature, instead of electricity or hot water. P5 explained that “*in high temperature environment, like summer, the hinges on the roof can open automatically, expanding the shading area*”.

To summarize, the three user-constructed shape-changing objects were developed for different purposes (toy, interactive device and architecture design), which indicates the versatility of the toolkit.

5.8.4.2 Analysis results of the questionnaires.

With the analysis results of the questionnaires, we find that almost all participants thought the toolkit can inspire them to design, which reveals that Mimosa can support creative practices. In addition, it seems that the toolkit is not easy to use. Even though, participants’ affective feelings were quite positive after using the toolkit. They especially felt “*amused*”, “*enchanted*” and “*pleased*” (see Figure 5.9).

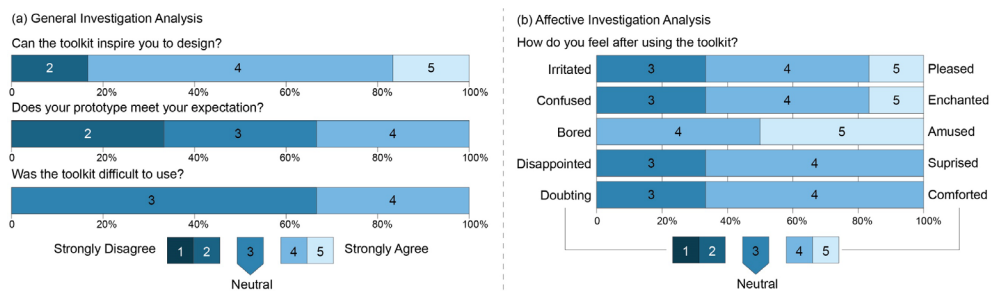


Figure 5.9 Analysis results of the questionnaire. (a) General investigation analysis; (b) Affective investigation analysis.

5.8.4.3 Observation and interview reflections.

(1) *Difficulties during the construction process.* As we observed, difficulties were discovered at every construction step. At the first step, *SMA pre-deformation*, Group C could not distinguish which SMA wires were for the *activate-to-open* hinge, and they asked for help. For the second step *Hinge Construction*, Group A and C had difficulties at inserting the split pins into the holes of acrylic hinge leaves. They also reflected this in the interview session. It is because each acrylic hinge leaf was glued by four acrylic blocks (see Figure 5.3(a)), and the deviation between holes of each two blocks could make the pins stuck. In addition, Group B messed up with the flipping direction of the hinge actuators, which led to an unexpected changing shape as stated in section 5.8.4.1. Group C also thought that the construction process was fiddly. In the final step, *body and hinge combination*, Group B used lots of superglue to bond the cardboard. The superglue was not strong enough and could soften the cardboard because it is mainly for plastic and glass use.

(2) *Engagement during the crafting process.* Participants showed a high level of engagement during the crafting process. They enjoyed collaborative discussions and sharing their creations, such as the *caterpillar facial expression* and *thumbs shape*. They delighted and playfully teased each other, fostering a relaxed and enjoyable atmosphere throughout the workshop.

(3) *Affordances of the toolkit.* Group A obtained the *caterpillar* as they planned finally. Even though they messed up the flipping direction of the hinge at the first time, the modular design of the toolkit allows them to disassemble and reconstruct the *caterpillar*. Group B planned to make a thumb that moves in the anterior-posterior direction. However, this was not possible due to the limitation of the SMA torsion length. They had to change their plan and made the thumbs move in the left-right direction. Group C did not have a concrete plan before constructing, just with a concept of *Liang Ting*. They discussed and made the shape-changing object at the same time. For example, P5 thought “*An octagonal roof is better than the square shape. And we miss a column*”. Then they began to cut the square roof into an octagonal shape and constructed the column with cardboard. This indicates that Mimosa’s modular design and compatibility with cardboard offer effective affordances. However, the provided SMA materials might impose certain limitations on its affordances.

(4) *Cardboard supports customization.* All three groups used cardboard to construct their shape-changing objects. Cardboard serves as a versatile medium in the toolkit. Its unique properties of being easily cut and shaped allow users to customize and craft their desired forms. As a result, the cardboard becomes a platform for creativity, enabling a diverse array of shape-changing objects to be brought to life by users’ artistic expressions. Group A capitalized on the distinctive attributes of cardboard, including both cutting and drawing. Before the activation of *caterpillar*, when the

cardboard green apple was knocked over, P2 was anxious and said “*Oh wait, my apple should be there!*”. She gestured for us not to activate *caterpillar* until she stood it. We learn that P2 really valued the importance of the customized cardboard, which could make their *caterpillar* come alive.

(5) *Application scenarios*. Participants were asked about the application scenarios of Mimosa in the interview session. P1 mentioned its application in the “*technical lessons of school*”. P2 said that it can be used as a validation toolkit in “*shape-changing furniture or fashion industry*”. P3 and P5 saw great potential for this toolkit to be developed into “*playful toys*” and “*artistic interaction devices*”. In addition, P5 and P6 especially liked the temperature-activation properties of the hinge actuator, which can “*make it sustainable*” (P5). For example, P5 described that “*a laptop stand which made of the SMA hinges could be activated and then lift up the overheated laptop automatically without applying electricity*”. P6, who has a research background on sustainable circular packaging systems, mentioned that the hinge can be “*triggered by food heat*”, and used in “*temperature-controlled containers for food preservation*”. In summary, participants’ reflections on the toolkits applications cover a variety of fields, including education, entertainment, fashion, furniture and food industry. P5 and P6’s feedback about sustainability is beyond our expectation, which is also definitely another benefit of the toolkit.

5.9 Discussion, Limitation, And Future Work

5.9.1 Mimosa Supports Creative Practices

As mentioned in the introduction, to develop a toolkit which can support creative practices, we selected 4 metrics as design principles of Mimosa, which are *usability*, *transparency*, *quality* and *agency*. Taking into account the insights gained from the application examples and workshop study, we critically examine whether our toolkit conforms to these metrics.

Usability. We try to lower the threshold of shape-morphing objects construction by combining simple and easily obtainable components in the toolkit. Application examples and user-constructed shape-changing objects indicate the *usability* of Mimosa. Although on the Likert scale regarding the difficulty of using toolkits, almost all participants chose the medium level (see [Figure 5.9](#)), they all succeeded in making fully functional demonstrators in 30 minutes, which is a very short time in compared with the existing similar toolkits (e.g. four hours of Jie’s work ([Qi et al., 2012](#)), a full day of *ShapeClip* ([Hardy et al., 2015](#))).

Transparency. In contrast to motor-based or pneumatic-based shape-changing toolkits, Mimosa can be defined as a *less transparent* toolkit, as the working principle of SMA is more complicated, and the method of activation is much more diverse. Even though essentially the SMA is activated by heat, the heat source can come from Joule effect, environment temperature (e.g. outdoor temperature in summer (P5), hot

food (P6)), or even body temperature (Hannula et al., 2006). The complexity of SMA (less transparency) could bring confusion or challenges of construction when using Mimosa (refers to section 5.8.4.3(1)), but the diverse activation approaches can unleash greater potential in more complex designs (section 5.8.4.3(5)). This discovery is consistent with the previous HCI research, which shows that a *less transparent* tool enable more creative and innovative shape-changing objects (McCullough, 1998).

Quality. Analysis result of Q2 in Figure 5.9 reveals that the not all participants expectations were fulfilled, whereas their affective feelings were quite positive after using Mimosa.

Agency. We enhance Mimosa’s *agency* by incorporating everyday materials (e.g. cardboard and textile) that encourage creativity and craftsmanship. Research shows that engaging users in tangible user interfaces through crafting can help to develop personalized devices (Jayathirtha et al., 2020; Jones et al., 2023; Perner-Wilson et al., 2010; Qi et al., 2018). User-constructed shape-changing objects and participants’ feedback on the toolkit’s application scenarios indicate the *high agency* of Mimosa.

5.9.2 Opportunities of Connecting Crafting Circuits Research

Electrical wires need to be used to connect SMA of the hinge actuators when the electrical heating method is selected. P2 reflected that “*when we use many hinges, it is fiddly to connect wires with SMA*”. This prompts us to reflect on how to optimize the wire connection process. We think conductive ink and thread could be potential solutions.

Mellis et al. developed simple and robust techniques for drawing circuits with conductive ink on paper, enabling off-the-shelf electronic components to be embedded directly into interactive artifacts (Mellis et al., 2013). Similar works can be found in (Jacoby et al., 2013; Koelle et al., 2022; Narumi et al., 2015; Wiethoff et al., 2012). In addition to paper and plastic, Zheng et al. proposed a method to instrument existing glazed ceramic ware with interactive electronic circuits (Zheng et al., 2023). With these approaches, it is possible to draw circuits on cardboard, or print conductive ink onto future ceramic hinge leaves. It is expected that all SMA wires from different hinges in a prototype can be connected together once the construction process is completed, and no more exposed electrical wires are needed (except the wires which are required to connect with power). Textile-related toolkit research refers to (Posch et al., 2021; Thar et al., 2018), in which modular electronics and conductive thread could be valuable reference for future upgrade of the textile hinge.

5.9.3 Limitations And Future Work

Toolkit components. The toolkit includes four types of SMA wires, which could confuse users when they need to select the right ones to construct the hinges, because all

SMA have a similar look. It could be better if SMAs are coated in different colours to distinguish each other.

The current hinge leaves of the toolkit only consist of three types of materials. To encourage more diverse handicraft and support creative practices, it is better to enrich the material selection by adding more options such as corrugated plastic sheets, hard foam and ceramics. Thin textile or materials like PLA that melt below the activation temperature of the SMA are not suitable for being used to make as hinge leaves. The diversity of materials also brought challenges and differences to the design process of the shape-changing objects. For example, if the thick textile materials are selected, sewing machines and scissors are useful tools for the constructing process, while for acrylic materials, superglue can be used for pasting, and laser cutting machines are required if users need to customize acrylic shapes. Users can also combine more than one type of material into a shape-changing objects (e.g., [Figure 5.7\(a\)](#)), but then they need to consider and choose a suitable adhesion method between different materials according to their design concepts. In the workshop, we only used acrylic and cardboard, and did not study the influence of material diversity on the construction process and users' experience. In the future, we will address on this, and might develop guidelines to help users select and construct with different materials.

Construction process. After the step of *pre-deforming the SMA wires*, users might mix up the flipping direction of the hinge (Group A). An approach should be presented in the future to help users with this issue. In addition, the connection method of the SMAs and hinge leaves will be redesigned to improve its usability.

Hardware. Only a Bluetooth remote control module and a distance sensing triggered gripper are developed at this stage. If Mimosa can combine other sensors, it will show much more possibilities in different scenarios. As discussed in [section 5.9.2](#), connecting the existing crafting circuits research can reduce the reliance on electrical wires, which can also enhance the aesthetics of the constructed shape-changing objects.

5.10 Conclusion

We present Mimosa, a constructive toolkit designed for creating shape-changing objects. The SMA hinges can provide substantial actuation forces. Moreover, they are lightweight with a small form factor, and thus have minimum effect on the aesthetics of the constructed shape-changing objects. The hinge leaves are provided in three types of materials, including acrylic, cardboard and textile. The high compatibility with everyday materials offers users space for creation. User can customize personalized shape-morphing objects through handicraft. Related hardware is provided, which demonstrates that users can control the shape-changing objects remotely, and the toolkit can combine with sensors to support electronic device design. Application examples in the field of robotics, toys and smart clothing are presented.

Mimosa aims to inspire designers to create their shape-changing objects with SMAs and everyday materials like cardboard and textile. The Workshop study showed that the toolkit is indeed can support creative practices and provided a good user experience.

Chapter 6

Discussion and Conclusion

This chapter addresses the primary research question formulated in Chapter 1, and discusses some main findings of this thesis, including reflections on the research of the translational and bending actuator elements, the Mimosa toolkit, and the review of SMA-based haptic wearable devices. In addition, the limitations and the future work are outlined, followed by a conclusion of the thesis.

6.1 Reflection on the Research Question

This thesis focuses on shape memory alloys' application in the design field. The main research question of this thesis was: *how to open up the potentials of shape memory alloys for designers?*

To uncover SMAs' potentials, I provided support for designers in three key aspects: (1) offering different types of basic SMA actuator elements; (2) developing simplified models to predict the performance of these actuator elements; (3) providing a toolkit that enables designers to effectively construct shape-morphing prototypes.

(1) Offering different types of SMA actuator elements

In Chapter 1, I hypothesized that all complex shape-changing behaviours could be realized with three fundamental actuator elements that can reproduce translational, bending and rotational motion. Based on this idea, I proposed a strategy to decompose complex movements into these three types of basic motions. I developed the tube-guided SMA actuator for the translational movement and the hinge actuator for bending movement (see Figure 6.1). They were small, able to perform the intended motions and easy to apply, as was shown by a series of demonstrators in Chapter 3 and 4. The rotational element is still a concept at this stage.

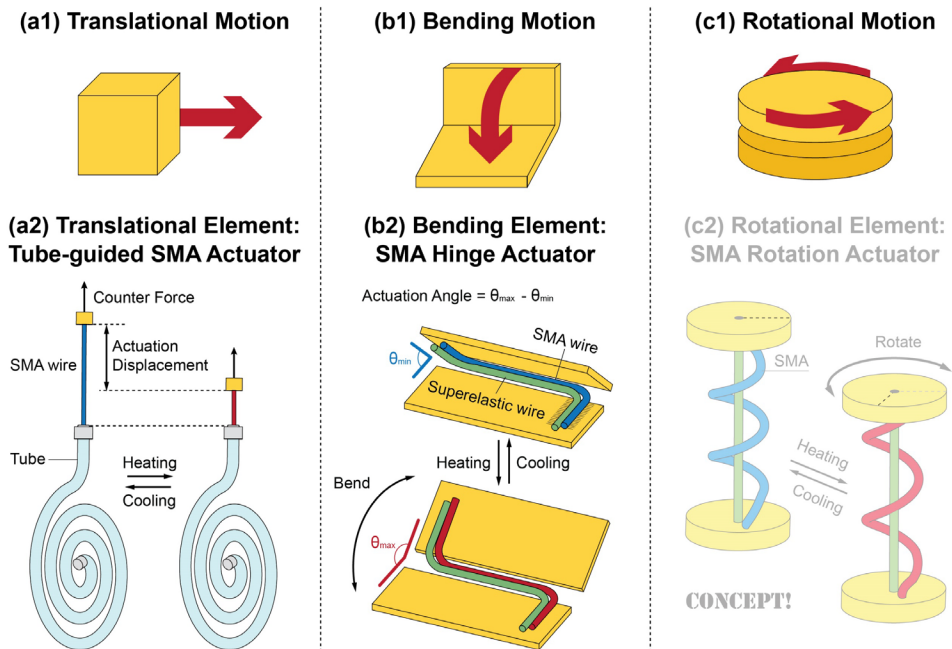


Figure 6.1 Three fundamental SMA actuator elements corresponding to different types of motions and their embodiments (bottom row). (a) The tube-guided SMA actuator for the translational motion (Chapter 3); (b) The SMA hinge actuator for the bending element (Chapter 4); (c) Concept of a SMA rotational actuator.

(2) Developing simplified models to predict the performance of the actuator elements

To assist designers, simplified mechanical models were developed to correlate the performance of the actuator elements with the material properties and geometric parameters. These models enable designers to predict the actuator systems' performance by simply inputting basic geometric parameters, and thus help them figure out the appropriate material dimensions without using the trial and error method. For example, with the mechanical model of the hinge actuator proposed in [Chapter 4](#), designers can determine the initial pre-trained angle and the torsion length of the SMA wire according to the required actuation angle of the hinge actuator.

(3) Providing a toolkit that enables designers to efficiently construct shape-morphing prototypes

A modular shape-changing constructive toolkit based on the SMA hinge element was developed, which allows designers to construct shape morphing artefacts using simple materials like cardboard and textiles. Additionally, the modular design allows for easy disassembly and reconstruction of prototypes. This enables quick adjustments to the shape-changing behaviour, facilitating rapid iterations in the design process and thus avoiding the time-consuming process of rebuilding the entire prototype.

6.2 Reflections on the Research of the Two Actuator Elements

This subsection reflects on the insights gained from the research on the translational and bending actuators, highlighting key findings and their advantages for applications.

(1) The Translational Element: The Tube-guided SMA Actuator

The performance of the tube-guided SMA actuator can be characterized by a simple mechanical model (Eq. (3.9)), with the model parameters provided in [Chapter 3](#). If the actuator elements are constructed using the same type of SMA and tube material, the values for these parameters (i.e., [Table 3.2](#) and [Table 3.3](#)) remain applicable, and no new material characterization experiments are needed. To achieve the desired actuation displacement, users simply need to determine the lengths, diameters, and counter force, then input these values into the model to assess if the predicted performance meets the requirements. Implementing the model in a dedicated design app would facilitate the design process even more.

The model incorporates the temperature-dependent viscoelastic behaviour of the tube material, increasing the model's complexity while guaranteeing accuracy, particularly during the early stages of activation. Experiments showed that the viscoelasticity of the tube resulted in a 3.6% strain change at 120 °C during the initial 15 minutes ([Figure 3.12](#)). Considering that the actuation strain of nitinol wire was only around 4%, throughout the first activation, the displacement variation caused by tube creep can offset the shrinkage of the SMA, preventing the actuator system from generating the desired actuation displacement (see the first 30 minutes in [Figure 3.10](#)). For

subsequent activations, however, creep had minimal effect on the actuation displacement.

To avoid or reduce the creep effect on the actuation displacement of the actuator system, several approaches can be employed. First, the Teflon can be replaced with a material which shows less creep (a metal or polymer with higher glass transition temperature). Second, using an SMA wire with a lower activation temperature is advisable, as high temperatures make the tube more susceptible to creep under stress. Third, a tube with a larger cross-sectional area can be selected. Figure 3.7 indicates that a stress of 3.92 MPa (i.e., applying 2 N on a 0.51 mm² cross-sectional area) initiates non-linear creep. However, for a tube with a cross-sectional area of 1.5 mm², a force of 2 N hardly causes creep in a short time because the corresponding stress is only 1.3 MPa.

The advantage of the tube-guided SMA actuator is that, it combines a large actuation stroke with a relatively compact shape since the tube does not need to be straight but can be rolled up and completely embedded in a surface. As shown in Figure 6.2, two haptic devices integrate the tube-guided SMA actuators into textile and TPU materials. These devices are small and flexible for comfortable wear.

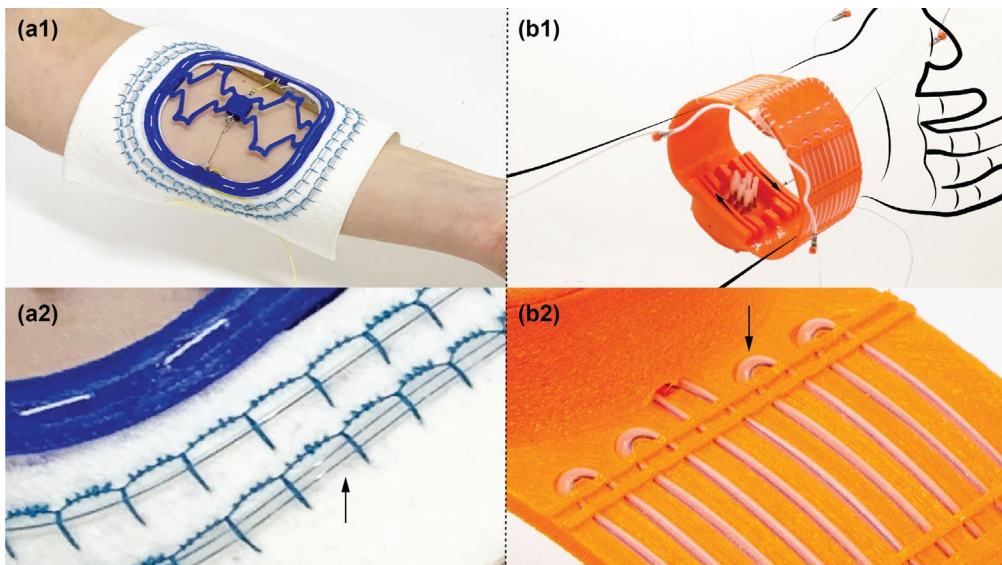


Figure 6.2 (a1) The haptic navigator; (b1) The brush-stroking bracelet. Details of the tube-guided SMA actuators are also shown in (a2) and (b2). Animations of these two prototypes can be viewed by scanning the QR codes in Figure 3.13.

(2) The Bending Element: The Hinge Actuator

The mechanical model of the SMA hinge actuator is given by Eq. (4.1), with variables detailed in Chapter 4. Although the semi-empirical material models involve various mathematical equations and parameters, for practical applications using the same

SMA and SE materials as in [Chapter 4](#), the parameter values in [Table 4.3](#) and [Table 4.4](#) can be directly applied. By incorporating geometric parameters (i.e., the pre-trained angle, and the torsion length of both the SMA and SE wire), *maximum and minimum actuation angle* of the actuator system can be predicted. Our studies reveal that increasing the SMA pre-trained angle results in larger *maximum* ($\Delta\theta_{max}$) and *minimum actuation angle* ($\Delta\theta_{min}$), whereas extending the SMA torsion length leads to a decrease in both $\Delta\theta_{max}$ and $\Delta\theta_{min}$ (see [Figure 4.11](#)). These could offer practical guidance to designers working with the SMA hinge actuator.

The SMA hinge actuator is compact and easy to apply. The SMA wires themselves form the hinge and can therefore be integrated between two stiff surfaces with minimum form factor. Given that the diameter of the SMA is 1 mm in the research, such a thin wire almost merges completely in the two hinge surfaces which it connects. Demonstrators and prototypes showed that this actuator allowed the design of elegant shape-morphing artefacts in which the actuators are barely noticeable. For a small hinge with a width of 1.2 cm and a thickness of 0.1 cm, the actuation force can reach up to 5.7 N. The features of small size, lightweight and high actuation force offer advantages in many space-constrained fields such as aerospace ([Basheer, 2020](#)) and medical applications ([Machado et al., 2003](#)).

6.3 Mimosa Toolkit for Rapid Prototyping

Mimosa is designed to inspire and support designers in creating shape-changing objects. Workshop studies show that the toolkit effectively motivates users to generate ideas and facilitates the rapid development of shape-changing prototypes. Our presentation of the toolkit and prototypes at the TEI'24 conference in Ireland also sparked interest among other research groups, encouraging them to explore the use of the hinge actuator. For example, a research group from the University of Akron is currently working with NASA on a project to develop an SMA actuated adaptive wing that promises improvements in aircraft efficiency, aerodynamic performance, and functionality ([James et al., 2024](#)). They think SMA actuators are lighter, lower-maintenance, and less complex than conventional electromechanical or hydraulic systems. Mimosa toolkit helped them to build prototypes quickly in the initial design stage (see [Figure 6.3](#)). In addition, a researcher from ATLAS institute, University of Colorado Boulder mentioned that the toolkit could be beneficial for their animated paper research.

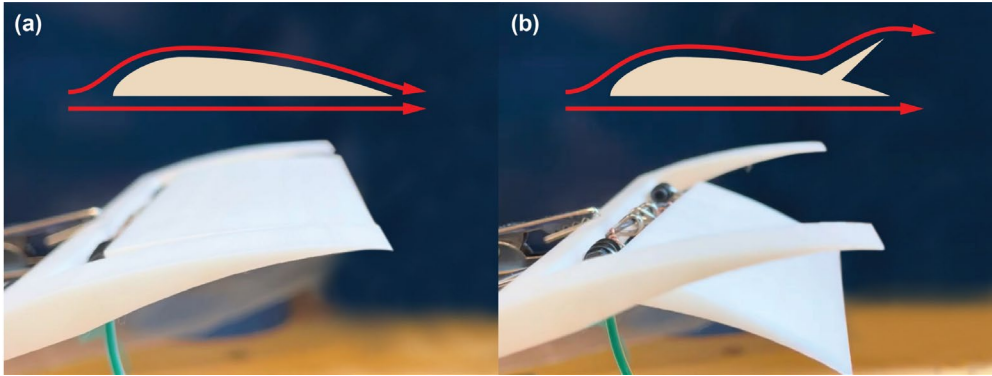


Figure 6.3 An SMA actuated adaptive aircraft wing constructed with Mimosa. (a) Before activation; (b) After activation (James et al., 2024).

6.4 Promoting SMA-based Haptic Wearable Devices

In the current haptic field, although technologies such as pneumatics and micromotors have achieved various types of haptic feedback (e.g., squeeze, stroke), only vibration is widely used in commercial devices. The development of SMA-based haptic devices requires collaboration between haptic designers and software engineers. A future is envisioned where haptic designers can efficiently create different types of haptic sensations, much like composers at a music festival, knowing which instruments and rhythms can convey the appropriate emotions. Furthermore, such haptic sensations should be able to be recorded and shared in file forms. To realize this, SMA researchers should collaborate with haptic designers to develop user guidelines and aesthetic theories about haptic experience. In addition, working with software engineers to create apps, digital haptic files or other transmission channels can contribute to the dissemination of haptic devices in the design field (MacLean et al., 2003; Schneider et al., 2017; Schneider et al., 2015).

6.5 Limitation and Future Work

6.5.1 SMA Actuator Elements

I intended to propose three types of SMA actuator elements for various motions. However, due to time limitation, I was only able to complete the translational and bending elements. The development of SMA rotation actuators remains a task in the future. Such rotational elements are not intended to produce continuous rotation like electromotors, but rather to exhibit a limited range of rotation angle (e.g., to mimic a wrist rotation).

In addition to the example in Figure 6.1(c), the SMA rotation actuator can also be constructed as the illustrations shown in Figure 6.4(a) and (b). Figure 6.4(a) is a ring-form actuator consisting of an SMA flat spring and a superelastic spring. Both springs are anchored at one end to the inner ring and at the other end to the outer ring. When the SMA is activated, it expands and drives the outer ring to rotate. The rotation

actuator in Figure 6.4(b) has an SMA strip embedded in an elastic substrate. The SMA strip has an original twist-shape, and thus it can rotate upon heating. These two actuators exhibit distinct features. Figure 6.4(a) can be design into a very thin form, while (b) can be configured to be a small-diameter actuator, as the width of the SMA strip can be less than 5 mm. Therefore, the two actuators can be selected and used across different applications.

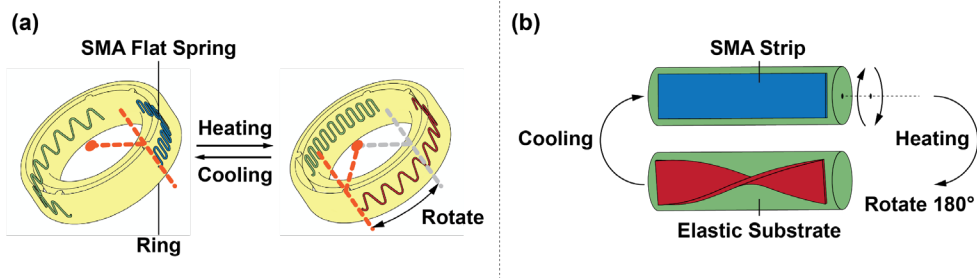


Figure 6.4 (a) A ring-form SMA rotation actuator; (b) A rotation actuator based on SMA strip.

With the three examples of SMA rotational element concepts, it can be seen that proposing more than one type of SMA actuator systems for each element would benefit designers by providing a wider range of options for diverse applications. Therefore, although the tube-guided SMA actuator and the hinge actuator have been developed for the translational and bending element respectively, this is just the beginning, and more SMA actuator systems will be created for these elements. The availability of more than one actuator type for each basic motion element could help designers in selecting appropriate actuators for different applications.

6.5.2 Computer Design Tools for SMA Actuators

Despite the development of simplified mechanical models for SMA actuators, designers still need to perform calculations using material geometric parameters. This process can demand considerable time and require skills in data analysis. Some researchers notice that computer technologies have the potential to reduce the consuming time and the expertise required to use SMA actuators (Meier et al., 2012; Wheeler et al., 2016). For example, the *Consortium for the Advancement of Shape Memory Alloy Research and Technology (CASMAART)*, which is established to promote the growth and adoption of SMA actuation technologies (Benafan et al., 2014), proposed a graphical user interface for the most frequently used SMA actuator systems (e.g., a translation actuator consisting of an SMA wire and a bias spring) (Wheeler et al., 2016). Note that this tool utilizes user-input martensite and austenite stress-strain responses to graphically display the result, which means that users need to conduct tensile tests on the SMA wire first. In addition, Meier et al. proposed a *computer-aided shape memory alloy development application* by combining a numerical SMA model and database (Meier et al., 2012). With input specifications

(e.g. displacement, force, and installation space), the application can analyse and evaluate whether users' requirements can be satisfied (Meier et al., 2012).

In the future, relevant computer application tools about the tube-guided SMA actuator element and the SMA hinge actuator can be developed. This would enable designers to obtain the mechanical performance of the actuators by inputting geometric parameters of SMA, without the need for analysing data and doing modelling work themselves.

6.5.3 Testing and Improving the Models with User Studies

An convincing approach for assessing usability or performance of a model is to conduct comparison experiments or user studies. For instance, Zakerzadeh et al. evaluated the accuracy of three hysteresis models of SMA actuators by comparison (Zakerzadeh et al., 2012). Similarly, in order to assess the capabilities, accuracy, and flexibility of the SMA actuator design tools, Wheeler et al. organized student teams to design functioning prototypes with the tools (Wheeler et al., 2016).

In principle, the proposed models are based on mechanical tests without using microstructural details, thus enhancing simplicity and intuitiveness. To confirm this, User studies should be arranged to evaluate whether the developed models are user-friendly for designers.

6.5.4 Upgrading the Toolkit for Complex Shape-changing Objects

Constructive assemblies and modular toolkits provide users an efficient way to explore creative concepts (Youn et al., 2022). Our study shows that the toolkit is particularly effective in sparking designers' interest in SMA actuators, as it does not require specialized knowledge of materials. Nevertheless, at present, only the SMA hinge actuator is included in the toolkit, which cannot provide the translational and rotational motion. This limitation may restrict its applicability in different application scenarios. In future work, the toolkit should be upgraded and improved by including more types of SMA actuator elements, thereby enabling designers to create more complex shape-changing objects.

6.6 Conclusion of the Thesis

This research aimed at unlocking the potentials of SMA materials for designers. To achieve this, I used a strategy to decompose complex movements into three fundamental motions, which are translation, bending and rotation. I intended to develop a reliable actuator element for each motion type. By selecting and combining different types of element, designers can reach complex shape-changing behaviours.

In the thesis, a state-of-the-art overview of SMA haptic wearables is first provided, serving as an entrance for designers to understand the capabilities and applications of SMAs in the haptic field. Research about the tube-guided SMA actuator (for the

translational motion) and the SMA hinge actuator (for bending motion) are introduced. Based on the SMA hinge actuator, I developed a modular constructive toolkit to inspire and support designers to create shape-changing objects. Workshop study revealed that users can finish their construction within an hour. This could offer designers an efficient way for testing their shape-changing prototypes.

In the future, the focus should be on expanding the range of SMA actuator elements available for designers, with particular attention to the rotation actuator, which is currently absent.

Appendix 1*

Supplement Information for the Tube-guided SMA Actuator

* This appendix is published along with:

Liu, Q., Ghodrat, S., & Jansen, K. M. B. (2022). Modelling and mechanical design of a flexible tube-guided SMA actuator. *Materials & Design*, 216, 110571.

<https://doi.org/10.1016/j.matdes.2022.110571>

A1.1 SMA Young's Modulus Test

Figure A1. 1 shows how the Young's modulus of the SMA wire, obtained by a DMA test at 1Hz, changes with rising temperature. The modulus decreases slowly between 30 °C and 65 °C, and then has a steep rise from 70 °C to 90 °C. After that, it keeps increasing at a slower rate. By plotting values at 30°C and 120°C, we can get the Young's modulus of the twinned martensite (at 30 °C) and the fully austenite phase (at 120 °C). Note that whereas in Figure 3.4 the phase transformation was stress induced, here it was triggered by a temperature increase.

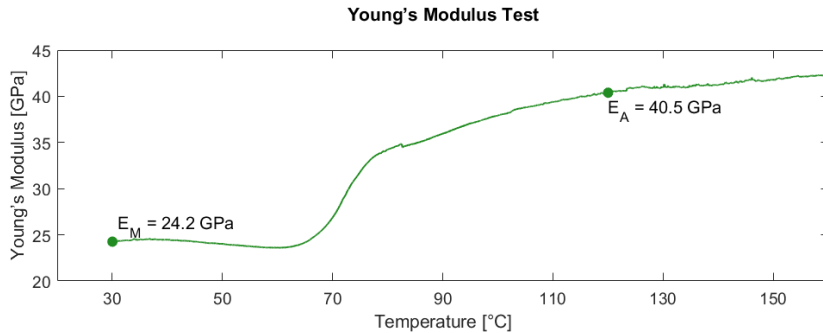


Figure A1. 1 The 1 Hz Young's modulus of the SMA wire as a function of temperature.

A1.2 Tube Thermal Expansion Test

In order to avoid start-up effects during heating, the 70-120 °C temperature range of the thermal expansion data was used for evaluation. The initial length of the tube specimen is 11 mm. The measured expansions are corrected for the expansion of the metal frame using a quartz reference plate (red line in Figure A1. 2). The corrected coefficient of thermal expansion of the tube is then calculated as $1.31 \times 10^{-4} \text{ } ^\circ\text{C}^{-1}$.

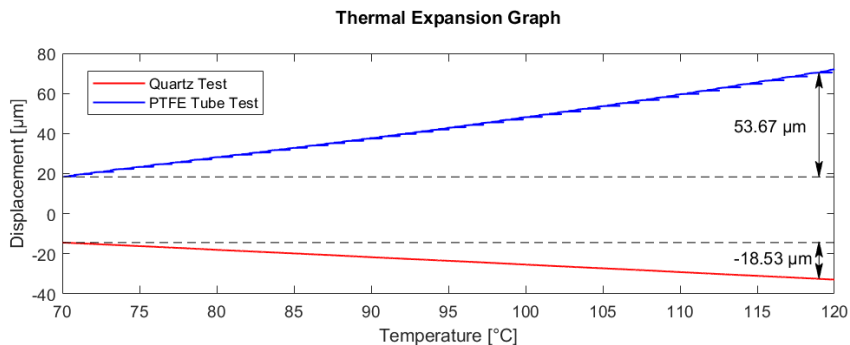


Figure A1. 2 Thermal expansion tests with Teflon and the quartz calibration sample.

A1.3 Tube Young's Modulus Test

Here we plot the strain-stress curve to measure the Young's modulus of the tube. As can be seen in the Figure A1. 3, the stress-strain curve exhibits a region of linear behaviour according to Hooke's law when the strain is below 0.7%. The slope of the

linear part is determined to be 533 MPa, which is the Young's modulus of the tube. With increasing stress, the elastic limit is exceeded with permanent strain remaining after complete release of the stress.

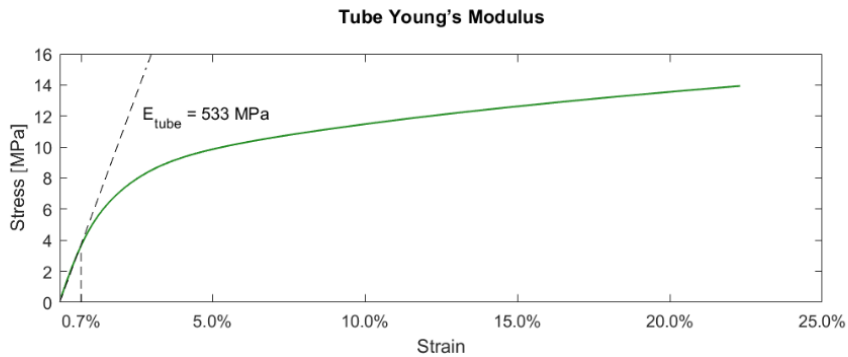


Figure A1.3 Young's modulus test of the tube.

A1.4 Model Simulation

A simulation in Matlab is conducted to better understand how the thermal expansion, creep of the tube and SMA actuation affect the stroke of the system under a cyclic temperature environment. Figure A1. 4(a) shows the simulated temperature change with time. The displacement of SMA actuation (based on Eq. (3.1)), thermal expansion (based on Eq. (3.4)) and creep (based on Eqs. (3.5)-(3.8)) are depicted in Figure A1. 4(b), whereas the system stroke (based on Eq. (3.9)) is shown in Figure A1. 4(c). The Zone II, III, IV refer to section 3.5.2.

In the first heating cycle Zone II, the system stroke is mainly affected by the thermal expansion and creep when the temperature is below A_s . Once it reaches the austenite start temperature, the SMA generates a huge contraction, which explains the drop (around the 30th minute) in Figure A1. 4(c). After the SMA wire has entirely transformed to austenite, its length no longer changes. However, the creep of the tube continues and produces a larger displacement. Thus, we can observe an increase on the system stroke curve (blue line) from the 40th to 50th minute. In general, the contraction caused by SMA actuation (5.1 mm) and thermal expansion (1.3 mm) can almost balance the expansion produced by the tube creep (5.8 mm). This can also explain the yellow curve in Figure 3.11(a), which always fluctuates around 0. In the subsequent cooling stage, Zone III and heating stage Zone IV, there are only minor changes of the creep, implying that only the thermal expansion and SMA actuation affect the system stroke. Therefore, as can be seen in Figure A1. 4(c), the stroke changes regularly except for the heating stage of the first cycle.

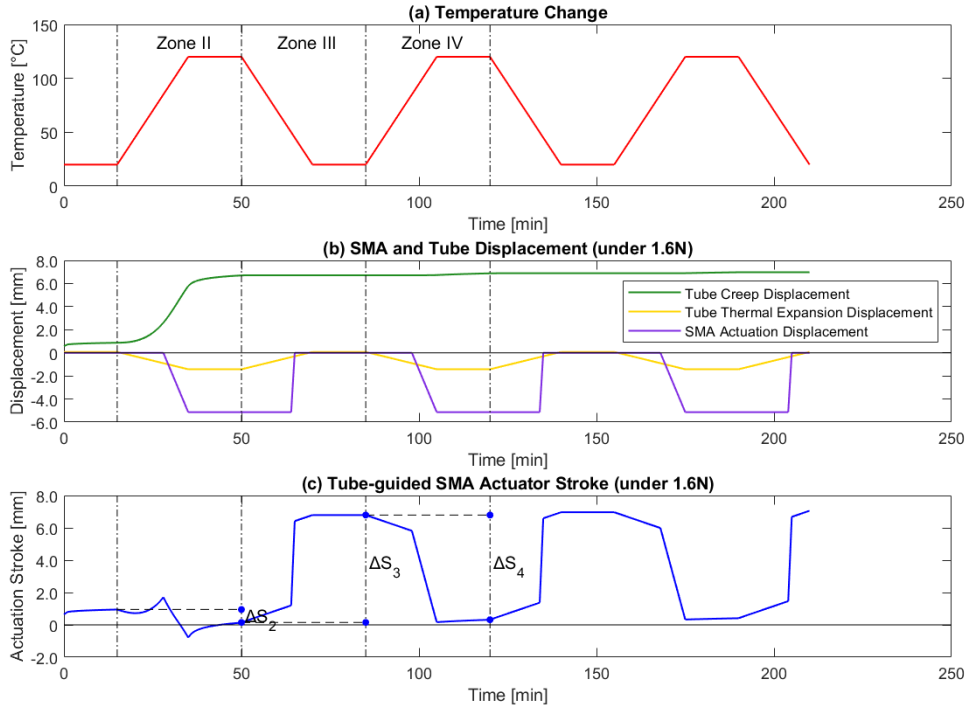


Figure A1. 4 Simulation of the thermal expansion, creep, SMA actuation displacement, and actuation stroke of the system under a cyclic temperature environment (constant force 1.6 N).

A1.5. Modelling of the Stress-strain Behaviour of the SMA

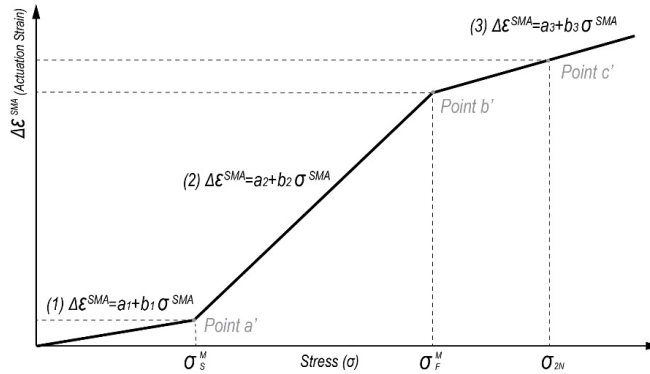


Figure A1.5 The SMA actuation strain increases with higher stress during heating and cooling, and three characteristic stages can be discerned.

(1) Elastic deformation of martensite ($0 < \sigma^{SMA} \leq \sigma_S^M$)

According to Hooke's law, we have:

$$\epsilon = \frac{\sigma^{SMA}}{E} \quad (A1.1)$$

Applying Eq. (A1.1) for the austenite and the martensite state, and then considering the difference we obtain the following:

$$\Delta\varepsilon_{SMA} = \sigma^{SMA} \left(\frac{1}{E_M} - \frac{1}{E_A} \right) \quad (A1.2)$$

Hence, we obtain for the values of a_1 and b_1 :

$$a_1 = 0 \quad (A1.3)$$

$$b_1 = \frac{1}{E_M} - \frac{1}{E_A} \quad (A1.4)$$

(2) Detwinning of martensite ($\sigma_S^M < \sigma^{SMA} \leq \sigma_F^M$)

As shown in Figure A1. 5, we have *Point a'* ($\sigma_S^M, a_1 + b_1\sigma_S^M$). When $\sigma^{SMA} = \sigma_F^M$, then $\Delta\varepsilon_{SMA}$ is the strain difference between the martensite and austenite state of the SMA wire. Therefore, we have *Point b'* ($\sigma_F^M, \varepsilon_F^M - \frac{\sigma_F^A}{E_A}$). With the *Point a'* and *Point b'*, the slope b_2 can be calculated as:

$$b_2 = \frac{\varepsilon_F^M - \frac{\sigma_F^A}{E_A} - b_1\sigma_S^M}{\sigma_F^M - \sigma_S^M} \quad (A1.5)$$

Inserting this in Eq. (A1.1), we obtain for a_2 :

$$a_2 = \varepsilon_F^M - \frac{\sigma_F^A}{E_A} - b_2\sigma_F^M \quad (A1.6)$$

(3) Deformation of detwinned martensite ($\sigma_F^M < \sigma^{SMA} \leq \sigma_{2N}$)

Similarly a_3 and b_3 become:

$$a_3 = \varepsilon_{2N}^M - \frac{\sigma_{2N}}{E_A} - b_3\sigma_{2N} \quad (A1.7)$$

$$b_3 = \frac{\varepsilon_{2N}^M - \frac{\sigma_{2N}}{E_A} - \varepsilon_F^M + \frac{\sigma_F^A}{E_A}}{\sigma_{2N} - \sigma_F^M} \quad (A1.8)$$

Appendix 2*

Comparison of Different SMA Hinge Actuators

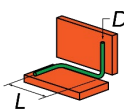
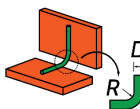
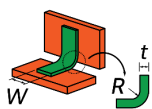
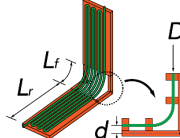
* This appendix is published along with the article:
Qiang Liu, Sepideh Ghodrat, and Kaspar M.B. Jansen.
Design and modelling of a reversible shape memory alloy torsion hinge actuator.
Materials & Design (2023): 112590.
<https://doi.org/10.1016/j.matdes.2023.112590>

A2.1 Materials and Setup

The actuation of a hinge connecting two stiff rectangular elements can in principle be done in four different ways (see Table A2. 1). The effectiveness of these four designs and the generated forces are expected to be different. For example, in bending mode, the material is partly compressed and partly elongated, whereas in tension mode, the material deforms uniformly. On the other hand, also the material dimensions and the designs itself will have an effect. It is therefore a priori not known which operation principle is most effective.

A comparative analysis of four distinct SMA-driven hinge designs is conducted to assess their actuation forces during activation. More information is provided in Table A2. 1.

Table A2. 1 Four types of SMA-actuated hinges.

	SMA Wire Torsion	SMA Wire Bend	SMA Sheet Bend	SMA Wire Tension
Graphics				
Materials	SMA wire (green) Rigid leaves (orange)	SMA wire (green) Rigid leaves (orange)	SMA sheet (green) Rigid leaves (orange)	SMA wire (green) Rigid leaves (orange)
Parameters	D : Diameter of wire L : Length of torsion part	D : Diameter of wire R : Radius of bending	t : Thickness of sheet R : Radius of bending W : Width of sheet	D : Diameter of wire L_f : Length of flexible part L_r : Length of rigid part d : distance between SMA wire and rotation point n : loop number SMA wire * Length of SMA = $n(2L_r + L_f)$
Reference	(Koh et al., 2014)		(Hawkes et al., 2010; Seigner et al., 2021)	(Kim et al., 2016; Wang et al., 2017; Wang, Rodrigue, Kim, et al., 2016)

As illustrated in Figure A2. 1, configurations (a), (b), and (c) consist of SMA components (green) paired with acrylic rigid leaves (orange). The SMA wires and sheets are pre-deformed and trained in 550 °C oven first, to obtain 0° original angle. Subsequently, the hinges are bent to a 90° angle and secured with a yellow acrylic support (refer to Figure A2. 2(a)). The experimental setup in Q800 can be seen in Figure A2. 2(b). A small hinge (see Figure A2. 2(a)) is anchored with the lower clamp of Q800. Displacement-control method is employed for testing. The displacement is programmed to maintain at 30 μm, and the temperature is increased from room temperature to 75 °C. When the SMA reach their transition temperatures, the hinges attempt to close but are countered by the lower clamp's antagonistic forces, which maintain the 90° angle, allowing for the measurement of actuation forces.

As for the SMA tension-driven hinge, a PTFE tube is used to guide the motion path of the SMA wire. The tube can also prevent the 3D printed PLA leaves from overheating during actuation (see Figure A2. 1(d)). A preliminary test (Figure A2. 2(c) and (d)) demonstrates that the hinge can achieve its maximum actuation angle (approximately 60°) when 14 volts is applied. Figure A2. 2(e) displays the test setup in Q800. Joule heating is used to heat the SMA wire. Actuation force and applied voltage are recorded manually during test, while the current is determined by calculating the SMA wire's resistance (18.5 Ω /m). The geometric parameters for all test samples are available in Table A2. 2.

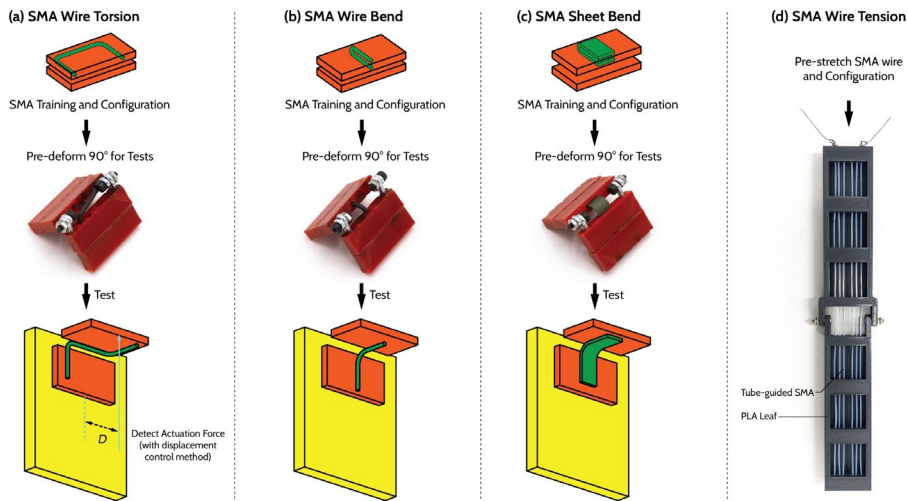


Figure A2. 1 Preparation of four types of SMA-actuated hinges for testing.

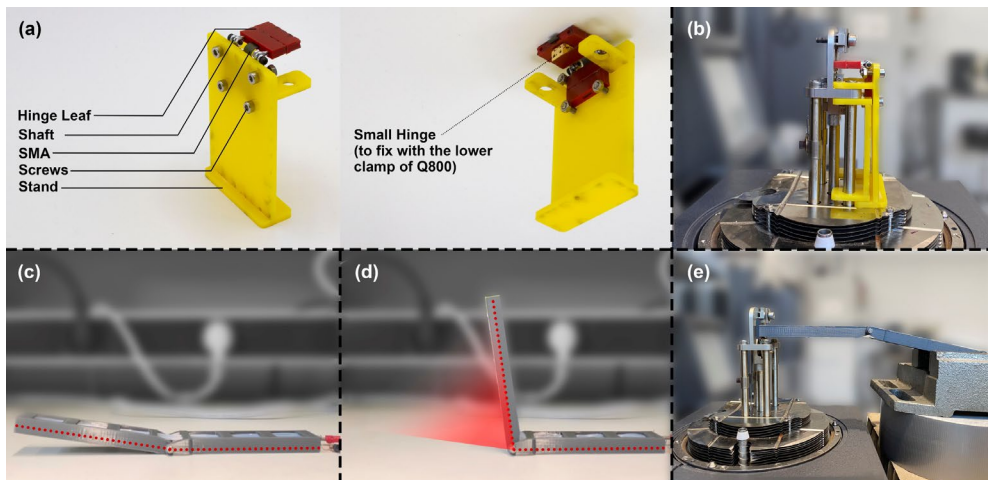


Figure A2. 2 (a) and (b): A setup in Q800 for tests of the SMA wire torsion, wire bending, and sheet bending mode. (c) and (d): Pre-test for SMA wire tension mode with applied voltage. (e): SMA wire tension mode setup for Q800 test.

Table A2. 2 Information and parameters of tested samples.

Types of Hinges	SMA Supplier	Sample	Activation Temperature	Geometric Parameters
SMA Wire Torsion	Nanografi	WT-1	$A_f = 45\text{-}50\text{ }^\circ\text{C}$	$D = 1.0\text{ mm}, L = 5.0\text{ mm}$
		WT-2	$A_f = 45\text{-}50\text{ }^\circ\text{C}$	$D = 1.0\text{ mm}, L = 7.8\text{ mm}$
		WT-3	$A_f = 45\text{-}50\text{ }^\circ\text{C}$	$D = 1.0\text{ mm}, L = 12.4\text{ mm}$
		WT-4	$A_f = 35\text{-}40\text{ }^\circ\text{C}$	$D = 1.5\text{ mm}, L = 8.4\text{ mm}$
		WT-5	$A_f = 35\text{-}40\text{ }^\circ\text{C}$	$D = 1.5\text{ mm}, L = 10.2\text{ mm}$
SMA Wire Bend	Nanografi	WB-1	$A_f = 45\text{-}50\text{ }^\circ\text{C}$	$D = 1.0\text{ mm}, R = 2.1\text{ mm}$
		WB-2	$A_f = 45\text{-}50\text{ }^\circ\text{C}$	$D = 1.0\text{ mm}, R = 2.4\text{ mm}$
		WB-3	$A_f = 45\text{-}50\text{ }^\circ\text{C}$	$D = 1.0\text{ mm}, R = 3.6\text{ mm}$
		WB-4	$A_f = 35\text{-}40\text{ }^\circ\text{C}$	$D = 1.5\text{ mm}, R = 3.0\text{ mm}$
		WB-5	$A_f = 35\text{-}40\text{ }^\circ\text{C}$	$D = 1.5\text{ mm}, R = 3.4\text{ mm}$
SMA Sheet Bend	Kelloggsresearchlabs	SB-1	$A_f = 45\text{ }^\circ\text{C}$	$t = 0.10\text{ mm}, W = 5.9\text{ mm}, R = 2.3\text{ mm}$
	Nexmetal	SB-2	$A_f = 50\text{ }^\circ\text{C}$	$t = 0.25\text{ mm}, W = 5.9\text{ mm}, R = 2.3\text{ mm}$
SMA Wire tension	Dynalloy Inc.	WE-1	$A_f = 90\text{ }^\circ\text{C}$	$L_f = 90\text{ mm}, L_f = 18\text{ mm}, n = 6,$ $d = 4\text{ mm}, D = 0.25\text{ mm}$

A2.2 Characterisation Results

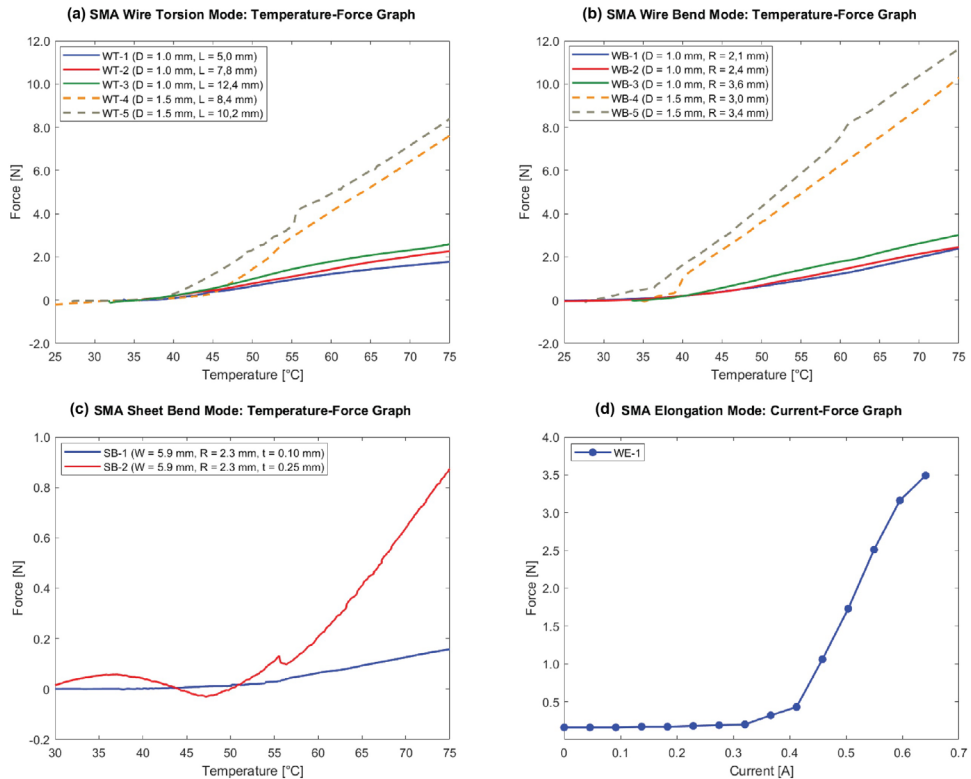


Figure A2. 3 Characterisation results of four types of SMA-actuated hinges.

(1) SMA wire torsion mode and bend mode

As depicted in Figure A2. 3(a) and (b), the actuation force of the hinge samples *WT-1/2/3* and *WB-1/2/3* (constructed with 1.0 mm diameter SMA wires) starts to rise at approximately 45 °C. The actuation force continues to grow between 45 °C and 75 °C

A

due to the increasing SMA Young's modulus at higher temperatures. Samples *WT-1/2/3* and *WB-1/2/3* achieve an actuation force of around 2.0 N at 75 °C. Upon comparing *WT-1*, *WT-2* and *WT-3* (see [Figure A2. 3\(a\)](#)), it becomes evident that with equal diameter SMA wire (D), a longer torsion length (L) in the torsion mode contributes to higher actuation force. Similarly, a larger bending radius (R) in the bending mode leads to higher force.

As shown in [Figure A2. 3\(a\)](#) and (b), *WT-4/5* and *WB4/5* which are fabricated with 1.5 mm diameter SMA wires exhibit higher growth rates after their austenite start temperature (35-40 °C). *WT-4/5* can reach around 8.0 N at 75 °C, while *WB4/5* achieve 10-12.0N, which are much higher compared to the sample made with 1.0 mm diameter SMA wires. It demonstrates that the SMA wire diameter has a substantial impact on actuation force in both torsion and bending modes.

(2) SMA sheet bend mode

Actuation force of two SMA sheet-actuated hinges is compared in [Figure A2. 3\(c\)](#). Both SMA sheets have the same width ($W = 5.9$ mm) and bending radius ($R = 2.3$ mm), while their thicknesses differ. It can be seen that the 2.3 mm thickness SMA sheet exhibits a higher force growth rate with temperature increase, and can generate about 0.9 N at 75 °C. Note that this is considerably lower than the forces generated with bending and torsion in [Figure A2. 3\(a\)](#) and (b).

(3) SMA tension mode

[Figure A2. 3\(d\)](#) shows how the actuation force of the SMA tension mode hinge changes with applied current. When the current is below 0.3 A, the force remains at around 0.2 N due to the gravity of a hinge leaf (refers to [Figure A2. 2\(e\)](#)). As the current increases, the actuation force rises, ultimately reaching 3.5 N at 14 V (approximately 0.65 A).

(4) Summary

The SMA sheet bend mode generates the lowest actuation force. Although we expected that a thicker SMA sheet would generate higher force, it cannot be done for a small hinge due to the risk of breakage when the bending radius is small, such as with a 0.5 mm sheet bending in a 5 mm radius. The tension mode can generate moderate force level. However, owing to the accommodation of the long SMA wire, the hinge is large and long.

On the other hand, both the bend and torsion modes of the SMA wire can produce high actuation forces, making them suitable options for designing small hinges, even though they also have some limitations. For the SMA wire bend mode, it cannot be used for thin-form-factor hinge, as the small bending radius could cause to material fracture. As for the torsion mode, the width of the hinge should comply with the length of the torsion part.

Appendix 3*

Supplement Information for the Reversible SMA Hinge Actuator

* This appendix is published along with the article:
Qiang Liu, Sepideh Ghodrat, and Kaspar M.B. Jansen.
Design and modelling of a reversible shape memory alloy torsion hinge actuator.
Materials & Design (2023): 112590.
<https://doi.org/10.1016/j.matdes.2023.112590>

A3.1 Analysis Methods

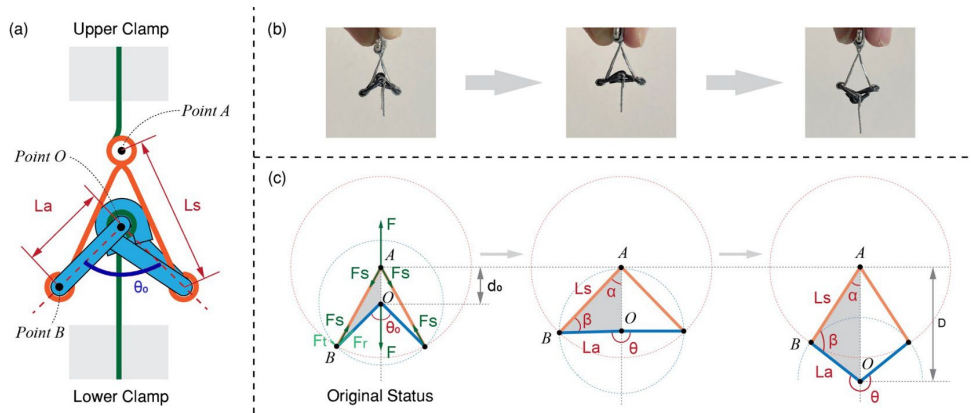


Figure A3. 1 (a) Geometric parameters of the test setting configuration. (b) Loading process of the configuration. (c) Geometric analysis corresponding to (b).

As can be seen in Figure A3. 1(a), A is a stationary point which is fixed with the upper clamp of Q800. B and O are flexible points which can move with the lower clamp. The distance of AB is a constant value, which is the length of aluminium structure (l_s), and the distance OB of is the length of SMA wire arm (l_a). The angle between two SMA wire arms is defined as the initial angle (θ_0). Figure A3. 1(b) shows how the configuration changes during the loading process. Corresponding to Figure A3. 1(b), geometric graphics are depicted in Figure A3. 1(c). Theoretically, the loading process can be regarded as the change of triangle ABO (grey areas in Figure A3. 1(c)), which has two sides (AB and OB) with constant length. Within the original status of triangle ABO , we have:

$$\cos\left(\pi - \frac{\theta_0}{2}\right) = \frac{d_0^2 + l_a^2 - l_s^2}{2d_0l_a} \quad (A3.1)$$

where θ_0 is the original angle between two SMA arms, d_0 is the original vertical length between point A and O , l_a is the length of SMA arm, l_s is the length of fixture structure.

During the loading process, we have:

$$D = d + d_0 \quad (A3.2)$$

where D is the length OA during testing, d is the displacement which can be obtained from testing.

With the Law of Cosines, two formulas of triangle ABO can be obtained:

$$\alpha = \arccos\left(\frac{D^2 + l_s^2 - l_a^2}{2Dl_s}\right) \quad (A3.3)$$

where α is the angle between OA and AB .

$$\beta = \arccos\left(\frac{l_a^2 + l_s^2 - D^2}{2l_a l_s}\right) \quad (A3.4)$$

where β is the angle between OB and AB .

By analysing the forces on *Point A* (see [Figure A3. 1\(c\)](#)), we have:

$$F_s = \frac{F}{2\cos\alpha} \quad (A3.5)$$

where F is the external applied force which can be obtained from testing, F_s is the internal force of fixture structure AB .

As for the forces on *Point B*, F_s can be divided into two component forces, and we have:

$$F_t = F_s \sin\beta \quad (A3.6)$$

where F_t is the tangential force that drive the SMA to rotate.

$$T = F_t l_a \quad (A3.7)$$

where T is the torque of SMA arm.

The actuation angle of SMA can be calculated as:

$$\theta_a = \theta - \theta_0 = 2(\alpha + \beta) - \theta_0 \quad (A3.8)$$

where θ_a is the actuation angle of SMA, θ is the angle of two SMA wire arms.

Shear strain and shear stress can be calculated with the formulas:

$$\gamma = \frac{r\theta_a}{l} \quad (A3.9)$$

where γ is the shear strain of SMA, r is the radius of the SMA wire, l is the body length of SMA.

$$\tau = \frac{Tr}{J} = \frac{2Tr}{\pi r^4} \quad (A3.10)$$

where J is the polar moment of inertia of SMA.

A3.2 Aluminium Structure Calibration

To figure out the influence of aluminium structure on experiment data, a calibration sample is constructed. As shown in [Figure A3. 2](#), three stainless steel rods with a 2.0 mm diameter are welded with two pieces of triangular stainless steel plates (2.0 mm thickness). Given that aluminium has a much lower Young's modulus, approximately one third of that of stainless steel ([Gardner et al., 2007](#)), and the geometric parameters

of stainless steel rods/plates are significantly greater than that of aluminium (0.3 mm thickness), it can be assumed that only the aluminium deforms during the loading process.

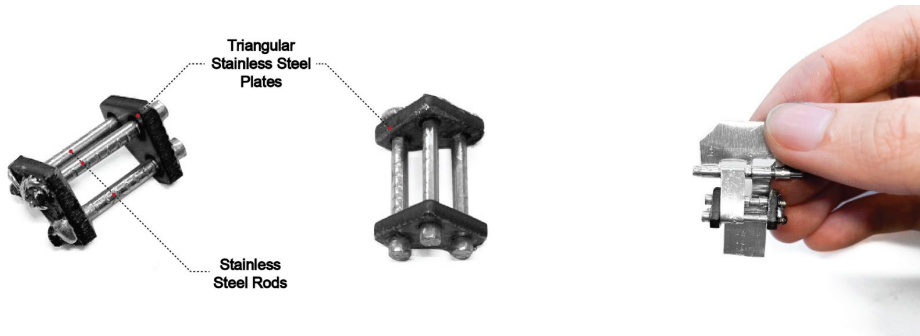


Figure A3. 2 Stainless steel sample for aluminium structure calibration.

The experiment is performed in room temperature with the force-control method. The calibration sample is subjected to an increasing force from 0 to 18 N at a rate of 1 N/min, followed by unloading to 0.05 N at the same rate. The force-displacement curve is depicted in Figure A3. 3. It reveals that the sample produces a 289 μm displacement under 18 N, with an approximate 50 μm plastic deformation after a loading-unloading cycle. The flexibility of the calibration sample can be determined by fitting the loading curve, yielding a value of 16.4 $\mu\text{m}/\text{N}$.

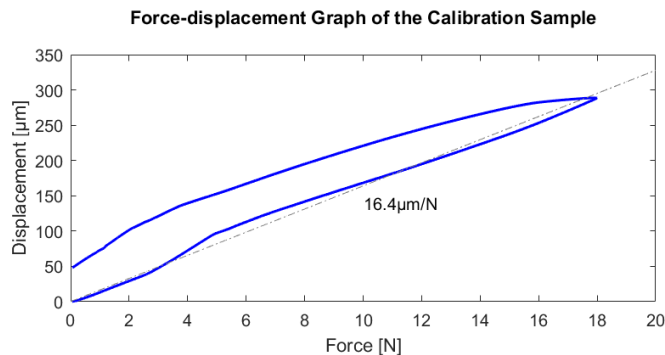


Figure A3. 3 Force-displacement graph of the calibration sample.

A3.3. Shape Memory Effect Tests for SMA

A3.3.1 Test Methods and Specimens

The purpose of the experiment is to corroborate the shape memory effect of SMA, thereby gaining a deeper understanding of their properties. A similar way of testing has been reported by Eschen et al. (Eschen, Granberry, & Abel, 2020; Eschen, Granberry, Holschuh, et al., 2020), even though these are tension tests on SMA knitted actuators. Three samples, labelled *SMA 1*, *3* and *4*, are subjected to various tests.

SMA 3 is loaded with a constant force (ranging from 1.0 N to 8.0 N in 1.0 N increments) at a rate of 1.0 N/min, while the temperature is held constant at $-40\text{ }^{\circ}\text{C}$. The temperature is then raised to $150\text{ }^{\circ}\text{C}$ at a $10\text{ }^{\circ}\text{C}/\text{min}$ rate and kept isothermal for a duration of 3 minutes. Finally, the force is reduced to zero. A similar procedure is performed for *SMA 4*, but with a force range of 5.0-9.0 N. Shear stress and strain values at $-40\text{ }^{\circ}\text{C}$ and $150\text{ }^{\circ}\text{C}$ in each force-control test are calculated using the Eqs. (A3.1)-(A3.10) listed in the supplement information.

SMA 1 is used for tests to obtain shear stress-strain curves at $-40\text{ }^{\circ}\text{C}$ and $150\text{ }^{\circ}\text{C}$, enabling the comparison with shear strain values of *SMA 3* and *4* under varying shear stress. The $-40\text{ }^{\circ}\text{C}$ test is conducted twice, adhering to the same procedure as (3) *Shear Stress-strain Tests at Different Temperatures*. However, at $150\text{ }^{\circ}\text{C}$, the force-control method is employed. The experiment of $150\text{ }^{\circ}\text{C}$ shear stress-strain test involves applying an increasing force (1 N/min) up to 18 N.

Dimensions of the specimens used in the tests can be seen in Table 4.1 in the Chapter 4 and the following Table A3. 1.

Table A3. 1 Dimensions of the configuration SMA samples used in tests.

Sample	Wire Radius r [mm]	Torsion Length L [mm]	SMA Arm Length L_a [mm]	SMA Initial Angle θ_0	Aluminium Structure Length L_s [mm]
<i>SMA 3</i>	0.50	15.04	8.04	110°	9.65
<i>SMA 4</i>	0.50	13.67	6.95	180°	7.70

A3.3.2 Test Results

In order to obtain a fundamental insight of the *actuation span* of the hinge during heating and cooling, we first investigate SMA's shape memory effect by applying a series of shear stress at low temperature and observe to which extent this deformation is recovered when heated to the actuation temperature.

As an example, the test with an applied force of 6 N is shown in Figure A3. 4(a). During the loading process of the first 6 minutes, an elevation in displacement is observed due to the phase transition from twinned to detwinned martensite. Upon heating, the displacement further increases up to 9 mm at 22.5 minutes (corresponding to $70\text{ }^{\circ}\text{C}$), indicating a reduction in the SMA's shear modulus. This phenomenon can be elucidated through Figure 4.3(c) in Chapter 4, where the shear modulus of SMA decreases during heating prior to reaching the martensite-austenite transformation stage (from $27.3\text{ }^{\circ}\text{C}$ to $34.9\text{ }^{\circ}\text{C}$). Above $70\text{ }^{\circ}\text{C}$, the shear recovery sets in and the displacement quickly decreases until 2 mm. When the load is removed (at 42 minutes), the displacement decreases to a value of about 0.3 mm. From this experiment, we take the displacement of full loading at $-40\text{ }^{\circ}\text{C}$ ($D_{-40^{\circ}\text{C}}^{SMA}$ at 6 minutes in Figure A3. 4(a)) and that of recovery at elevated temperature during unloading ($D_{150^{\circ}\text{C}}^{SMA}$ at 35 minutes), to recalculate them to shear strain. Shear stress is calculated

with the applied force (6 N). Shear stress and strain values are plotted in Figure A3. 4(b) as a blue triangle (low temperature deformation) and red sphere (high temperature recovery). The other data points in Figure A3. 4(b) correspond to experiments at different load levels.

Figure A3. 4(b) shows that the actuation strain is less than 1% for actuation stresses below 100 MPa but becomes considerable large above about 150 MPa. The preferred actuation stress is between 150-200 MPa. It can be observed that 13 sets of shear stress-strain data gathered from force-control tests distribute around the SMA I' shear stress-strain curves. It is reasonable because SMA 1, 2 and 3 are made with a same material, even though they are constructed in different hinge-shape dimensions (see Table 4.1 and section A3.1). The shear modulus at 150 °C, derived from Figure 4.3(c), is represented by a red dash-dotted line in Figure A3. 4(b), also displaying a strong agreement with the corresponding SMA I's shear stress-strain curve and the red sphere data point.

In addition, it is noteworthy that for each set of shear stress-strain data, the martensite shear stress deviates from the austenite's, even under a constant applied force. This discrepancy can be attributed to the fact that the torque exerted on the hinge-shaped specimens is subject to variations in its angle (see supplement information).

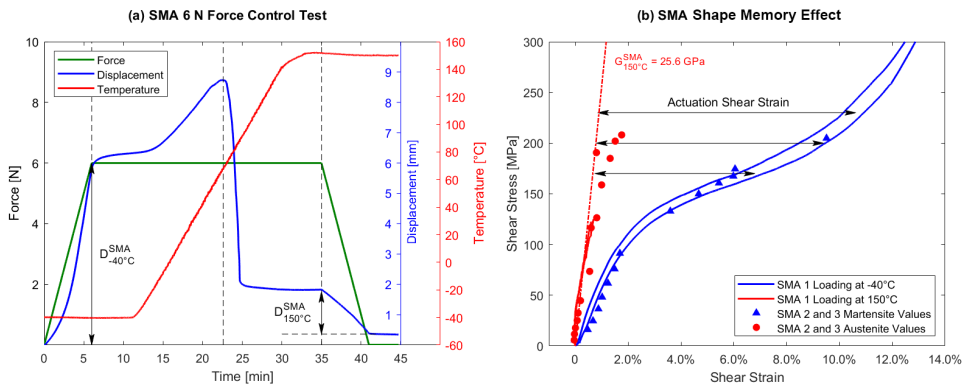


Figure A3. 4 (a) 6 N force control test on SMA 3. (b) SMA shear stress-strain curves at -40 °C and 150 °C with 13 sets of shear stress-strain data gathered from the force-control tests. The dash-dotted red line corresponds to the SMA shear modulus at 150 °C from Fig. 4.3(c). The two blue lines represent two loading tests of SMA 1 at -40 °C.

A

A3.4 Superelastic Effect Tests for SE

The test method can be seen in section 4.3.4 of the Chapter 4. Figure A3. 5 in a supplementary graph of the Figure 4.5.

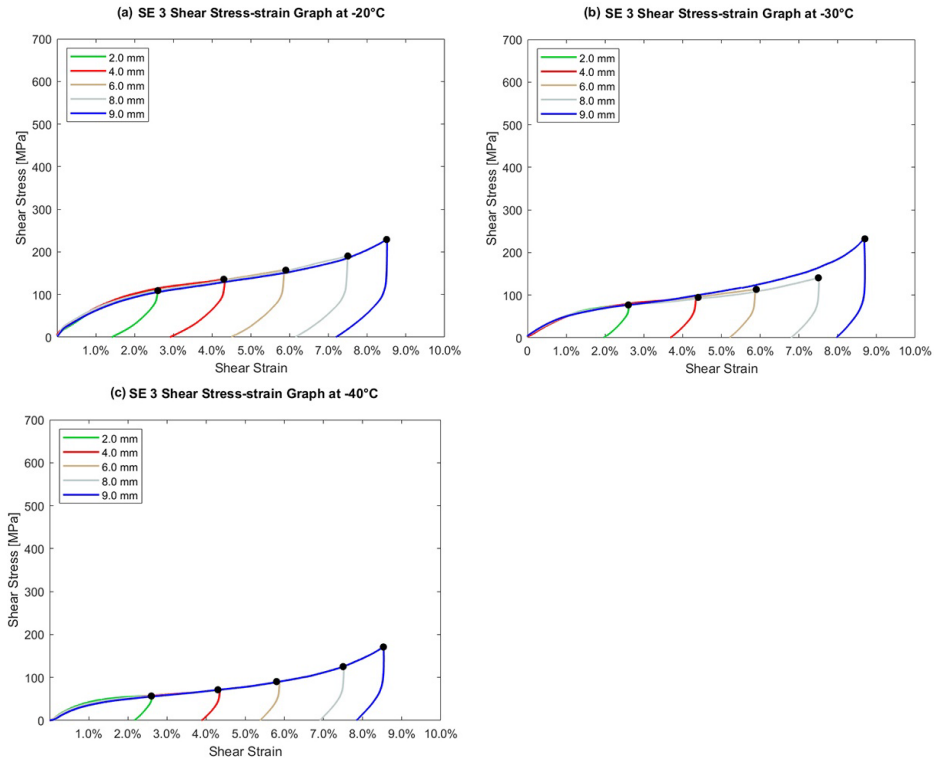


Figure A3. 5 Shear stress-strain graph of SE from -20 °C to -40 °C. It can be seen that the superelastic properties begin to diminish at low temperature.

A3.5 Actuation Force of the Hinge System

To evaluate the actuation force the hinge system, $S_{ys} 2$ is used for test in Q800. The upper and lower aluminium structures (see Figure 4.8) are used to fix with the clamps of Q800. The displacement-control mode is selected for the test. The displacement is programmed as 10 μm during the whole test. As can be seen in Figure A3. 6, when the temperature increases from 23 °C to 45 °C, the force stays at a same level. After 45 °C, the hinge system reaches it actuation temperature and tries to open, but is encountered by the antagonist force of the Q800. It shows that the actuation force reaches 5.2 N at 97 °C. Note that the actuation force in the graph is the force after calculation with Eqs. (A3.1)-(A3.10), and it is the F_t indicated in Figure A3. 1.

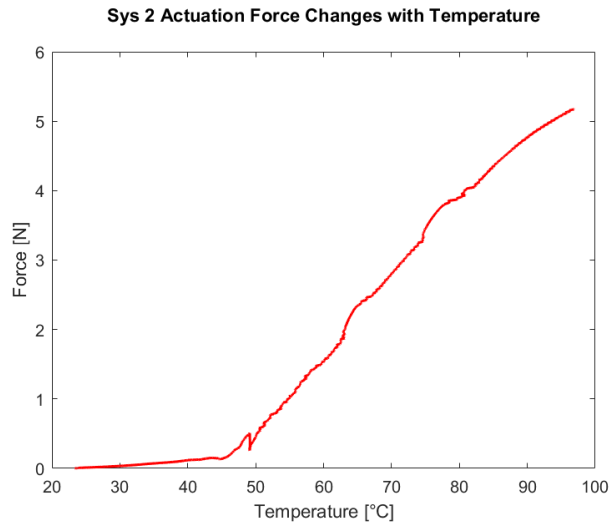


Figure A3. 6 Force-temperature graph of the Sys 2.

A3.6 Actuation Temperatures of the Hinge System

The reversible hinge actuator is a combination of the characteristics of both SE and SMA. Therefore, its actuation temperatures are affected by two different types of nitinol wire.

The hysteresis (temperature difference between heating and cooling activation), shaded areas in [Figure 4.9](#) in [Chapter 4](#), reflects the onsets and finishes of the SMA activation temperatures. If we determine the activation temperature with the slope method (see black dash-dotted lines of *Sys 4*), and compare this with the DSC results for the SMA ([Table 4.2](#)). We see that the hinge opening temperature range (from 46°C to 92 °C) is much wider than the corresponding SMA transition (between 30.2 °C and 37 °C), whereas the hinge closing seems to be much more dominated by the SMA behaviour alone (start and finish temperatures of 16.6 °C and -2.5 °C, respectively). The actuation temperatures of the hinge system are actually affected by the *locked state* (see [section 4.6.2.2](#)). When SMA torque-angle curves have *intersection points* with SE's, the hinge angle begins to change. Once the temperature rises or falls to a certain threshold, the two curves no longer intersect, and the hinge system will be locked and maintained at a constant angle.

A3.7 Influence of External Force on the Hinge Actuation Angle

In some application scenarios (e.g. [Figure 4.12](#)), the actuation angles of the hinge systems are affected by external forces. For example, when a gripper is activated to grab an item, the object also applies force on the hinge to impede its complete closure. To figure out the impact of such external forces on the hinges' actuation angles, a series of force-control tests are performed on the *Sys 4* (see [Table 4.5](#) for dimensions).

The fundamental methodology of the experiments is to fix two aluminium tags of the *Sys 4* configuration (see Figure 4.8) with the clamps of Q800 and apply a constant force (see Figure 4.2(b)). Angle changes are monitored during heating and cooling. The test procedure is programmed as follows: First, *Sys 4* is heated to 150 °C at a rate of 8 °C/min. Following a 5-minute isothermal soak, the specimen is applied 2 N at a rate of 2 N/min. The force is then consistently maintained while *Sys 4* is subjected to a cooling-heating cycle (-40 °C to 150 °C). The same experimental method is also used in tests of 4 N and 6 N. The displacement data is converted into the angle changes of the hinge system using the equations presented in section A3.1. Note that in these experiments, the force F (as depicted Figure A3. 1) is maintained constant, instead of F_t , which could be different from the force situation in actual applications.

The experimental outcomes, as depicted in Figure A3. 7(a), reveal that the angle-temperature curves for 0, 2 N, 4 N, and 6 N forces share a similar shape but differ in their opening and closing angles. At high-temperature environment, *Sys 4* is activated and reaches the *maximum actuation angle* (θ_{max}), while during cooling, the hinge system closes at the *minimum actuation angle* (θ_{min}). By comparing different curves in Figure A3. 7(a), it can be seen that a higher force always leads to a larger θ_{max} as well as θ_{min} . This finding can be explained with Figure 4.2(b), which shows that the lower clamp always applies a downward force to the torsion part, thereby enlarging the angle throughout the entire cooling-heating cycle.

The data collected from Figure A3. 7(a), including θ_{max} , θ_{min} and $\Delta\theta$ for each applied load, are represented in Figure A3. 7(b) using round dots, squares, and triangles, respectively. It can be seen that the applied force has large influence on the θ_{min} , indicating a challenge for the hinge system to fully close under higher forces. It further leads to a small *angle span* ($\Delta\theta$). For example, when 6 N is applied, the $\Delta\theta^{6N}$ is only 29°, which is about half of $\Delta\theta^0$.

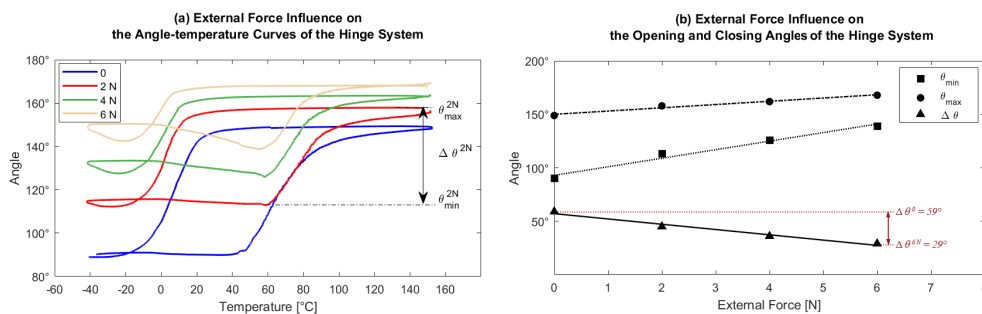


Figure A3. 7 (a) External force influence on the angle-temperature curves of the hinge system. (b) External force influence on the opening and closing angles (θ_{max} , θ_{min} and $\Delta\theta$) of the hinge system. Data points are obtained from Figure A3. 7(a), and three linear functions are fitted in Matlab based on the data points.

References

- Ackerley, R., Carlsson, I., Wester, H., Olausson, H., & Backlund Wasling, H. (2014). Touch perceptions across skin sites: differences between sensitivity, direction discrimination and pleasantness. *Frontiers in behavioral neuroscience*, 8, 54.
- Acome, E., Mitchell, S. K., Morrissey, T., Emmett, M., Benjamin, C., King, M., . . . Keplinger, C. (2018). Hydraulically amplified self-healing electrostatic actuators with muscle-like performance. *Science*, 359(6371), 61-65.
- Agharese, N., Cloyd, T., Blumenschein, L. H., Raitor, M., Hawkes, E. W., Culbertson, H., & Okamura, A. M. (2018). *HapWRAP: Soft growing wearable haptic device*. Paper presented at the 2018 IEEE International Conference on Robotics and Automation (ICRA).
- Ahmed, I., Harjunen, V., Jacucci, G., Hoggan, E., Ravaja, N., & Spapé, M. M. (2016). *Reach out and touch me: Effects of four distinct haptic technologies on affective touch in virtual reality*. Paper presented at the Proceedings of the 18th ACM International Conference on Multimodal Interaction.
- Ali, H. F., & Kim, Y. (2023). Design procedure and control of a small-scale knee exoskeleton using shape memory alloy springs. *Microsystem Technologies*, 1-10.
- Alur, A., Shrivastav, P., & Jumde, A. (2014). Haptic technology: a comprehensive review of its applications and future prospects. *Int. J. Comput. Sci. Inf. Technol*, 5, 6039-6043.
- Amemiya, T., & Sugiyama, H. (2008). *Design of a haptic direction indicator for visually impaired people in emergency situations*. Paper presented at the Computers Helping People with Special Needs: 11th International Conference, ICCHP 2008, Linz, Austria, July 9-11, 2008. Proceedings 11.
- An, S.-M., Ryu, J., Cho, M., & Cho, K.-J. (2012). Engineering design framework for a shape memory alloy coil spring actuator using a static two-state model. *Smart Materials and Structures*, 21(5), 055009.
- ASTM-E3098-17. (2018). Standard Test Method for Mechanical Uniaxial Pre-strain and Thermal Free Recovery of Shape Memory Alloys. *ASTM Standard*.
- Balasubramanian, M., Srimath, R., Vignesh, L., & Rajesh, S. (2021). *Application of shape memory alloys in engineering—A review*. Paper presented at the Journal of Physics: Conference Series.
- Barati, B., Karana, E., & Hakkert, P. (2020). Understanding Experiential Qualities of Light-Touch-Matters: Towards a Tool Kit. *Journal of Design Thinking*, 1(1), 1-20.
- Basheer, A. A. (2020). Advances in the smart materials applications in the aerospace industries. *Aircraft Engineering and Aerospace Technology*, 92(7), 1027-1035.
- Benafan, O., Brown, J., Calkins, F., Kumar, P., Stebner, A., Turner, T., . . . Young, M. (2014). Shape memory alloy actuator design: CASMART collaborative best practices and case studies. *International Journal of Mechanics and Materials in Design*, 10, 1-42.
- Bhatnagar, T., Marquardt, N., Miodownik, M., & Holloway, C. (2021). *Transforming a Monolithic Sheet of Nitinol into a Passive Reconfigurable Tactile Pixel Array Display at Braille Resolution*. Paper presented at the 2021 IEEE World Haptics Conference (WHC).
- Bhatnagar, T., Upadhyay, V., Sharma, A., Rao, P. M., Miodownik, M., Marquardt, N., & Holloway, C. (2021). *Drawing Erasable Tactile Diagrams on Tacilia*.
- Biswas, S., & Visell, Y. (2019). Emerging material technologies for haptics. *Advanced Materials Technologies*, 4(4), 1900042.
- Blake, J., & Gurocak, H. B. (2009). Haptic glove with MR brakes for virtual reality. *IEEE/ASME Transactions on mechatronics*, 14(5), 606-615.
- Blauvelt, G., Wrench, T., & Eisenberg, M. (1999). *Integrating craft materials and computation*. Paper presented at the Proceedings of the 3rd conference on Creativity & Cognition.
- Brabyn, J. A. (1982). New developments in mobility and orientation aids for the blind. *IEEE Transactions on Biomedical Engineering*(4), 285-289.
- Brinson, L. C., Bekker, A., & Hwang, S. (1996). Deformation of shape memory alloys due to thermo-induced transformation. *Journal of Intelligent material systems and structures*, 7(1), 97-107.
- Brooks Jr, F. P., Ouh-Young, M., Batter, J. J., & Jerome Kilpatrick, P. (1990). Project GROPEHaptic displays for scientific visualization. *ACM SIGGraph computer graphics*, 24(4), 177-185.
- Brown, R. (1999). *Handbook of polymer testing: physical methods*: CRC press.
- Brunnström, K., Dima, E., Qureshi, T., Johanson, M., Andersson, M., & Sjöström, M. (2020). Latency impact on quality of experience in a virtual reality simulator for remote control of machines. *Signal Processing: Image Communication*, 89, 116005.
- Buechley, L., & Perner-Wilson, H. (2012). Crafting technology: Reimagining the processes, materials, and cultures of electronics. *ACM Transactions on Computer-Human Interaction (TOCHI)*, 19(3), 1-21.

References

- Buehler, W. J., Gilfrich, J. V., & Wiley, R. (1963). Effect of low-temperature phase changes on the mechanical properties of alloys near composition TiNi. *Journal of applied physics*, 34(5), 1475-1477.
- Burdea, G. C. (1996). *Force and touch feedback for virtual reality*: John Wiley & Sons, Inc.
- Burdea, G. C. (1999). *Haptic feedback for virtual reality*. Paper presented at the Virtual reality and prototyping workshop.
- Cao, F., Saraiji, M. Y., & Minamizawa, K. (2018). Skin+ programmable skin as a visuo-tactile interface. In *ACM SIGGRAPH 2018 Posters* (pp. 1-2).
- Catkin, B., & Patoglu, V. (2023). Preference-Based Human-in-the-Loop Optimization for Perceived Realism of Haptic Rendering. *IEEE Transactions on Haptics*.
- Chang, W.-S., & Araki, Y. (2016). *Use of shape-memory alloys in construction: a critical review*. Paper presented at the Proceedings of the Institution of Civil Engineers-Civil Engineering.
- Chen, H.-Y., Yang, H., Chi, H.-J., & Chen, H.-M. (2013). Physiological effects of deep touch pressure on anxiety alleviation: The weighted blanket approach. *Journal of Medical and Biological Engineering*, 33(5), 463-470.
- Chernyshov, G., Tag, B., Caremel, C., Cao, F., Liu, G., & Kunze, K. (2018). *Shape memory alloy wire actuators for soft, wearable haptic devices*. Paper presented at the Proceedings of the 2018 ACM International Symposium on Wearable Computers.
- Choi, K. Y., & Ishii, H. (2021). *Therms-Up!: DIY Inflatables and Interactive Materials by Upcycling Wasted Thermoplastic Bags*. Paper presented at the Proceedings of the Fifteenth International Conference on Tangible, Embedded, and Embodied Interaction.
- Choi, K. Y., Lee, J., ElHaoui, N., Picard, R., & Ishii, H. (2021). *Aspire: clippable, mobile pneumatic-haptic device for breathing rate regulation via personalizable tactile feedback*. Paper presented at the Extended Abstracts of the 2021 CHI Conference on Human Factors in Computing Systems.
- Choi, S., & Kuchenbecker, K. J. (2012). Vibrotactile display: Perception, technology, and applications. *Proceedings of the IEEE*, 101(9), 2093-2104.
- Cismasiu, C. (2010). *Shape memory alloys: BoD—Books on Demand*.
- Coelho, M., Ishii, H., & Maes, P. (2008). SurfleX: a programmable surface for the design of tangible interfaces. In *CHI'08 extended abstracts on Human factors in computing systems* (pp. 3429-3434).
- Compton, C., Woelfle, H., Dahunsi, B. O., Pettys-Baker, R., Subash, N., Priebe, M., & Holschuh, B. (2021). *Dynamic, Discreet, Robotic Compression Garment for Real-Time Stress Assessment and Intervention*. Paper presented at the 2021 International Symposium on Wearable Computers.
- Cook, A. M., & Polgar, J. M. (2014). *Assistive technologies-e-book: principles and practice*: Elsevier Health Sciences.
- Copaci, D., Blanco, D., & Moreno, L. E. (2019). *Flexible shape-memory alloy-based actuator: Mechanical design optimization according to application*. Paper presented at the Actuators.
- Cross, W. B., Kariotis, A. H., & Stimler, F. J. (1969). *Nitinol characterization study*. Retrieved from
- Dancu, A., Hedler, C., Nielsen, S. A., Frank, H., Kening, Z., Pelling, A., . . . Fjeld, M. (2015). *Emergent interfaces: constructive assembly of identical units*. Paper presented at the Proceedings of the 33rd Annual ACM Conference Extended Abstracts on Human Factors in Computing Systems.
- Dong, X., Zhang, F., Wang, L., Liu, Y., & Leng, J. (2022). 4D printing of electroactive shape-changing composite structures and their programmable behaviors. *Composites Part A: Applied Science and Manufacturing*, 157, 106925.
- Duerig, T. W., Melton, K., & Stöckel, D. (2013). *Engineering aspects of shape memory alloys*: Butterworth-Heinemann.
- Dunne, L. E., Profita, H., Zeagler, C., Clawson, J., Gilliland, S., Do, E. Y.-L., & Budd, J. (2014). *The social comfort of wearable technology and gestural interaction*. Paper presented at the 2014 36th annual international conference of the IEEE engineering in medicine and biology society.
- Duvall, J. C., Dunne, L. E., Schleif, N., & Holschuh, B. (2016). *Active "hugging" vest for deep touch pressure therapy*. Paper presented at the Proceedings of the 2016 ACM International Joint Conference on Pervasive and Ubiquitous Computing: Adjunct.
- DYNALLOY. (2021a). Technical Characteristics of Actuator Wires. Retrieved from <https://www.dynalloy.com/pdfs/TCF1140.pdf>
- DYNALLOY. (2021b). Technical Characteristics of FLEXINOL® Actuator Wires. Retrieved from <https://www.dynalloy.com/pdfs/TCF1140.pdf>
- Eggeler, G., Hornbogen, E., Yawny, A., Heckmann, A., & Wagner, M. (2004). Structural and functional fatigue of NiTi shape memory alloys. *Materials Science and Engineering: A*, 378(1-2), 24-33.
- Eid, M. A., & Al Osman, H. (2016). Affective Haptics: Current Research and Future Directions. *IEEE Access*, 4, 26-40. doi:10.1109/access.2015.2497316
- Eisenberg, M., & Eisenberg, A. N. (1998). Middle tech: blurring the division between high and low tech in education. In *The design of children's technology* (pp. 243-273).
- El Saddik, A., Orozco, M., Eid, M., & Cha, J. (2011). *Haptics technologies: Bringing touch to multimedia*: Springer Science & Business Media.
- Eschen, K., Granberry, R., & Abel, J. (2020). Guidelines on the design, characterization, and operation of shape memory alloy knitted actuators. *Smart Materials and Structures*, 29(3), 035036.

- Eschen, K., Granberry, R., Holschuh, B., & Abel, J. (2020). Amplifying and Leveraging Generated Force Upon Heating and Cooling in SMA Knitted Actuators. *ACS Appl Mater Interfaces*. doi:10.1021/acsami.0c14206
- Eskildsen, P., Morris, A., Collins, C. C., & Bach-y-Rita, P. (1969). Simultaneous and successive cutaneous two-point thresholds for vibration. *Psychonomic Science*, 14(4), 146-147.
- Esposito, N., Vigliani, R. M., & Ferrari, V. (2018). *Wearable Tactile Interfaces Using SMA Wires*. Paper presented at the International Conference on Virtual Reality and Augmented Reality.
- Felton, S. M., Tolley, M. T., Shin, B., Onal, C. D., Demaine, E. D., Rus, D., & Wood, R. J. (2013). Self-folding with shape memory composites. *Soft Matter*, 9(32), 7688-7694.
- Fernandes, D. J., Peres, R. V., Mendes, A. M., & Elias, C. N. (2011). Understanding the shape-memory alloys used in orthodontics. *International Scholarly Research Notices*, 2011.
- Ferry, J. D. (1980). *Viscoelastic properties of polymers*: John Wiley & Sons.
- Follmer, S., Leithinger, D., Olwal, A., Hogge, A., & Ishii, H. (2013). *inFORM: dynamic physical affordances and constraints through shape and object actuation*. Paper presented at the Uist.
- Foo, E. W., Lee, J. W., Ozbek, S., Compton, C., & Holschuh, B. (2019). *Iterative design and development of remotely-controllable, dynamic compression garment for novel haptic experiences*. Paper presented at the Proceedings of the 23rd International Symposium on Wearable Computers.
- Frenzel, J., George, E. P., Dlouhy, A., Somsen, C., Wagner, M.-X., & Eggeler, G. (2010). Influence of Ni on martensitic phase transformations in NiTi shape memory alloys. *Acta Materialia*, 58(9), 3444-3458.
- Friske, M., Wu, S., & Devendorf, L. (2019). *AdaCAD: Crafting software for smart textiles design*. Paper presented at the Proceedings of the 2019 CHI Conference on Human Factors in Computing Systems.
- Fukumoto, M., & Sugimura, T. (2001). *Active click: tactile feedback for touch panels*. Paper presented at the CHI'01 extended abstracts on Human factors in computing systems.
- Galiana, I., Hammond, F. L., Howe, R. D., & Popovic, M. B. (2012). *Wearable soft robotic device for post-stroke shoulder rehabilitation: Identifying misalignments*. Paper presented at the 2012 IEEE/RSJ International Conference on Intelligent Robots and Systems.
- Gardner, L., Cruise, R. B., Sok, C. P., Krishnan, K., & Ministro Dos Santos, J. (2007). *Life-cycle costing of metallic structures*. Paper presented at the Proceedings of the Institution of Civil Engineers-Engineering Sustainability.
- Gemperle, F., Kasabach, C., Stivoric, J., Bauer, M., & Martin, R. (1998). *Design for wearability*. Paper presented at the digest of papers. Second international symposium on wearable computers (cat. No. 98EX215).
- Genc, C., Roinesalo, P., Raudanjoki, O., & Hakkila, J. (2021). *Exploring a Textile-based Shadow Lamp Display Incorporating Shape Memory Alloys*. Paper presented at the Proceedings of the 20th International Conference on Mobile and Ubiquitous Multimedia.
- Ghodrat, S., Sandhir, P., & Huisman, G. (2023). Exploring shape memory alloys in haptic wearables for visually impaired people. *Frontiers in Computer Science*, 5. doi:10.3389/fcomp.2023.1012565
- Goertz, R. C. (1952). Fundamentals of general-purpose remote manipulators. *Nucleonics*, 36-42.
- Goertz, R. C., & Thompson, W. M. (1954). Electronically controlled manipulator. *Nucleonics (US) Ceased publication*, 12.
- Gordon, I., Voos, A. C., Bennett, R. H., Bolling, D. Z., Pelphrey, K. A., & Kaiser, M. D. (2013). Brain mechanisms for processing affective touch. *Human brain mapping*, 34(4), 914-922.
- Granberry, R., Eschen, K., Holschuh, B., & Abel, J. (2019). Functionally Graded Knitted Actuators with NiTi-Based Shape Memory Alloys for Topographically Self-Fitting Wearables. *Adv Mater Technol*, 4(11). doi:10.1002/admt.201900548
- Grandin, T. (1992). Calming effects of deep touch pressure in patients with autistic disorder, college students, and animals. *Journal of child and adolescent psychopharmacology*, 2(1), 63-72.
- Gratz-Kelly, S., Krüger, T., Rizzello, G., Seelecke, S., & Moretti, G. (2023). An audio-tactile interface based on dielectric elastomer actuators. *Smart Materials and Structures*, 32(3), 034005.
- Greco, C., Kotak, P., Pagnotta, L., & Lamuta, C. (2022). The evolution of mechanical actuation: from conventional actuators to artificial muscles. *International Materials Reviews*, 67(6), 575-619.
- Gupta, A., Irudayaraj, A. A. R., & Balakrishnan, R. (2017). *Hapticclench: Investigating squeeze sensations using memory alloys*. Paper presented at the Proceedings of the 30th Annual ACM Symposium on User Interface Software and Technology.
- Haans, A., & IJsselstein, W. (2006). Mediated social touch: a review of current research and future directions. *Virtual Reality*, 9(2-3), 149-159.
- Hamdan, N. A.-h., Wagner, A., Voelker, S., Steimle, J., & Borchers, J. (2019). *Springlets: Expressive, flexible and silent on-skin tactile interfaces*. Paper presented at the Proceedings of the 2019 CHI Conference on Human Factors in Computing Systems.
- Hannaford, B., & Winters, J. (1990). Actuator properties and movement control: biological and technological models. In *Multiple muscle systems* (pp. 101-120): Springer.
- Hannula, S. P., Söderberg, O., Jämsä, T., & Lindroos, V. (2006). Shape memory alloys for biomedical applications. *Advances in Science and Technology*, 49, 109-118.

- Hardy, J., Weichel, C., Taher, F., Vidler, J., & Alexander, J. (2015). *Shapeclip: towards rapid prototyping with shape-changing displays for designers*. Paper presented at the Proceedings of the 33rd Annual ACM Conference on Human Factors in Computing Systems.
- Hartl, D. J., & Lagoudas, D. C. (2007). Aerospace applications of shape memory alloys. *Proceedings of the Institution of Mechanical Engineers, Part G: Journal of Aerospace Engineering*, 221(4), 535-552.
- Hatzfeld, C., & Kern, T. A. (2016). *Engineering haptic devices*: Springer.
- Hawkes, E., An, B., Benbernou, N. M., Tanaka, H., Kim, S., Demaine, E. D., . . . Wood, R. J. (2010). Programmable matter by folding. *Proceedings of the National Academy of Sciences*, 107(28), 12441-12445.
- Haynes, A., Simons, M. F., Helps, T., Nakamura, Y., & Rossiter, J. (2019). A Wearable Skin-Stretching Tactile Interface for Human-Robot and Human-Human Communication. *IEEE Robotics and Automation Letters*, 4(2), 1641-1646. doi:10.1109/lra.2019.2896933
- He, Y., Nie, A., Pei, J., Ji, Z., Jia, J., Liu, H., . . . Zhu, Y. (2020). Prevalence and causes of visual impairment in population more than 50 years old: The Shaanxi Eye Study. *Medicine*, 99(20).
- Heikkinen, J., Olsson, T., & Väänänen-Vainio-Mattila, K. (2009). *Expectations for user experience in haptic communication with mobile devices*. Paper presented at the Proceedings of the 11th International Conference on Human-Computer Interaction with Mobile Devices and Services.
- Helps, T., Vivek, A., & Rossiter, J. J. R. (2019). Characterization and Lubrication of Tube-Guided Shape-Memory Alloy Actuators for Smart Textiles. 8(4), 94.
- Hensel, H., & Schafer, K. (1984). *Thermoreception and temperature regulation in man*: Springer.
- Ho, T. Y. K., Nirmal, A., Kulkarni, M. R., Accoto, D., & Mathews, N. (2022). Soft actuator materials for electrically driven haptic interfaces. *Advanced Intelligent Systems*, 4(2), 2100061.
- Holschuh, B. T., & Newman, D. J. (2016). Morphing compression garments for space medicine and extravehicular activity using active materials. *Aerospace medicine and human performance*, 87(2), 84-92.
- Huang, X., Nohava, J., Zhang, B., & Ramirez, A. (2011). Nanoindentation of NiTi shape memory thin films at elevated temperatures. *International Journal of Smart and Nano Materials*, 2(1), 39-49.
- Huisman, G. (2017). Social touch technology: A survey of haptic technology for social touch. *IEEE transactions on haptics*, 10(3), 391-408.
- Huisman, G., Frederiks, A. D., Dijk, B. V., Hevlen, D., & Kröse, B. (2013, 14-17 April 2013). *The TaSSt: Tactile sleeve for social touch*. Paper presented at the 2013 World Haptics Conference (WHC).
- Hwang, D., Lee, J., & Kim, K. (2017). On the design of a miniature haptic ring for cutaneous force feedback using shape memory alloy actuators. *Smart Materials and Structures*, 26(10). doi:10.1088/1361-665X/aa860d
- Ipakchian Askari, S., Huisman, G., Haans, A., & IJsselsteijn, W. A. (2022). Exploring views on affective haptic devices in times of COVID-19. *Frontiers in Computer Science*, 93.
- Iwata, H., Yano, H., Nakaizumi, F., & Kawamura, R. (2001). *Project FEELEX: adding haptic surface to graphics*. Paper presented at the Proceedings of the 28th annual conference on Computer graphics and interactive techniques.
- Jablonski, N. G. (2021). Social and affective touch in primates and its role in the evolution of social cohesion. *Neuroscience*, 464, 117-125.
- Jackson, C., Wagner, H., & Wasilewski, R. (1972). *The alloy with a memory, 55-Nitinol: its physical metallurgy, properties, and applications*. Retrieved from
- Jacoby, S., & Buechley, L. (2013). *Drawing the electric: storytelling with conductive ink*. Paper presented at the Proceedings of the 12th International Conference on Interaction Design and Children.
- James, L., Raymond, R., Jennifer, L., & Nicholas, G. (2024). An SMA Actuated Aircraft Adaptive Wing. Retrieved from <https://www.youtube.com/shorts/HlpPN3D5nA4>
- Janke, L., Czaderski, C., Motavalli, M., & Ruth, J. (2005). Applications of shape memory alloys in civil engineering structures—Overview, limits and new ideas. *Materials and structures*, 38, 578-592.
- Jayathirtha, G., & Kafai, Y. B. (2020). Interactive Stitch Sampler: A Synthesis of a Decade of Research on Using Electronic Textiles to Answer the Who, Where, How, and What for K-12 Computer Science Education. *ACM Transactions on Computing Education (TOCE)*, 20(4), 1-29.
- Jewitt, C., Price, S., Steimle, J., Huisman, G., Golmohammadi, L., Pourjafarian, N., . . . Ornati, M. (2021). Manifesto for digital social touch in crisis. *Frontiers in Computer Science*, 97.
- Johansson, R. S., Trulsson, M., Olsson, K., & Westberg, K.-G. (1988). Mechanoreceptor activity from the human face and oral mucosa. *Experimental brain research*, 72, 204-208.
- Johnson, K. O. (2001). The roles and functions of cutaneous mechanoreceptors. *Current opinion in neurobiology*, 11(4), 455-461.
- Jones, L., Nousir, A., Chen, R., Liu, A., Donovan, M., Wallace, E., & Nabil, S. (2023). *Making From Home: Reflections on Crafting Tangible Interfaces for Stay-at-home Living*. Paper presented at the Proceedings of the Seventeenth International Conference on Tangible, Embedded, and Embodied Interaction.
- Jones, L. A., & Berris, M. (2002). *The psychophysics of temperature perception and thermal-interface design*. Paper presented at the Proceedings 10th symposium on haptic interfaces for virtual environment and teleoperator systems. HAPTICS 2002.
- Jones, L. A., & Lederman, S. J. (2006). *Human hand function*: Oxford university press.

- Jones, L. A., Nakamura, M., & Lockyer, B. (2004). *Development of a tactile vest*. Paper presented at the 12th International Symposium on Haptic Interfaces for Virtual Environment and Teleoperator Systems, 2004. HAPTICS'04. Proceedings.
- Kalra, S., Bhattacharya, B., & Munjal, B. (2017). Design of shape memory alloy actuated intelligent parabolic antenna for space applications. *Smart Materials and Structures*, 26(9), 095015.
- Karana, E., Barati, B., Rognoli, V., & Zeeuw Van Der Laan, A. (2015). Material driven design (MDD): A method to design for material experiences. *International journal of design*, 9(2), 35-54.
- Katterfeldt, E.-S., Dittert, N., & Schelhowe, H. (2009). *EduWear: smart textiles as ways of relating computing technology to everyday life*. Paper presented at the Proceedings of the 8th International Conference on Interaction Design and Children.
- Kim, H.-C., Yoo, Y.-I., & Lee, J.-J. (2008). Development of a NiTi actuator using a two-way shape memory effect induced by compressive loading cycles. *Sensors and Actuators A: Physical*, 148(2), 437-442.
- Kim, H.-I., Han, M.-W., Song, S.-H., & Ahn, S.-H. (2016). Soft morphing hand driven by SMA tendon wire. *Composites Part B: Engineering*, 105, 138-148.
- Kim, H., Everitt, A., Tejada, C., Zhong, M., & Ashbrook, D. (2021). *Morpheusplug: A toolkit for prototyping shape-changing interfaces*. Paper presented at the Proceedings of the 2021 CHI Conference on Human Factors in Computing Systems.
- Kim, H., Jeon, H., Jeong, Y., & Kim, Y. (2022). *Development of Impact Absorber Mechanism for Wearable Exoskeleton Using Shape Memory Alloy Spring*. Paper presented at the Converging Clinical and Engineering Research on Neurorehabilitation IV: Proceedings of the 5th International Conference on Neurorehabilitation (ICNR2020), October 13–16, 2020.
- Kim, J. (2023). *SereniSleeve-Designing Shape Memory Based Wearables for Anxiety Modulation*.
- Kim, J. H., Huang, K., White, S., Conroy, M., & Kao, C. H.-L. (2021). *KnitDermis: Fabricating tactile on-body interfaces through machine knitting*. Paper presented at the Designing Interactive Systems Conference 2021.
- Kim, S., Gu, S., & Kim, J. (2022). Variable Shape and Stiffness Feedback System for VR Gloves Using SMA Textile Actuator. *Fibers and Polymers*, 23(3), 836-842.
- Knoop, E., & Rossiter, J. (2015a). *The tickler: a compliant wearable tactile display for stroking and tickling*. Paper presented at the Proceedings of the 33rd Annual ACM Conference Extended Abstracts on Human Factors in Computing Systems.
- Knoop, E., & Rossiter, J. (2015b). *The Tickler: A Compliant Wearable Tactile Display for Stroking and Tickling*. Paper presented at the Proceedings of the 33rd Annual ACM Conference Extended Abstracts on Human Factors in Computing Systems, Seoul, Republic of Korea. <https://doi-org.tudelft.idm.oclc.org/10.1145/2702613.2732749>
- Kobayashi, F., Ikai, G., Fukui, W., & Kojima, F. (2011). Two-fingered haptic device for robot hand teleoperation. *Journal of Robotics*, 2011.
- Koelle, M., Nicolae, M., Nittala, A. S., Teyssier, M., & Steimle, J. (2022). *Prototyping Soft Devices with Interactive Bioplastics*. Paper presented at the Proceedings of the 35th Annual ACM Symposium on User Interface Software and Technology.
- Koh, J.-s., Kim, S.-r., & Cho, K.-j. (2014). *Self-folding origami using torsion shape memory alloy wire actuators*. Paper presented at the International Design Engineering Technical Conferences and Computers and Information in Engineering Conference.
- Koizumi, N., Yasu, K., Liu, A., Sugimoto, M., & Inami, M. (2010). Animated paper: A toolkit for building moving toys. *Computers in Entertainment (CIE)*, 8(2), 1-16.
- Kontarinis, D. (1993). *Tactile display of contact shape in dextrous telemanipulation*. Paper presented at the ASME.
- Kopic, C., & Gohlke, K. (2016). *InflatIBits: A Modular Soft Robotic Construction Kit for Children*.
- Ku, P.-S., Huang, K., & Kao, C. H.-L. (2022). *Patch-O: Deformable Woven Patches for On-body Actuation*. Paper presented at the Proceedings of the 2022 CHI Conference on Human Factors in Computing Systems.
- Kumar, A., & Dhanalakshmi, K. (2022). *Simulation of Shape Memory Wire based Exoskeleton for Flexion and Extension of Upper limb*. Paper presented at the 2022 IEEE 7th International conference for Convergence in Technology (I2CT).
- Kundu, R. K., Rahman, A., & Paul, S. (2021). A study on sensor system latency in vr motion sickness. *Journal of Sensor and Actuator Networks*, 10(3), 53.
- Kus, K., & Breczko, T. (2010). DSC-investigations of the effect of annealing temperature on the phase transformation behaviour in Ni-Ti shape memory alloy. *Materials Physics and Mechanics*, 9(1), 75-83.
- Lagoudas, D. C. (2008). *Shape memory alloys: modeling and engineering applications*: Springer.
- Lai, J., Song, A., Shi, K., Ji, Q., Lu, Y., & Li, H. (2023). Design and Evaluation of a Bidirectional Soft Glove for Hand Rehabilitation-Assistance Tasks. *IEEE Transactions on Medical Robotics and Bionics*.
- Laidler, K. J. (1984). The development of the Arrhenius equation. *Journal of chemical Education*, 61(6), 494.
- Lara-Quintanilla, A., & Bersee, H. E. (2016). A study on the contraction and cooling times of actively cooled shape memory alloy wires. *Journal of Intelligent material systems and structures*, 27(3), 403-417.
- Lazar, J., Feng, J. H., & Hochheiser, H. (2017). *Research methods in human-computer interaction*: Morgan Kaufmann.

References

- Lederman, S. J., & Klatzky, R. L. (1987). Hand movements: A window into haptic object recognition. *Cognitive psychology*, 19(3), 342-368.
- Lee, H.-G., Chung, S., & Lee, W.-H. (2013). Presence in virtual golf simulators: The effects of presence on perceived enjoyment, perceived value, and behavioral intention. *New media & society*, 15(6), 930-946.
- Lee, H. T., Seichepine, F., & Yang, G. Z. (2020). Microtentacle Actuators Based on Shape Memory Alloy Smart Soft Composite. *Advanced Functional Materials*, 30(34), 2002510.
- Lee, J.-Y., Eom, J., Choi, W.-Y., & Cho, K.-J. (2018). *Soft LEGO: bottom-up design platform for soft robotics*. Paper presented at the 2018 IEEE/RSJ International Conference on Intelligent Robots and Systems (IROS).
- Leigh, S.-w., Denton, T., Parekh, K., Peebles, W., Johnson, M., & Maes, P. (2018). *Morphology extension kit: A modular robotic platform for physically reconfigurable wearables*. Paper presented at the Proceedings of the Twelfth International Conference on Tangible, Embedded, and Embodied Interaction.
- Leithinger, D., Lakatos, D., DeVincenzi, A., Blackshaw, M., & Ishii, H. (2011). *Direct and gestural interaction with relief: a 2.5 D shape display*. Paper presented at the Proceedings of the 24th annual ACM symposium on User interface software and technology.
- Lewis, N., York, A., & Seelecke, S. (2013). Experimental characterization of self-sensing SMA actuators under controlled convective cooling. *Smart Materials and Structures*, 22(9), 094012.
- Li, Y., Mi, X., Tan, J., & Gao, B. (2009). Thermo-mechanical cyclic transformation behavior of Ti-Ni shape memory alloy wire. *Materials Science and Engineering: A*, 509(1-2), 8-13.
- Liang, C., & Rogers, C. A. (1997). One-dimensional thermomechanical constitutive relations for shape memory materials. *Journal of Intelligent material systems and structures*, 8(4), 285-302.
- Lim, B., Kim, K., & Hwang, D. (2017). *On the design of the 5-DoF finger-wearable cutaneous haptic device*. Paper presented at the 2017 IEEE International Conference on Robotics and Biomimetics (ROBIO).
- Lim, B., Lee, C., & Hwang, D. (2021). Development of Embedded Sensor System for 5-DOF Finger-Wearable Tactile Interface. *IEEE/ASME Transactions on mechatronics*, 26(4), 1728-1736.
- Lin, M. C., & Otaduy, M. (2008). *Haptic rendering: foundations, algorithms, and applications*: CRC Press.
- Liu, G., Gao, F., Wang, D., & Liao, W.-H. (2022). Medical applications of magnetorheological fluid: a systematic review. *Smart Materials and Structures*, 31(4), 043002.
- Liu, Q., Ghodrati, S., & Jansen, K. M. (2022). Modelling and Mechanical Design of A Flexible Tube-guided SMA Actuator. *Materials & Design*, 110571.
- Liu, Y., Boyles, J. K., Genzer, J., & Dickey, M. D. (2012). Self-folding of polymer sheets using local light absorption. *Soft matter*, 8(6), 1764-1769.
- Liu, Z., Lan, X., Bian, W., Liu, L., Li, Q., Liu, Y., & Leng, J. (2020). Design, material properties and performances of a smart hinge based on shape memory polymer composites. *Composites Part B: Engineering*, 193, 108056.
- Löken, L. S., Wessberg, J., Morrison, I., McGlone, F., & Olsson, H. (2009). Coding of pleasant touch by unmyelinated afferents in humans. *Nature neuroscience*, 12(5), 547-548.
- Loomis, J. M., & Lederman, S. J. (1986). Tactual perception. *Handbook of perception and human performances*, 2(2), 2.
- Lu, Q., Ou, J., Wilbert, J., Haben, A., Mi, H., & Ishii, H. (2019). *milliMorph--Fluid-Driven Thin Film Shape-Change Materials for Interaction Design*. Paper presented at the Proceedings of the 32nd Annual ACM Symposium on User Interface Software and Technology.
- Lücker, M., Huisman, G., Liu, Q., & Ghodrati, S. Shape-memory origami for gentle haptic feedback.
- Lutanto, A., Ubaidillah, U., Prabowo, A. R., Imaduddin, F., & Adiputra, D. (2023). *Recent developments in the design and application of magnetorheological fluids in the medical field*. Paper presented at the AIP Conference Proceedings.
- Mabe, J. H., Ruggieri, R. T., Rosenzweig, E., & Yu, C.-J. M. (2004). *NiTiNol performance characterization and rotary actuator design*. Paper presented at the Smart Structures and Materials 2004: Industrial and Commercial Applications of Smart Structures Technologies.
- Machado, L., & Savi, M. (2003). Medical applications of shape memory alloys. *Brazilian journal of medical and biological research*, 36, 683-691.
- MacLean, K., & Enriquez, M. (2003). *Perceptual design of haptic icons*. Paper presented at the Proc. of EuroHaptics.
- Manfredi, L., Huan, Y., & Cuschieri, A. (2017). Low power consumption mini rotary actuator with SMA wires. *Smart Materials and Structures*, 26(11), 115003.
- Mao, Z., Xu, Z., & Wang, Q. (2020). Shape memory alloy actuator with active cooling device and deflectable winglet application. *Smart Materials and Structures*, 29(10), 105026.
- Martinez Castro, J. F., Buso, A., Wu, J., & Karana, E. (2022). *Tex (alive): A toolkit to explore temporal expressions in shape-changing textile interfaces*. Paper presented at the Proceedings of the 2022 ACM Designing Interactive Systems Conference.
- Massie, T. H., & Salisbury, J. K. (1994). *The phantom haptic interface: A device for probing virtual objects*. Paper presented at the Proceedings of the ASME winter annual meeting, symposium on haptic interfaces for virtual environment and teleoperator systems.
- Matsunaga, T., Totsu, K., Esashi, M., & Haga, Y. (2013). Tactile display using shape memory alloy micro-coil actuator and magnetic latch mechanism. *Displays*, 34(2), 89-94. doi:10.1016/j.displa.2013.03.001
- McCullough, M. (1998). *Abstracting craft: The practiced digital hand*: MIT press.

- McGlone, F., Wessberg, J., & Olsson, H. (2014). Discriminative and affective touch: sensing and feeling. *Neuron*, 82(4), 737-755.
- Medical, B. (2014). Medical gallery of blausen medical 2014. *WikiJournal of Medicine*, 1(2), 1-79.
- Meier, H., & Czechowicz, A. (2012). Computer-aided development and simulation tools for shape-memory actuators. *Metallurgical and Materials Transactions A*, 43, 2882-2890.
- Mellis, D. A., Jacoby, S., Buechley, L., Perner-Wilson, H., & Qi, J. (2013). *Microcontrollers as material: crafting circuits with paper, conductive ink, electronic components, and an "untookit"*. Paper presented at the Proceedings of the 7th International Conference on Tangible, Embedded and Embodied Interaction.
- Messerschmidt, M. A., Muthukumarana, S., Hamdan, N. A.-H., Wagner, A., Zhang, H., Borchers, J., & Nanayakkara, S. C. (2022). ANISMA: A Prototyping Toolkit to Explore Haptic Skin Deformation Applications Using Shape-Memory Alloys. *ACM Transactions on Computer-Human Interaction*, 29(3), 1-34.
- Miriyev, A., Stack, K., & Lipson, H. (2017). Soft material for soft actuators. *Nature Communications*, 8. doi:10.1038/s41467-017-00685-3
- Mirvakili, S. M., Pazukha, A., Sikkema, W., Sinclair, C. W., Spinks, G. M., Baughman, R. H., & Madden, J. D. (2013). Niobium nanowire yarns and their application as artificial muscles. *Advanced Functional Materials*, 23(35), 4311-4316.
- Mohd Jani, J., Leary, M., Subic, A., & Gibson, M. A. (2014). A review of shape memory alloy research, applications and opportunities. *Materials & Design (1980-2015)*, 56, 1078-1113. doi:10.1016/j.matdes.2013.11.084
- Morgan, N., & Broadley, M. (2004). Taking the art out of smart!-Forming processes and durability issues for the application of NiTi shape memory alloys in medical devices. *Proceedings for the Materials and Processes for Medical Devices Conference, Anaheim, CA*, 247-252.
- Morrison, I., Loken, L., & Olsson, H. (2009). The Skin as a Social Organ. *Experimental brain research. Experimentelle Hirnforschung. Expérimentation cérébrale*, 204, 305-314. doi:10.1007/s00221-009-2007-y
- Morrison, I., Löken, L. S., & Olsson, H. (2010). The skin as a social organ. *Experimental brain research*, 204, 305-314.
- Motzki, P. (2020). *Efficient SMA actuation—Design and control concepts*. Paper presented at the Proceedings.
- Mountcastle, V. B., & Darian-Smith, I. (1968). Neural mechanisms in somesthesia. *Medical physiology*, 2, 1372-1423.
- Mun, S., Yun, S., Nam, S., Park, S. K., Park, S., Park, B. J., . . . Kyung, K.-U. (2018a). Electro-active polymer based soft tactile interface for wearable devices. *IEEE transactions on haptics*, 11(1), 15-21.
- Mun, S., Yun, S., Nam, S., Park, S. K., Park, S., Park, B. J., . . . Kyung, K. U. (2018b). Electro-Active Polymer Based Soft Tactile Interface for Wearable Devices. *IEEE Trans Haptics*, 11(1), 15-21. doi:10.1109/TOH.2018.2805901
- Murat, B., & Marinella, F. (2018). *Materials that move: smart materials, intelligent design*: Springer.
- Muthukumarana, S., Elvitigala, D. S., Cortes, J. P. F., Matthies, D. J. C., & Nanayakkara, S. (2019). *PhantomTouch: Creating an Extended Reality by the Illusion of Touch using a Shape-Memory Alloy Matrix*. Paper presented at the SIGGRAPH Asia 2019 XR.
- Muthukumarana, S., Elvitigala, D. S., Forero Cortes, J. P., Matthies, D. J. C., & Nanayakkara, S. (2020). *Touch me Gently: Recreating the Perception of Touch using a Shape-Memory Alloy Matrix*. Paper presented at the Proceedings of the 2020 CHI Conference on Human Factors in Computing Systems.
- Muthukumarana, S., Elvitigala, D. S., Wu, Q., Pai, Y. S., & Nanayakkara, S. (2021). *Jammyfy: Interactive Multi-sensory System for Digital Art Jamming*. Paper presented at the IFIP Conference on Human-Computer Interaction.
- Muthukumarana, S., Messerschmidt, M. A., Matthies, D. J., Steimle, J., Scholl, P. M., & Nanayakkara, S. (2021). *Clothiles: A prototyping platform to fabricate customized actuators on clothing using 3d printing and shape-memory alloys*. Paper presented at the Proceedings of the 2021 CHI Conference on Human Factors in Computing Systems.
- Nabil, S., Kučera, J., Karastathi, N., Kirk, D. S., & Wright, P. (2019). *Seamless seams: Crafting techniques for embedding fabrics with interactive actuation*. Paper presented at the Proceedings of the 2019 on Designing Interactive Systems Conference.
- Nagi, S. S., Rubin, T. K., Chelvanayagam, D. K., Macefield, V. G., & Mahns, D. A. (2011). Allodynia mediated by C-tactile afferents in human hairy skin. *The Journal of physiology*, 589(16), 4065-4075.
- Nair, V. S., & Nachimuthu, R. (2022). The role of NiTi shape memory alloys in quality of life improvement through medical advancements: A comprehensive review. *Proceedings of the Institution of Mechanical Engineers, Part H: Journal of Engineering in Medicine*, 236(7), 923-950.
- Nakagaki, K., Follmer, S., & Ishii, H. (2015). *Lineform: Actuated curve interfaces for display, interaction, and constraint*. Paper presented at the Proceedings of the 28th Annual ACM Symposium on User Interface Software & Technology.
- Nakamura, M., & Jones, L. (2003). *An actuator for the tactile vest—a torso-based haptic device*. Paper presented at the 11th Symposium on Haptic Interfaces for Virtual Environment and Teleoperator Systems, 2003. HAPTICS 2003. Proceedings.

References

- Nakao, T., Kunze, K., Isogai, M., Shimizu, S., & Pai, Y. S. (2020). *FingerFlex: Shape Memory Alloy-based Actuation on Fingers for Kinesthetic Haptic Feedback*. Paper presented at the 19th International Conference on Mobile and Ubiquitous Multimedia.
- Nakao, T., Santana, S. K., Isogai, M., Shimizu, S., Kimata, H., Kunze, K., & Pai, Y. S. (2019). ShareHaptics: a modular haptic feedback system using shape memory alloy for mixed reality shared space applications. In *ACM SIGGRAPH 2019 Posters* (pp. 1-2).
- Nakayasu, A. (2010). Himawari: shape memory alloy motion display for robotic representation. In *CHI'10 Extended Abstracts on Human Factors in Computing Systems* (pp. 4327-4332).
- Nakayasu, A. (2016). *Luminescent tentacles: a scalable SMA motion display*. Paper presented at the Proceedings of the 29th Annual Symposium on User Interface Software and Technology.
- Nam, C. S., Li, Y., Yamaguchi, T., & Smith-Jackson, T. L. (2012). Haptic user interfaces for the visually impaired: Implications for haptically enhanced science learning systems. *International Journal of Human-Computer Interaction*, 28(12), 784-798.
- Narumi, K., Shi, X., Hodges, S., Kawahara, Y., Shimizu, S., & Asami, T. (2015). *Circuit eraser: A tool for iterative design with conductive ink*. Paper presented at the Proceedings of the 33rd Annual ACM Conference Extended Abstracts on Human Factors in Computing Systems.
- Nizamani, A. M., Daudpoto, J., & Nizamani, M. A. (2017). Development of faster SMA actuators. *Shape memory alloys-fundamentals and applications*, 106-126.
- Norrsell, U., Eliasson, B., Frizell, M., Wallin, B. G., Wesslau, C., & Olausson, H. (2001). Tactile directional sensibility for haptically enhanced science learning systems. *Muscle & nerve*, 24(11), 1496-1502.
- Papadopoulou, A., Berry, J., Knight, T., & Picard, R. (2019). *Affective sleeve: Wearable materials with haptic action for promoting calmness*. Paper presented at the International Conference on Human-Computer Interaction.
- Parisi, D. (2018). *Archaeologies of touch: Interfacing with haptics from electricity to computing*: U of Minnesota Press.
- Park, J., Kim, M., Lee, Y., Lee, H. S., & Ko, H. (2015). Fingertip skin-inspired microstructured ferroelectric skins discriminate static/dynamic pressure and temperature stimuli. *Science advances*, 1(9), e1500661.
- Pawluk, D. T., Adams, R. J., & Kitada, R. (2015). Designing haptic assistive technology for individuals who are blind or visually impaired. *IEEE transactions on haptics*, 8(3), 258-278.
- Perner-Wilson, H., Buechley, L., & Satomi, M. (2010). *Handcrafting textile interfaces from a kit-of-no-parts*. Paper presented at the Proceedings of the fifth international conference on Tangible, embedded, and embodied interaction.
- Posch, I., & Fitzpatrick, G. (2021). The matter of tools: designing, using and reflecting on new tools for emerging eTextile craft practices. *ACM Transactions on Computer-Human Interaction (TOCHI)*, 28(1), 1-38.
- Posch, I., Subasi, O., Rosner, D. K., Frankjaer, R., Zoran, A., & Pérez-Bustos, T. (2019). *Troubling innovation: Craft and computing across boundaries*. Paper presented at the Extended abstracts of the 2019 chi conference on human factors in computing systems.
- Priebe, M., Foo, E., & Holschuh, B. (2020). *Shape memory alloy haptic compression garment for media augmentation in virtual reality environment*. Paper presented at the Adjunct Publication of the 33rd Annual ACM Symposium on User Interface Software and Technology.
- Probst, K., Seifried, T., Haller, M., Yasu, K., Sugimoto, M., & Inami, M. (2011). Move-it: interactive sticky notes actuated by shape memory alloys. In *CHI'11 Extended Abstracts on Human Factors in Computing Systems* (pp. 1393-1398).
- Qi, J., & Buechley, L. (2012). *Animating paper using shape memory alloys*. Paper presented at the Proceedings of the SIGCHI conference on human factors in computing systems.
- Qi, J., Buechley, L., Huang, A. b., Ng, P., Cross, S., & Paradiso, J. A. (2018). *Chibitronics in the wild: engaging new communities in creating technology with paper electronics*. Paper presented at the Proceedings of the 2018 CHI Conference on Human Factors in Computing Systems.
- Raffle, H. S., Parkes, A. J., & Ishii, H. (2004). *Topobo: a constructive assembly system with kinetic memory*. Paper presented at the Proceedings of the SIGCHI conference on Human factors in computing systems.
- Raisamo, R., Salminen, K., Rantala, J., Farooq, A., & Ziat, M. (2022). Interpersonal Haptic Communication: Review and Directions for the Future. *International Journal of Human-Computer Studies*, 102881.
- Rajput, G. S., Vora, J., Prajapati, P., & Chaudhari, R. (2022). Areas of recent developments for shape memory alloy: A review. *Materials Today: Proceedings*, 62, 7194-7198.
- Rao, A., Srinivasa, A. R., & Reddy, J. N. (2015). *Design of shape memory alloy (SMA) actuators* (Vol. 3): Springer.
- Romanishin, J. W., Gilpin, K., & Rus, D. (2013). *M-blocks: Momentum-driven, magnetic modular robots*. Paper presented at the 2013 IEEE/RSJ International Conference on Intelligent Robots and Systems.
- Russell, L. (1965). Travel Pathsounder proceedings of the Rotterdam Mobility Research Conference. In: New York: American Foundation for the Blind.
- Sadiq, H., Wong, M.-B., Al-Mahaidi, R., & Zhao, X. (2010). The effects of heat treatment on the recovery stresses of shape memory alloys. *Smart Materials and Structures*, 19(3), 035021.
- Saket, B., Prasajo, C., Huang, Y., & Zhao, S. (2013). *Designing an effective vibration-based notification interface for mobile phones*. Paper presented at the Proceedings of the 2013 conference on Computer supported cooperative work.

- Salehi, M., Hamed, M., Nohouji, H. S., & Arghavani, J. (2013). Mechanical properties identification and design optimization of nitinol shape memory alloy microactuators. *Smart Materials and Structures*, 23(2), 025001.
- Sandhir, P. (2021). Integrating shape memory materials in haptic technology as an aid for the visually impaired.
- Schneider, O., MacLean, K., Swindells, C., & Booth, K. (2017). Haptic experience design: What hapticians do and where they need help. *International Journal of Human-Computer Studies*, 107, 5-21. doi:10.1016/j.ijhcs.2017.04.004
- Schneider, O. S., Israr, A., & MacLean, K. E. (2015). *Tactile animation by direct manipulation of grid displays*. Paper presented at the Proceedings of the 28th annual ACM symposium on user interface software & technology.
- Schoessler, P., Windham, D., Leithinger, D., Follmer, S., & Ishii, H. (2015). *Kinetic blocks: Actuated constructive assembly for interaction and display*. Paper presented at the Proceedings of the 28th Annual ACM Symposium on User Interface Software & Technology.
- Seilingo, E. P., Bianchi, M., Grioli, G., & Bicchi, A. (2010). Rendering softness: Integration of kinesthetic and cutaneous information in a haptic device. *IEEE Transactions on Haptics*, 3(2), 109-118.
- Seelecke, S., & Müller, I. (2004). Shape memory alloy actuators in smart structures: Modeling and simulation. *Appl. Mech. Rev.*, 57(1), 23-46.
- Seigner, L., Tshikwand, G. K., Wendler, F., & Kohl, M. (2021). *Bi-Directional Origami-Inspired SMA Folding Microactuator*. Paper presented at the Actuators.
- Sellitto, A., & Riccio, A. (2019). Overview and future advanced engineering applications for morphing surfaces by shape memory alloy materials. *Materials*, 12(5), 708.
- Simons, M. F., Haynes, A. C., Gao, Y., Zhu, Y., & Rossiter, J. (2020). *In Contact: Pinching, Squeezing and Twisting for Mediated Social Touch*. Paper presented at the Extended Abstracts of the 2020 CHI Conference on Human Factors in Computing Systems.
- Singhal, A., Jain, P., Chanana, P., Jain, D., Paul, R., Balakrishnan, M., & Rao, P. V. M. (2013). *Application of Shape Memory Alloy (SMA) Based Actuation for Refreshable Display of Braille*. <https://doi.org/10.1115/DETC2013-13159>
- Siu, A. F., Chase, E. D., Kim, G. S.-H., Boadi-Agyemang, A., Gonzalez, E. J., & Follmer, S. (2021). Haptic guidance to support design education and collaboration for blind and visually impaired people. *Design Thinking Research: Translation, Prototyping, and Measurement*, 167-180.
- Sofla, A., Meguid, S., Tan, K., & Yeo, W. (2010). Shape morphing of aircraft wing: Status and challenges. *Materials & Design*, 31(3), 1284-1292.
- Solazzi, M., Provancher, W. R., Frisoli, A., & Bergamasco, M. (2011). *Design of a SMA actuated 2-DoF tactile device for displaying tangential skin displacement*. Paper presented at the 2011 IEEE World Haptics Conference.
- Sproewitz, A., Billard, A., Dillenbourg, P., & Ijspeert, A. J. (2009). *Roombots-mechanical design of self-reconfiguring modular robots for adaptive furniture*. Paper presented at the 2009 IEEE international conference on robotics and automation.
- Srivastava, R., Alsamhi, S. H., Murray, N., & Devine, D. (2022). Shape memory alloy-based wearables: a review, and conceptual frameworks on HCI and HRI in Industry 4.0. *Sensors*, 22(18), 6802.
- Srivastava, R., Singh, M., Gomes, G. D., Murray, N., & Devine, D. (2022). *SM-EXO: Shape Memory alloy-based Hand EXOSkeleton for Cobot Application*. Paper presented at the 2022 31st IEEE International Conference on Robot and Human Interactive Communication (RO-MAN).
- Stanley, A. A., & Kuchenbecker, K. J. (2011, 21-24 June 2011). *Design of body-grounded tactile actuators for playback of human physical contact*. Paper presented at the 2011 IEEE World Haptics Conference.
- Stevens, J. (1991). Thermal Sensibility. The Psychology of Touch. MA Heller and W. Schiff. In: Hillsdale, NJ, Lawrence Erlbaum Associates, Inc.
- Stöckel, D. (1995). The shape memory effect-phenomenon, alloys and applications. *Proceedings: Shape Memory Alloys for Power Systems EPRI*, 1, 1-13.
- Stoeckel, D. (2000). Nitinol medical devices and implants. *Minimally invasive therapy & allied technologies*, 9(2), 81-88.
- Suh, A., & Prophet, J. (2018). The state of immersive technology research: A literature analysis. *Computers in Human Behavior*, 86, 77-90.
- Suhonen, K., Väänänen-Vainio-Mattila, K., & Mäkelä, K. (2012). *User experiences and expectations of vibrotactile, thermal and squeeze feedback in interpersonal communication*. Paper presented at the The 26th BCS Conference on Human Computer Interaction 26.
- Sun, R., Onose, R., Dunne, M., Ling, A., Denham, A., & Kao, H.-L. (2020). *Weaving a Second Skin: Exploring Opportunities for Crafting On-Skin Interfaces Through Weaving*. Paper presented at the Proceedings of the 2020 ACM Designing Interactive Systems Conference.
- Surbled, P., Clerc, C., Le Pioufle, B., Ataka, M., & Fujita, H. (2001). Effect of the composition and thermal annealing on the transformation temperatures of sputtered TiNi shape memory alloy thin films. *Thin Solid Films*, 401(1-2), 52-59.
- Suzumori, K., Wada, A., & Wakimoto, S. (2013). New mobile pressure control system for pneumatic actuators, using reversible chemical reactions of water. *Sensors and Actuators A: Physical*, 201, 148-153.

References

- Tahouni, Y., Qamar, I. P., & Mueller, S. (2020). *NURBSforms: A Modular Shape-Changing Interface for Prototyping Curved Surfaces*. Paper presented at the Proceedings of the Fourteenth International Conference on Tangible, Embedded, and Embodied Interaction.
- Takahashi, K., Mitsuhashi, H., Murata, K., Norieda, S., & Watanabe, K. (2011). *Improving shared experiences by haptic telecommunication*. Paper presented at the 2011 International Conference on Biometrics and Kansei Engineering.
- Takeda, Y., & Sawada, H. (2013). *Tactile actuators using SMA micro-wires and the generation of texture sensation from images*. Paper presented at the 2013 IEEE/RSJ International Conference on Intelligent Robots and Systems.
- Tanaka, K., & Nagaki, S. (1982a). A thermomechanical description of materials with internal variables in the process of phase transitions. *Ingenieur-Archiv*, *51*(5), 287-299.
- Tanaka, K., & Nagaki, S. J. I.-A. (1982b). A thermomechanical description of materials with internal variables in the process of phase transitions. *51*(5), 287-299.
- Taylor, P., Moser, A., & Creed, A. (1998). A sixty-four element tactile display using shape memory alloy wires. *Displays*, *18*(3), 163-168.
- Terrile, S., Miguelañez, J., & Barrientos, A. (2021). A Soft Haptic Glove Actuated with Shape Memory Alloy and Flexible Stretch Sensors. *Sensors*, *21*(16), 5278.
- Terry, M., & Mynatt, E. D. (2002). *Recognizing creative needs in user interface design*. Paper presented at the Proceedings of the 4th Conference on Creativity & Cognition.
- Teyssier, M. (2020). *Anthropomorphic devices for affective touch communication*. Institut polytechnique de Paris.
- Thar, J., Stönnner, S., Heller, F., & Borchers, J. (2018). *Yawn: Yet another wearable toolkit*. Paper presented at the Proceedings of the 2018 ACM International Symposium on Wearable Computers.
- Torres, C., Li, W., & Paulos, E. (2016). *ProxyPrint: Supporting crafting practice through physical computational proxies*. Paper presented at the Proceedings of the 2016 ACM Conference on Designing Interactive Systems.
- Tsujita, T., Sase, K., Konno, A., Nakayama, M., Chen, X., Abe, K., & Uchiyama, M. (2013). Design and evaluation of an encountered-type haptic interface using MR fluid for surgical simulators. *Advanced Robotics*, *27*(7), 525-540.
- Ullmer, B., & Ishii, H. (2000). Emerging frameworks for tangible user interfaces. *IBM systems journal*, *39*(3.4), 915-931.
- Vahid, D. G., Jones, L., Girouard, A., & Frankel, L. (2021). *Shape changing FABRIC samples for interactive fashion design*. Paper presented at the Proceedings of the Fifteenth International Conference on Tangible, Embedded, and Embodied Interaction.
- Vallbo, A., & Johansson, R. (1978). The tactile sensory innervation of the glabrous skin of the human hand. *Active touch*, *2954*, 29-54.
- Vallgård, A., & Redström, J. (2007). *Computational composites*. Paper presented at the Proceedings of the SIGCHI conference on Human factors in computing systems.
- Van Erp, J. B., & Toet, A. (2015). Social touch in human-computer interaction. *Frontiers in digital humanities*, *2*, 2.
- van Hattum, M. T., Huisman, G., Toet, A., & van Erp, J. B. (2022). Connected Through Mediated Social Touch: "Better Than a Like on Facebook." A Longitudinal Explorative Field Study Among Geographically Separated Romantic Couples. *Frontiers in psychology*, *13*, 291.
- Velazquez, R., Pissaloux, E., Hafez, M., & Szewczyk, J. (2005). *A low-cost highly-portable tactile display based on shape memory alloy micro-actuators*. Paper presented at the IEEE Symposium on Virtual Environments, Human-Computer Interfaces and Measurement Systems, 2005.
- Veldhoen, T. (2019). Designing a Shape Shifting Object.
- Villoslada, A., Flores, A., Copaci, D., Blanco, D., & Moreno, L. (2015). High-displacement flexible shape memory alloy actuator for soft wearable robots. *Robotics and Autonomous Systems*, *73*, 91-101.
- Viscuso, S., Gualandris, S., de Ceglia, G., & Visentin, V. (2021). Shape memory alloys for space applications. In *Shape Memory Alloy Engineering* (pp. 609-623): Elsevier.
- Wang, F., Wang, L., Wang, Y., & Wang, D. (2022). Highly bendable ionic electroactive polymer actuator based on carboxylated bacterial cellulose by doping with MWCNT. *Applied Physics A*, *128*(10), 911.
- Wang, R., & Quek, F. (2010a). *Touch & talk: contextualizing remote touch for affective interaction*. Paper presented at the Proceedings of the fourth international conference on Tangible, embedded, and embodied interaction.
- Wang, R., & Quek, F. (2010b). *Touch & talk: Contextualizing remote touch for affective interaction*.
- Wang, W., Kim, N.-G., Rodrigue, H., & Ahn, S.-H. (2017). Modular assembly of soft deployable structures and robots. *Materials Horizons*, *4*(3), 367-376.
- Wang, W., Rodrigue, H., & Ahn, S.-H. (2016). Deployable soft composite structures. *Scientific reports*, *6*(1), 1-10.
- Wang, W., Rodrigue, H., Kim, H.-I., Han, M.-W., & Ahn, S.-H. (2016). Soft composite hinge actuator and application to compliant robotic gripper. *Composites Part B: Engineering*, *98*, 397-405.
- Watson, D., & Clark, L. A. (1994). The PANAS-X: Manual for the positive and negative affect schedule-expanded form.
- Weinstein, S. (1968). *Intensive and extensive aspects of tactile sensitivity as a function of body part, sex and laterality*. Paper presented at the the First Int'l symp. on the Skin Senses, 1968.

- Wheeler, R. W., Benafan, O., Gao, X., Calkins, F. T., Ghanbari, Z., Hommer, G., . . . Stebner, A. P. (2016). *Engineering design tools for shape memory alloy actuators: CSMART collaborative best practices and case studies*. Paper presented at the Smart Materials, Adaptive Structures and Intelligent Systems.
- Wiethoff, A., Schneider, H., Rohs, M., Butz, A., & Greenberg, S. (2012). *Sketch-a-TUI: low cost prototyping of tangible interactions using cardboard and conductive ink*. Paper presented at the Proceedings of the Sixth International Conference on Tangible, Embedded and Embodied Interaction.
- Williams, M. L., Landel, R. F., & Ferry, J. D. (1955). The temperature dependence of relaxation mechanisms in amorphous polymers and other glass-forming liquids. *Journal of the American Chemical Society*, 77(14), 3701-3707.
- Winter, S. H., & Bouzit, M. (2007). Use of magnetorheological fluid in a force feedback glove. *IEEE Transactions on Neural Systems and Rehabilitation Engineering*, 15(1), 2-8.
- Woodworth, R., & Schlosberg, H. (1954). *Experimental Psychology*, (rev. ed.) New York: Holt, 1954. *Department of Psychology University of Massachusetts Amherst, Massachusetts, 1002*.
- Wu, S., & Devendorf, L. (2020). *Unfabricate: designing smart textiles for disassembly*. Paper presented at the proceedings of the 2020 CHI conference on human factors in computing systems.
- Xie, Q., Meng, Q., Yu, W., Wu, Z., Xu, R., Zeng, Q., . . . Yu, H. (2023). Design of a SMA-based soft composite structure for wearable rehabilitation gloves. *Frontiers in Neurobotics*, 17, 1047493.
- Xie, Q., Meng, Q., Yu, W., Xu, R., Wu, Z., Wang, X., & Yu, H. (2023). Design of a soft bionic elbow exoskeleton based on shape memory alloy spring actuators. *Mechanical Sciences*, 14(1), 159-170.
- Yamamura, S., & Iwase, E. (2021). Hybrid hinge structure with elastic hinge on self-folding of 4D printing using a fused deposition modeling 3D printer. *Materials & Design*, 203, 109605.
- Yang, T. H., Kim, J. R., Jin, H., Gil, H., Koo, J. H., & Kim, H. J. (2021). Recent advances and opportunities of active materials for haptic technologies in virtual and augmented reality. *Advanced Functional Materials*, 31(39), 2008831.
- Yang, X., & Druga, S. (2019). *Legoons: Inflatable Construction Kit for Children*. Paper presented at the Extended Abstracts of the Annual Symposium on Computer-Human Interaction in Play Companion Extended Abstracts.
- Yao, L., Niiyama, R., Ou, J., Follmer, S., Della Silva, C., & Ishii, H. (2013). *PneUI: pneumatically actuated soft composite materials for shape changing interfaces*. Paper presented at the Proceedings of the 26th annual ACM symposium on User interface software and Technology.
- Yarosh, S., Mejia, K., Unver, B., Wang, X., Yao, Y., Campbell, A., & Holschuh, B. (2017). SqueezeBands: Mediated Social Touch Using Shape Memory Alloy Actuation. *Proceedings of the ACM on Human-Computer Interaction*, 1(CSCW), 1-18. doi:10.1145/3134751
- Yarosh, S., Wang, X., & Yao, Y. (2022). Perceptions of visual and multimodal symbolic mediated social touch: Role of technology modality, relationship, and task emotional salience. *International Journal of Human-Computer Studies*, 159, 102757.
- Yi, S., Weinberg, C., Eschen, K., & Abel, J. (2017). *Preliminary experimental study of the effect of shape setting on knitted SMA structures*. Paper presented at the Smart Materials, Adaptive Structures and Intelligent Systems.
- Yin, J., Hinchet, R., Shea, H., & Majidi, C. (2021). Wearable soft technologies for haptic sensing and feedback. *Advanced Functional Materials*, 31(39), 2007428.
- Yoshikawa, W., Sasabe, A., Sugano, K., Tsuchiya, T., Tabata, O., & Ishida, A. (2006). *Vertical drive micro actuator using SMA thin film for a smart button*. Paper presented at the 19th IEEE International Conference on Micro Electro Mechanical Systems.
- You, I., Choi, S. E., Hwang, H., Han, S. W., Kim, J. W., & Jeong, U. (2018). E-skin tactile sensor matrix pixelated by position-registered conductive microparticles creating pressure-sensitive selectors. *Advanced Functional Materials*, 28(31), 1801858.
- Youn, H. J., & Shtarbanov, A. (2022). *PneuBots: Modular Inflatables for Playful Exploration of Soft Robotics*. Paper presented at the CHI Conference on Human Factors in Computing Systems Extended Abstracts.
- Zakerzadeh, M. R., & Sayyaadi, H. (2012). Experimental comparison of some phenomenological hysteresis models in characterizing hysteresis behavior of shape memory alloy actuators. *Journal of Intelligent material systems and structures*, 23(12), 1287-1309.
- Zhang, B., & Sra, M. (2021). *Pneumod: A modular haptic device with localized pressure and thermal feedback*. Paper presented at the Proceedings of the 27th ACM Symposium on Virtual Reality Software and Technology.
- Zhang, J., Cong, M., Liu, D., Du, Y., & Ma, H. (2022). A lightweight variable stiffness knee exoskeleton driven by shape memory alloy. *Industrial Robot: the international journal of robotics research and application*, 49(5), 994-1007.
- Zhang, P., Kamezaki, M., Hattori, Y., & Sugano, S. (2022). *A Wearable Fingertip Cutaneous Haptic Device with Continuous Omnidirectional Motion Feedback*. Paper presented at the 2022 International Conference on Robotics and Automation (ICRA).
- Zheng, C., Han, B., Liu, X., Devendorf, L., Tan, H., & Yen, C. C. (2023). *Crafting Interactive Circuits on Glazed Ceramic Ware*. Paper presented at the Proceedings of the 2023 CHI Conference on Human Factors in Computing Systems.

References

- Zhu, L., Wang, B., Handschuh-Wang, S., & Zhou, X. (2020). Liquid metal-based soft microfluidics. *Small*, *16*(9), 1903841.
- Zoran, A., Shilkrot, R., Nanyakkara, S., & Paradiso, J. (2014). The hybrid artisans: A case study in smart tools. *ACM Transactions on Computer-Human Interaction (TOCHI)*, *21*(3), 1-29.
- Zuo, K., Zhang, Y., Liu, K., Li, J., & Wang, Y. (2023). Design and experimental study of a flexible finger rehabilitation robot driven by shape memory alloy. *Measurement Science and Technology*, *34*(8), 084004.

Acknowledgements

I would like to express my deepest gratitude to all those who supported and guided me throughout my PhD journey.

First of all, thank you to my supervisors, Prof.dr.ir. Kaspar Jansen and Dr. Sepideh Ghodrat. Thank you for your trust and for giving me the opportunity to do research at TU Delft. Thank you for your patience during my first year, helping me adapt to PhD life and the new environment in the Netherlands. Thank you for all of the professional guidance you gave me during my whole PhD career. Now the journey ends. I will treasure the good times we had experienced.

Thank you to all doctoral committee members. You spent time reading and reviewing my work. Some of you have come from far away to attend my defense.

Thank you to all technicians and colleagues in the Applied Lab, Mascha Slingerland, Adrie Kooijman, Martin Verwaal, and Linda Plaude. You contributed a lot to my experiment equipment and my prototypes. Thank you to Gijs Huisman, we had a nice experience of writing a paper and a good time in Cork, Ireland. Thank you to all members of the Materializing Futures Group (e.g., Alice Buso, Beyza Bozali, Jiho Kim), I learnt a lot from your research. Thank you to all colleagues in B-4-360, we had experienced nice lunch time and birthday celebration moments together.

Thank you to my friends: Yunzhong Zhou, Xueqing Miao, Fenghua Yang, Tingting Wang, Di Yan, Jun Xu, Helen Yuan, Siyuan Huang, Zhuochao Peng, Xinhe Yao, Tianhao He, Yuexin Huang, Jiwei Zhou, Dantong Qin, Xun Zhang, Hanchu Sun, Cehao Yu, Qianyi Chen. Some of you cook well and feed me with delicious food. Some of you share your research experience with me and guide me with light. Some of you play badminton well and crush me every time. A few of you did nothing but good at rambling. I will cherish these good memories.

Thank you to my girlfriend Jiyang. Maintaining a relationship across two continents is far from easy. As your day was dawning, my night was falling. It was pity for me that I cannot always be with you during your waking hours, even online, to share our happiness and sadness. A new journey is about to start. I am happy that this time, we can go through together.

Thank you to my families. You make who I am. Thank you to my country. You had been my strongest support throughout this journey.

About the Author

Qiang LIU was born on May 24, 1994 in Guangdong Province. After graduating from high school in Taishan, he started his undergraduate life in China University of Geosciences (Wuhan) in 2013. He majored in industrial design and obtained a Bachelor Degree of Engineering after four years of study. After that, he was admitted into Hunan University to study Product Design under the supervision of Prof. Li Yi. He earned a Master Degree of Fine Art in June, 2020. In the same year, he went to the Netherlands and began his PhD study in Delft University of Technology.

Qiang worked with Prof.dr.ir. Kaspar Jansen and Dr. Sepideh Ghodrat in TU Delft. His PhD research focuses on shape memory alloys' applications in the design field. He aims to open up SMAs' potential for designers. To achieve this objective, he developed some fundamental actuator elements which can be used directly, and mathematical models for predicting actuators' performance. He developed a modular toolkit for creating shape-changing objects, and presented the toolkit at TEI'24 in Cork, Ireland.

List of Publications

Liu, Q., Ghodrat, S., & Jansen, K. M. B (2022). Modelling and mechanical design of a flexible tube-guided SMA actuator. *Materials & Design*, 216, 110571.

DOI: [10.1016/j.matdes.2022.110571](https://doi.org/10.1016/j.matdes.2022.110571)

Liu, Q., Ghodrat, S., Huisman, G., & Jansen, K. M. B (2023). Shape memory alloy actuators for haptic wearables: A review. *Materials & Design*, 112264.

DOI: [10.1016/j.matdes.2023.112264](https://doi.org/10.1016/j.matdes.2023.112264)

Liu, Q., Ghodrat, S., & Jansen, K. M. B (2024). Design and modelling of a reversible shape memory alloy torsion hinge actuator. *Materials & Design*, 237, 112590.

DOI: [10.1016/j.matdes.2023.112590](https://doi.org/10.1016/j.matdes.2023.112590)

Liu, Q., Ghodrat, S., & Jansen, K. M. B (2024, February). Mimosa: Modular Self-folding Hinges Kit for Creating Shape-changing Objects. In *Proceedings of the Eighteenth International Conference on Tangible, Embedded, and Embodied Interaction* (pp. 1-13). DOI: [10.1145/3623509.3633381](https://doi.org/10.1145/3623509.3633381)

Lücker, M., Huisman, G., **Liu, Q.**, and Ghodrat, S. Shape-memory origami for gentle haptic feedback. In *2023 IEEE World Haptics Conference (WHC)*, Work-in-Progress. IEEE, 2023.

